

Electronic, Vibronic, and Structural Properties of Fluorinated Rubrene

Dissertation

der Mathematisch-Naturwissenschaftlichen Fakultät
der Eberhard Karls Universität Tübingen

zur Erlangung des Grades eines
Doktors der Naturwissenschaften
(Dr. rer. nat.)

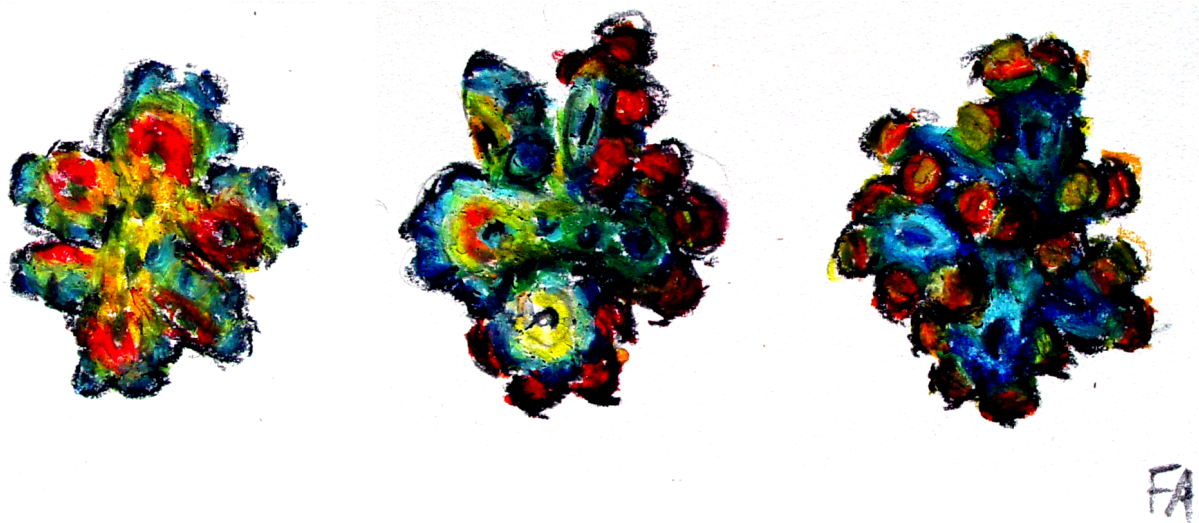
vorgelegt von

Falk Anger

aus Freiburg im Breisgau

Tübingen

2015



Gedruckt mit Genehmigung der Mathematisch-Naturwissenschaftlichen Fakultät der Eberhard Karls Universität Tübingen.

Tag der mündlichen Qualifikation: 18.12.2015

Dekan: Prof. Dr. Wolfgang Rosenstiel

1. Berichterstatter: Prof. Dr. Frank Schreiber

2. Berichterstatter: Prof. Dr. Alfred Meixner

CONTENTS

1	Introduction	1
1.1	Applications of organic semiconductors (OSCs)	1
1.2	Relevant properties of OSCs	3
1.2.1	Optical properties	3
1.2.2	Interfaces of OSCs and their energy alignment	4
1.2.3	Molecular vibrational fingerprint and transport properties of OSCs	4
1.2.4	Molecular order and crystallinity	5
1.2.5	Stability of OSCs	5
1.3	Materials under investigation	5
1.3.1	The rubrene (RUB) molecule	6
1.3.2	Applications of RUB	7
1.3.3	Partially (F ₁₄ -RUB) and fully (PF-RUB) fluorinated rubrene	8
1.4	Outline	9
2	Fundamentals	13
2.1	Optical properties in continuous media	13
2.1.1	Kramers-Kronig relation	13
2.1.2	Absorption of electromagnetic waves in media	15

CONTENTS

2.1.3	Diffraction and transmission of electromagnetic waves at an interface	16
2.1.4	Brewster's angle condition	17
2.2	Vibrational properties of molecules	18
2.2.1	Electric dipole moment and polarizability	18
2.2.2	Molecular symmetry and optical excitation of vibrational modes	19
2.3	Electronic excitation and ionization of molecules	21
2.3.1	The Franck-Condon principle	21
2.3.2	Electron transfer in a medium	24
2.3.3	Photoemission from solids	25
3	Methods	29
3.1	Theoretical methods	29
3.1.1	The Hartree-Fock (HF) approach	29
3.1.2	Density functional theory (DFT)	30
3.1.3	Hybrid functionals	31
3.1.4	Basis sets	31
3.1.5	Time-dependent density functional theory (TD-DFT)	32
3.1.6	Computation of molecular properties using TURBMOLE 6.4	32
3.2	Experimental methods	34
3.2.1	Sample preparation	34
3.2.2	Cyclic voltammetry (CV)	37
3.2.3	Spectroscopic ellipsometry	40
3.2.4	Photoluminescence (PL) spectrometry, Raman spectrometry, and light microscopy	42
3.2.5	Fourier-transform infrared (FT-IR) spectrometry	44
3.2.6	Photoelectron spectrometry (PES) at a synchrotron light source	46
3.2.7	Atomic force microscopy (AFM)	48
3.2.8	X-ray reflectivity (XRR) and grazing incidence X-ray diffraction (GIXD)	49

4	Electronic excitation of RUB, F₁₄-RUB, and PF-RUB	51
4.1	Optical Properties of RUB, F ₁₄ -RUB, and PF-RUB in thin films and solution	52
4.1.1	Experimental conditions	52
4.1.2	Experimental spectra	52
4.1.3	DFT calculations	55
4.1.4	Comparison of experimental and theoretical values	57
4.1.5	Concluding remarks	59
4.2	Oxidation potential of RUB, F ₁₄ -RUB, and PF-RUB	59
4.2.1	Experimental conditions	59
4.2.2	Optical absorption of thin films	60
4.2.3	Electrochemical properties in solution	62
4.2.4	DFT calculations	64
4.2.5	Concluding remarks	66
4.3	Ultraviolet and X-ray photoelectron spectroscopy of PF-RUB and F ₁₄ -RUB on Au(111) and Ag(111)	66
4.3.1	Experimental conditions	67
4.3.2	Valence spectra	67
4.3.3	Core-level spectra	71
4.3.4	Discussion	73
4.3.5	Concluding remarks	78
5	Vibronic excitation of RUB, F₁₄-RUB, and PF-RUB	79
5.1	Computed vibrational modes	80
5.1.1	Infrared (IR) modes	80
5.1.2	Raman modes	81
5.2	Experimental IR and Raman spectra	84
5.2.1	Experimental conditions	84
5.2.2	IR and Raman spectra of PF-RUB	85
5.2.3	Molecular conformation of PF-RUB	88
5.2.4	Raman imaging of PF-RUB thin films	93

CONTENTS

5.2.5	IR and Raman spectra of F ₁₄ -RUB	95
5.3	Concluding remarks	97
6	Structure and morphology of F₁₄-RUB and PF-RUB thin films	101
6.1	Crystal structures of fluorinated rubrene	102
6.2	Pristine thin films	106
6.2.1	Thin film growth	106
6.2.2	Postgrowth dewetting	107
6.3	Morphology and structure of matured thin films	109
6.3.1	Thin film morphology	109
6.3.2	Grazing incidence X-ray diffraction	110
6.4	Concluding remarks	116
7	Summary and outlook	117
7.1	Rubrene with different degree of fluorination: Molecules in solution, pristine thin films on SiO ₂ , and DFT computa- tions in free space	118
7.2	Ordered structures of fluorinated rubrene molecules in thin films	120
7.3	Application potential of fluorinated rubrene and outlook	122
	Appendix	125
A	Extended cyclic voltammograms	125
B	Raman spectra of PF-RUB and F ₁₄ -RUB thin films acquired at 785 nm	126
	List of figures	129
	List of tables	133
	List of abbreviations	135
	Bibliography	137

CHAPTER 1

INTRODUCTION

Nature provides a large variety of organic materials exceeding the number of known inorganic compounds by far [1]. During the recent past it has become clear that organic semiconductors (OSCs) offer a substantial potential for applications in the field of opto-electronics, not at least due to their almost unlimited tunability [2–6]. Plenty of work has been put into the development of devices made of OSCs, for example organic light-emitting diodes (OLEDs) [7], organic solar cells [8–19], organic field effect transistors (OFETs) [20–24], and non-volatile memory elements [25–28]. As a consequence of immense progress emerging from investigating applications for OSCs during the recent past, better adjusted and more specified materials have been highly requested [29–31]. This study examines two novel OSCs that were synthesized by Y. Sakamoto and T. Suzuki (Institute for Molecular Science, Okazaki, Japan), namely perfluoro-5,6,11,12-tetraphenyltetracene ($C_{42}F_{28}$, PF-RUB) and 1,2,3,4-tetrafluoro-5,12-bis(2,3,4,5,6-pentafluorophenyl)-6,11-diphenyltetracene ($C_{42}F_{14}H_{14}$, F_{14} -RUB). The compounds are derivatives of the well-studied rubrene (5,6,11,12-tetraphenyltetracene, $C_{42}H_{28}$, RUB), which is known for its very high charge carrier mobility of holes.

1.1 Applications of organic semiconductors (OSCs)

The conjugated π -electron system, which is significantly involved in their optical and charge transport properties [32], is the reason why OSCs appear as colorful dyes covering the entire visible spectrum in general. Rubrene (lat. *ruber*, red), in particular, first synthesized in 1926 [33], is known for its deep red color. OSCs have received increasing attention during the last years and have become a serious competitor for

inorganic semiconductors in the field of opto-electronics. However, despite strong improvements in several aspects like charge carrier mobility that nowadays reaches the conductivity of amorphous silicon, it is unlikely that inorganic semiconductors will be replaced totally. Most probably, OSCs will be an alternative option to inorganic semiconductors, each being used for applications according to their respective advantages.

Generally, one distinguishes between two classes of OSCs, polymers and oligomers [27]. While polymers are long chains of typical subunits (monomers) assembled together, oligomers are small-molecule OSCs without specific periodicity. Oligomers usually consist of aromatic hydrocarbons, which include polycyclic aromatic compounds like rubrene or pentacene [30].

Opto-electronic organic devices can be constructed to be very thin, which makes them lightweight, highly flexible and transparent for applications like large-area electronic displays [34]. One of their greatest advantages is their flexibility [34–36], which allows for the construction of devices in completely new industrial areas such as clothing. Yet, they can be driven at low voltages [37]. On the other hand, feasible production methods and generally cheap raw materials make OSCs promising candidates for low-cost electronics [38]. By means of functional painting or printing using ink-jet technology, OSCs permit completely new ways to fabricate devices [39]. Moreover, since the interaction cross section of light with OSCs is very high, remarkably thin structures are already sufficient for effective opto-electronic devices, which is of particular interest e. g. for transparent displays. Moreover, several organic materials have anisotropic properties that can be utilized as for instance in applications like liquid crystal displays (LCDs). Polar molecules can be employed in device architectures to modify the hole injection barrier at surfaces.

Due to their chemical properties, OSCs can be processed at relatively low temperatures. Nevertheless, crystals and thin films of OSCs are very sensitive to impurities and already tiny amounts of impurities can seriously influence their properties negatively. One reason for the swift advance of OSCs during the last decades rests on the improvement of ultrahigh vacuum (UHV) techniques that allow for thin films of organic compounds with a very high degree of purity [40,41]. While organic molecular beam deposition (OMBD) under UHV conditions is often used for small-molecule OSCs, spin-coating is very popular for the processing of polymers.

Nevertheless, the reaction potential of OSCs remains a challenging task since hydrocarbons are very sensitive to oxygen [42]. One strategy to overcome this problem is the substitution of either particular molecular sidegroups or hydrogen atoms by fluorine, which is the most electronegative element. Despite several efforts to synthesize

more stable RUB derivatives that often contain fluorine atoms, an extensive or even complete fluorination as in the case of the newly synthesized F₁₄-RUB and PF-RUB has not been presented [43–48].

1.2 Relevant properties of OSCs

Whereas inorganic semiconductors can be modified by doping *i. e.* including of foreign atoms, which donate or accept electrons, one can tune OSCs by substituting chemical groups in the respective compound. This ability to exchange functional groups within the molecules explains the huge number and versatility of available organic materials. It alters the compounds entirely and has strong implications on many physical properties. Particularly important are the optical and electronic properties of the materials, but also their aggregation behavior, which are significant for the function and performance of applications.

1.2.1 Optical properties

The optical properties of OSCs are of particular interest for nearly all applications in the field of opto-electronics. The energy gap between the highest occupied molecular orbital (HOMO) and the lowest unoccupied molecular orbital (LUMO), which corresponds to the energy gap between valence and conduction band in inorganic semiconductors, is often located at energies corresponding to visible light. Excitation from the HOMO to the LUMO in OSCs usually results in the creation of excitons that are weakly bound electron-hole pairs and are located at one or a few molecules [1, 49–51]. In OPVs, excitons can be generated by incident light and can become separated into a free electron and a free hole at an interface. Thereby, the energy of the exciton determines the upper limit of the open circuit voltage. In an analogous process in OLEDs, free electrons and holes, which are supplied by electrodes, can form an exciton in an organic layer. When releasing the energy of the exciton upon decay, the OLED can emit light. Hence, the HOMO-LUMO transition of an OSC directly determines the efficiency of OPVs and the color emitted by an OLED buildt of the material [7, 10, 13], which underlines the importance in elaborate fundamental understanding of the optical properties of the OSC. Since charge separation occurs at the interface of a donor and acceptor material in OPV devices, excitonic life-time and diffusion length are of particular interest.

1.2.2 Interfaces of OSCs and their energy alignment

Modern devices of OSCs are composed in a complex way with intricate architecture usually involving many layers of different materials [10, 18, 52, 53]. Knowledge of the absolute energy level alignment at the interfaces of the respective layers hence plays an important role [54]. In order to minimize the internal resistance of the device, it is crucial that the energy levels of the contacting electrodes, which often consist of a metal (in many cases aluminum) and transparent indium tin oxide (ITO), and of the organic layers are matched properly [55, 56]. However, it is a challenge to find organic compounds for the different organic layers of the device with suitable ionization potentials (IPs) that in addition are structurally compatible with each other [57]. Of particular interest are materials that are structurally similar to established OSCs like RUB, which shows a very high hole mobility, but with different IP. This can be achieved by fluorination. Moreover, one way to modify the interface between two OSCs is by introducing an interlayer with static dipole moment in between [58]. Importantly, F₁₄-RUB has a strong dipole moment along its molecular axis, while being structurally very similar to RUB.

1.2.3 Molecular vibrational fingerprint and transport properties of OSCs

The atomic nuclei within each molecule can vibrate, leading to every compound having its own unique vibrational fingerprint. The vibrations are very sensitive to the molecular geometry and the surroundings. This enables us to receive information about the molecular conformation that can point towards different crystal structures as well as information about the environment of the molecule. Moreover, knowledge of the molecular vibrations leads to the understanding of the charge transport mechanism in OSCs, which in turn also depends strongly on the respective molecular arrangement [59–61]. At low temperatures, crystals of many OSCs show band transport analogously to inorganic semiconductors. However, at RT it is assumed that in OSCs generally so-called hopping transport dominates, although some compounds like crystalline RUB seem to show band transport even at room temperature (RT) [62, 63]. In this regime, the charges literally ‘jump’ from molecule to molecule, which is combined with a ‘deformation’ of the involved molecules [64]. These ‘deformations’ can relax in terms of molecular vibrations, which, in fact, can be studied.

1.2.4 Molecular order and crystallinity

The ordering on a molecular level is in many cases essential for the functionality of an organic device, since it influences the optical properties, governs many interface effects and can crucially change the charge carrier transport [10,20]. This depends strongly on the respective compound, but also on other parameters like temperature or pressure. Molecules can form disordered systems, aggregate in a large variety of crystalline structures differing in their respective unit cells, or can nucleate in several polymorphs at the same time [65–67]. In many cases, crystals with a certain unit cell are preferred, however, for very bulky molecules as RUB or its derivatives, it is not straight-forward to predict the respective arrangement in which the molecules nucleate under a given condition [65]. Moreover, not all molecular arrangements are stable over time, particularly in the case of compounds that can adopt chiral molecular conformations. Nucleation into a desired crystal structure can be a challenging task [68]. A popular strategy to influence the growth behavior of organic thin films is to modify the substrate by another organic material, e. g. a self-assembled monolayer (SAM) [6,69,70].

1.2.5 Stability of OSCs

One of the largest challenges using OSCs is their tendency to oxidize readily in the presence of air and light [1], which seriously impacts the performance [42]. While for some time it was speculated that defects introduced by oxygen in RUB could explain the large charge carrier mobility [71–74], this idea was later rejected [75,76]. In recent years it has been discussed how oxidation of RUB can be avoided most effectively [45,77] and several attempts to find suitable RUB derivatives that show less susceptibility to oxidation have been presented [43–48].

1.3 Materials under investigation

In the following, the compounds that are studied in this thesis are briefly introduced (Fig. 1.1). While RUB has been studied extensively and also been employed for several applications, the partially fluorinated F₁₄-RUB and the perfluorinated PF-RUB are new materials.

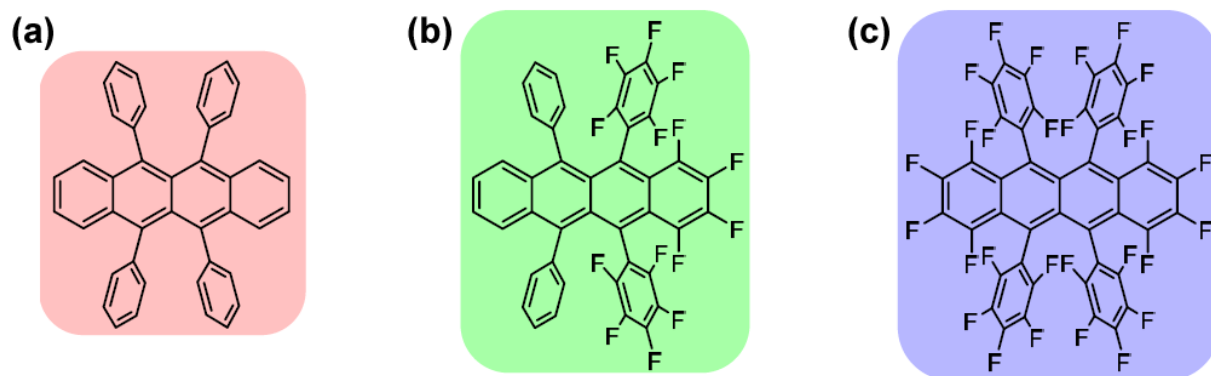


Figure 1.1: Molecular structure of (a) rubrene (RUB, C₄₂H₂₈), (b) partially fluorinated rubrene (F₁₄-RUB, C₄₂F₁₄H₁₄), and (c) perfluororubrene (PF-RUB, C₄₂F₂₈). The fluorinated compounds were synthesized and provided after purification with gradient sublimation by Prof. T. Suzuki and Prof. Y. Sakamoto (Institute for Molecular Science, Okazaki, Japan).

1.3.1 The rubrene (RUB) molecule

Amongst semiconducting organic materials, rubrene (C₄₂H₂₈, RUB) has attracted significant attention during the last years due to its very high charge carrier mobility [78–82] and its large exciton diffusion length of up to 4 μm [83–86]. The RUB molecule (5,6,11,12-tetraphenyltetracene) can be segmented into a tetracene backbone and four phenyl rings that are attached to it. In the HOMO and the LUMO, most of the electron density is located on the tetracene backbone of the molecule. Due to steric repulsion of the phenyl rings, the molecule can adopt different stable conformations in free space. At least two stable isomers either with twisted or planar backbone have been observed for the free RUB molecule, which can be represented by a *D*₂ (twisted) or e. g. the 0.16 eV more energy consuming *C*_{2h} (planar) symmetry, respectively [87]. While RUB molecules in gas phase, solution, and disordered thin films adopt the energetically favored twisted conformation, they occur planarized in crystals. A disadvantage of RUB is its tendency to form peroxide or endoperoxide under ambient conditions, which is reduced in the bulk of a crystal [88], but has strong impact on its surface or on thin films [89].

Among small-molecule semiconductors with high charge carrier mobility, as e. g. pentacene [90, 91], the highest hole mobility so far has been reported for RUB ($\mu_h = 40 \text{ cm}^2/\text{Vs}$) [78–80], which is comparable to the charge mobility of amorphous silicon. The intricate molecular structure, which makes RUB a bulky molecule, leads to an increased effective intermolecular distance in crystals or thin films compared to

other small-molecule semiconductors. Intuitively, a wider molecular spacing reduces the charge carrier mobility, since both hopping and band transport should become less likely. Nevertheless, the phenyl wings which are responsible for the wider spacing of the RUB molecules in a crystal, apparently force the tetracene backbones of the molecules into positions that increase the charge carrier mobility [92,93]. In RUB crystals, the hole mobility, which is higher than for electrons, is strongly anisotropic [84,94]. In contrast to most other OSCs, crystalline RUB appears to exhibit band transport even at room temperature [95]. The large distance between π -electron parts contribute to both easier ionizability and lower polarizability (1.1 eV) of the molecules, which lies 0.6 eV below that of most common OSCs [96].

1.3.2 Applications of RUB

Several applications have been reported for RUB, among them OPVs, OLEDs, and OFETs. Since there is a rapid advancement in the investigation and implementation of OSCs at the moment, this section is not intended to provide a complete overview and rather reviews briefly the most important developments of applications of RUB during the last ten years.

RUB has been used in bulk heterojunction (BHJ) solar cells in combination with other organic materials like tetracyanoquinodimethane (TCNQ) [97] or C_{60} [98]. Other approaches to find suitable ways to construct OPVs of RUB in combination with C_{60} involve bilayers of thin films [99,100], which have also been annealed in order to increase the crystallinity of RUB in the OPVs [85]. Moreover, it has been shown that a RUB interlayer can be used to improve the open circuit voltage in C_{60} /pentacene heterostructure OPVs [101] or can serve to adapt the energy alignment of organics in OLEDs [102]. RUB has also been used as a dopant in C_{60} or CuPc films for OPVs [103], or with 4,4'-bis[N-(1-naphthyl)-N-phenylamion]biphenyl (α -NPD) and tris(8-hydroxyquinolato)-aluminium (Alq_3) for OLED [104] applications.

Due to the very high charge carrier mobility in RUB crystals there have been many studies about the construction of OFETs containing RUB single crystals [105–111]. Also, ideas for their realization in industrial mass production with printing techniques have been presented [36,112]. Beside OFETs from single crystals, RUB organic thin film transistors (OTFTs) are of interest, since they are usually much simpler to process than single crystals. These were produced by either directly depositing RUB on SiO_2 , with [113] or without annealing [114], or by growth on organic substrates, in order to increase the crystallinity, e. g. in form of heterostructures combined with pentacene or

SAMs [115,116]. In some cases the samples also were annealed after deposition [117].

1.3.3 Partially (F_{14} -RUB) and fully (PF-RUB) fluorinated rubrene

In order to tune the electronic and optical properties of RUB, but also to enhance its stability against oxygen and tendency to form crystals, several efforts have been made to synthesize specific RUB derivatives. Different ways to modify particular atoms with sidegroups or with substitution of chemically different elements have been reported [118–121], but a major or even complete replacement of the surrounding hydrogen atoms of RUB has so far not been achieved. Partial or complete fluorination is a typical strategy for the modification of OSCs [31, 122]. With the same molecular geometry as RUB, the newly synthesized perfluoro-5,6,11,12-tetraphenyltetracene ($C_{42}F_{28}$, PF-RUB) and 1,2,3,4-tetrafluoro-5,12-bis(2,3,4,5,6-pentafluorophenyl)-6,11-diphenyltetracene ($C_{42}F_{14}H_{14}$, F_{14} -RUB) molecules provide an electronic structure that is very different from RUB.

In fact, one of the most efficient ways to tune the electronic energy level alignment of OSCs is partial or complete fluorination [120, 123–126]. In particular, the position of the HOMO and LUMO can be fine-tuned. At the same time, fluorination is a very effective way to mitigate the molecular reactivity with oxygen [127], since fluorine is the most electronegative element [87, 120, 123, 125, 128]. The large electronegativity of fluorine is expected to have a strong impact on the electronic properties of the material and also hinder oxidation most effectively [48]. Moreover, fluorinated analogues are an obvious choice for structurally compatible donor-acceptor combinations in organic electronics [129–131] since fluorinated and unsubstituted molecules usually have very similar geometries. Interestingly, not many fluorinated analogues of common unsubstituted OSCs have been studied, partly due to their nontrivial synthesis, which requires special know-how and off-standard facilities. Nevertheless, fluorination of OSCs has gained importance during the last years [132, 133] due to its very broad potential for applications and since a vast variety of small-molecule OSCs could be (per)fluorinated [122], as e. g. tetracyanoquinodimethane (TCNQ) [134], phthalocyanines [135], pentacene [123, 136, 137], tetracene [137], or oligothiophenes [138]. In some cases, substitution of organic molecules can be used to change an OSC from a hole- to an electron-conducting material, which can be compared with doping of inorganic semiconductors with foreign atoms. As it turns out, the fully or partially fluorinated RUB derivatives have significantly increased ionization energies compared to RUB. While leaving the gap intact, this makes the fluorinated variants particularly interesting as acceptor materials for organic solar cells.

The fully fluorinated PF-RUB and the partially fluorinated rubrene were synthesized and purified by temperature gradient sublimation [139] by Prof. Y. Sakamoto and Prof. T. Suzuki (Institute for Molecular Science, Okazaki, Japan). Note, that F₁₄-RUB differs from RUB and PF-RUB by its lower symmetry and associated strong dipole moment. Unsubstituted rubrene (C₄₂H₂₈, RUB) was purchased from Arcos and purified by gradient sublimation. Tab. 1.1 reports the evaporation temperatures of the three materials that were measured within our vacuum system when depositing a thin film with a rate of $\sim 2 \text{ \AA}/\text{min}$. Under these conditions PF-RUB thin films on native SiO₂ substrates are supposed to grow amorphous [87].

Compound	Measured evaporation temperature at $\sim 2 \text{ \AA}/\text{min}$
PF-RUB	$\sim 96 \text{ }^\circ\text{C}$
F ₁₄ -RUB	$\sim 135 \text{ }^\circ\text{C}$
RUB	$\sim 155 \text{ }^\circ\text{C}$

Table 1.1: Measured temperatures of the crucible for evaporation of the three compounds from our Knudsen cells with $\sim 2 \text{ \AA}/\text{min}$. The fluorinated materials have a significantly lower evaporation temperature than RUB.

All three compounds are red colored dyes (Fig. 1.2) with similar optical properties. In a sealed glass cuvette, we observe a strong red color for the three compounds diluted in Cl₂CH₂ directly after preparation. Within one day, the color changes rapidly for RUB, which becomes almost completely transparent, apparently due to oxidation [140]. Still being red, we note by eye a slight decrease in the saturation of F₁₄-RUB after two months. For PF-RUB, however, we observe still after one year only a slight decrease in the strength of the red color (see Sec. 4.2).

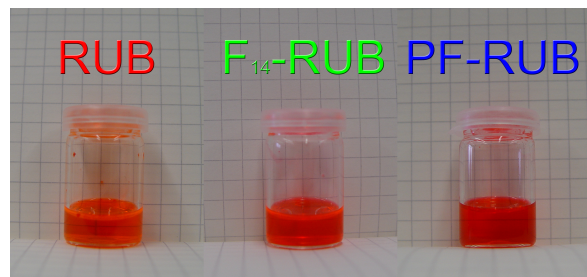


Figure 1.2: All three materials (RUB, F₁₄-RUB, and PF-RUB) are red colored organic dyes. The red color is owed to the position of the HOMO-LUMO transition of the compounds, which absorbs green light. The molecules are diluted ($\sim 2 \text{ mol/l}$) in CH₂Cl₂. For more details on the optical properties of the compounds, see Sec. 4.1 and 4.2.

1.4 Outline

This work studies PF-RUB and F₁₄-RUB, which are two novel derivatives of RUB and show a systematic increase in their degree of fluorination. Note that the partially flu-

orinated F_{14} -RUB essentially differs from the other two compounds by its associated dipole moment along its backbone. The work is based on four publications (Anger et al. [87, 141–143]) that report on the optical, electronic, and vibrational properties of the fluorinated rubrenes (F_{14} -RUB and PF-RUB) and have been found by experimental and theoretical research. However, in some chapters the results presented in this work reach beyond the information provided in the publications, in particular Chap. 6 contains to a large extent unpublished material.

A short review of the underlying physical laws and dependencies is presented in Chap. 2 that is intended to remind the reader of important relations and definitions used in this work and is meant to support him or her in later chapters. The theoretical and experimental methods used in this thesis are presented and explained in Chap. 3. The chapters thereafter (Chaps. 4, 5, and 6), report on the results of this work that deal with the properties of the fluorinated rubrenes in comparison to RUB. After that, the most essential points raised in these chapters are reviewed and condensed within a final conclusion that also ventures an outlook. The chapters reporting the results of this work (Chaps. 4, 5, and 6) are shortly outlined in the following.

Chap. 4 Electronic excitation of RUB, F_{14} -RUB, and PF-RUB

- Sec. 4.1 is based on a study [87] comparing the optical properties of PF-RUB and F_{14} -RUB, both in thin films and as monomers in solution compared to unsubstituted RUB. All three compounds show similar optical absorption bands and photoluminescence line shapes. The results are interpreted with density functional (DFT) computations of the orbital energies and time-dependent density functional theory (TD-DFT) for the HOMO-LUMO transition. Red shifts induced by the surrounding solvent or organic thin films remain much smaller than for polyacenes, in agreement with previous observations for RUB and existing models for the solvatochromic shifts.
- In Sec. 4.2, we examine the stability of PF-RUB and F_{14} -RUB against oxidation in comparison to RUB in solution with cyclic voltammetry (CV), and in thin films with spectroscopic ellipsometry [143]. One of the challenges in organic and hybrid electronics concerns the stability against exposure to ambient gases, including in particular oxygen [111, 144]. This is especially relevant for thin films, which are easier to produce than single crystals and, thus, more attractive for applications, but can often exhibit a more grainy morphology which allows oxygen to penetrate into the material [88, 145, 146]. It turns out that the fluorinated rubrenes

have a significantly increased IP, which makes them more stable against oxidation than RUB.

- Sec. 4.3 reports on thin films of fully and partially fluorinated rubrene deposited on Au(111) and Ag(111) that were investigated using ultraviolet (UPS) and X-ray photoelectron (XPS) spectroscopy [141]. We demonstrate that fluorination of the molecules is an efficient way for tuning the metal-organic interface dipole and the hole injection barrier. Moreover, the results indicate that the pronounced electrostatic dipole moment of partially fluorinated rubrene (F_{14} -RUB) has a strong impact on the growth mode of these molecules. Most notably, we infer that the first layer of F_{14} -RUB on Au(111) and Ag(111) is formed by molecules with alternating orientation of their dipole moments whereas the second layer shows a nearly uniform orientation.

Chap. 5 Vibronic excitation of RUB, F_{14} -RUB, and PF-RUB

- We investigate the vibrational properties of PF-RUB and F_{14} -RUB compared to RUB in thin films on silicon wafers with a native oxide layer as well as on silicon wafers covered with a SAM and in dichloromethane solution [142]. In comparison with computed Raman and IR spectra, we can assign the molecular modes and identify two molecular conformations for PF-RUB with twisted and planar tetracene backbone of the molecule. Moreover, we employ Raman imaging techniques to study the morphology and distribution of the molecular conformation, in PF-RUB thin films.

Chap. 6 Structure and morphology of F_{14} -RUB and PF-RUB thin films

- Using X-ray reflectivity (XRR), grazing incidence X-ray diffraction (GIXD) and atomic force microscopy (AFM), the structure and morphology of PF-RUB and F_{14} -RUB thin films are investigated. It is evidenced that pristine thin films of F_{14} -RUB and PF-RUB on SiO_2 grow smooth and disordered. However, similarly to RUB, depending on the substrate thin films of the fluorinated materials show strong and complex dewetting behavior. Matured thin films show a (poly)crystalline structure and are compared with unit cell parameters of the materials that have been found by Y. Sakamoto and T. Suzuki.

CHAPTER 2

FUNDAMENTALS

This chapter reviews the most important physical laws and dependencies that appear in this thesis. It is intended to support the reader in later chapters. Since it is reviewing the most important terms and definitions only briefly, it lies in the nature of this chapter that it remains incomplete and can mention only some selected topics of relevance.

The first section deals about optical properties in continuous media as it is known from classical physics. Then, in the second part the symmetry and vibrational properties of the compounds of interest are discussed in a semi-classical way. The last part reviews a quantum mechanical description of molecular properties, but also their ionizability in media.

2.1 Optical properties in continuous media

This section recapitulates the most important properties of electromagnetic waves interacting with continuous media.

2.1.1 Kramers-Kronig relation

When an electromagnetic wave with electric field \vec{E} and magnetic field \vec{H} travels within a continuous medium, the fields are related to the material by

$$\vec{D} = \varepsilon_0 \vec{E} + \vec{P} = \varepsilon_0 \varepsilon_r \vec{E} \qquad \vec{B} = \mu_0 \vec{H} + \vec{J} = \mu_0 \mu_r \vec{H}. \qquad (2.1)$$

Here, \vec{P} (\vec{J}) is the linear response function that is conjugated to the electric (magnetic) field \vec{E} (\vec{H}), the macroscopic electric (magnetic) polarization. The electric (magnetic) susceptibility χ_e (χ_m) is then defined as

$$\chi_e = \frac{1}{\varepsilon_0} \frac{\partial P}{\partial E} \quad \chi_m = \frac{1}{\mu_0} \frac{\partial J}{\partial H} \quad (2.2)$$

and is related to the permittivity and permeability *via* $\varepsilon_r = \chi_e + 1$ and $\mu_r = \chi_m + 1$, respectively. As a consequence, one defines for the propagation of an electromagnetic wave through a medium the complex refractive index \tilde{n} by

$$\tilde{n}^2(\omega) = (n + ik)^2 = \mu_r(\omega) \cdot \varepsilon_r(\omega) \quad (2.3)$$

It consists of real and imaginary part n and k (extinction coefficient), respectively, and is related to the relative permittivity ε_r and permeability μ_r of the medium. In most materials μ_r is very close to 1 for optical frequencies. This reduces Eq. 2.3 to

$$\tilde{n}^2(\omega) = \varepsilon_r(\omega) = \varepsilon_1(\omega) + i\varepsilon_2(\omega), \quad (2.4)$$

where we have split up the the relative permittivity into its real and imaginary parts, $\varepsilon_1 = n^2 - k^2$ and $\varepsilon_2 = 2nk$, respectively.

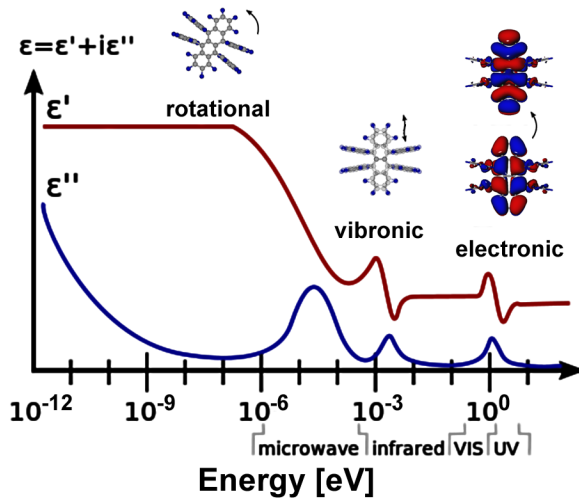


Figure 2.1: Real and imaginary part of the dielectric function. Molecules can absorb electromagnetic waves in different energy regions leading to absorption peaks in ε_2 . Depending on the amount of energy, different excitations (electronic, vibronic or rotational) can occur. Ionization of the molecules happens at even higher energies (not shown in this sketch, see Fig. 2.7). ε_1 and ε_2 are related to each other since they are Kramers-Kronig consistent. Graphic adapted with modification from Ref. [147].

Moreover, real and imaginary part of the permittivity are linked by the Kramers-Kronig relation, which generally can be applied to conjugated physical quantities that

are connected by a susceptibility.

$$\frac{\varepsilon_1(\omega)}{\varepsilon_0} - 1 = \frac{1}{\pi} \mathcal{P} \int_{-\infty}^{\infty} \frac{\frac{\varepsilon_2(\omega')}{\varepsilon_0}}{\omega' - \omega} d\omega' \quad \frac{\varepsilon_2(\omega)}{\varepsilon_0} = -\frac{1}{\pi} \mathcal{P} \int_{-\infty}^{\infty} \frac{\frac{\varepsilon_1(\omega')}{\varepsilon_0} - 1}{\omega' - \omega} d\omega' \quad (2.5)$$

The underlying mechanism is the impulse-response principle. \mathcal{P} designates the Cauchy principal value. This means that both $\varepsilon_1(\omega)$ and $\varepsilon_2(\omega)$ contain all information of the respective other component, provided that the function is known for all ω (Fig. 2.1).

2.1.2 Absorption of electromagnetic waves in media

An electromagnetic wave described by its electric field $\vec{E}(\vec{x}, t)$ usually becomes attenuated when passing through a medium with refractive index \tilde{n} .

$$\begin{aligned} \vec{E}(\vec{x}, t) &= \vec{E}_0 e^{i(\vec{k} \cdot \vec{x} - \omega t)} \underbrace{=} \vec{E}_0 e^{i(\frac{\tilde{n}\omega x}{c} - \omega t)} \underbrace{=} \vec{E}_0 e^{i(\frac{(n+ik)\omega x}{c} - \omega t)} \\ &= \vec{E}_0 e^{i(\frac{n\omega x}{c} - \omega t)} e^{-\frac{k\omega x}{c}} \end{aligned} \quad (2.6)$$

Here, $\vec{k} = \tilde{n}\omega\hat{e}_x/c$ is the dispersion relation in the medium, c denotes the speed of light. The transmitted intensity $I(\omega)$ is given by

$$\begin{aligned} I(\omega) &= \frac{1}{2} \varepsilon_0 c |\tilde{n}| \cdot |\vec{E}(\vec{x}, t)|^2 = \frac{1}{2} \varepsilon_0 c |\tilde{n}| \cdot \underbrace{E_0^2}_{=I_0} \cdot \underbrace{|e^{i(\frac{n\omega x}{c} - \omega t)}|^2}_{=1} \cdot |e^{-\frac{k\omega x}{c}}|^2 \\ &= I_0 e^{-\frac{2k\omega}{c}x} = I_0 e^{-\xi(\omega)x}, \end{aligned} \quad (2.7)$$

which is known as Beer-Lambert-Bouguer law. It introduces the attenuation coefficient $\xi(\omega)$ that is related to the extinction coefficient k .

One application of the Beer-Lambert-Bouguer law is the measurement of a solute (e. g. organic molecules) that is diluted in a transparent solvent. For sufficiently low concentration of the solute, its influence on the real part of the refractive index can be neglected ($n(\omega) \approx n_{\text{solvent}}(\omega)$), but $\varepsilon_2(\omega) \approx \varepsilon_{2,\text{solute}}(\omega)$ is dominated by the solute. As a consequence, the attenuation coefficient $\xi(\omega)$ becomes proportional to $\varepsilon_{2,\text{solute}}(\omega)$,

$$\xi(\omega) = \frac{2\omega k_{\text{total}}(\omega)}{c} \approx \frac{\omega \varepsilon_{2,\text{solute}}(\omega)}{c n_{\text{solvent}}(\omega)}. \quad (2.8)$$

Electronic transitions of molecules in solution depend strongly on the type of solvent and can have additional bathochromic or hypsochromic shifts $\Delta\nu$ that can be determined from the slope of the solvatochromic plot [148,149],

$$\Delta\nu = p\varphi(\tilde{n}^2), \quad \text{with} \quad \varphi(\tilde{n}^2) = (\tilde{n}^2 - 1)/(\tilde{n}^2 + 2). \quad (2.9)$$

2.1.3 Diffraction and transmission of electromagnetic waves at an interface

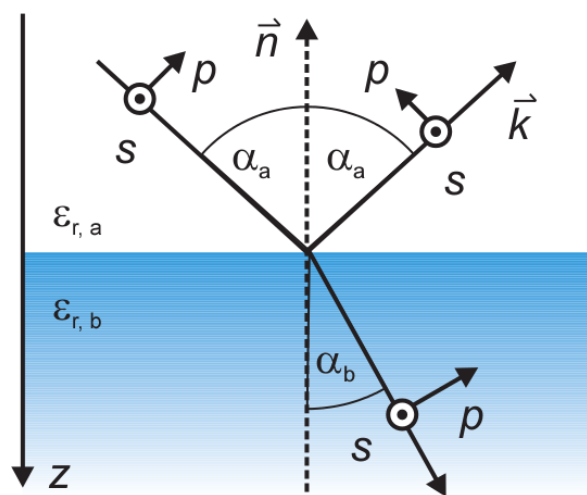


Figure 2.2: Diffraction of an electromagnetic wave at a continuous interface from a medium a with refractive index $\varepsilon_{r,a}$ to a medium b with $\varepsilon_{r,b} > \varepsilon_{r,a}$. The incident wave is split up into a reflected and refracted beam. In general all rays have a perpendicular (s , German “senkrecht”) and parallel (p , German “parallel”) component, with respect to the page. Slightly modified taken from Ref. [150].

When an electromagnetic wave travels from a medium a of refractive index \tilde{n}_a into a second medium b of refractive index \tilde{n}_b , both reflection and refraction can occur (Fig. 2.2). The relation between the angles α_a and α_b is given by Snell’s law.

$$\frac{\sin \alpha_a}{\sin \alpha_b} = \frac{\tilde{n}_b}{\tilde{n}_a} \quad (2.10)$$

The incident electromagnetic wave can be decomposed into two planar waves with parallel (p) and perpendicular (s) polarization. Depending on the phase shift and the amplitudes E_p^{in} and E_s^{in} of the electric field of the two waves, the light is polarized either linearly (no phase shift) or elliptically (general case). The Fresnel equations describe how much of the light is reflected ($r_{s/p}$) and refracted ($t_{s/p}$), *i. e.* transmitted, at the interface.

$$r_p = \frac{\sqrt{\varepsilon_{r,b}} \cos \alpha_a - \sqrt{\varepsilon_{r,a}} \cos \alpha_b}{\sqrt{\varepsilon_{r,b}} \cos \alpha_a + \sqrt{\varepsilon_{r,a}} \cos \alpha_b} \quad \text{and} \quad r_s = \frac{\sqrt{\varepsilon_{r,a}} \cos \alpha_a - \sqrt{\varepsilon_{r,b}} \cos \alpha_b}{\sqrt{\varepsilon_{r,a}} \cos \alpha_a + \sqrt{\varepsilon_{r,b}} \cos \alpha_b} \quad (2.11)$$

$$t_p = \frac{2\sqrt{\varepsilon_{r,a}} \cos \alpha_a}{\sqrt{\varepsilon_{r,b}} \cos \alpha_a + \sqrt{\varepsilon_{r,a}} \cos \alpha_b} \quad \text{and} \quad t_s = \frac{2\sqrt{\varepsilon_{r,a}} \cos \alpha_a}{\sqrt{\varepsilon_{r,a}} \cos \alpha_a + \sqrt{\varepsilon_{r,b}} \cos \alpha_b} \quad (2.12)$$

The reflectance R and transmittance T are for each, s and p , polarization related to the Fresnel coefficients r and t , respectively.

$$R_{p/s} = |r_{p/s}|^2 \quad \text{and} \quad T_{p/s} = \frac{\sqrt{\varepsilon_{r,b}} \cos \alpha_b}{\sqrt{\varepsilon_{r,a}} \cos \alpha_a} |t_{p/s}|^2 \quad (2.13)$$

Interaction of an electromagnetic wave at more than one interface, leads to more complex models that can be described by a matrix formalism [150].

2.1.4 Brewster's angle condition

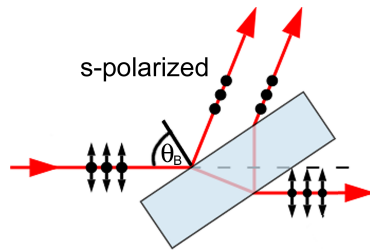


Figure 2.3: Transmission of an electromagnetic wave through a slice under the Brewster's angle condition ($\theta = \theta_B$). Multiply reflected beams are exclusively s -polarized.

A special case occurs for the so-called Brewster's angle condition, which is reached for $\alpha_a + \alpha_b = 90^\circ$. In this situation, the direction of the reflected parallel component is colinear with the wavevector of the incident wave. As a consequence no parallel polarized light is reflected ($R_p = 0$) or in other words, the reflected light is purely perpendicular polarized. The Brewster's angle of silicon is at $\theta_B \approx 74.1^\circ$. The advantage of measuring under the Brewster's angle condition has been exploited in this thesis in two aspects.

1. For ellipsometry measurements, the ratio r_s/r_p is of importance (Sec. 3.2.3). For $R_p \rightarrow 0$, this fraction becomes extreme which results in an improvement of the signal-to-noise ratio.

2. Silicon is transparent for electromagnetic waves in the infrared. The surface of a (polished) wafer reflects the incident beam well, which leads to multiple reflection between the surfaces (Fig. 2.3). In a setup with the incident beam entering the wafer under the Brewster's angle condition ($\theta = \theta_B$), all multiply refracted beams are *s*-polarized. Hence, on shining purely *p*-polarized onto the wafer in Brewster's angle condition, disturbing multiply refracted beams can be effectively suppressed.

2.2 Vibrational properties of molecules

This section summarizes the electric properties of molecules and how they are connected to their ability to be excited vibronically. It follows a semiclassical description.

2.2.1 Electric dipole moment and polarizability

Being uncharged by definition, neutral molecules do not possess an electric monopole and only some neutral molecules have a static dipole moment (as e. g. F₁₄-RUB). Nevertheless, almost all compounds can develop a dipole moment upon application of an electric field. The polarizability

$$\alpha(\omega) = \frac{\mu_{\text{ind}}}{\varepsilon_0 E(\omega)}. \quad (2.14)$$

of a molecule is a measure for its ability to respond to an external electric field $E(\omega)$ and form an electric dipole moment μ_{ind} [96, 151].

While the macroscopic dielectric constant ε_r of a material depends strongly on the ordering of the molecules, the polarizability is a molecular property. Analogously to ε_r , the polarizability $\alpha(\omega)$ is in general a tensor with complex entries. The Clausius-Mossotti relation connects the macroscopic permittivity ε_r with the molecular polarizability $\alpha(\omega)$ for homogeneous and isotropic diluted media,

$$\frac{\varepsilon_r(\omega) - 1}{\varepsilon(\omega) + 2} = \frac{N\alpha(\omega)}{3\varepsilon_0}, \quad (2.15)$$

with the volume density N of the molecules and the average molecular polarizability $\alpha(\omega)$. Generally, the polarizability $\alpha(\omega)$ of a molecule increases with the volume being

occupied by its electrons. As a consequence, in a simplified picture the overall polarizability of molecules containing fluorine is expected to be larger than the polarizability of molecules containing hydrogen.

2.2.2 Molecular symmetry and optical excitation of vibrational modes

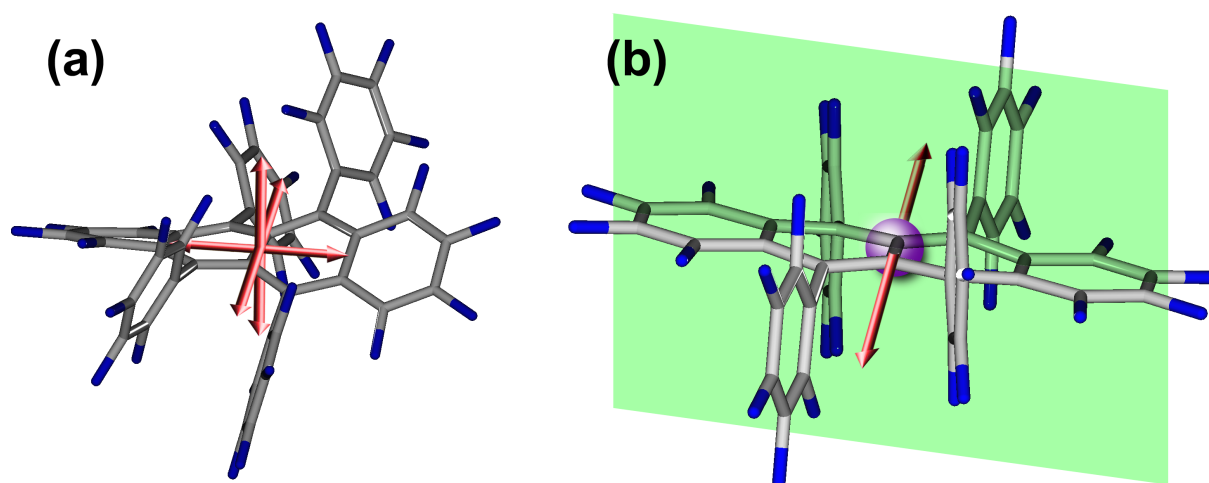


Figure 2.4: (a) Twisted and (b) planar conformation of the rubrene molecule. While the twisted molecule (a) is invariant to rotation by π around x -, y -, and z -axis (red arrows), each, the planar conformer (b) is mirror symmetric according to the yz -plane (green), is invariant under rotation by π around the x -axis (red arrow), and has a center of inversion (pink ball). Hence, the twisted and planar conformations can be described by the point groups D_2 and C_{2h} , respectively. The symmetry of the partially fluorinated F_{14} -RUB molecule is reduced. Its twisted conformer is invariant to rotation by π merely around the y -axis, whereas its planar conformation is only mirror symmetric (in the yz -plane). Thus, the twisted and planar conformations of the F_{14} -RUB molecule can be described by the point groups C_2 and C_s , respectively.

A non-linear molecule in free space has a total number of $3N - 6$ vibrational modes, where N is the number of atoms in the molecule. In analogy to a classical model, the energy of a molecular vibration is determined by the reduced mass μ of the involved atoms and by the type of vibration (e. g. stretching or bending), which is described by the coupling constant k ,

$$\hbar\omega \propto \sqrt{\frac{k}{\mu}}. \quad (2.16)$$

Point group	Representation of vibrational modes	
	with changing dipole moment (direction)	without changing dipole moment
D_2	$B_1(z), B_2(y), B_3(x)$	A
C_{2h}	$A_u(z), B_u(x, y)$	A_g, B_g
C_2	$A(z), B(x, y)$	
C_s	$A'(x, y), A''(z)$	

Table 2.1: The vibrations of the RUB, PF-RUB, and F_{14} -RUB molecules that have all an identical molecular backbone can be described by elements of different molecular point groups, depending on their respective symmetry. Some of the elements (symmetries) are conjugated with a change in the dipole moment and are thus IR active. For the centrosymmetric RUB and PF-RUB molecules (D_2 and C_{2h} point group), Raman and IR active modes are mutually exclusive (in particular modes with A and A_g symmetry, respectively, are Raman active). In the case of F_{14} -RUB, vibrations belonging to A and A' representation of the C_2 and C_s point group, respectively, are Raman active.

In quantum mechanics, the energy $\hbar\omega$ needed for a vibronic excitation is quantized. Vibrational modes can be excited optically by absorption of electromagnetic waves in the infrared (IR) or by scattering of visible light, the Raman effect [152]. Alternatively to optical activation can vibrons be thermally occupied.

The optical activities of the vibrational modes depend strongly on the redistribution of the molecular charges and their associated change in the molecular symmetry, which is inferred from the respective molecular vibration [153]. The backbone of the rubrene (RUB) molecule can adopt different conformations, e. g. it can have a twisted or planar backbone that correspond to different molecular symmetries, which can be described by the point groups D_2 and C_{2h} , respectively. Fig. 2.4 shows the symmetry of these two conformers. The symmetry is reduced for the partially fluorinated F_{14} -RUB molecule (point groups C_2 and C_s for twisted and planar, respectively), which is unsubstituted at one side, while it is fluorinated at the other half.

Each of the vibrational modes of the molecular models in Fig. 2.4 can be assigned to one symmetry representation listed in Tab. 2.1. Excitation from an initial to a final vibronic state can be accompanied by a non-zero transition dipole moment $d\mu/dQ \neq 0$, or by a non-zero transition polarization $d\alpha/dQ \neq 0$. This determines, if a vibrational mode is either infrared(IR)-active ($d\mu/dQ \neq 0$), Raman-active ($d\alpha/dQ \neq 0$), none of them, or both of them (Fig. 2.5). Vibrational modes of centrosymmetric molecules cannot be both Raman and IR active at the same time. Note that, this rule applies for RUB and

PF-RUB since they are centrosymmetric, but it is not valid for F_{14} -RUB.

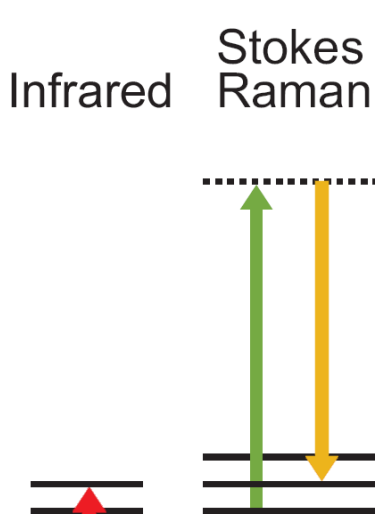


Figure 2.5: *Left: If a vibrational mode is accompanied by a change in the electric dipole moment of the molecule ($d\mu/dQ \neq 0$), an electromagnetic wave with energy $\hbar\omega$ can be absorbed and the mode becomes excited. The energy for molecular vibrations usually lies in the near-infrared region, thus having an energy $\hbar\omega \sim 100$ meV.*

Right: Another way for optical excitation of a molecular vibration is given for vibrational modes providing a change in the electric polarization ($d\alpha/dQ \neq 0$) upon excitation. In a two-photon process (Raman-scattering), a photon with much higher energy than necessary for the excitation of the vibron can be scattered at the molecule and trigger a vibrational transition. In the Raman process, the photon scatters slightly redshifted from the molecule (Stokes Raman) upon excitation, whereas the photon becomes blueshifted, if the vibron is relaxed during the process (Anti-Stokes Raman, not shown).

2.3 Electronic excitation and ionization of molecules

This Section gives a short overview over the electronic excitation and relaxation of molecules and their connection to vibronic excitation [151]. More precisely, it introduces the Franck-Condon principle and the electron-phonon coupling constant S (Huang-Rhys parameter). Moreover, it discusses shortly the ionization potential (IP) of molecules in continuous media and also the photoemission from the surface of a solid.

2.3.1 The Franck-Condon principle

Molecular orbitals

In a quantum mechanical description, every atom, molecule or crystalline solid has a certain number of discrete energy states E_i that can be assigned to orbitals. In equilibrium, the molecule resides in its ground state, which is the state with overall lowest energy. The highest occupied molecular orbital (HOMO) and the lowest unoccupied molecular orbital (LUMO) correspond to the conducting and valence band in inorganic semiconductors, respectively. Being in thermodynamical equilibrium, molecular excitations follow a Boltzmann distribution, if they can be considered to be isolated on

specific molecules, as e. g. vibronic excitations. Vibrational modes are most likely unoccupied at room temperature since the energies that are needed to excite a vibron on a molecule are usually much larger than thermal energy ($\hbar\omega \gg k_B T$).

The energy E of an eigenstate of a molecule can be determined by the Schrödinger equation with Hamiltonian \hat{H}

$$\hat{H}|\Psi\rangle = E|\Psi\rangle. \quad (2.17)$$

The adiabatic (or Born-Oppenheimer) approximation allows a separation of the electronic and vibrational dynamics of the neutral ground state of a molecule, [154]

$$\Psi = \psi \cdot \chi \quad \text{and} \quad \hat{H} = \hat{H}_\psi + \hat{H}_\chi, \quad (2.18)$$

where ψ denotes the electronic and χ the vibrational component of the wavefunction. In other words, this can be understood in terms of an almost instantaneous transition between the electronic states versus a relatively slow motion of the heavy nuclei of the molecule. Electronic transitions occur on a timescale of $\sim 10^{-15}$ s, while atomic nuclei relax on an essentially larger timescale of roughly $\sim 10^{-13}$ s. The probability of an electronic transition (excitation of a vibron) can be described by the oscillator strength f , which is related to the transition dipole by $f \propto (d\mu/dQ)^2$. The electronic potential of a two-atomic molecule is described by a Morse potential, which defines the energies and eigenstates of the molecular vibrations. Usually, the Morse potential is approximated by a harmonic oscillator model with equidistant energy levels in some set of normal coordinates Q .

$$\hat{H}_\chi = \frac{\hat{p}^2}{2m} + \frac{m\hat{\omega}^2}{2} \quad (2.19)$$

This approximation leads to deviations for vibrational modes that are computed using the harmonic oscillator from the real modes following the true potential, which flattens out particularly for higher energies. In order to account for this deviation, the energy axes of computed vibrational spectra are usually rescaled with a linear scaling factor $\lesssim 1.00$ [142, 155].

Displaced harmonic oscillator

It is a good approximation to assume that the potential of the electronically first excited state has a similar shape as the ground state (Fig. 2.6), which implies that the

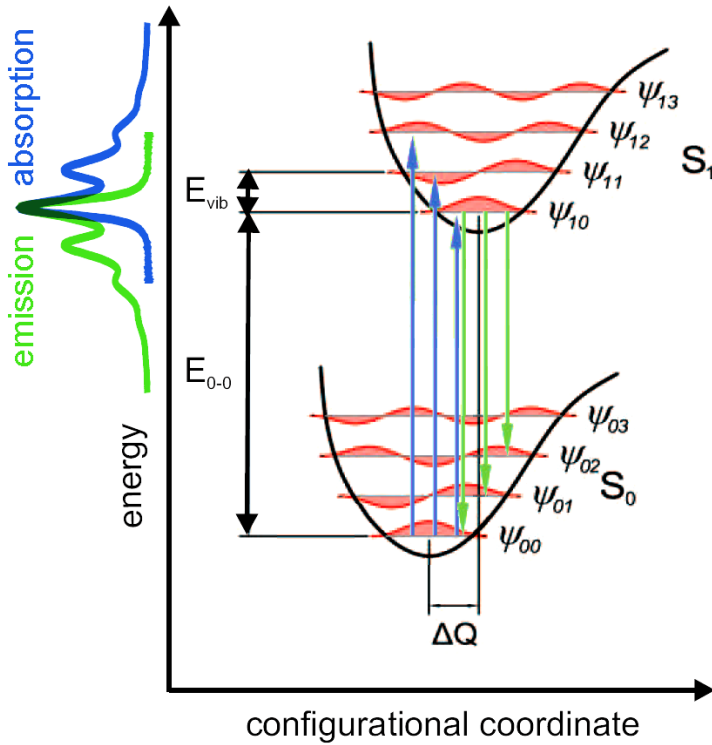


Figure 2.6: The Franck-Condon principle explains the intensities observed for vertical electronic transitions. Each state (S_0 , S_1) is superimposed by a number of vibronic sub-niveaus ψ_{ml} for each vibrational mode n . Since ground and excited state are slightly displaced within the configurational coordinate, it is likely that in addition to electronic excitation for different vibrational modes a certain number of vibronic states become occupied. This results in a vibronic progression, which can be observed in emission and absorption measurements. Slightly modified adapted from Ref. [150].

vibrational modes in both ground and excited state are almost identical [1, 156]. The projection of the difference between relaxed molecular geometry of the ground and excited state onto the complete basis of vibrational eigenvectors results in a coordinate shift q_n and a vibronic coupling constant g_n for each mode n ,

$$g_n = \sqrt{\frac{m\omega_n}{2\hbar}} q_n. \quad (2.20)$$

The energy needed for a molecule to reach its fully relaxed geometry after a vertical transition is the reorganization energy λ , which can be expressed in terms of g_n ,

$$\lambda = \sum_n g_n^2 \hbar \omega_n = \sum_n S_n \hbar \omega_n. \quad (2.21)$$

Here, S_n denotes the Huang-Rhys parameter (also electron-phonon coupling constant) of a respective mode n with energy $\hbar \omega_n$. The vertical transition probability of mode n from the electronically excited and vibronic ground state to the electronically ground

state with vibronic occupation ν is given according to the Franck-Condon principle,

$$P_n[|\Psi_{10}\rangle \rightarrow |\Psi_{0\nu}\rangle] = |\langle\Psi_{0\nu}|\Psi_{10}\rangle|_n^2 \propto \frac{S_n^\nu}{\nu!} e^{-S_n}. \quad (2.22)$$

Not all vibrational coupling constants are equal and often only a few modes dominate, which makes it useful to assume an effective Huang-Rhys parameter S_{eff} , in combination with an effective vibrational mode $\hbar\omega_{\text{eff}}$. This leads to a simplification of Eq. 2.21 to $\lambda = S_{\text{eff}}\hbar\omega$ [157]. As a result, the intensity of an electronic transition at E_{00} (vertical electronic transition energy without vibronic transition) follows a Poisson distribution (Fig. 2.6) that is characterized by a vibronic progression

$$I(E) = A \sum_{m=0} \frac{S_{\text{eff}}^m}{m! \sigma_m \sqrt{2\pi}} \exp\left(\frac{-(E - E_{00} - m \cdot \hbar\omega_{\text{eff}})^2}{2\sigma_m^2}\right). \quad (2.23)$$

The widths σ_m of the peaks in the vibronic progression are determined by the distribution of the dominant vibrational coupling constants S_n . According to Kasha's rule, there is a mirror symmetry between photon absorption and emission (Fig. 2.6). The energy needed for vibronic excitations ($\hbar\omega_{\text{eff}}$) are commonly one order of magnitude smaller than for the electronic excitation [158]. For rubrene, the spacing of the vibronic progression has been found to be $\hbar\omega_{\text{eff}} \approx 170$ meV [159], while its vertical excitation energy was measured to $E_{00}^{\text{abs}} = 2.34$ eV and $E_{00}^{\text{emis}} = 2.21$ eV for absorption and emission, respectively [87]. The difference, which is often found between the E_{00} transition of absorption and emission for molecules in solution or thin films is called Stokes shift. One reason for this shift is that not only the molecule itself has to be reorganized (reorganization energy λ), but also the environment of the molecule consumes energy to adapt to the new state of the particular molecule (compare Sec. 2.3.2).

2.3.2 Electron transfer in a medium

Molecules in solution, thin films or crystals can be ionized. A possible scenario could be a charge transfer (or transport) within a molecular crystal, or between a dissolved molecule and an ionic solution. Such an electron transfer can be described in terms of Marcus theory, which considers Gibbs free energy in dependence of a configurational coordinate Q [160]. Accompanied by an electron transfer is a rearrangement of charges that affects the crystal or solvent environment.

If an ionized molecule is embedded in a polarizable medium [161], the field energy is reduced by the screening induced from the dielectric constant $\epsilon_{\text{solvent}}$ of the surround-

ing medium [162]. As a consequence, the electron affinity (EA) and the ionization potential (IP) of the ionized molecule become larger. The electronic polarization energy of the cation P_+ can be evaluated experimentally as the difference between the ionization potential IP_{medium} of the molecular system in the medium (crystal, solution) and the ionization potential IP_{gas} of the molecular system in vacuum or the gas phase, [96]

$$P_+ = IP_{\text{medium}} - IP_{\text{gas}}. \quad (2.24)$$

Moreover, it can be estimated from the ionic radius r_{ion} and the dielectric constant $\epsilon_{\text{solvent}}$ of the medium,

$$P_+ = \frac{q^2}{4\pi\epsilon_0} \frac{1}{2r_{\text{ion}}} \left(1 - \frac{1}{\epsilon_{\text{solvent}}} \right), \quad (2.25)$$

where $q = e$ accounts for the transfer of a single and $q = 2e$ for a double elementary charge. In case of equal radii of the cationic and the anionic species, the respective polarization energies are equal, $P_- = P_+$. Hence, with respect to a molecule in free space, EA_{medium} and IP_{medium} become modified due to the presence of the polarizable environment

$$EA_{\text{medium}} = EA_{\text{vac}} - P_- \quad IP_{\text{medium}} = IP_{\text{vac}} + P_+. \quad (2.26)$$

2.3.3 Photoemission from solids

The photoelectric effect

Under the influence of an electromagnetic wave with energy $\hbar\omega$ in the range of ultraviolet (UV) or X-ray radiation, an electron can be removed completely from its molecular orbital, which is called the photoelectric effect [163]. The probability $P[i \rightarrow f]$ per unit time for a transition from an initial state Ψ_i of fixed energy E_i (molecular orbital) to a continuum of final states, *i. e.* a final state Ψ_f with energy E_f (vacuum), is given by what is known as the Golden Rule,

$$P[i \rightarrow f] = \frac{2\pi}{\hbar} |\langle \Psi_f | \hat{H}' | \Psi_i \rangle|^2 \delta(E_f - E_i - \hbar\omega). \quad (2.27)$$

Thereby, $\langle \Psi_f | \hat{H}' | \Psi_i \rangle$ denotes the matrix element of the perturbing Hamiltonian \hat{H}' between the final Ψ_f and initial states Ψ_i . The transition probability determines the experimentally observed peak intensities. Using photoemission spectroscopy (PES) techniques [164], more precisely by ultra-violet photoemission spectroscopy (UPS) and

X-ray photoemission spectroscopy (XPS), the entire electronic structure (Fig. 2.7) of a material can be studied.

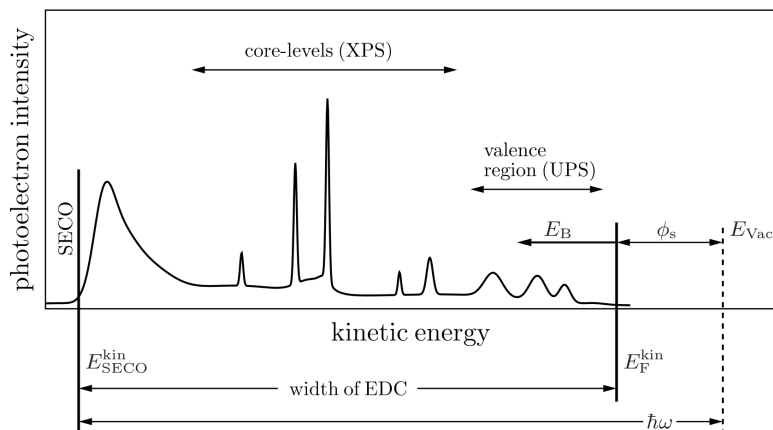


Figure 2.7: Overview over the energy distribution curve (EDC) and energies relevant for PES techniques. While the kinetic energy E^{kin} of the secondary electrons is determined by the photon energy $\hbar\omega$, the binding energy E_B of occupied orbitals is measured from the Fermi-edge E_F^{kin} ($E_F^B = 0$). Taken from Ref. [165].

Ionization potential of thin films on metal substrates

The ionization potential of a molecule at the surface of organic solids is higher than in the bulk, where the ion is surrounded by polarizable molecules [96]. In comparison to the bulk, the molecular environment in a thin film on a metal substrate is much more complex due to the influence of the interfaces (metal/organic, organic/vacuum). Hence, in thin films consistent molecular polarization energies P_+ and P_- are difficult to define, which is why the physical quantities are usually named in a slightly different way than they were introduced in Sec. 2.3.2. The ionization potential (IP) and electron affinity (EA), respectively, are usually defined by the energy separation of the HOMO and the LUMO from the vacuum level (VL) with energy E_{Vac} , the polarization energies P_+ and P_- are commonly not considered. The sample work function ϕ_s of a solid is specified by the energy separation between the Fermi level E_F and E_{Vac} (Fig. 2.7). The kinetic energy E_{kin} of the detected electron and the binding energy of the electron in its orbital are connected by the energy $\hbar\omega$ of the incident photon and the work function ϕ_s of the sample

$$E_{kin} = \hbar\omega - E_B - \phi_s. \quad (2.28)$$

Surface dipole moment

In general, at a metal/vacuum interface a surface dipole pointing into the metal is generated since the metal electrons spread an electric field out of the surface. Neutral molecules that are deposited onto the metal surface repel this field caused by the electrons and push it back into the surface (push-back effect). They weaken the interface dipole created by the metal electrons, since it becomes superimposed by a dipole moment induced in the molecules. Photo electrons that leave the sample have in consequence higher kinetic energy E_{kin} than electrons from the clean metal substrate, which is observed by the electron analyzer and yields a smaller work function ϕ_s .

In the case of molecules with static dipole moment d perpendicular to the surface, an additional change $\Delta\phi$ in the work function can be observed, which can be estimated by the Helmholtz equation

$$\Delta\phi = \frac{ed \cdot N_{\text{dip}}}{\varepsilon_r \varepsilon_0}, \quad (2.29)$$

where N_{dip} is the surface density of the dipole moments and ε_r the permittivity of the compound.

CHAPTER 3

METHODS

This chapter presents the methods that have been used in this work. Since the study contains both experimental but also theoretical results, the chapter is divided into two different sections. First, the theoretical methods are presented shortly. In the second section, which is considerably larger, the focus lies on the experimental methods. It covers a large number of experimental techniques that were deployed for this study.

3.1 Theoretical methods

This section provides a brief overview over the theoretical methods used in this work [151,156]. Most of the quantum chemical computations were performed with the quantum chemical software package TURBOMOLE 6.4 [166] at the high performance cluster of the university of Tübingen, which is part of BWGRID [167]. In particular cases GAUSSIAN 03 [168] was employed. The molecular properties presented in this work were computed exclusively for isolated molecules in free space. Visualizations of the molecular models were created using the software package MOLDEN [169].

3.1.1 The Hartree-Fock (HF) approach

In many-body electronic structure calculations, the molecular nuclei are usually assumed to be fixed with electrons moving in the static electric field created by the nuclei (Born-Oppenheimer approximation). The stationary electronic state for all electrons is then described by the wavefunction Ψ that satisfies the time-independent Schrödinger

equation of the system ($H\Psi = E\Psi$). The Hartree-Fock (HF) method describes the N -particle system with an N -body wave function Ψ that is defined by the Slater determinant of N spinorbitals.

$$\Psi = \frac{1}{\sqrt{N!}} \begin{vmatrix} \psi_1(x_1) & \psi_2(x_1) & \dots & \psi_n(x_1) \\ \psi_1(x_2) & \psi_2(x_2) & \dots & \psi_n(x_2) \\ \vdots & \vdots & \ddots & \vdots \\ \psi_1(x_n) & \psi_2(x_n) & \dots & \psi_n(x_n) \end{vmatrix} \quad (3.1)$$

The spinorbitals $\psi_i(x_j)$ are a product of orbital wavefunction and spin function. Using variation theory, the HF-method looks for the spinorbitals $\psi_i(x_j)$ that yield the 'best' wavefunction Ψ by minimizing iteratively the energy expectation value \mathcal{E} defined as the Rayleigh ratio

$$\mathcal{E} = \frac{\int \Psi^* H \Psi dx}{\int \Psi^* \Psi dx}. \quad (3.2)$$

The solution returned by the HF method yields the ground state HF wavefunction and energy \mathcal{E} of the system. However, the equation which needs to be solved in order to find the optimized spinorbitals $\psi_i(x_j)$ already requires the knowledge of the spinorbitals $\psi_i(x_j)$ themselves. As a consequence, this dilemma (and hence the optimization process) is finally solved for a self-consistent field (SCF) of spinorbitals $\psi_i(x_j)$, which is why the HF-method is often also called SCF method [151].

3.1.2 Density functional theory (DFT)

An alternative method to the HF method is density functional theory (DFT) [170], which is usually computationally cheaper for quantum chemical computations. In DFT, the energy $E_{\text{DFT}}[\rho]$ of a many electron system can be determined by using functionals, *i. e.* functions of the spatially dependent electron density $\rho(\vec{r})$. A common ansatz using the DFT energy considers the kinetic energy $T_S[\rho]$, the attraction between the electrons and the nuclei $E_{\text{ne}}[\rho]$, the Coulomb repulsion $J[\rho]$, and the exchange-correlation $E_{\text{XC}}[\rho]$,

$$E_{\text{DFT}}[\rho] = T_S[\rho] + E_{\text{ne}}[\rho] + J[\rho] + E_{\text{XC}}[\rho]. \quad (3.3)$$

The electron density ρ can thereby be described by the Kohn-Sham (KS) orbitals that are found by solving the KS equations. Similar to the HF method, the KS orbitals

can be expressed in a set of basis functions and the functional KS equations can be solved in a self-consistent fashion. A difficulty within the KS equations is to calculate the exchange-correlation energy E_{XC} . In the local-density approximation (LDA), the exchange-correlation is $E_{XC} = \int \rho(\vec{r}) \varepsilon_{XC}[\rho(\vec{r})] d\vec{r}$, where $\varepsilon_{XC}[\rho(\vec{r})]$ is the exchange-correlation energy per electron in a homogeneous electron gas of constant density. It is an approximation depending only on the electron density and therefore is the simplest way to model the exchange-correlation. The generalized gradient approximations (GGA) is also still local, but additionally to LDA, it includes the gradient of the density at the same coordinate.

3.1.3 Hybrid functionals

Hybrid functionals are approximations to the exchange-correlation energy functional in DFT that incorporate some of the exact non-local exchange from HF in combination with local exchange and correlation from DFT approaches. A very popular hybrid functional is B3LYP (Becke, three parameter, Lee-Yang-Parr) [171, 172]. It includes HF corrections in conjunction with DFT correlation (index C) and exchange (index X),

$$E_{XC}^{\text{B3LYP}} = E_X^{\text{LDA}} + a_0(E_X^{\text{HF}} - E_X^{\text{LDA}}) + a_X(E_X^{\text{GGA}} - E_X^{\text{LDA}}) + E_C^{\text{LDA}} + a_C(E_C^{\text{GGA}} - E_C^{\text{LDA}}), \quad (3.4)$$

with the three parameters ($a_0 = 0.20$, $a_X = 0.72$, $a_C = 0.81$). It forms a mixture of both, HF and DFT methods and in this work it was used for most computations.

3.1.4 Basis sets

In principle, a complete set and thus an infinite number of basis functions must be used to represent the spinorbitals $\psi_i(x_j)$ exactly, which is obviously impossible to perform in practice. For a more realistic ansatz to compute the properties of a molecule, one could just place one orbital centered on each of the atomic nuclei (so-called Slater-type orbitals (STOs)). However, this results in the impractical evaluation of many two-electron integral problems, which can be overcome by Gaussian-type orbitals (GTOs) [173] that are easier to compute in practice. To compensate the disadvantage that the GTOs give poorer representation of the orbitals than the STOs, it is common to increase the number of basis functions instead. In this work, if not denoted differently, a triple-zeta valence plus polarization (TZVP) basis set was used, which provides three basis functions as representation for each orbital.

3.1.5 Time-dependent density functional theory (TD-DFT)

Time-dependent density functional theory (TD-DFT) is an extension to common DFT and is useful to investigate the response of molecular systems in the presence of time-dependent potentials, like electric or magnetic fields. It allows the determination of polarizabilities (as e. g. needed for the computation of Raman spectra), excitation energies, and electronic absorption spectra. For TD-DFT, the KS orbitals and the density $\rho(\vec{r})$ become all time dependent, and the Hamiltonian for the computation of Eq. 3.3 receives an additional potential V_{ext} to consider the applied field.

3.1.6 Computation of molecular properties using TURBMOLE 6.4

Fig. 3.1 sketches the computation procedure of the molecular orbitals and vibrational modes using TURBMOLE 6.4. After optimization of the molecular geometry of the different isomers calculated with DFT using the B3LYP hybrid functional (*jobex*), the molecular orbitals were computed (*dscf*), which yields the respective HOMO, LUMO, and other orbital energies. Using *aoforce*, the complete set of vibrational eigenvectors were calculated with the corresponding oscillator strengths for the respective vibrational modes that show infrared (IR) activity. The computed Raman intensities (Sec. 5.1) rely on the ground state geometry (GS) of each isomer calculated with DFT using the B3LYP hybrid functional, and on the respective excited state geometry (ES) calculated with time-dependent DFT, as implemented in TURBOMOLE [174,175]. These deformations were projected on the complete set of vibrational eigenvectors, allowing to deduce non-vanishing Huang-Rhys factors S_j for internal modes of the highest symmetry, corresponding to the A representation of the D_2 (RUB, PF-RUB) and C_2 isomer (F₁₄-RUB), to A_g for the C_{2h} isomer (RUB, PF-RUB), and A' for the C_s isomer (F₁₄-RUB), respectively. The calculated cross sections in the resonant Raman spectra were then obtained as $\sigma_j \propto S_j(\hbar\omega_j)^2$. The ionized species of the respective isomers were computed after modification of the molecular charge of the models.

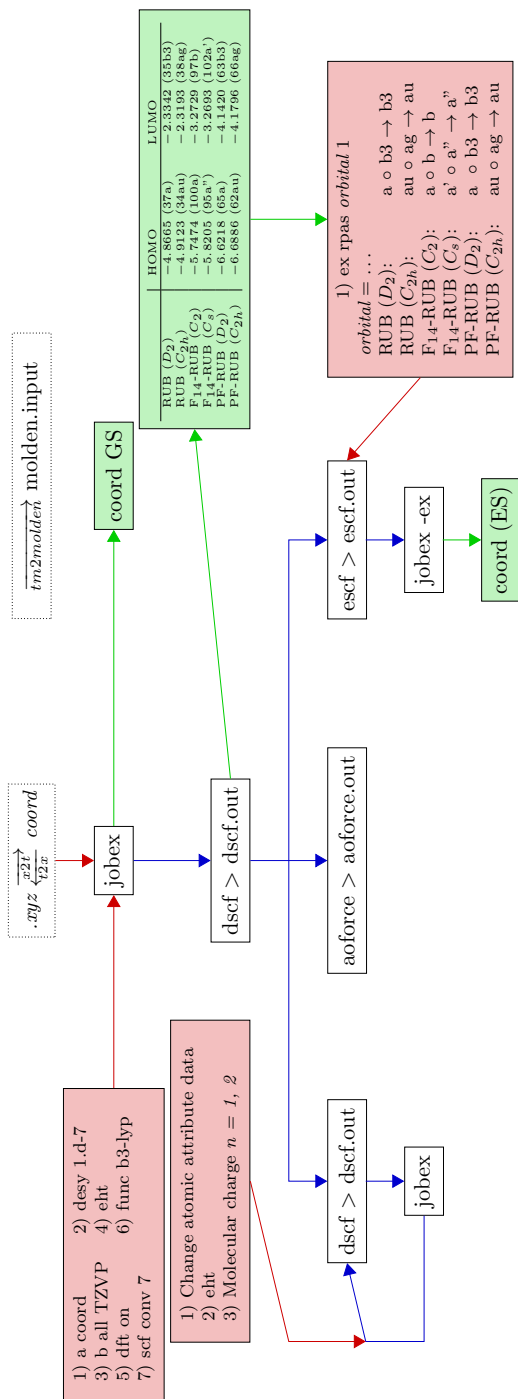


Figure 3.1: Scheme for quantum chemical computation using TURBOMOLE 6.4. White boxes contain commands entered into the program package, blue arrows denote the order of consecutive commands. Green boxes exemplarily represent outputs from specific commands (green arrows). Red boxes designate parameters passed to the program. Dotted boxes contain auxiliary commands that were used e. g. for conversion of the data to the visualization program MOLDED [169]. For further details, see text.

3.2 Experimental methods

This section elucidates the sample preparation and introduces the experimental instruments used in this work. The majority of the instruments belong to the field of optical techniques that possess the advantage to be non-invasive methods, *i. e.* the sample is not touched (and thus not modified) by the instrument and can also be studied under protective atmosphere or vacuum conditions. In particular the infrared spectrometer was set up for thin film characterization in transmission during the time of this work and is now established.

3.2.1 Sample preparation

The samples studied in this work were thin film samples deposited on a (modified) silicon wafer or metal single crystal, but also molecules diluted in dichloromethane (Cl_2CH_2) were investigated. The thin films were produced with organic molecular beam deposition (OMBD) [66,70], which proceeded, if not denoted differently in the particular section, with our in-house vacuum system (Sec. 3.2.1) under ultra high vacuum (UHV) conditions.

Substrates

This section explains how the substrates were treated, which includes preparation and/or cleaning processes. In order to vary the surface energy, some of the wafers were covered with a self assembling monolayer (SAM) before thin film growth like for the investigation of the vibrational properties of the molecules (Chap. 5). Single crystal metal substrates were used for photoelectron spectroscopy, exclusively.

Silicon wafer. The silicon wafers (one side polished, thickness $500\ \mu\text{m}$, surface with (100) orientation) were bought from SI-MAT with a slight boron-doping. Since the wafers were stored in air, they were covered by a thin oxide-layer of about 2 nm thickness. The substrates were cleaned in an ultrasonic cleaner, consecutively with acetone, isopropanol and highly purified water for 5 min, each. Thereafter they were attached to a tantalum sample holder using conductive silver paste. In order to remove the water and fix the silver paste they were dried out shortly on a heating (1 min) and put into the loading chamber of a UHV-system. Before starting the growth process, the substrate was heated up to $\sim 300\ ^\circ\text{C}$ for several hours.

Self assembled monolayer (SAM). The surface energy γ plays an important role for the wetting behavior of organic thin films. In order to increase the surface energy γ_{silicon} of the silicon wafers, their surface was covered with octadecyltrichlorosilane ($\text{C}_{18}\text{H}_{37}\text{Cl}_3\text{Si}$, OTS) acting as SAM.

In order to cover the silicon wafers with the SAM, they were rinsed as described in Sec. 3.2.1. The cleaned silicon wafers were heated to at least 100°C to ensure water-free surfaces and were proceeded further in a nitrogen purged flowbox. There, the wafers were put into a solution consisting of 80 % toluene and 20 % Octadecyltrichlorosilane (OTS), see Fig. 3.2. Being covered with the SAM after 2 days in solution, the wafers were rinsed by a bath in toluene, acetone, isopropanol and water for ~ 2 min, each. In order to protect the SAM layer before thin film deposition, the SAM covered wafers were heated merely to moderate temperatures ($\sim 100^\circ\text{C}$), in contrast to the bare silicon substrates.

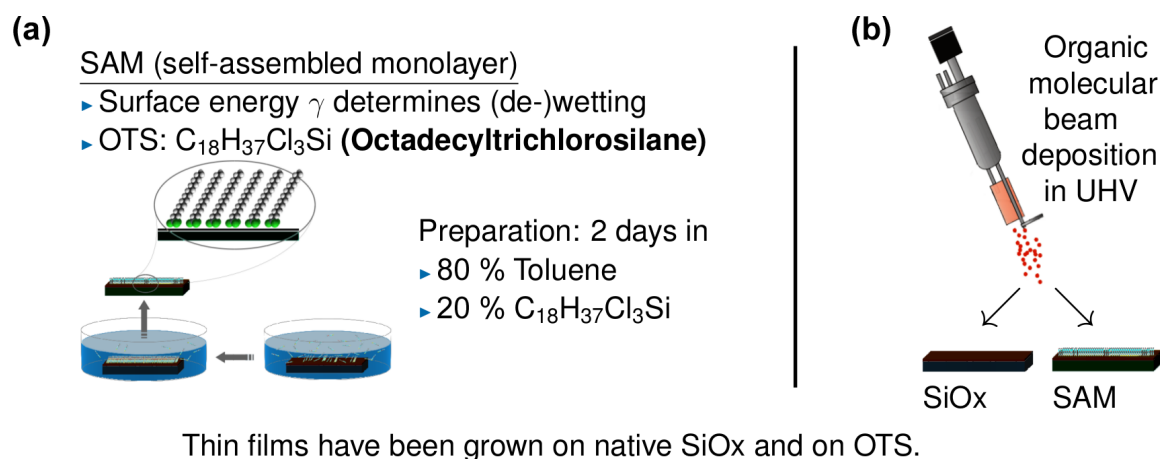


Figure 3.2: (a) Fabrication procedure of the self assembled monolayer (SAM) on the silicon wafer. The amphiphilic octadecyltrichlorosilane (OTS) serving as SAM was diluted (20 %) in toluene (80 %) before adsorption on the silicon wafer. (b) After coverage of the wafer, thin film growth was carried out simultaneously on both, the bare (SiO_x) and the SAM covered silicon wafer.

Metal single crystals (Au(111), Ag(111)). Au(111) and Ag(111) single crystals were used for photoelectron spectroscopy. Since the experiments were performed at the synchrotron (BESSY II), the substrates were provided by the beamline (SURICAT). Further details on the substrate cleaning process and thin film growth is described in Sec. 3.2.6.

Solution samples. The solvent used in this work was exclusively dichloromethane (Cl_2CH_2). Measurements in solution were performed to determine the oxidation and reduction potential of the compounds using cyclic voltammetry (Sec. 4.2), but also for the characterization of the vibrational properties via infrared and Raman spectroscopy (Secs. 5.2.2 and 5.2.5). The molar concentration was 1.4 mM/l (2.6 mM/l) for PF-RUB and F_{14} -RUB (RUB) in the cyclic voltammetry experiment and ~ 2 mM/l for all materials used for the vibration measurements.

Organic molecular beam deposition and thin film growth

A common and also industrially relevant technique for organic thin film growth is organic molecular beam deposition (OMBD) [40,66]. Molecules were evaporated (rate 1–3 Å/min) from a Knudsen cell into a vacuum chamber under UHV-conditions ($\sim 10^{-10}$ to 10^{-9} mbar). The temperature of the Knudsen cell is thereby used to control the growth rate, which is usually left constant throughout deposition process (for temperature values see Sec. 1.3.3). The thin film thickness was measured by a water-cooled quartz crystal microbalance (QCM) and real-time ellipsometry measurements, which turned out to be a very precise indicator for the very smooth growing thin films. Fig. 3.3 shows the Knudsen cell, which was used for evaporation of the fluorinated rubrene molecules. The cell contains two quartz crucibles that can be heated independently and were most of the time filled with PF-RUB and F_{14} -RUB. A turnable shutter covers either of the crucibles, permitting the respective other crucible to ‘free sight’ into the chamber. The evaporation temperature of the materials was measured by a thermocouple within the quartz cuvette. Depending on the winding of the heating wire around the cuvette and the exact position of the thermocouple, the evaporation temperature was determined to ~ 90 – 100 °C, ~ 120 – 130 °C, and ~ 150 – 160 °C for PF-RUB, F_{14} -RUB, and RUB, respectively (compare Sec. 1.3.3). Cross-talk between the two materials in the cell could be excluded due to the different evaporation temperatures. Upon heating one of the crucibles, thermal conductivity of the cell resulted in an increase in temperature of the other crucible by about half of the value (measured in °C). RUB and PF-RUB were never mounted together in the Knudsen cell.

Vacuum system

Our in-house vacuum system, which was used for preparation of all thin film samples presented in this study (except the thin films on single crystal metals discussed in Sec. 4.3) is depicted in Fig. 3.4. It consists of a loading chamber, which can be vented for

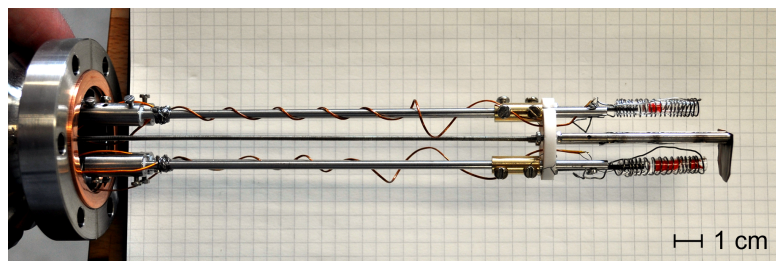


Figure 3.3: Knudsen cell used for evaporation of F_{14} -RUB and PF-RUB (only in few cases of RUB) thin films. The cell contains two quartz crucibles, which are filled with the materials (red powder at the right end of the cell).

sample transport into and out of the system. A turbomolecular pump can be switched from the loading chamber to the main chamber, when venting the loading chamber. The sample is transported via a transfer rod into the main chamber and put onto the sample holder, which is controlled by a manipulator. Using the latter, the sample is brought into its final growth position, next to the QCM and the Knudsen cells. The main chamber is pumped permanently by an ion-getterpump and a Ti-sublimation pump. It is only occasionally vented for maintenance reasons or as in the case of real-time oxidation measurements of thin films of the three compounds, which are discussed in Sec. 4.2.

3.2.2 Cyclic voltammetry (CV)

Cyclic voltammetry is a methodology that is widely used to investigate the electrochemical properties of an analyte in solution [177]. It can provide information about the stability of a compound and allows the determination of its oxidation and reduction potentials from an electrochemical method. A voltammogram is a simple and direct method for measuring the standard reduction potential E^0 of an electrochemical half-reaction. The $Fe^{III/II}$ redox couple of ferrocene ($\eta^5-C_5H_5$)₂Fe, is an electrochemically reversible system in acetonitrile solution and is often used as an internal or pseudo reference in the solution. In many cases, the formal potentials of the first oxidation and reduction of a complex can be correlated to the energies of its HOMO and LUMO. The redox behavior of RUB, F_{14} -RUB and PF-RUB in solution and in the absence of oxygen was studied by means of cyclic voltammetry in 0.1 M NBu_4PF_6/CH_2Cl_2 at a Pt disk electrode under planar diffusion conditions.

Equipment and measurement

Cyclic voltammograms were recorded with a PGSTAT101 POTENTIOSTAT from METROHM (Filderstadt, Germany) under argon atmosphere in a gas tight three elec-

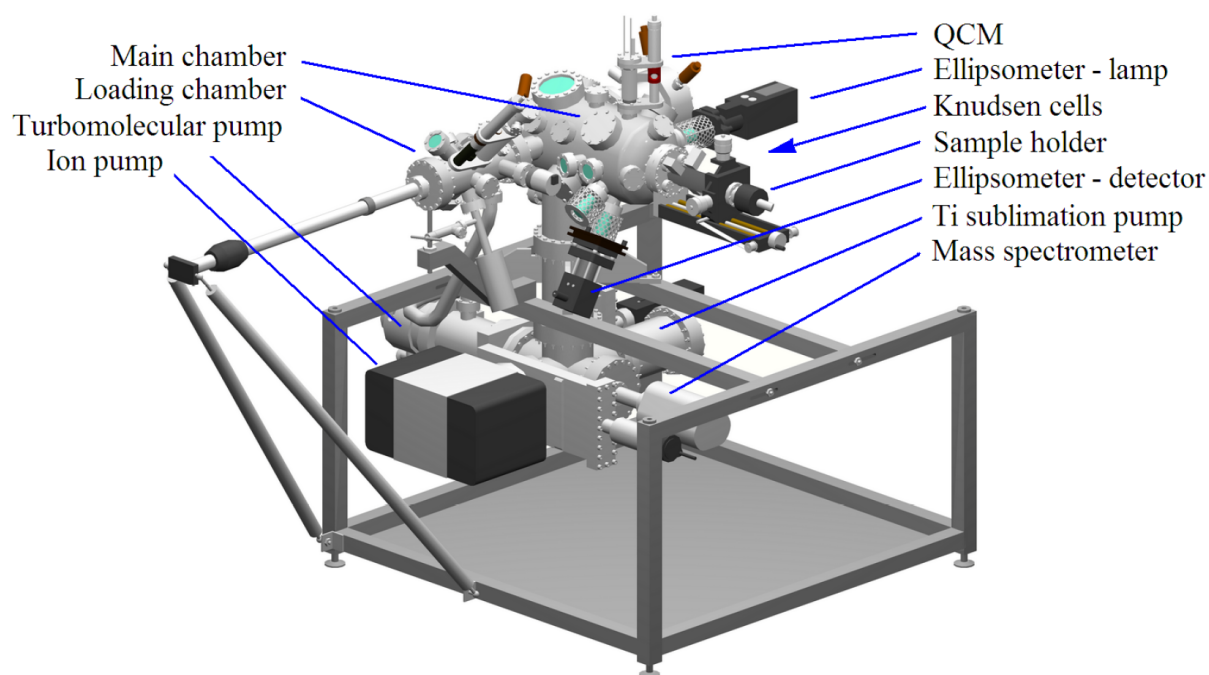


Figure 3.4: In-house ultra high vacuum (UHV)-system. The UHV of the main chamber is maintained by an ion-getterpump and a Ti-sublimation pump. A turbomolecular pump can be switched between the main chamber and the loading chamber. In order to perform real-time ellipsometry, a WOLLAM 2000 spectroscopic ellipsometer can be mounted on the chamber. The mass spectrometer shown in the sketch was not used on a daily basis, but after venting of the whole system of great value for leak detection. The drawing is taken from Ref. [176].

trode cell. The working electrode consisted of a Pt disk (nominal diameter $d = 1$ mm) sealed in glass, a Pt wire was used as counter electrode. An Ag wire coated with an AgCl-layer which was directly immersed into the electrolyte solution served as (*pseudo*-)reference electrode. All potentials are given *versus* the formal potential of the standard potential redox couple Fc/Fc⁺ (Ferrocene/Ferrocenium) [178]. Fc is used as internal standard (added after the substrate measurements). Typical half wave potentials of Fc/Fc⁺ were found between +0.32 V and +0.35 V (vs. Ag/AgCl *pseudo*-reference). Voltammograms were recorded in deaerated (Argon bubbling) CH₂Cl₂ containing NBu₄PF₆ acting as the supporting electrolyte (0.1 M). CH₂Cl₂ was dried prior to use with activated Al₂O₃ (80 °C for several days). Cyclic voltammograms were not background corrected. For the estimation of half wave potentials voltammograms recorded with 100 mV/s were used.

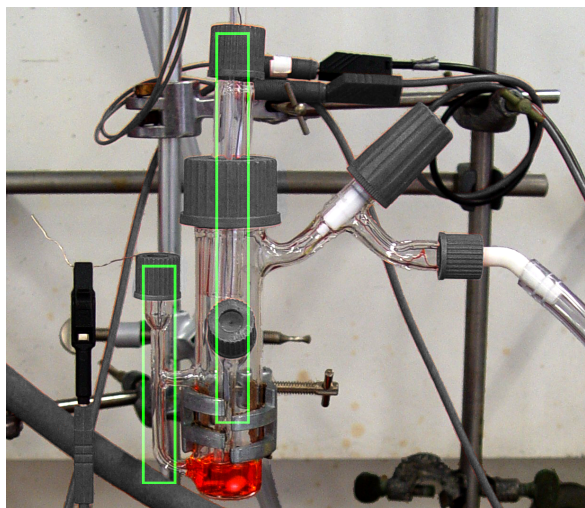


Figure 3.5: Cyclic voltammetry setup. The voltammograms were recorded in deaerated (Argon bubbling) CH_2Cl_2 containing NBu_4PF_6 acting as the supporting electrolyte (0.1 M). The diluted compound (red) is located at the bottom of the test tube, green frames show the position of the electrodes merged into the solvent. Substrate concentrations were 2.6 mM in the case of RUB and 1.4 mM for F_{14} -RUB and PF-RUB.

Data evaluation

The midpoint potential of two (anodic and cathodic) peaks in a voltammogram can be expressed in terms of the standard reduction potential E^0 by using the Nernst equation, and can be approximated by it for equal diffusion coefficients of the reduced and oxidized species (D_R and D_O) [179],

$$E_{\text{Midpoint}} = \frac{E_{\text{cathodic}} + E_{\text{anodic}}}{2} = E^0 + \frac{RT}{nF} \ln \left(\sqrt{\frac{D_R}{D_O}} \right) \approx E^0. \quad (3.5)$$

Thereby is n the number of electrons transferred in the process, and F and R are the Faraday and universal gas constant, respectively. At room temperature ($T = 298 \text{ K}$), the anodic and cathodic peaks should be separated by

$$\Delta E_p = |E_{\text{cathodic}} - E_{\text{anodic}}| = 2.3 \frac{RT}{nF} = \frac{59}{n}. \quad (3.6)$$

In case of the standard potential redox couple Fc/Fc^+ , the HOMO and the LUMO can be determined from CV measurements by

$$\begin{aligned} E_{\text{HOMO}} &= -(E_{\text{Midpoint,ox}} + 5.1)(\text{eV}) \\ E_{\text{LUMO}} &= -(E_{\text{Midpoint,red}} + 5.1)(\text{eV}). \end{aligned} \quad (3.7)$$

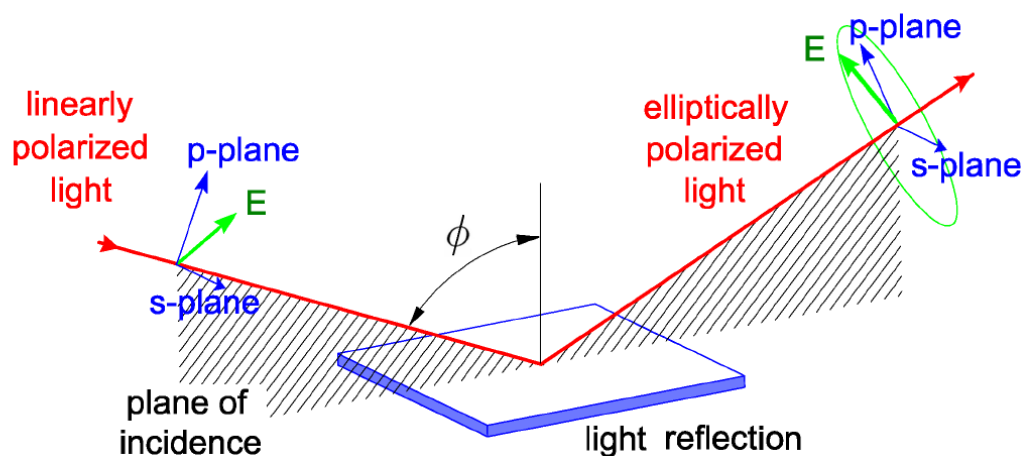


Figure 3.6: Schematic of spectroscopic ellipsometry: A linearly polarized ultra-violet beam is shined onto the sample, and reflected with altered (generally elliptical) polarization. The apparatus used in this work is a WOLLAM M-2000 ROTATING COMPENSATOR ellipsometer. It is equipped with a Xenon lamp, covering the range of $\sim 1.2 - 5.1$ eV. In order to perform *in-situ* measurements, the ellipsometer was mounted on the UHV system (Sec. 3.2.1) for acquisition.

3.2.3 Spectroscopic ellipsometry

Spectroscopic ellipsometry (Fig. 3.6) is a very sensitive method for the investigation of thin films [180, 181]. Linearly polarized ultraviolet light is shined onto the sample, where the polarization of the light becomes changed by the molecules in the thin film (Sec. 2.1.3). The beam is reflected by the sample and passed towards a CCD detector, where the intensity and polarization of the light is recorded. Ellipsometry measures the complex reflectance ratio ρ that depends on the change in the amplitude component Ψ and the phase difference Δ , between incident and reflected beam.

$$\rho = \frac{r_p}{r_s} = \tan \Psi \exp(i\Delta) \quad (3.8)$$

The polarization of the light is controlled by a polarizer put between light source and sample, and an analyzer located between sample and detector. Both, polarizer and analyzer, rotate during measurement in order to ensure the acquisition of the light for all polarizations.

Layer	Thickness
Organic layer (<i>i. e.</i> RUB, F ₁₄ -RUB, or PF-RUB)	fitted (20 . . . 100 nm)
Native silicon oxide	fitted (\sim 1.3 nm)
Silicon (wafer)	500 μ m

Figure 3.7: Layer model used during real-time acquisition of *in situ* ellipsometry measurements. Before thin film deposition, the thickness of the silicon oxide layer with known optical properties was fitted. Upon thin film growth, the film thickness could be determined by fitting of the optical properties under the boundary condition of a transparent thin film in the region between 1.2–1.9 eV. Due to the high sensitivity of ellipsometry, even submonolayer coverages could be detected.

Equipment and measurement

In order to acquire optical spectra of the pristine films, their absorption spectra were studied *in situ* with a WOOLLAM M-2000 spectroscopic ellipsometer [182] during and directly after thin film growth. The ellipsometer with a broad band Xe lamp (75 W, 250–1000 nm) was mounted with a fixed angle $\phi \approx 61^\circ$ on the UHV system (Sec. 3.2.1). This is not far away from the Brewster’s angle condition of silicon (74°), which maximizes the difference between r_p and r_s (Sec. 2.1.4). During thin film growth, the thickness could be determined using spectroscopic ellipsometry as a fit parameter of the optical properties of the overall layered system under the boundary condition of a transparent region of the deposited molecules between 1.2–1.9 eV (Fig. 3.7). The evaluated thin film thickness was confirmed afterwards by complementary X-ray reflectivity measurements.

Data evaluation

Since ellipsometry is an indirect method, Ψ and Δ cannot be converted directly into the electric constants ε_1 and ε_2 . Hence, a point-by-point fit, i.e. an individual fit for each photon energy separately, has to be performed according Eq. 3.8. The result of this point-by-point fit may, however, still deviate slightly from a physically meaningful function $\varepsilon_r(\omega)$ due to noise artifacts and/or inaccurate fit parameters [176]. In order to achieve a Kramers-Kronig consistent function for the optical properties in the measured interval, as presented in Sec. 4.1, the data created by the point-by-point fit was modeled to a continuous function. This was realized by a Cauchy model for the sili-

con oxide and an oscillator model for the organic layer on top of it using a commercial software package (WVASE32). Further details on the fitting procedure can be found in Refs. [150,176].

3.2.4 Photoluminescence (PL) spectrometry, Raman spectrometry, and light microscopy

Although physically very different, photoluminescence (PL) and Raman spectroscopy were acquired with the same equipment. Moreover, the light microscope pictures presented in this work, were also acquired with this system. In that case, the samples were illuminated with a commercial halogen lamp.

In a PL experiment, the material becomes excited with a laser at constant energy and the relaxation of the created excitons is monitored thereafter. Hence, PL yields data on the electronic relaxation, which is complementary to ellipsometry that *inter alia* provides information on the absorption properties of a sample.

Raman scattering is a two-photon process, in which one photon with an energy of visible light is shined onto the sample and after interaction with a particular molecule results in an outgoing photon. Thereby, the vibronic configuration of a molecule in the sample becomes changed and can be measured by the energy difference between incident and scattered light. It is a complementary method to infrared spectroscopy.

Equipment and measurement

PL and Raman spectra were acquired using a HORIBA JOBIN YVON LABRAM HR 800 spectrometer, which is equipped with a confocal optical microscope (Fig. 3.8) and a CCD-1024×256-OPEN-3S9 as detector. The confocality of the microscopy allows a precise focusing on a very thin layer of the sample. Raman (PL) spectra were obtained with use of a grating with 1800 (150) lines/mm and after acquisition corrected by the quantum efficiency of the detector of the spectrometer. The spectrometer is supplied with two lasers, one of which is a He-Ne laser with 633 nm (1.96 eV), the other one is a frequency doubled Nd:YAG with 532 nm (2.33 eV). The theoretically minimal laser spot diameter d_{min} on the sample can be estimated by the numerical aperture NA of the objective (OLYMPUS ×50 long range distance objective with NA = 0.5) via

$$d_{min} = \frac{1.22\lambda}{NA}. \quad (3.9)$$

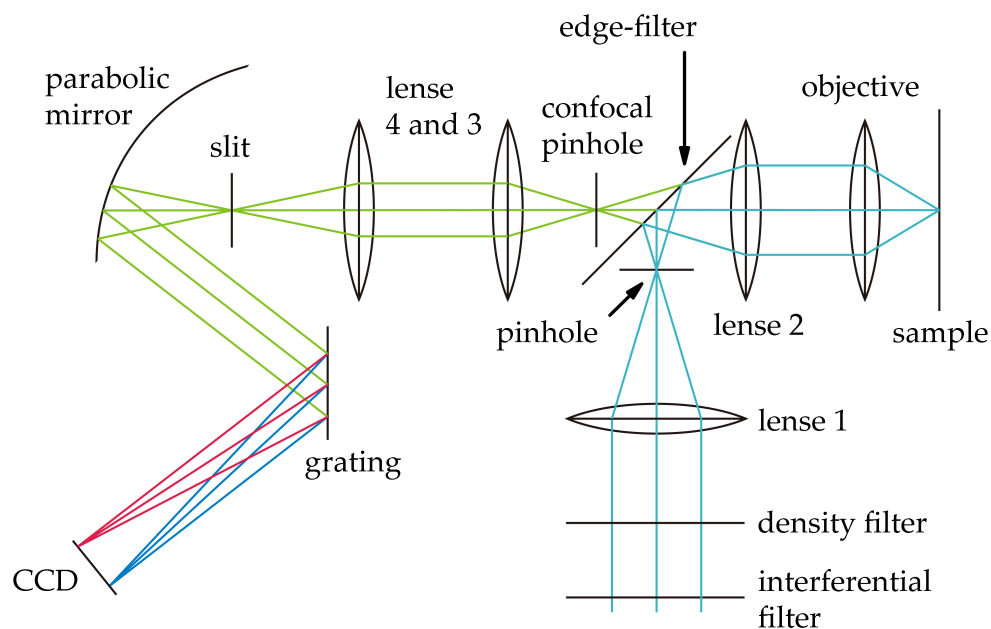


Figure 3.8: Schematic of the beam path of the confocal Raman spectrometer (HORIBA JOBIN YVON LABRAM HR 800 spectrometer). The incident laser is passed through a pinhole and projected on the sample. The Stokes shifted Raman scattered light reflected from the sample passes the edge-filter. Having been diffracted by a grating, it is recorded by a CCD. For further information, see Ref. [183].

This estimation results in a spot size of $\sim 1.2 \mu\text{m}$ ($1.5 \mu\text{m}$) for the Nd:YAG (He-Ne) laser. Nevertheless, when scanning over the sample surface using a piezo with a step size of $0.5 \mu\text{m}$ (Raman imaging), it was still possible to distinguish between the optical properties of the particular pixels on the sample (Chap. 5). Additional information on the spectrometer and its component including a detailed discussion of the beam path (Fig. 3.8) can be found in Ref. [183] and Refs. therein. The samples were mounted on a THMS600 HEATING AND FREEZING STAGE from LINKAM, which allows the acquisition of PL and Raman measurements in protective atmosphere accompanied by simultaneous cooling of the samples down to 77 K. Protective atmosphere is particularly useful for safeguarding the sample against moisture and photooxidation. PL measurements at low temperatures can sharpen Raman [184] and PL [131] peaks in comparison to room temperature and can also hinder thermally activated electronic transitions to decay non-radiatively [131]. Raman measurements of solutions were performed using a quartz glass cuvette.

Data evaluation

Thin film spectra usually show a pronounced Raman peak of the silicon substrate at 520 cm^{-1} [185]. If deviating, the energy axes of the measured Raman spectra were shifted in order to coincide with the nominal position of the Si-peak at 520 cm^{-1} . PL spectra shown in Sec. 4.1, were normalized to their covered area. For the Raman spectra shown in Chap. 5, the PL background was subtracted for clarity.

3.2.5 Fourier-transform infrared (FT-IR) spectrometry

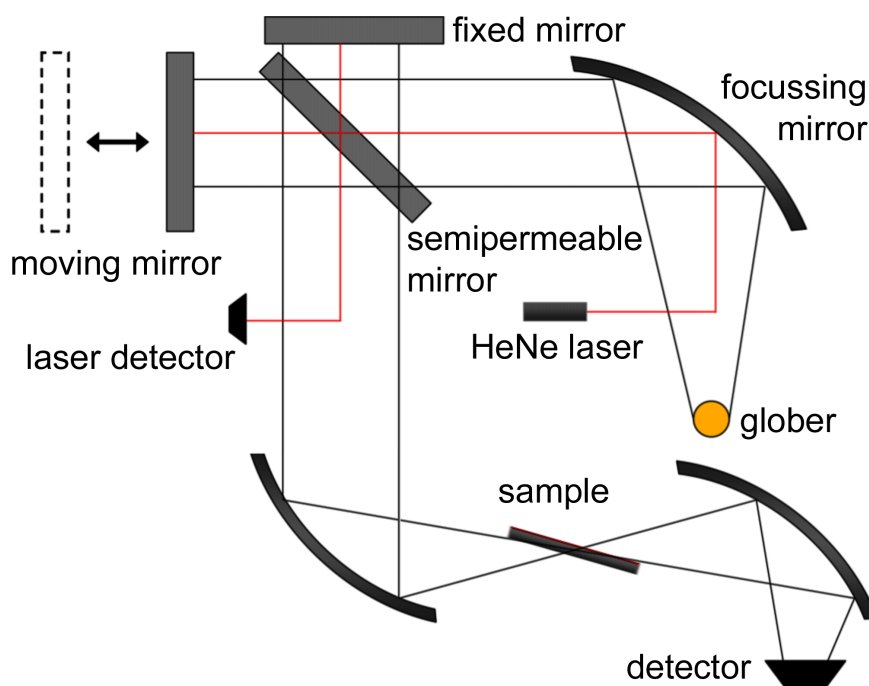


Figure 3.9: Schematic beam path of the FT-IR Spectrometer. Broad IR is emitted from the globar and passed into the Fourier transform mirror system. Different mirror positions x allow the measurement of the interference pattern in the detector $I(x)$. After acquisition in different mirror positions x , $I(\tilde{\nu})$ is extracted via Fourier transform. The thin film sample is mounted under the Brewster's angle for silicon (74°C). Slightly modified taken from Ref. [186].

Infrared spectroscopy is a powerful technique for the determination of vibrational modes. For centrosymmetric molecules like RUB and PF-RUB, it is sensitive to vibrational modes that are complementary to Raman active modes (see Chap. 5). When a

molecule interacts with an electromagnetic wave of frequency ω , it can undergo a transition from an initial to a final state of energy difference $\hbar\omega$ through the coupling of the electromagnetic field to the transition dipole moment. In contrast to Raman scattering, the photon becomes absorbed entirely by the molecule.

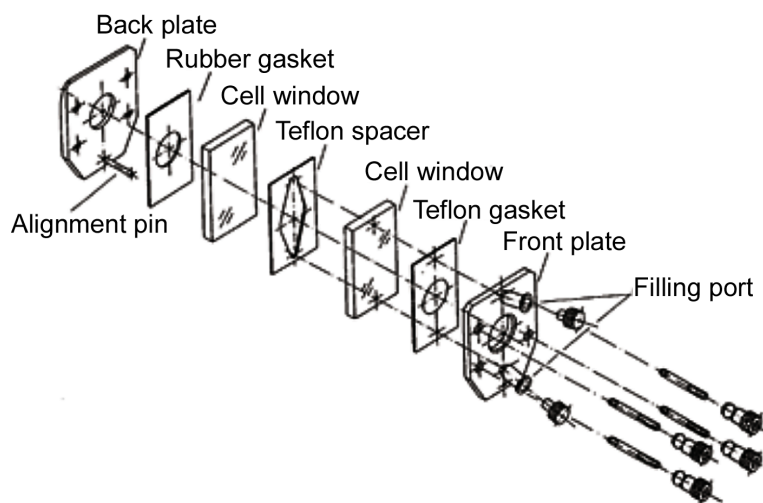


Figure 3.10: Schematic of the A145 liquid cell from BRUKER used for IR spectroscopy. The measurement volume of the solution is located between the two cell windows and is essentially determined by the thickness of the teflon spacer. After assembling of all parts, the liquid is filled into the cell through one of the filling ports.

Equipment and measurement

IR spectra of the thin film and solution samples were obtained in transmission mode with a VERTEX 70 (BRUKER) Fourier transform infrared (FT-IR) spectrometer with a PMA 50 detector unit attached (Fig. 3.9). Since the detector is sensitive only for IR energies above $\sim 800 \text{ cm}^{-1}$, no spectral information could be obtained for lower wavenumbers. In order to reduce artefacts in the resulting spectra caused by absorption of rotational bands of water, the spectrometer is continuously purged with nitrogen. In particular after mounting a sample, which permits wet air into the system, the equipment was purged for 30 min before starting the measurement. The aperture determining the diameter of the IR beam was set to 1 mm during the experiment. Further details on the instrument can be found in Ref. [186].

The thin film samples were mounted with a tilt angle of 74° against the incident beam, which is near to the Brewster's angle of silicon (Sec. 2.1.4). In addition, the IR beam was p-polarized by a polarizer before shining onto the sample, which ensures avoiding of back-reflection at the smooth side of the silicon wafer (Sec. 3.2.1). The measurement

of molecules dissolved in Cl_2CH_2 were performed with help of a A145 LIQUID CELL from BRUKER with CaF_2 crystals (Fig. 3.10).

Data evaluation

Since the measurement for both thin film and solution samples were performed in transmission, the intensity of the measured modes follows the Beer-Lambert-Bouguer law (Sec. 2.1.2). The intensity I of the resulting IR spectra was determined using $I = (I_{\text{Sample}} - I_0)/I_0$, where I_{Sample} describes the intensity of the thin film with substrate (or the molecules dissolved in solution), and I_0 stands for the measured substrate only (or the absorption of the pure solvent). Solution spectra could not be monitored in energy regions with strong IR absorption of the solvent CH_2Cl_2 ($\approx 930 \text{ cm}^{-1}$, $1230\text{--}1300 \text{ cm}^{-1}$, $1410\text{--}1450 \text{ cm}^{-1}$) [187]. Hence, it was impossible to acquire vibrational information of the molecules in these regions.

3.2.6 Photoelectron spectroscopy (PES) at a synchrotron light source

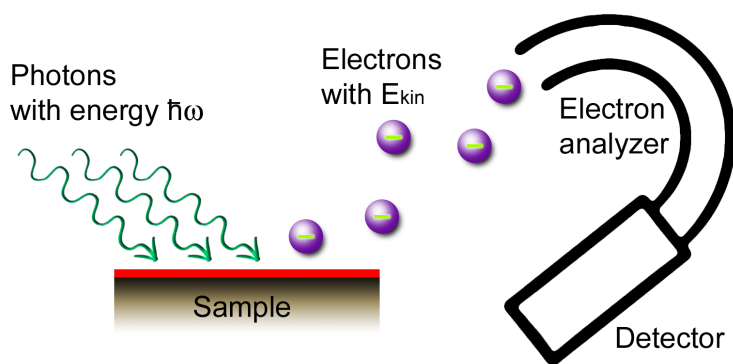


Figure 3.11: Principle of photoelectron spectroscopy (PES). Photons with energy $\hbar\omega$ hit the thin film sample deposited on a conducting substrate. Secondary electrons removed from the molecular orbitals pass the analyzer and reach the detector.

One way to study the absolute energy level alignment of a material is by means of photoelectron spectroscopy (PES) [54, 164], Fig. 3.11. PES techniques base on the application of the photoelectric effect (Sec. 2.3.3), leading to the emission of secondary electrons by photons in the energy range of ultraviolet or X-ray that are detected by the analyzer. While ultraviolet photoelectron spectroscopy (UPS) focuses on the outer shell orbitals of the compound with higher occupation energies like the HOMO, X-ray photoelectron spectroscopy (XPS) yields information about the core levels of the molecules (Fig. 3.12). Since the energy of the impinging photons is finite, there are secondary electrons with a maximum kinetic energy, which lead to a sharp edge in the

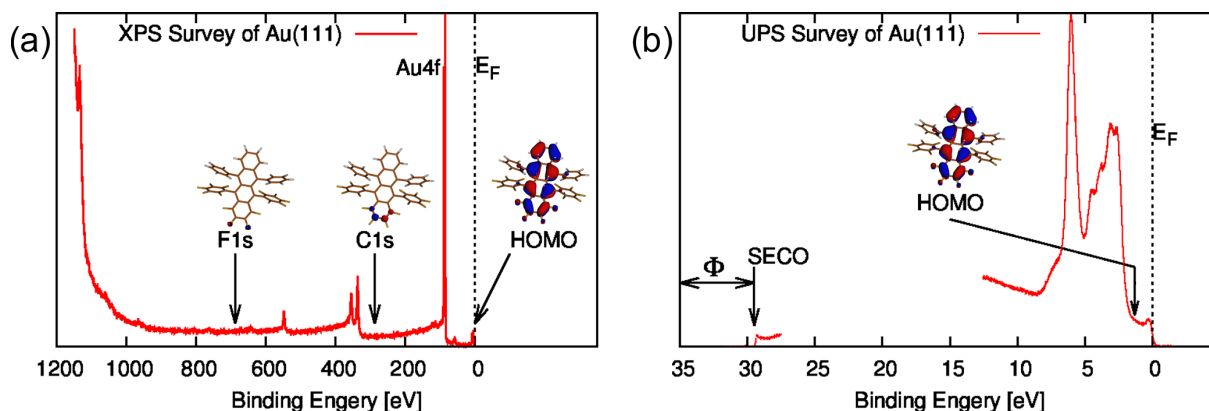


Figure 3.12: (a) X-ray photoelectron spectrum ($\hbar\omega = 1200$ eV) and (b) ultraviolet photoelectron spectrum ($\hbar\omega = 35$ eV) of Au(111), each without molecules deposited. The XPS survey covers a large range showing several Au(111) peaks including the two peaks of Au4f used for normalization of the energy axis, beginning from the Fermi level at $E_B = 0$. The arrows at the molecular models point to the binding energies of the respective molecular orbitals. Hence, upon deposition of fluorinated RUB molecules new peaks are expected in these regions. While F1s and C1s orbitals are expected to be observable (arrows), the H1s orbital energies are superimposed by metal bands at large binding energies. The UPS survey focusses particularly on lower binding energies. It is in particular used to investigate the HOMO level, which is the orbital with the lowest binding energy and thus near the Fermi level. Further details, see text.

PES spectra that is known as secondary electron cutoff (SECO). This cutoff gives information about the workfunction of the material. In order to observe a well defined SECO, often a negative bias voltage is applied to prevent electrons without or with only low kinetic energy from reaching the detector. Usually, UPS and XPS experiments are performed under vacuum conditions, since gas in the environment of the beam would absorb too much of its intensity. Moreover, in order to avoid charging of the sample upon X-ray radiation, a conducting substrate is needed.

Equipment and measurement

UPS and XPS measurements were performed at the SURICAT beamline of BESSY II in Berlin using a SCIENTA SES 100 electron analyzer. Sample preparation proceeded in a preparation chamber (base pressure $< 2 \times 10^{-9}$ mbar), which was connected to an analysis chamber (base pressure $< 5 \times 10^{-10}$ mbar) allowing sample transfer without breaking UHV conditions. Clean Au(111) and Ag(111) crystals were prepared by re-

peated cycles of Ar^+ sputtering and annealing to 450°C before thin film deposition. The surface cleanliness was confirmed by XPS. Thin film growth was performed at a base pressure of 2×10^{-9} mbar at room temperature and controlled by a quartz crystal microbalance. UPS (XPS) measurements were performed with $\hbar\omega = 35$ eV (1200 eV) photon energy at normal incidence. The secondary electron cutoff (SECO) was measured at -10 V sample bias. The measured work functions for the clean substrates are 5.48 eV for Au(111) and 4.55 eV for Ag(111), which is in good agreement with values reported previously [188,189].

Data evaluation

The energy axes of the UPS and XPS data were calibrated by features that occur at established energies. While the energy axis of the UPS data were normalized to the Fermi-edge, the metal peaks Au4f and Ag3d were used as orientation for the XPS data in case of Au(111) and Ag(111), respectively. The Shirley-background of the XPS measurements was removed.

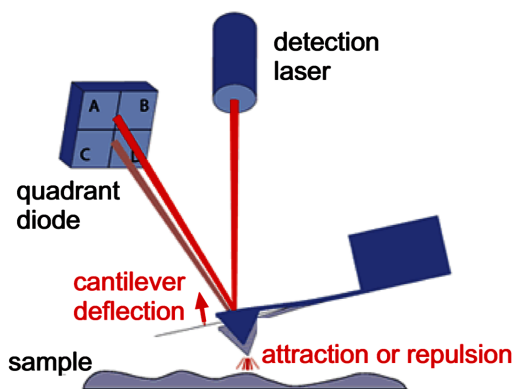


Figure 3.13: Principle of an atomic force microscope (AFM). A tip attached to a movable cantilever scans over a sample surface. Depending on the forces at a given spot, the cantilever is attracted or repulsed by the sample due to interaction with the surface. When scanning over the sample, the movement of the cantilever in z -direction, which is generated by the interaction, can be measured. A photo diode detects the reflection of a laser beam at the cantilever. Taken from Ref. [191].

3.2.7 Atomic force microscopy (AFM)

Atomic force microscopy (AFM) is a widely employed tool to obtain information about the topology of a sample. Its principle is based on a fine tip interacting with the sample surface, which is depicted in Fig. 3.13. The tip is attached to a cantilever, which in turn is in contact with a piezo crystal that allows approaching of the cantilever (and hence the tip) towards the sample, but also scanning in xy -direction over the sample.

With help of a laser, tiny movements of the cantilever occurring in z -direction can be monitored, when the sample is scanned.

The AFM pictures presented in this work were acquired with a JPK NANOWIZARD II from DIGITAL INSTRUMENTS in tapping mode. The setup was run with an N-type Si tip (radius $r < 10$ nm) from APPNANO, common measurements were performed at tip speeds of $v = 0.5 \mu\text{m/s}$. Evaluation of the data was performed with GWYDDION [190].

3.2.8 X-ray reflectivity (XRR) and grazing incidence X-ray diffraction (GIXD)

Commonly, X-ray diffraction is the method of choice for crystal structure analysis, but also for organic thin film characterization regarding thickness or roughness. It bases on the elastic scattering of electro-magnetic waves with a wavelength on atomic or molecular length scale (X-rays). A more detailed description of different X-ray scattering techniques can be found in the literature [192]. Fig. 3.14 shows the scattering geometry of (a) X-ray reflectivity (XRR) and (b) grazing incidence X-ray diffraction (GIXD).

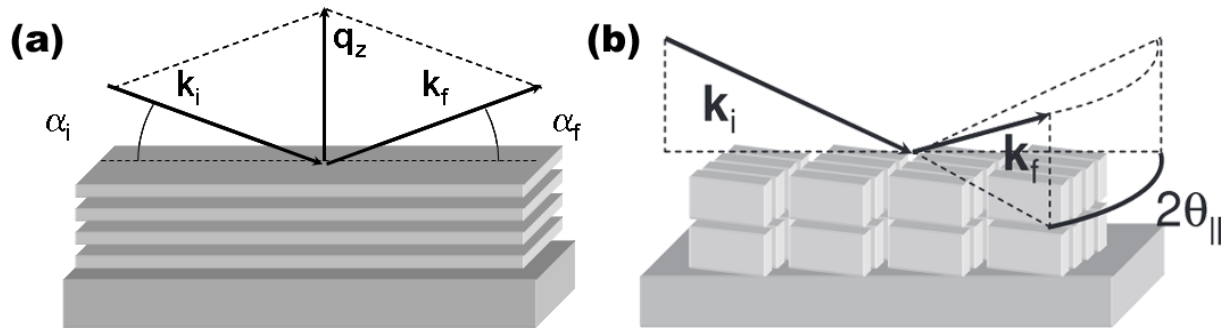


Figure 3.14: Scattering geometries of X-ray reflectivity (XRR) and grazing incidence X-ray diffraction (GIXD). While XRR allows to determine structural properties in out-of-plane direction, for GIXD refractive indices < 1 of the samples are utilized for the investigation of the in-plane properties. The graphics are slightly modified from Ref. [66].

X-ray reflectivity (XRR)

For XRR incident (\vec{k}_i) and reflected (\vec{k}_f) wave vectors are aligned in-plane and under identical angles $\alpha_i = \alpha_f$, which allows the determination of the out-of-plane component of the scattering vector $\vec{q} = \vec{k}_f - \vec{k}_i$. In the case of elastic scattering the energy of

incident and reflected beam are equal ($|\vec{k}_f| = |\vec{k}_i|$), which leads to

$$q_z = \frac{4\pi}{\lambda} \sin(\alpha_i). \quad (3.10)$$

For samples consisting of several smooth interfaces forming layers, the diffraction can be described in analogy to ellipsometry by a matrix formalism (Sec. 2.1.3). Moreover, if the layer thickness d is constant for the particular layers, Bragg peaks can be observed for special angles of incidence α_{Bragg} obeying the condition

$$n\lambda = 2d \sin(\alpha_{\text{Bragg}}) \quad (n = 1, 2, 3, \dots). \quad (3.11)$$

Grazing incidence X-ray diffraction (GIXD)

In contrast to visible light, for many materials (like silicon) the real part of the refractive index becomes in the X-ray regime smaller than 1, which results in a total reflection below a critical angle $\alpha_c > 0^\circ$. On irradiation below the critical angle α_c , an evanescent wave is formed that is exponentially damped in the material. This effect is used for grazing incidence X-ray diffraction (GIXD), that can give information about the in-plane (poly)crystallinity of a sample.

Equipment and measurement

In particular XRR spectra were obtained with our in-house XRD 3003 TT X-ray reflectometer from GE/SEIFERT. The system is equipped with a copper anode and a monochromator permitting Cu $K_{\alpha 1}$ radiation ($\lambda = 1.54 \text{ \AA}$) to be shined onto the sample.

GIXD spectra shown in this work (Sec. 6.3.2) were obtained at the SWISS LIGHT SOURCE (MS-X04SA/SURFACE DIFFRACTION beamline) [193] at 13.996 keV ($\lambda = 0.886 \text{ \AA}$) using a PILATUS detector. The incidence angle $\alpha = 0.12^\circ$ of the beam was below the critical angle of SiO_2 .

During measurement the samples were kept at room temperature and under protective atmosphere, both at the home diffractometer as well as at the SWISS LIGHT SOURCE.

CHAPTER 4

ELECTRONIC EXCITATION OF RUB, F₁₄-RUB, AND PF-RUB

This chapter consists of three sections, each shedding light on different aspects of optical and electronic properties of the fluorinated rubrene molecules. The first section (Sec. 4.1) is devoted to the optical properties of RUB, F₁₄-RUB, and PF-RUB in thin films and solution in comparison to DFT results. It discusses the relative energy alignment of the HOMO-LUMO gap in dependence on the degree of fluorination and the molecular environment, like thin film, solution or free space [87]. This is followed by a study on the oxidation potential of the molecules in Sec. 4.2 of molecules in both thin films and in solution¹. The last section (Sec. 4.3) presents photoelectron spectroscopy (PES) of F₁₄-RUB and PF-RUB thin films on Au(111) and Ag(111)². Here, the tunability of the molecular energy levels by fluorination is shown and discussed together with DFT results. Most importantly, there is evidence for an alignment of the partially fluorinated F₁₄-RUB molecules, which show a very strong dipole moment along their backbone.

¹Reprinted in part with permission from Anger et al. *J. Phys. Chem. C* *accepted* (Ref. [143]), (DOI: 10.1021/acs.jpcc.5b12293), copyright 2016 American Chemical Society.

²Reprinted in part with permission from Anger et al. *J. Phys. Chem. C* **119**, 6769 (2015) (Ref. [141]), (DOI: 10.1021/jp511822g), copyright 2015 American Chemical Society.

4.1 Optical Properties of RUB, F₁₄-RUB, and PF-RUB in thin films and solution

This section presents the optical properties of RUB, F₁₄-RUB, and PF-RUB [87]. Absorption (ellipsometry) and PL emission allow a determination of the relative alignment of the HOMO and the LUMO level of the compounds. An alignment relative to the vacuum level is provided in Sec. 4.2 for solution and in Sec. 4.3 for thin films.

4.1.1 Experimental conditions

Thin films of the three materials were grown on silicon wafers covered by a native oxide layer using organic molecular beam deposition techniques [41,70] at a constant growth rate of roughly 2 Å/min. The films were grown under ultra high vacuum conditions with a thickness of 20 nm on substrates kept at room temperature (RT). Under these conditions RUB thin films are observed to grow amorphous [194] with a predominance of its twisted isomer [159,195,196].

In order to acquire optical spectra of the pristine films, their absorption spectra were studied *in situ* with a WOOLLAM M-2000 spectroscopic ellipsometer [182] directly after growth, before notable dewetting occurs. Photoluminescence (PL) spectra were acquired using a HORIBA JOBIN YVON LABRAM HR 800 spectrometer with a CCD-1024×256-OPEN-3S9 as detector, within two days after growth on smooth samples in a protective atmosphere, as confirmed by complementary investigations with X-ray reflectivity. Excitation for PL was performed using a frequency doubled Nd:YAG laser at 532 nm (2.33 eV). Solution spectra in dichloromethane (CH₂Cl₂) were obtained using a JASCO V-570 spectrophotometer and a JASCO FP-6600 spectrofluorophotometer, for absorption and for PL measurements, respectively.

4.1.2 Experimental spectra

Absorption spectra (ϵ_2 for thin films and α/ω for solution) and PL spectra at room temperature of RUB, F₁₄-RUB, and PF-RUB are shown in Fig. 4.1. The overall shape is remarkably similar. In order to access the vibronic features, the intensity of the PL spectra was divided by a factor $\omega^3 \cdot n^3(\omega)$ [197]. The energetically lowest peak in the absorption spectra of RUB, F₁₄-RUB, and PF-RUB lies at 2.34 eV (2.34 eV), 2.30 eV (2.30 eV), and 2.33 eV (2.30 eV), respectively, in thin films (in solution). In all three spectra, fur-

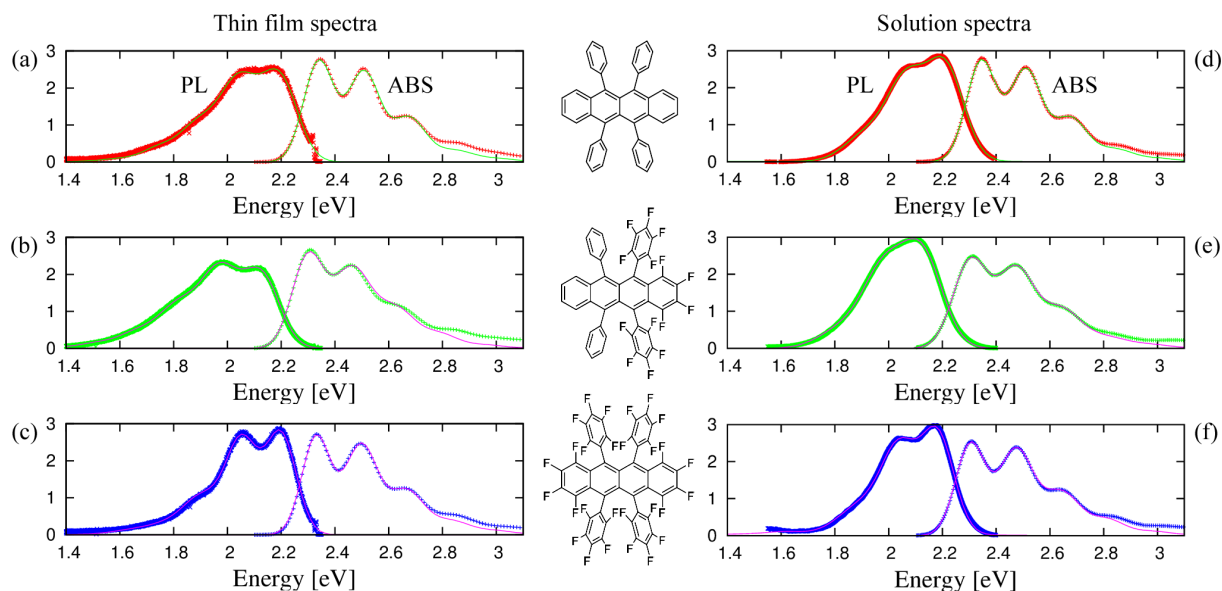


Figure 4.1: Photoluminescence (PL) and absorption (ABS, *i. e.* ϵ_2 in thin films and α/ω in solution) of smooth RUB ($C_{42}H_{28}$), F₁₄-RUB ($C_{42}F_{14}H_{14}$), and PF-RUB ($C_{42}F_{28}$) thin films of 20 nm thickness, (a), (b), and (c), respectively, and in dichloromethane (CH_2Cl_2), (d), (e), and (f), respectively. The PL spectra shown are divided by $\omega^3 n^3(\omega)$ with respect to the measured intensity, giving more direct access to the vibronic progression of an effective internal vibration. The spectra are obtained at RT and for better comparison, their integrated intensity is normalized to 1. Line: Fit according to Eq. (4.1).

ther peaks follow towards higher energies, each with decreasing intensity with a spacing of approximately 0.17 eV. The highest emission peak is found at 2.20 eV (2.21 eV), 2.14 eV (2.12 eV), and 2.20 eV (2.18 eV) for RUB, F₁₄-RUB, and PF-RUB, respectively, in thin films (in solution). Also in luminescence, we observe further peaks with decreasing intensity towards lower energies, each with a similar spacing as in the absorption spectra. Thin film spectra obtained at 77 K (not shown) do not exhibit additional transition bands, compared to those at RT. Both, absorption and PL spectra of RUB match literature spectra well [71, 198, 199].

The most intense peaks in the absorption and PL emission spectra of RUB in Fig. 4.1(a) and (d) are known to stem from the corresponding HOMO-LUMO transition, while the equally spaced further peaks belong to a vibronic progression of the same electronic transition [71, 159, 199, 200]. Since for F₁₄-RUB and PF-RUB we do not observe any further peaks within the investigated energy range, also for these materials we assign

the most intense peaks in absorption and PL to the HOMO-LUMO transition and the less intense peaks to the vibronic progression.

As discussed elsewhere in more detail [159], the shape of the absorption spectrum of RUB is determined by the deformation in the relaxed excited state which can be obtained with density functional theory (DFT). More specifically, a calculated reorganization energy in the excited potential surface of about 0.21 eV can be divided into a contribution of about 0.05 eV arising from low-frequency internal vibrations and about 0.16 eV assigned to internal vibrations of high frequency, clustering around an *effective* mode energy of about 0.17 eV. Therefore, the apparent E_{00} transition of this effective internal mode is expected at about 0.05 eV above the overall E_{00} transition related to the lowest vibrational levels of all internal modes. The spectra in Fig. 4.1 agree semi-quantitatively with this calculation: For RUB, the difference between the lowest subband of absorption and the highest subband of PL is about $\Delta E_{00} = 0.14$ eV, somewhat larger than 2×0.05 eV = 0.10 eV expected from the contribution of the low-frequency internal modes to the reorganization energies on the ground and excited state potentials. The additional PL redshift of 0.04 eV might arise from thermalization of the excitation towards sites with a particularly low transition energy defined by the local surroundings, or to a principal deficiency of the density functional method chosen previously [159].

The different subbands in absorption and (rescaled) PL depicted in Fig. 4.1 can be fitted to a Poisson progression over consecutive levels of an effective internal vibration with energy $\hbar\omega_{\text{eff}}$,

$$I(E) = A \sum_n \frac{S^n}{n!} \frac{1}{\sigma_n \sqrt{2\pi}} \exp \left[-\frac{(E_{00} + n\hbar\omega_{\text{eff}} - E)^2}{2\sigma_n^2} \right], \quad (4.1)$$

where S is the Huang-Rhys factor of the effective mode. The fit results are shown in Tab. 4.1(a, b), and it turns out that the effective mode has to be chosen slightly differently for absorption and PL. For RUB, the fitted Huang-Rhys factors for absorption and PL are in excellent agreement with the DFT value of $S = 0.985$ for a calculated effective mode at 0.162 eV [159]. This demonstrates that PL from our amorphous films probes the photophysics of monomers, in sharp contrast to the crystalline phase, where intermolecular interactions result in completely different PL spectra [199,201]. Arithmetically weighting the centers of gravity in absorption ($\langle E_{\text{abs}} \rangle$) and emission ($\langle E_{\text{PL}} \rangle$), we find the experimental HOMO-LUMO transition for RUB, F₁₄-RUB, and PF-RUB thin films at 2.28 eV, 2.21 eV, and 2.28 eV, respectively, for thin films and at 2.30 eV, 2.24 eV, and 2.27 eV for solution. The observed redshift is thereby much lower than the redshift of other organic compounds, e. g. pentacene, which shows a more pronounced redshift

from solution to thin film, both in its unsubstituted and in its fluorinated variant [128]. However, those molecules form a strict crystalline order, which is not the case for RUB thin films.

	RUB	F ₁₄ -RUB	PF-RUB
(a) THIN FILM			
E_{00}^{abs} [eV]	2.34	2.30	2.33
S_{abs}	0.96	1.00	1.03
$\hbar\omega_{\text{abs}}$ [eV]	0.17	0.16	0.17
$\langle E_{\text{abs}} \rangle$ [eV]	2.50	2.46	2.50
E_{00}^{PL} [eV]	2.20	2.14	2.20
S_{PL}	0.97	1.10	0.95
$\hbar\omega_{\text{PL}}$ [eV]	0.15	0.16	0.15
$\langle E_{\text{PL}} \rangle$ [eV]	2.05	1.96	2.06
(b) SOLUTION			
E_{00}^{abs} [eV]	2.34	2.30	2.30
S_{abs}	0.97	0.97	1.07
$\hbar\omega_{\text{abs}}$ [eV]	0.17	0.17	0.17
$\langle E_{\text{abs}} \rangle$ [eV]	2.50	2.45	2.48
E_{00}^{PL} [eV]	2.21	2.12	2.18
S_{PL}	0.84	0.72	0.91
$\hbar\omega_{\text{PL}}$ [eV]	0.14	0.14	0.14
$\langle E_{\text{PL}} \rangle$ [eV]	2.09	2.03	2.06
(c) DFT CALCULATION			
HOMO [eV]	-4.62	-5.37	-6.09
LUMO [eV]	-2.10	-2.92	-3.67
gap [eV]	2.52	2.45	2.42
transition (TD-DFT) [eV]	2.19	2.10	2.06
f_{osc}	0.160	0.146	0.137
transition dipole [D]	1.73	1.68	1.65
twisted [eV]	0. (D_2)	0. (C_2)	0. (D_2)
planar [eV]	0.16 (C_{2h})	0.21 (C_s)	0.30 (C_{2h})
transition state [eV]	0.28 (D_{2h})	0.29 (C_{2v})	0.51 (D_{2h})

Table 4.1: Fitted values of RUB, F₁₄-RUB, and PF-RUB absorption and emission spectra of the thin films (a) and solution (b). (c) Top: Frontier orbital energy levels of the three model compounds, gap energies, and transition energies obtained with time-dependent DFT for the most stable twisted conformation at the B3LYP/6-31G(d) level. Bottom: Relative energies of different isomers of the three model compounds. The relative energies are reported with respect to the most stable twisted conformation, including the point group of each isomer.

4.1.3 DFT calculations

Our DFT calculations for the most stable isomers are visualized by a molecular electrostatic potential (MEP) plot mapped on the electron density surface for $0.01/a_{\text{B}}^3$ in Fig. 4.2. The color coding indicates the inversion of the MEP for RUB and PF-RUB due to the different electron affinity of fluorine and hydrogen. The plot illustrates well

the huge dipole moment of F₁₄-RUB, along its backbone. For each of the three compounds under study, two stable isomers can occur, related by an unstable transition state with higher symmetry. In a DFT calculation at the B3LYP/6-31G(d) level as obtained with the GAUSSIAN program package [168] for all three cases a geometry with a twisted backbone is the most stable isomer, realizing a D_2 point group for RUB and PF-RUB, and C_2 for F₁₄-RUB, respectively. The DFT results in Tab. 4.1(c) are reported with respect to the most stable isomer of each molecule. For RUB, the twisted D_2 conformation is 0.16 eV more stable than the C_{2h} isomer resembling the molecular geometry in the crystalline phase, with a D_{2h} isomerization barrier of 0.28 eV between them. With 0.16 eV, the B3LYP energy difference between the two stable isomers is somewhat below the Hartree-Fock/6-31G(d) value of 0.21 eV found earlier [196]. The isomerization barrier is lower than the Hartree-Fock value of 0.34 eV as well, as expected from previous investigations of torsional potentials involving phenyl groups [202]. The perfluorinated compound shows a particularly large stabilization of 0.51 eV with respect to the highly symmetric D_{2h} transition state and of 0.30 eV when compared to the C_{2h} isomer with a planar backbone and tilted fluorinated phenyl groups. In RUB, the stabilization of the D_2 is only 0.28 eV with respect to the D_{2h} transition state, and 0.16 eV with respect to the C_{2h} isomer. The comparison between RUB and PF-RUB reveals that distortions away from the highest symmetry are stabilized by the fluorination, presumably by a steric hindrance between the fluorinated phenyl wings.

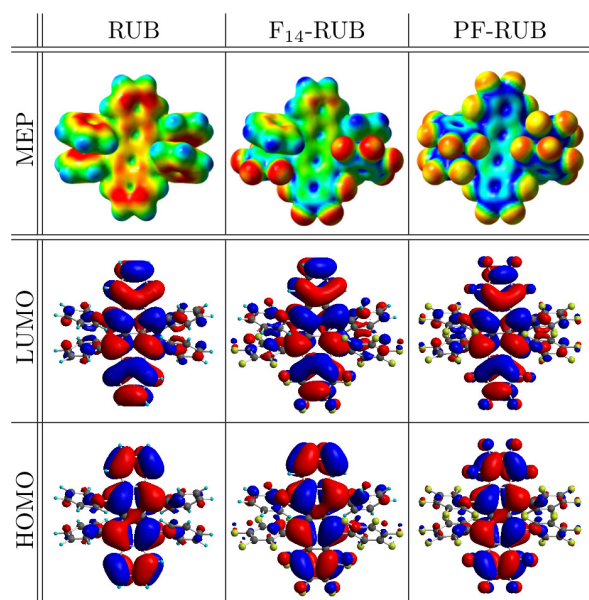


Figure 4.2: Molecular electrostatic potential (top) mapped on the electron density surface for $0.01/a_B^3$, with positive potential (blue) close to H atoms and the positively charged core of PF-RUB, and negative potential (red) around F atoms and the negatively charged core of RUB. LUMO (middle) and HOMO (bottom) of RUB, F₁₄-RUB, and PF-RUB in the twisted conformation. Calculated with B3LYP/6-31G(d).

For RUB and PF-RUB, all isomers have no dipole moment, whereas the dipole moment of F₁₄-RUB becomes more pronounced for the less stable isomers: The most stable twisted isomer (C_2) has a dipole moment of 4.22 Debye, growing towards 4.89 Debye (C_s) and 5.10 Debye (C_{2v}). This extraordinarily large dipole moment, which probably is the most fundamental difference to RUB and PF-RUB, suggests that F₁₄-RUB does not just follow a linear interpolation of the (optical) properties of the two other materials.

As expected, the fully or partially fluorinated compounds have significantly higher frontier orbital energies, making the fluorinated variants particularly interesting as acceptor materials for organic solar cells. In F₁₄-RUB, the respective shifts are -0.75 eV (HOMO) and -0.82 eV (LUMO), values roughly doubled for the perfluorinated compound, with -1.47 eV (HOMO) and -1.57 eV (LUMO). From the visualization of the orbitals in Fig. 4.2, it is obvious that the π and π^* states do not extend significantly over the hydrogen atoms, whereas each fluorine gives a small anti-bonding contribution with a sign change of the orbital along the respective C-F bond.

4.1.4 Comparison of experimental and theoretical values

For F₁₄-RUB and PF-RUB, the absorption and PL spectra resemble protonated RUB. The absorption of F₁₄-RUB shows a significant redshift of about 0.04 eV with respect to RUB, and together with a Stokes shift being larger by 0.04 eV, the PL spectra occur at about 0.08 eV below RUB. Surprisingly, PF-RUB does not shift further to the red, but instead the positions and shapes of absorption and PL spectra are very similar to RUB. Since the 'nonlinear' shift (HOMO-LUMO transition energies versus the degree of fluorination of the molecules) occurs also in solution, it is not only a thin film effect.

The general underestimation of the HOMO-LUMO transition of RUB, F₁₄-RUB, and PF-RUB by TD-DFT calculation is a well-known phenomenon for the acene group [203] that resembles the backbone of RUB and its here presented derivatives. However, the monotonous increase of the frontier orbital energies with increasing fluorination predicted by our DFT calculations reproduces chemical trends observed for other polyaromatic compounds, e. g. partially or fully fluorinated phthalocyanines and polyacenes [204,205].

In the emission spectra, reorientation of the dipoles of the solvent can cause an additional redshift of the spectra. For this reason, the further discussion will be restricted to absorption spectra. The redshift $\Delta\nu$ of the absorption spectra of RUB in thin films and solution in comparison to the free molecule due to polarizability differences of ground

and excited state molecules can be estimated by an equation following Renge [148],

$$\Delta\nu = p\varphi(n^2), \quad (4.2)$$

with $\varphi(n^2) = (n^2 - 1)/(n^2 + 2)$, the refractive index n of the solvent, and the slope p of the solvatochromic plot [148]. This results in a solvent shift of -0.06 eV for RUB in CH₂Cl₂ solution ($n^2 \approx 2$) and -0.11 eV for RUB thin films with a refractive index of $n_{\text{RUB}}^2 \approx \epsilon_{1,\text{RUB}} \approx 3.25$ at E_{00} , as obtained from ellipsometry. The latter value is based on the assumption of the RUB thin film as a 'solution of RUB molecules in RUB', which should be a good approximation for disordered thin films, as in the present case. From these values of the solvent shifts and the observed E_{00} transitions in Tab. 4.1, RUB in CH₂Cl₂ (in the film) yields an estimate of $E_{00} = 2.40$ eV (2.45 eV) in the gas phase. As the solvation cavity of RUB in the thin film might be larger, the solvation shift of -0.11 eV is likely to be somewhat overestimated, so that a gas phase value of $E_{00} = 2.40$ eV seems to be more realistic.

For the other compounds, an evaluation of the solvent shift has to account for the smaller transition dipoles in Tab. 4.1 and an increase of the molecular volume by a factor of 1.17 for F₁₄-RUB and by 1.29 for PF-RUB. As suggested by Bayliss [206], the solvent shift should scale with the squared transition dipole divided by the molecular volume, so that the solvent shift in F₁₄-RUB should be smaller by a factor of about 0.8 and in PF-RUB by a factor of about 0.7. Hence, from the observed E_{00} in solution, both F₁₄-RUB and PF-RUB should have gas phase values close to $E_{00} = 2.35$ eV, and the average vertical transition energies in the gas phase should be about $\langle E_{\text{abs,RUB}} \rangle = 2.56$ eV, $\langle E_{\text{abs,F14-RUB}} \rangle = 2.53$ eV, and $\langle E_{\text{abs,PF-RUB}} \rangle = 2.54$ eV. This estimate for the molecular transition energy of RUB is remarkably close to the calculated B3LYP/6-31G(d) gap of 2.52 eV, whereas the TD-DFT value for the lowest transition is severely underestimated, a deficiency known from other acenes [203]. The calculated DFT gap energy and the lowest transition energy in TD-DFT show stronger chemical trends than the observed spectra, a shortcoming which might be influenced by the poorer convergence of the variational basis for the fluorine-containing compounds. Altogether, taking into account the very large shifts of frontier orbital energies, it is quite remarkable that the optical spectra of the three compounds are so similar. This finding resembles the observed behavior of fluorinated phthalocyanines, but is in sharp contrast to the stronger spectroscopic shifts between pentacene and perfluoropentacene, both in solution and in the crystalline phase [131].

Overall, the agreement between DFT and experiment is remarkably good, after the shift and corrections by the dielectric environment are considered. This can presumably also be attributed to the amorphous structure of the system that avoids strong

crystal effects as observed in the case of fluorinated phthalocyanines or pentacene. Also, the relative similarity of the RUB and PF-RUB spectra is remarkable. Some of the deviations found for F₁₄-RUB within this series may be related to its strong dipole moment, which is yet to be explored and exploited.

4.1.5 Concluding remarks

To conclude, the optical properties of F₁₄-RUB and PF-RUB have been determined both from thin films and in solution. While the position of the HOMO-LUMO transition of PF-RUB surprisingly resembles the HOMO-LUMO transition of unsubstituted RUB, F₁₄-RUB is slightly redshifted. Due to its strong dipole moment of 4.22 Debye in its most stable conformation, F₁₄-RUB provides a significant potential for applications.

4.2 Oxidation potential of RUB, F₁₄-RUB, and PF-RUB

In this section we report on the oxidation potential of partially fluorinated (C₄₂F₁₄H₁₄, F₁₄-RUB) and perfluorinated rubrene (C₄₂F₂₈, RUB) studied by cyclic voltammetry (CV) in solution and by spectroscopic ellipsometry in thin films in combination with density functional theory computations. The derivatives show a systematic increase in fluorination against rubrene (C₄₂H₂₈, RUB), which results in increasing stability and oxidation potential of the fluorinated derivatives.

4.2.1 Experimental conditions

Thin films of the three materials were deposited at room temperature under high vacuum conditions on silicon wafers covered by a native oxide layer. By keeping the molecular flux at a constant growth rate of 1.1 Å/min monitored by a quartz crystal microbalance (QCM), films with thicknesses of 20 nm were prepared. Under these conditions RUB, F₁₄-RUB, and PF-RUB are known to form amorphous thin films [87]. About 90 min after thin film deposition, air was dosed into the UHV chamber up to a pressure of 50 mbar. Real-time data of the oxidation process were obtained using spectroscopic ellipsometry with a broad band Xe lamp (75 W, 250-1000 nm), while the samples were exposed to air [127]. The ellipsometer (WOLLAM M-2000 SE) was equipped with a rotating compensator for accurate measurement of the polarization and a CCD camera enabling simultaneous detection of all wavelengths, allowing minimization of

the acquisition time ($t = 1$ min). In order to measure the samples *in situ*, the ellipsometer was mounted on the vacuum system with strain free quartz windows resulting in a fixed angle of incidence of $\sim 61^\circ$. Data acquisition started directly with the partial venting process of the vacuum system until after 4–10 min a pressure of 50 mbar was reached, which then was kept constant.

The ionization potential (IP) and electron affinity (EA) of the RUB, F₁₄-RUB, and PF-RUB molecules in solution were computed with the B3LYP functional and TZVP basis set using TURBOMOLE 6.4 [166]. The values for IP and EA of the RUB and PF-RUB (F₁₄-RUB) molecules in D_2 (C_2) symmetry were estimated from the energies of the ionized species under the consideration of the polarization energy of the solvent (CH_2Cl_2).

4.2.2 Optical absorption of thin films

Fig. 4.3 shows the real-time absorption spectra (ϵ_2) obtained from thin films covered with 20 nm of RUB, F₁₄-RUB, and PF-RUB using spectroscopic ellipsometry. The ellipsometric raw data consisting of the parameters Ψ and Δ was converted into the dielectric function $\epsilon_1 + i\epsilon_2$ using a commercial software package (WVASE32). The data was modeled with an isotropic layer accounting for the organic thin film deposited on the native silicon dioxide, which is in each case represented by one layer for the dioxide and for the silicon layer, respectively. The spectra shown were acquired in intervals of 100 min beginning with the exposure to air at a pressure of 50 mbar into the vacuum chamber. The time resolution of the spectra was determined by their integration time of 1 min.

At $t = 0$ min (still under vacuum conditions) we observe the HOMO-LUMO transition of the unoxidized RUB, F₁₄-RUB, and PF-RUB thin films at 2.34 eV, 2.30 eV, and 2.33 eV, respectively, which is in good agreement with previously reported values [141]. All compounds show a pronounced vibronic progression of the HOMO-LUMO transition that can be well fitted with a spacing of ~ 0.17 eV [87]. For RUB, an additional distinct transition can be observed at 4.03 eV [127], and also for the fluorinated materials F₁₄-RUB and PF-RUB we find similar peaks (3.95 eV and 4.03 eV, respectively).

These observations clearly show that the relative energy alignment of the three materials is very similar, merely the optical transitions of F₁₄-RUB are slightly redshifted by -0.05 eV compared to PF-RUB and RUB [87], which is in clear contrast to the effects found upon perfluorination of pentacene, where strong modifications of the optical characteristics are observed [128]. This evidences that the optical properties of the compounds do not change fundamentally with the degree of fluorination. The ion-

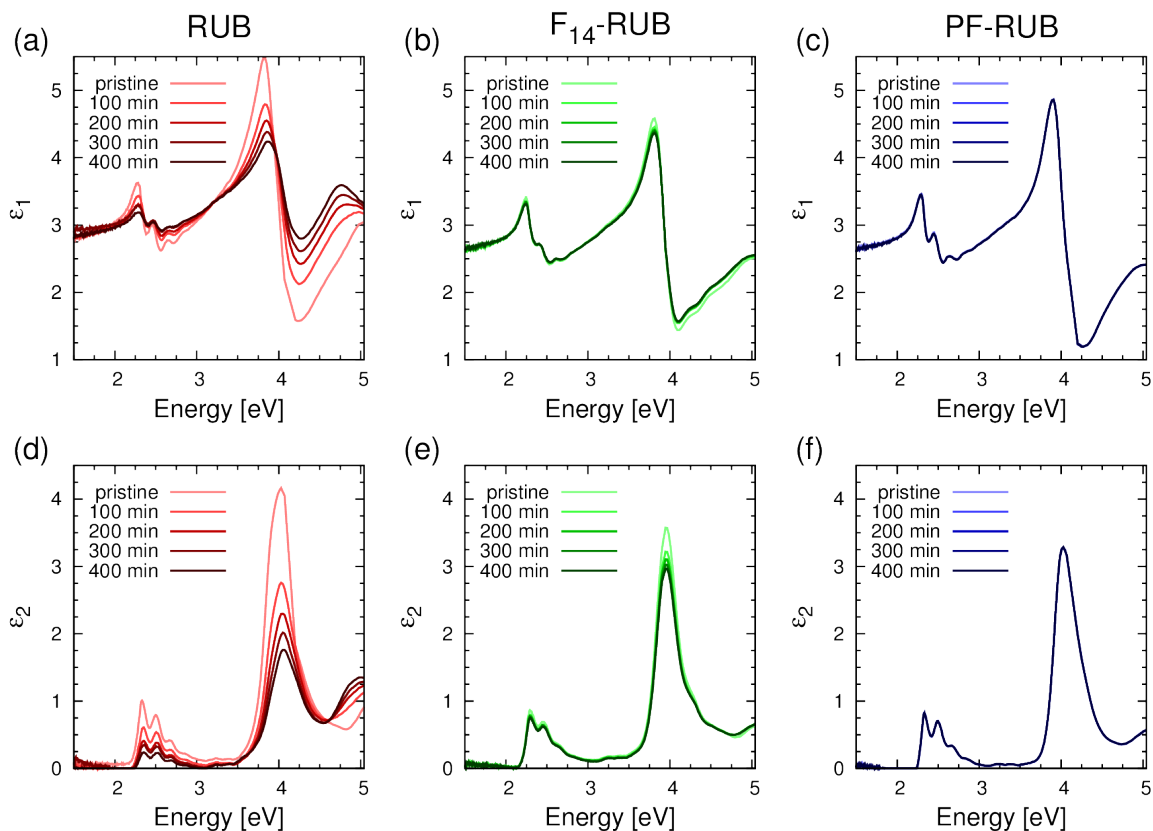


Figure 4.3: Real time observation of the optical properties of RUB, F₁₄-RUB, and PF-RUB (ϵ_1 : (a), (b), and (c), respectively, and ϵ_2 : (d), (e), and (f), respectively) thin films using spectroscopic ellipsometry. 90 min after deposition (20 nm), the thin films were exposed to air (50 mbar). While the unsubstituted rubrene shows strong oxidation effects resulting in bleaching of the fundamental optical excitations [44, 127], for the partially fluorinated F₁₄-RUB clearly weaker and for the fully fluorinated PF-RUB no changes in the spectra of ϵ_1 and ϵ_2 can be observed.

ization potential, however, was shown to differ by ~ 1.7 eV (~ 1.5 eV) from RUB to PF-RUB (F₁₄-RUB) [141].

It is well-known that RUB becomes transparent in the visible spectral region upon exposure to light and oxygen since photooxidation leads to the formation of transparent rubrene-endoxide or -peroxide [44, 127, 144, 198]. In good agreement with this expectation, we observe a distinct decrease in intensity of the HOMO-LUMO transition of RUB when permitting air to enter the vacuum system [127]. Simultaneously, the transition

at ~ 4 eV is getting weaker, and a new transition at ~ 5 eV related to photooxidized RUB becomes stronger [127].

For F₁₄-RUB the observed change in the absorption spectra is qualitatively similar to that observed for RUB, however, it is considerably less pronounced with respect to both, reaction speed and absolute strength of change. The intensity decrease of the HOMO-LUMO transition and also of the transition at ~ 4.03 eV is clearly less pronounced than for RUB. As a result, the residual absorption signal after 400 min is still stronger than that which is found only after 100 min for RUB with respect to the initial signals. In contrast to these two cases, we do not observe any changes in the optical spectra of PF-RUB upon exposure to air within the duration of the experiment. Obviously, F₁₄-RUB thin films are considerably and PF-RUB thin films far more stable against oxidation in comparison to RUB.

The tendency of thin films to be subjected to a reaction with oxygen depends in addition to the chemical properties crucially on the particular thin film structure. Regions of disordered RUB thin films allow oxygen much easier to penetrate the material than regions in crystalline form [89, 146]. Besides of the higher oxidation potential, this has an additional influence on the reduced oxidation of the fluorinated rubrene thin films, since particularly for PF-RUB dewetting towards a more (poly)crystalline structure within short time has been reported [142].

4.2.3 Electrochemical properties in solution

Electrochemical methods like CV allow for the investigation of the general electrochemical properties of a redox-active compound in solution. Both, oxidation and reduction processes at the electrode interface can be examined by means of the same method, including the determination of redox potentials [177]. Moreover, from the potential values of the corresponding oxidative or reductive processes, values for the energy levels of the highest occupied molecular orbital (HOMO) and the lowest unoccupied molecular orbital (LUMO) can be estimated [179].

The redox behavior of RUB, F₁₄-RUB and PF-RUB in solution, including the determination of redox potentials and in the absence of oxygen was studied by means of CV in 0.1 M NBu₄PF₆/CH₂Cl₂ at a Pt disk electrode under planar diffusion conditions. Cyclic voltammograms of RUB (Fig. 4.4, bottom) show a first chemically reversible oxidation (solid line, cation formation) and a chemically reversible reduction (dashed line, anion formation) with peak potentials for the oxidation (E_p^{ox}) and the reduction (E_p^{red}) of +0.39 V and -2.16 V, respectively. The half wave potentials of the anodic and cathodic

redox couple is found at +0.33 V ($E_{1/2}^{\text{ox}}$, oxidation) and -2.09 V ($E_{1/2}^{\text{red}}$, reduction). Both values are in good agreement with previously reported data [43,47,120,207]. At higher potentials, a second chemically irreversible oxidation (formation of the dianion) wave located at around +1.0 V [47] is observed (see Appendix, p. 125).

The anodic and cathodic I - E curves of the partially fluorinated F₁₄-RUB (Fig. 4.4, middle) show a chemically reversible oxidation (solid line, cation formation) and a chemically reversible reduction (dashed line, anion formation) with half wave potentials of $E_{1/2}^{\text{ox}} = +0.91$ V and $E_{1/2}^{\text{red}} = -1.55$ V (Tab. 4.2). At lower potentials a chemically irreversible redox wave at around -1.87 V is visible, which becomes reversible for fast scan rates: fast decomposition of the doubly reduced species, see Appendix, p. 125.

Cyclic voltammograms of PF-RUB (Fig. 4.4, top) show two chemically reversible reduction processes with half wave potentials of -0.96 V and -1.65 V. We attribute the two redox processes to the stepwise formation of the dianion via an anionic species. In contrast to F₁₄-RUB, the dianionic species formed during the second reduction of PF-RUB (-1.65 V) seems to be more stable within the time scale of the voltammetric experiment. The second electron transfer process is chemically reversible even at slow scan rates ($v \leq 200$ mV s⁻¹). A chemically irreversible oxidation wave at considerably high potentials (close to the limit of the potential window of the electrolyte, Fig. 4.4, top, solid line) is revealed by the anodic potential cycle of PF-RUB. The peak potential of the oxidation is +1.94 V ($v = 100$ mV s⁻¹).

An increase in the degree of fluorination leads to an increase of the oxidation peak potentials of +1.6 V when going from RUB (+0.33 V) via F₁₄-RUB (+0.91 V) to PF-RUB (+1.94 V), because of the electron withdrawing effect of the fluorine atoms that are attached to the RUB core. Simultaneously, the reduction potential increases by about +1.1 V from -2.09 V (RUB) to -0.96 V (PF-RUB) due to the same reason.

Under the assumption that the redox couple Fc/Fc⁺ (redox potential standard [178]) is located at -5.1 eV in the Fermi energy scale [179], the HOMO ($E_{\text{HOMO}}^{\text{exp}}$) and LUMO ($E_{\text{LUMO}}^{\text{exp}}$) energy values of RUB, F₁₄-RUB and PF-RUB can be estimated from the half wave potentials of the oxidation and the first reduction according to

$$\begin{aligned} E_{\text{HOMO}}^{\text{exp}} &= -(E_{1/2}^{\text{ox}} + 5.1)[\text{eV}] \\ E_{\text{LUMO}}^{\text{exp}} &= -(E_{1/2}^{\text{red}} + 5.1)[\text{eV}]. \end{aligned} \tag{4.3}$$

As follows from the redox potentials, PF-RUB reveals the lowest HOMO (-7.0 eV) and lowest LUMO (-4.1 eV) level whereas RUB exhibits the highest HOMO (-5.4 eV) and highest LUMO (-3.0 eV) level. The energy level of the partially fluorinated compound F₁₄-RUB is located between the unsubstituted RUB and the perfluorinated PF-RUB, at

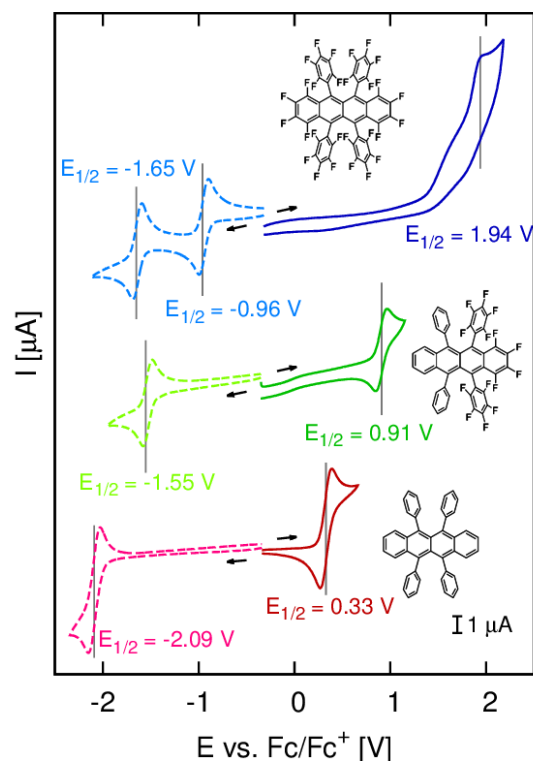


Figure 4.4: Anodic (solid lines) and cathodic (dashed lines) cyclic voltammograms of RUB (a), $c = 2.3$ mM, F₁₄-RUB (b), $c = 1.4$ mM, and PF-RUB (c), $c = 1.4$ mM, in 0.1 M NBu_4PF_6/CH_2Cl_2 at Pt recorded with a scan rate of $v = 100$ mVs^{-1} . Arrows indicate scan direction, anodic and cathodic I - E curves were recorded separately, voltammograms were not background corrected. The shoulder in (c) located at around +1.6 V is attributed to impurities in the electrolyte (revealed by measuring the background current in the absence of substrate)

$E_{HOMO}^{exp} = -6.0$ eV and $E_{LUMO}^{exp} = -3.6$ eV, which is in good agreement with recent observations obtained with photoelectron spectroscopy in the solid state [141]. Indeed, the perfluorinated compound PF-RUB is thermodynamically more stable against oxidation (high *oxidation* potential, low HOMO level) than F₁₄-RUB and much more stable than RUB, but is readily reduced (high *reduction* potential, low LUMO level).

4.2.4 DFT calculations

For a more quantitative analysis of the ionization energies of the three compounds, we performed density functional theory (DFT) computations (TZVP/B3LYP) with the quantum chemistry program package TURBOMOLE 6.4 [166]. Relying on the ionization potential and electron affinity of the three free (gas phase) molecules with twisted backbone [141], the ionization potential (IP_+^{sol}) and electron affinity (EA_-^{sol}) of the ion-

ELECTRONIC EXCITATION OF RUB, F₁₄-RUB, AND PF-RUB

	RUB	F ₁₄ -RUB	PF-RUB
Cyclic voltammetry			
$E_{1/2}^{2\text{nd red}}$ [V]		$-2.14 \pm 0.01^{\text{a}}$	-1.65 ± 0.01
$E_{1/2}^{\text{red}}$ [V]	-2.09 ± 0.01	-1.55 ± 0.01	-0.96 ± 0.03
$E_{1/2}^{\text{ox}}$ [V]	$+0.33 \pm 0.01$	$+0.91 \pm 0.01$	$+1.94^{\text{b}}$
$E_{1/2}^{2\text{nd ox}}$ [V]	$+1.00 \pm 0.01$	$+1.43 \pm 0.01$	
HOMO and LUMO energies (exp.)			
$E_{\text{LUMO}}^{\text{exp}}$ [eV]	-3.0	-3.6	-4.1
$E_{\text{HOMO}}^{\text{exp}}$ [eV]	-5.4	-6.0	-7.0
$E_{\text{gap,ec}}^{\text{exp}}$ [eV]	2.4	2.4	2.9
Electron affinities and ionization potential (DFT)			
EA_{2-}^{sol} [eV]		-2.6	-3.5
EA_{-}^{sol} [eV]	-2.1	-3.1	-3.9
IP_{+}^{sol} [eV]	-5.1	-6.0	-6.9
IP_{2+}^{sol} [eV]	-5.7	-6.5	
$E_{\text{gap,ec}}^{\text{DFT}}$ [eV]	3.0	2.9	3.0
$E_{\text{gap,opt}}^{\text{exp}}$ [eV]	2.3	2.2	2.3

^a Estimated from voltammograms recorded with $v \geq 500 \text{ mV s}^{-1}$.

^b Value of E_{p}^{ox} is used, since the oxidation becomes chemically irreversible due to the instability of the solvent.

Table 4.2: Half wave potential values $E_{1/2}^{\text{ox}}$ and $E_{1/2}^{\text{red}}$ derived from cyclic voltammetric experiments in 0.1 M $\text{NBu}_4\text{PF}_6/\text{CH}_2\text{Cl}_2$ at a Pt electrode ($v = 100 \text{ mV s}^{-1}$). All $E_{1/2}$ are vs. Fc/Fc^+ and are mean values over several cycles. The resulting $E_{\text{HOMO}}^{\text{exp}}$, $E_{\text{LUMO}}^{\text{exp}}$, and the electrochemical HOMO-LUMO gap $E_{\text{gap,ec}}^{\text{exp}}$ ($= E_{\text{LUMO}}^{\text{exp}} - E_{\text{HOMO}}^{\text{exp}}$) for the three compounds are compared with computed DFT (TZVP/B3LYP) values (see text). For the estimation of the computed LUMO-1 level, a polarization energy $P_{2-} = P_{2+} = 4P_{-} = 4P_{+}$ was used. Values for the optical gap ($E_{\text{gap,opt}}^{\text{opt}}$) obtained from molecules diluted in CH_2Cl_2 are taken from Ref. [87].

ized species in solution were estimated via [161]

$$IP_{+}^{\text{sol}} = IP_{+}^{\text{gas}} - P_{+} \quad \text{and} \quad EA_{-}^{\text{sol}} = EA_{-}^{\text{gas}} + P_{-} \quad (4.4)$$

Thereby, P_{+} and P_{-} designate the polarization energies arising from the embedding into a medium with dielectric constant differing from one. The polarization energies in dichloromethane with refraction index $\epsilon_{\text{Solvent}} = 9.08$ is calculated by [208]

$$P_{+} = \frac{e^2}{4\pi\epsilon_0} \frac{1}{2r_{\text{Ion}}} \left(1 - \frac{1}{\epsilon_{\text{Solvent}}} \right), \quad (4.5)$$

where r_{Ion} is the radius of the ionized molecules. For an effective ion radius $r_{\text{Ion}} = r_{+} = r_{-} = 7.0 \text{ \AA}$ [207] for both cation and anion of all three compounds, Eq. 4.5 yields a polarization energy of $P_{+} = P_{-} = 0.92 \text{ eV}$ for the simply ionized molecules, which is in good agreement between theory and experiment. Tab. 4.2 summarizes the characteristic potential values and orbital energies of RUB, F₁₄-RUB and PF-RUB derived

from cyclic voltammetric experiments and DFT computations. From the experimental $E_{\text{HOMO}}^{\text{exp}}$ and $E_{\text{LUMO}}^{\text{exp}}$ values the electrochemical HOMO-LUMO gap was obtained from $E_{\text{gap,ec}}^{\text{exp}} = E_{\text{LUMO}}^{\text{exp}} - E_{\text{HOMO}}^{\text{exp}}$. The electrochemical gap $E_{\text{gap,ec}}^{\text{exp}}$ increases when going from RUB (2.4 eV) to F₁₄-RUB (2.6 eV) to PF-RUB (3.1 eV), which lies slightly above the optical gap $E_{\text{gap,opt}}^{\text{exp}}$ [87]. The high value of PF-RUB is a result of the non-linear increase of the redox potentials with increasing F-content within the RUB core.

4.2.5 Concluding remarks

In summary, we have investigated partially fluorinated (F₁₄-RUB) and perfluorinated rubrene (PF-RUB) in thin films and solution with respect to their stability against oxygen. As we observe by real time absorption experiments of thin films that were exposed to air for several hours, both the partially fluorinated F₁₄-RUB and the fully fluorinated PF-RUB are much more stable against oxygen than unsubstituted rubrene. While oxidation of the thin films through oxygen has been investigated in the solid state, the electrochemical behavior (oxidation/reduction) in solution has been examined by cyclic voltammetric measurements. In addition, we further investigated the reduction and oxidation potentials of the three compounds in solution by comparison with DFT calculations. Both, experiments in the solid state and in solution show that the fully fluorinated PF-RUB is much more and the partially fluorinated F₁₄-RUB is considerably more stable than RUB, due to an increased oxidation potential. As a consequence, we believe that both fluorinated rubrene derivatives form promising candidates as an alternative to unsubstituted rubrene (RUB) in terms of stability against photooxidation processes in organic electronics. A systematic decrease in oxidizability depending on the degree of fluorination is in good agreement with observations from other rubrene derivatives with less fluorine substitutions [47, 120].

4.3 Ultraviolet and X-ray photoelectron spectroscopy of PF-RUB and F₁₄-RUB on Au(111) and Ag(111)

In this section the ultraviolet (UPS) and X-ray photoelectron spectra (XPS) of the fully and partially fluorinated compound are presented [141]. UPS reveals information about the absolute energy level alignment of the materials near below the Fermi-edge. This yields in particular the absolute position of the HOMO level, which thus forms a complementary information to the optical properties of the materials (Sec. 4.1). For the

three different molecules we find a gradual increase of the ionization potential with the degree of fluorination. Moreover, the results indicate that the pronounced electrostatic dipole moment of F₁₄-RUB has a strong impact on the growth mode of these molecules. Most notably, it is inferred that the first layer of F₁₄-RUB on Au(111) and Ag(111) is formed by molecules with alternating orientation of their dipole moments whereas the second layer shows a nearly uniform orientation.

4.3.1 Experimental conditions

The measurements were performed at the synchrotron (BESSY II, SURICAT beamline). The samples are thin films of PF-RUB and F₁₄-RUB that were deposited on Au(111) and Ag(111). The samples were grown as a thickness series ranging from 0 Å - 120 Å. A detailed description of the instrumentation and sample preparation process can be found in Sec. 3.2.6.

4.3.2 Valence spectra

Fig. 4.5 shows the valence spectra of PF-RUB and F₁₄-RUB on Au(111) and Ag(111). Generally, upon deposition of PF-RUB and F₁₄-RUB, we observe a decrease of the prominent metal valence states at binding energies $E_B > 2$ eV for Au(111) and $E_B > 4$ eV for Ag(111), respectively, while at the same time new peaks related to the molecular electronic states appear.

Photoemission peaks were fitted with a vibronic progression with its center of mass at E_0 ,

$$I(E) = A \sum_n \frac{S^n}{n!} \frac{1}{\sigma_n \sqrt{2\pi}} \exp \left[-\frac{(E_0 + \Delta E - E)^2}{2\sigma_n^2} \right], \quad (4.6)$$

as it has been suggested for HOMO-LUMO transitions of the same materials [87], using the Gaussian width σ_i and spacing of the vibronic progression ΔE as fit parameters. Particularly for the Huang-Rhys parameter $S = 0.6$ we used the value obtained from angle resolved UPS measurements on RUB [157].

For the spectra of PF-RUB on Au(111), we carefully subtract the clean metal spectrum from each recorded spectrum, since many of the interesting features are superimposed by peaks of the underlying metal. The background-subtracted spectra of PF-RUB on Au(111) are depicted in the inset of Fig. 4.5(a). Despite the remaining substrate derived

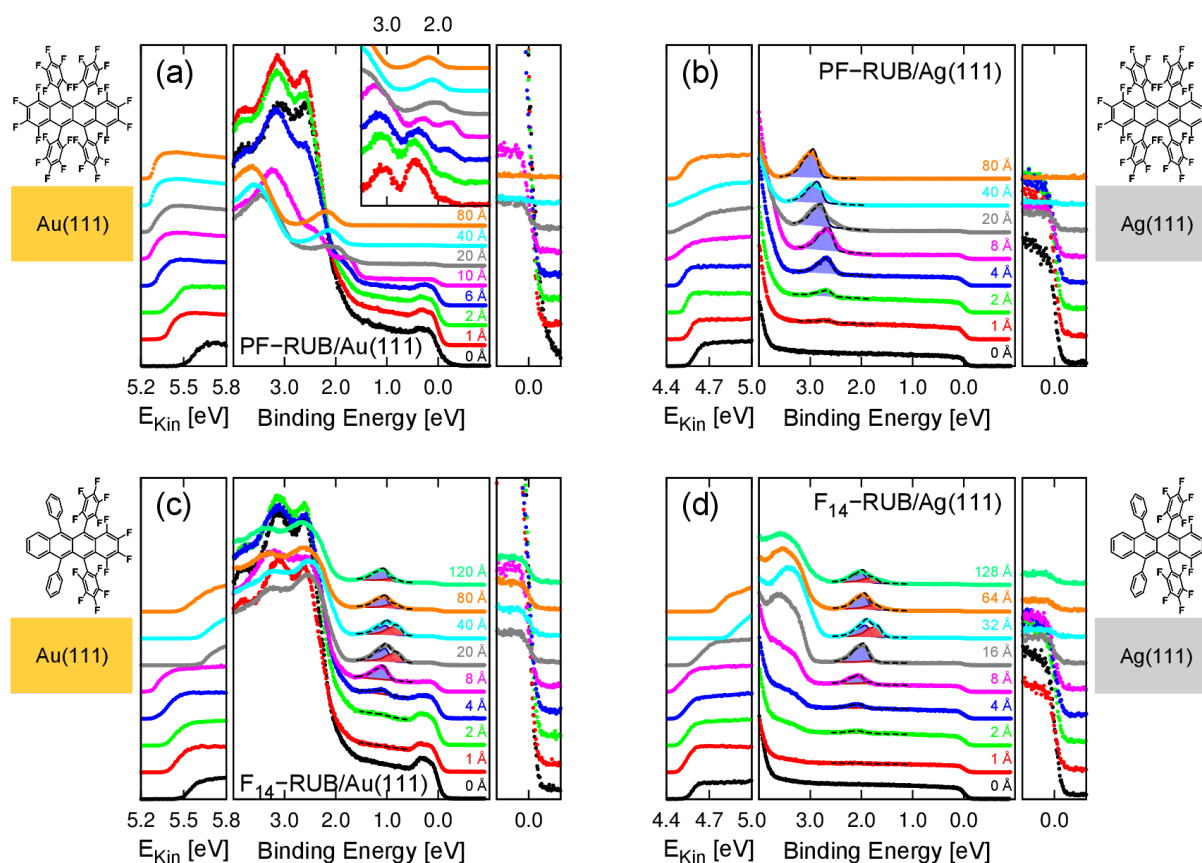


Figure 4.5: Valence spectra of PF-RUB on (a) Au(111) and (b) Ag(111) and of F₁₄-RUB on (c) Au(111) and (d) Ag(111). The HOMO peak of PF-RUB on Ag(111) is fitted with one (blue), the HOMO peak of F₁₄-RUB with two (blue and red) vibronic progressions, according to Eq. 4.6. The subfigures on the left of each spectrum show the secondary electron cutoff. On the right of the spectra a zoom into the region of the Fermi-edge is provided. In order to detect the HOMO peak of PF-RUB on Au(111) the spectrum of the pristine substrate was subtracted (inset of (a)).

artifact at $E_B \sim 2.40$ eV, this enables us to determine the HOMO onset at approximately 1.60 eV for lower film thicknesses. The onset moves with increasing film thickness to $E_B \sim 1.80$ eV binding energy up to the maximum film thickness of 80 Å (Fig. 4.9(a) and (b)). For PF-RUB on Ag(111) (Fig. 4.5b), the HOMO onset is found at $E_B \sim 2.40$ eV for nominal coverages below 5 Å and shifts to 2.60 eV for a thickness of 80 Å. The position of the HOMO onset of PF-RUB on both metals is found to be at a substantially

lower binding energy than it has been observed for the hydrogenated RUB [209–211]. In the case of F₁₄-RUB, we find the HOMO onset at $E_B = 0.85$ eV on Au(111) and 1.75 eV on Ag(111) at a nominal thickness of 4 Å, as can be seen in Fig. 4.5(c) and (d). Thus, the HOMO of F₁₄-RUB on Au(111) and Ag(111) lies between the corresponding values for PF-RUB and RUB [209, 210]. This is qualitatively in good agreement with the behavior predicted by DFT calculations [87] and shows the tunability of the absolute energy levels of the RUB molecule by partial and complete substitution with fluorine. Note, however, that F₁₄-RUB essentially differs from RUB and PF-RUB due to a strong dipole moment along its backbone, generated by its geometry. On both substrates at a thickness of approximately 20 Å a new HOMO peak appears as a shoulder of the previously observed HOMO [212, 213]. The new HOMO becomes dominant over the former HOMO at roughly 24 Å and vanishes again for thicker films. In order to quantify this observation, we fitted the resulting broad HOMO with two peaks according to Eq. (4.6) with an offset of 0.2 eV from each other. The resulting position of the HOMO onset shifts towards the Fermi-edge with increasing molecular thickness, reaching $E_B = 0.60$ eV on Au(111) and 1.45 eV on Ag(111) at about 20 Å and moves slightly towards again higher binding energy for thicker films. At 120 Å we determine the HOMO onset at 0.80 eV (1.60 eV) for F₁₄-RUB on Au(111) (Ag(111)).

In order to study the coverage behavior of the molecules on the substrate, we also take a closer look at the Fermi-edge. At the right hand side of Fig. 4.5 (a - d), the intensity at the Fermi-edge of the respective measurements is shown in more detail. While the Fermi-edge vanishes for PF-RUB deposited on Au(111) and Ag(111) at higher nominal coverages, we still observe a pronounced Fermi-edge for F₁₄-RUB even at the highest investigated film thicknesses.

Figs. 4.5 (a - d) show the secondary electron cutoff of the respective samples, which reflects the change in the work function. Upon completion of the first nominal monolayer (~ 8 Å) of PF-RUB the work function decreases by about 0.25 eV on Au(111) and 0.10 eV on Ag(111). It remains constant for all thicknesses above the first monolayer. During the formation of the first nominal layer of F₁₄-RUB, we observe a similar decrease of the work function, with about 0.20 eV on Au(111) and 0.10 eV on Ag(111). Upon the formation of the nominal second layer of F₁₄-RUB we observe – in strong contrast to PF-RUB – a linear increase of the work function on both metals. At about 24 Å a maximum work function increase of roughly 0.40 eV compared to the first nominal layer is reached for Au(111) and Ag(111). With further deposition the work function slightly decreases again and is found at 0.05 eV (–0.15 eV) for F₁₄-RUB on Au(111) (Ag(111)) for 120 Å. A schematic of the energy level alignment of PF-RUB and F₁₄-RUB on both Au(111) and Ag(111) relative to the vacuum energy E_{Vac} is given in Fig. 4.6.

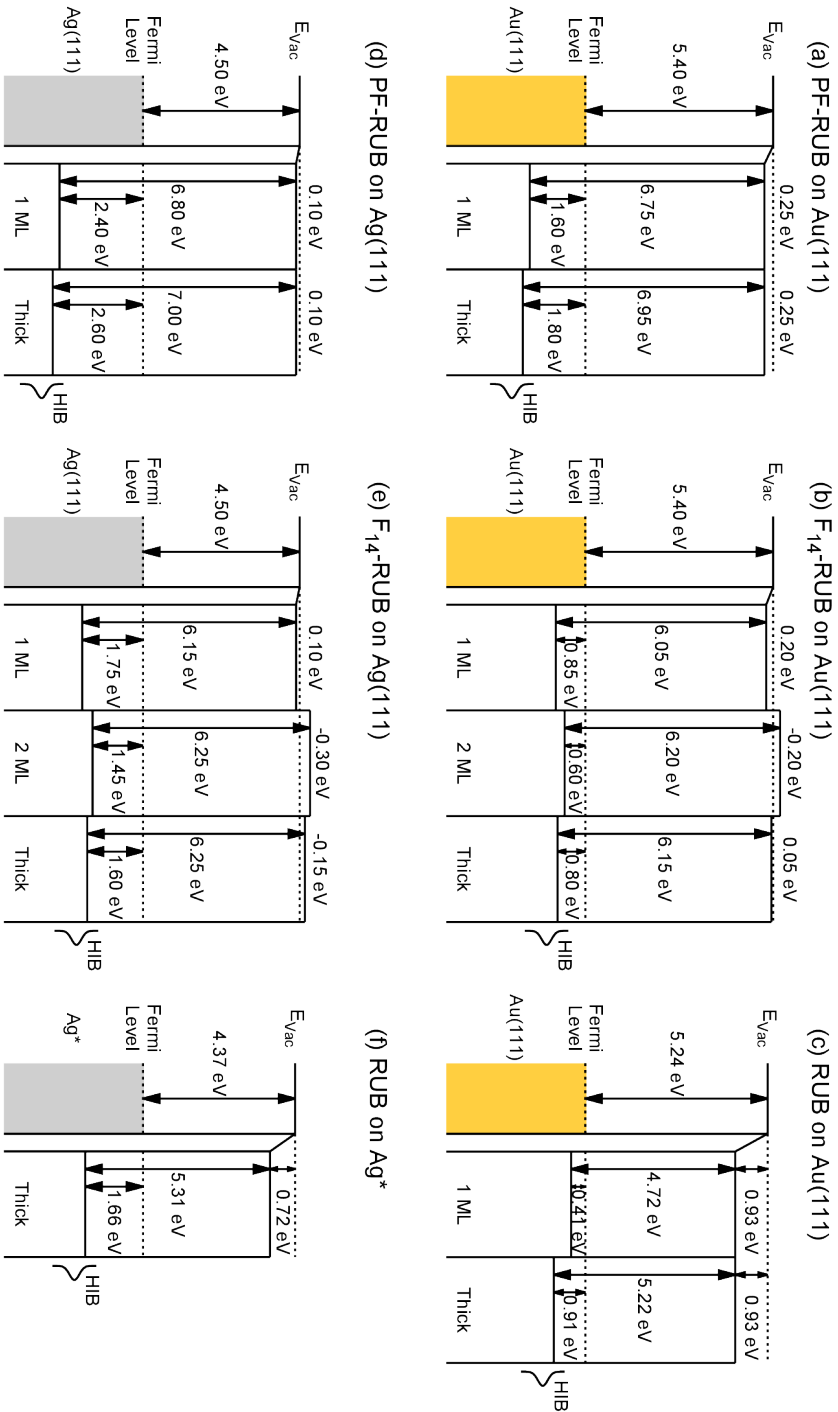


Figure 4.6: Energy level alignment of PF-RUB, F_{14} -RUB, and RUB on Au(111), (a), (b), and (c), respectively, and on Ag(111), (d), (e), and (f), respectively. The hole injection barriers (HIBs) of the thin films are shown in relation to the vacuum (E_{vac}) and Fermi level. The energy difference between the HOMO onset and the Fermi level thereby defines the HIB. Values for schematics (c) and (f) are taken from Refs. [209] and [210] (*no UPS data is available for RUB on Ag(111)), respectively. Note that F_{14} -RUB does not show a monotonic shift in the alignment with increasing layers.

4.3.3 Core-level spectra

In order to investigate the chemical composition and electronic states of the molecules, XPS measurements were performed. Spectra were recorded at the energies of the C1s, F1s and respective dominant metal core-levels (Au4f and Ag3d). Fig. 4.7 shows the XPS results of PF-RUB and F₁₄-RUB on Au(111) and Ag(111).

For all samples we observe one peak in the F1s region. In the C1s region two peaks appear for PF-RUB and three peaks for F₁₄-RUB on both metals. These chemically shifted peaks are designated as C1s (i), (ii), and (iii) where the C1s (ii) peak of F₁₄-RUB occurs only as shoulder of the C1s (iii) peak. The different peaks originate from the non-equivalent binding sites within the molecules. For both molecules every carbon atom is bound to three further atoms, of which at least two are carbon atoms. The C1s (i), (ii), and (iii) peaks are assigned to carbon atoms bound to a hydrogen, carbon, and fluorine, respectively, as their third binding partner.

This assignment is corroborated by density functional calculations with the B3LYP hybrid functional performed with TURBOMOLE 6.4 [214]: The sequence of C1s core-levels in PF-RUB and F₁₄-RUB is reproduced, giving a splitting of 1.6 eV in PF-RUB (corresponding to (i)-(ii), observed 2.0 eV). For F₁₄-RUB the splitting between the C atoms bound to either H or F is calculated to 2.8 eV (corresponding to (i)-(iii), observed 3.1 eV), the C atoms surrounded by three carbons occurring in between, as observed (ii). Due to the B3LYP functional and the TZVP basis set used, the binding energies of all core-levels are underestimated by about 7 eV with respect to the experimental findings, in the same range as in previous B3LYP/SV(P) calculations for PTCDA [215]. Despite this systematic offset of the DFT calculations, the relative shifts between C atoms with different bond configurations in PF-RUB and F₁₄-RUB remain quite reliable. Note that the calculated core-levels of the two possible isomers [87] of either F₁₄-RUB (*C*₂, *C*_s) or PF-RUB (*D*₂, *C*_{2h}) are so similar that these isomers cannot be distinguished by analyzing the measured XPS spectra with a FWHM of about 0.7 eV.

For a quantitative analysis all amplitudes and binding energies were fitted using a Voigt profile. The widths were fixed for each specific peak (*i. e.* Au4f, Ag3d, C1s, F1s). Weighting the ratio of the integrated C1s and F1s peak intensities with the sensitivity factors and the transmission of the electron analyzer, the ratio of carbon to fluorine atoms can be determined experimentally [216]. We find a ratio of ~ 3 for F₁₄-RUB and ~ 1.5 for PF-RUB, which is in good agreement with the ratio of carbon and fluorine atoms in the respective molecules (Fig. 4.8).

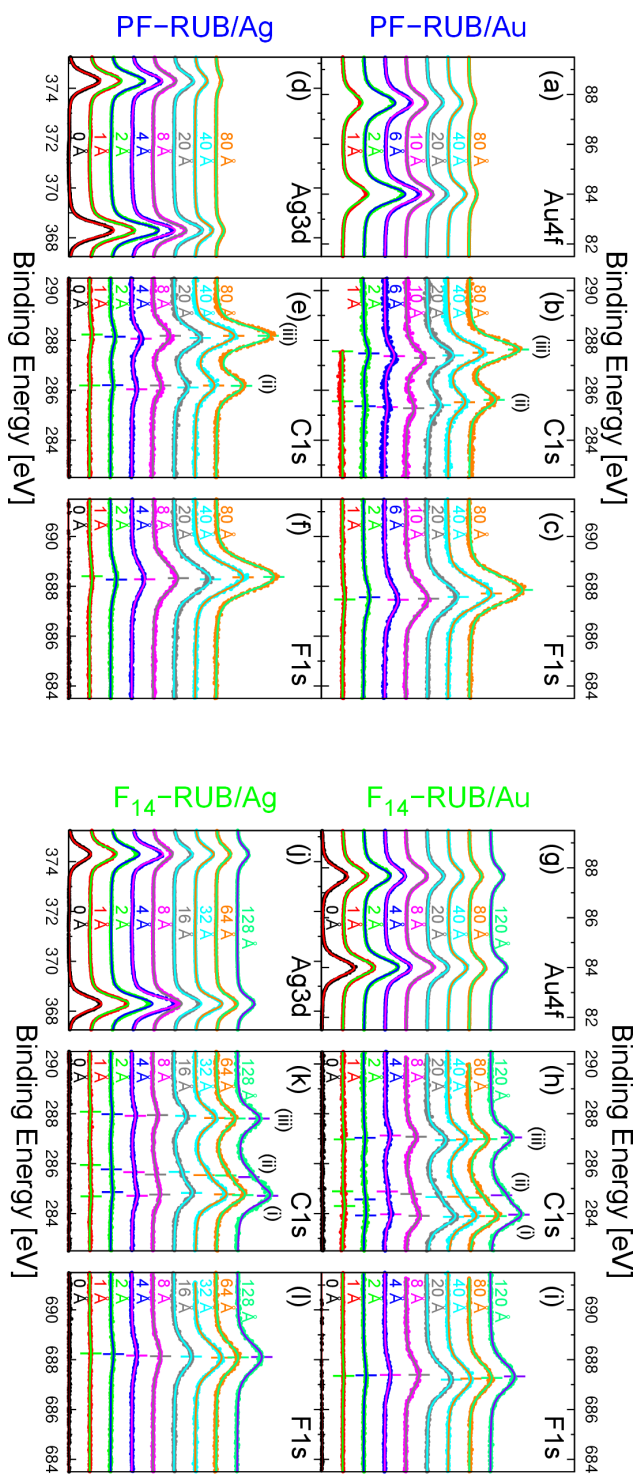


Figure 4.7: Core-level spectra of PF-RUB on Au(111) (a - c) and Ag(111) (d - f) and F₁₄-RUB on Au(111) (g - i) and Ag(111) (j - l). The Shirley-background of the peaks is removed. The spectra are fitted using Voigt profile, with constant width and Gaussian/Lorentzian ratio for each species of peak, *i. e.* metal, C1s, and F1s. Peak positions of the C1s and F1s peaks are marked with a short vertical line. Whereas PF-RUB shows two C1s peaks, (i) and (ii), we observe a third peak (iii) for F₁₄-RUB. For further explanation, see text. Note that the metal peaks decrease less in intensity with increasing film thickness for F₁₄-RUB than for PF-RUB.

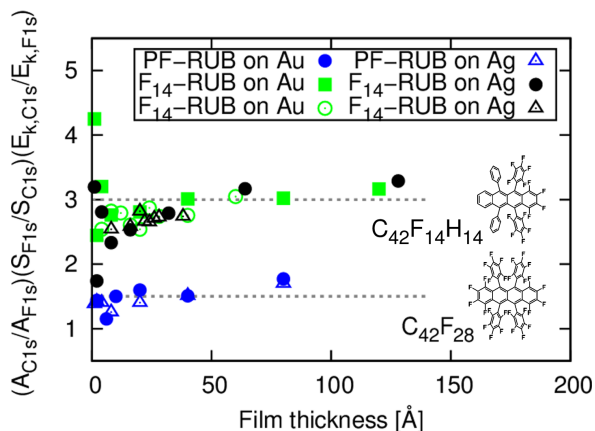


Figure 4.8: Comparing the areas A_C and A_F of the $C1s$ and $F1s$ peaks, we can confirm the ratio of the number of C and F atoms in the molecules from the XPS measurements. Using $(A_{C1s}/A_{F1s})(S_{F1s}/S_{C1s})(E_{k,C1s}/E_{k,F1s})$ we insert $(S_{F1s}/S_{C1s}) = 2.87$ for the ratio of the sensitivity factors and the ratio of the kinetic energies $(E_{k,C1s}/E_{k,F1s}) = 1.78$ in order to account for the transmission function of the electron analyzer. We obtain a ratio of ~ 3 for F_{14} -RUB and ~ 1.5 for PF -RUB, which corresponds nicely to the ratio of C to F atoms in the respective molecules. The gray dotted lines are a guide for the eye.

For both materials we observe a rigid shift of all energy levels with increasing film thickness. This indicates that the molecules do not interact strongly with the substrate and are only weakly bound [217,218]. The resulting curves for PF -RUB are found in Fig. 4.9(a) and (b) and for F_{14} -RUB in Fig. 4.9(c) and (d). The plot for F_{14} -RUB comprises green open and black closed circles denoting two sets of data of two respective samples. The second (black) curve was taken to measure the interesting region of 20-40 Å in more detail (corresponding raw spectra are not shown here).

4.3.4 Discussion

In the case of PF -RUB on both metals we observe a complete disappearance of the Fermi-edge (cf. Fig. 4.5(a) and (b)) as well as rapidly decreasing intensities of the metal core-levels (Fig. 4.7(a) and (d)) with increasing film thickness. This indicates that the metal surface is completely covered by a closed layer of molecules, analogously to RUB grown on the same substrates [209,210]. Thus, the molecules grow either layer-by-layer (Frank-van der Merve) or, as observed for RUB, layer-plus-island (Stranski-Krastanov) [211,219]. In contrast, for F_{14} -RUB the Fermi-edge remains clearly visible even at the highest coverage (cf. Fig. 4.5(c) and (d)) and also the intensities of the metal core-levels show a less distinct dependence on the film thickness (Fig. 4.7(g) and (j)) compared to PF -RUB. This indicates strong island growth (Vollmer-Weber) which is often found for organic molecules on metals [220–222]. It plays a crucial role for the evaluation of the data of F_{14} -RUB, since the spectral features of possibly lower lying layers have to be considered for each measurement.

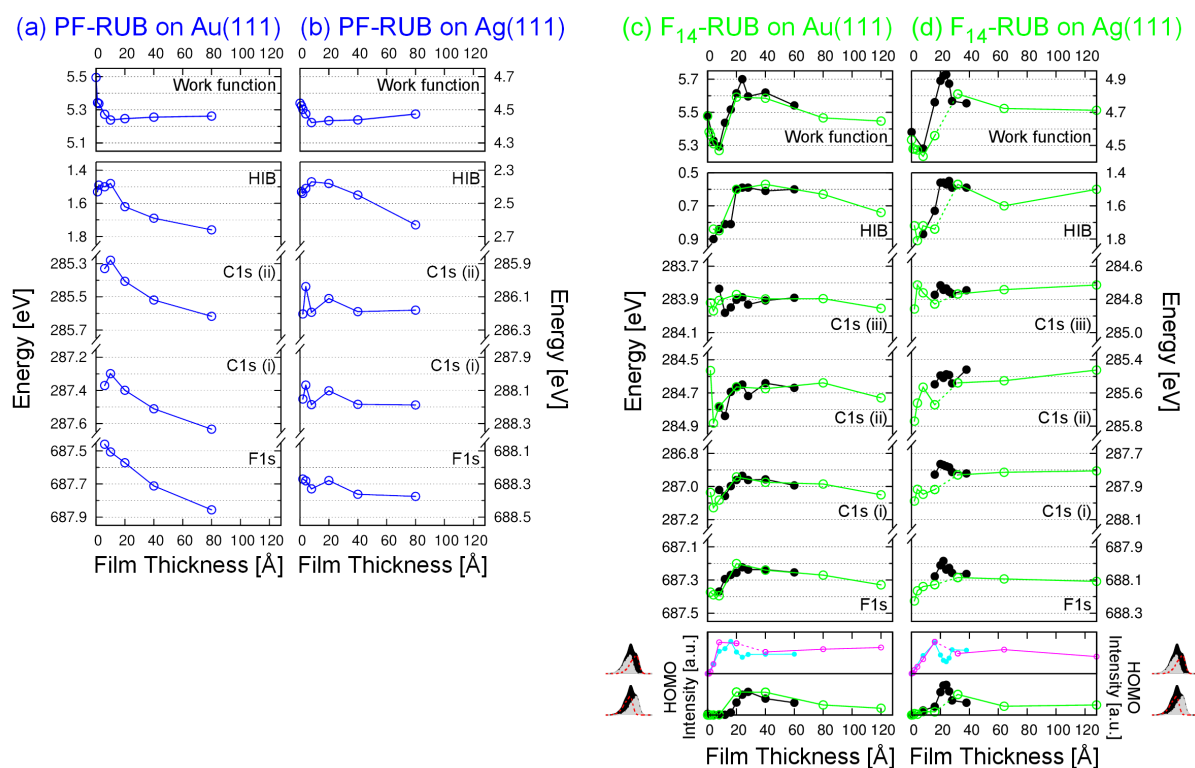


Figure 4.9: Left: Energy level alignment of work function, HIB and core-levels (C1s and F1s) depending on the film thickness, for PF-RUB. Panel (a) shows the results on Au(111) and (b) on Ag(111). For both metal substrates, the respective energy levels show the same trends with thickness. The values are obtained from the fit results of Figs. 4.5 and 4.7.

Right: Energy level alignment of work function, HIB and core-levels (C1s and F1s) depending on the film thickness, for F₁₄-RUB. Panel (c) shows the results on Au(111) and (d) on Ag(111). Green and black (together with pink and cyan) stand for two different samples. Whereas the values for the green (and pink) sample give an overview over general trends, black (and cyan) datapoints focus particularly on the nominal thickness below 40 Å. For both metal substrates, the respective energy levels show the same trends with thickness. The values are obtained from the fit results of Figs. 4.5 and 4.7. The graphs at the very bottom show the intensity of the two vibronic progressions used for fitting the HOMO peak in the UPS. The new HOMO (green/black curves in lowest graph) rises particularly above ~ 20 Å and the former HOMO (pink/cyan curves) loses intensity. At roughly 40 Å the new HOMO vanishes. The new HOMO is shifted by 0.2 eV towards the Fermi-edge, the green curve corresponds to the pink curve, whereas black corresponds to cyan.

PF-RUB on Au(111) and Ag(111)

For PF-RUB on Au(111) (Fig. 4.9(a)) we observe an almost linear decrease $\Delta\phi$ in the work function up to a nominal thickness of 8 Å, which we assign to the formation of the first monolayer. This decrease can be explained by the so called push-back effect [54, 223, 224]. For RUB on Au(111) $\Delta\phi = -0.93$ eV [209] and for pentacene on Au(111) $\Delta\phi = -0.95$ eV [225] have been reported. For PF-RUB we measure a decrease of only $\Delta\phi = -0.25$ eV which is significantly smaller. This difference could be explained by a larger bonding distance caused by the perfluorination of the molecule as it has been explained for perfluoropentacene on Au(111) [225] and on Cu(111) [226]. With further increase of the film thickness the work function remains constant. This means that after completion of the first layer the surface dipole is not modified by additional molecules and hence no change in the work function occurs. For the hole injection barrier (HIB) a linear trend up to 8 Å can be observed. Upon completion of the first layer the HIB decreases by roughly 0.20 eV. This shift can be fully explained by the screening of the photohole [227]. Further increase of the film thickness leads to an apparent increase of the HIB by up to 0.35 eV at 80 Å which seemingly saturates for higher molecular depositions. This can again be explained by photohole screening. In this case, the vanishing contribution of the metal to the screening is the driving factor. With increasing film thickness the photohole is less screened and in turn the HIB seemingly increases.

For PF-RUB on Ag(111) (Fig. 4.9(b)) we find qualitatively the same behavior and the same arguments hold. Up to nominal 8 Å film thickness the work function decreases by $\Delta\phi = -0.10$ eV, which again is much lower than $\Delta\phi = -0.72$ eV reported for RUB on Ag(111) [210]. In contrast to Au(111), the core-levels do not follow exactly the same trends of the HIB for the film on Ag(111). A possible explanation could be a slightly rougher growth mode on Ag(111), thus allowing to observe more contribution of lower layers to the XPS core-levels even at higher nominal film thickness.

F₁₄-RUB on Au(111) and Ag(111)

For F₁₄-RUB the interpretation of its growth is more complex than for PF-RUB or RUB due to its strong intrinsic dipole moment along the long molecular axis [87]. In Fig. 4.9(c) and (d) the results for F₁₄-RUB on Au(111) and Ag(111) are shown, respectively. Since the phenomena observed for both metals are qualitatively identical, the following discussion exemplarily refers to only F₁₄-RUB on Au(111). Similarly to PF-RUB, we observe a linear decrease of the work function up to a nominal thickness of

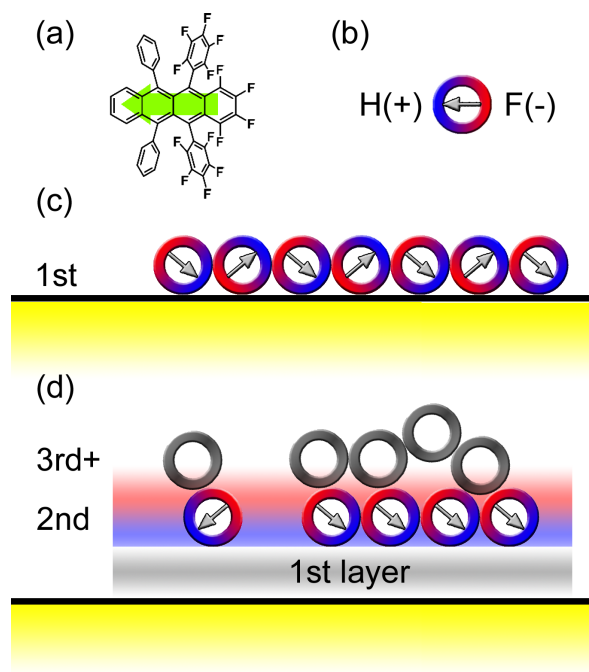


Figure 4.10: (a) Chemical structure of F₁₄-RUB with a green arrow indicating the direction of the electrostatic dipole moment. (b) Schematic of the polar F₁₄-RUB molecule, the arrow indicates the direction of its static dipole moment, pointing from the fluorinated ('-', red) part towards the hydrogenated ('+', blue) side. (c) Proposed growth model for F₁₄-RUB on Au(111) and Ag(111). The first layer consists of alternating dipoles, which leads to a canceling out of an overall effective dipole moment perpendicular to the substrate. This is different for the second layer: A majority of the molecular dipole moments is oriented and pointing with the fluorinated part of the molecules away from the substrate. In the third and further layers there is no preferential orientation of the molecules and the dipole moment from the second layer becomes shielded.

8 Å which refers to the formation of the first layer. The absolute value of $\Delta\phi = -0.20$ eV is virtually identical to that of PF-RUB on the same substrate. Obviously, very similar to PF-RUB, a push-back effect occurs that can be explained by a larger distance of F₁₄-RUB to the substrate compared to RUB. Surprisingly, in the first layer the large static dipole moment of the molecule, which we expect to result in a drastically changed workfunction compared to PF-RUB, does not come into effect.

For RUB, the complex three-dimensional structure of the molecule leads to intricate structures and superstructures as reported for RUB on Au(111) and Ag(111) [218,228–231]. Deposited on Au(111), it was found that the molecules orient themselves with a tilt angle of their twisted backbone of roughly 40° relative to the surface [196,232]. Due to the similar geometry of the molecules, it appears reasonable that also PF-RUB and F₁₄-RUB molecules align themselves in a similar twisted and inclined conformation for their first layers on the metal. If the F₁₄-RUB molecules, however, do not lie flatly on the surface there is a component of their static dipole moment perpendicular to the substrate surface. Showing a very similar behavior as PF-RUB monolayers (without static dipole moment), F₁₄-RUB molecules seem to adsorb in an arrangement which neutralizes the overall dipole within the first layer. This suggests an alternating arrangement [212,233] as shown in Fig. 4.10, where the molecules are inclined with re-

spect to the surface. Adjacent molecules have inverted orientation in this configuration that results in an overall zero dipole moment perpendicular to the substrate surface.

Between 8 Å and 24 Å nominal thickness we observe a distinct increase of the work function. This can be related to the growth beyond the first monolayer. The work function change compared to the first layer reaches a maximum of $\Delta\phi = +0.40$ eV. This points to the formation of a dipole moment within the second molecular layer. Hence, we propose that the molecules within the second layer are inclined with their fluorinated end ('-' partial charges) pointing away from the surface. This leads to a dipole moment perpendicular to the surface plane which becomes gradually stronger with the increasing number of molecules within the second layer.

In order to estimate this increase of the work function, we consider a simple model using the intrinsic dipole moment $d = 4.2$ D along the backbone of the molecule, as obtained from DFT calculations for the twisted conformation of F₁₄-RUB [87]. If we furthermore describe the molecule with a sphere of 10 Å diameter being densely packed (surface density $N_{\text{dip}} = 1.155 \cdot 10^{18} \text{ m}^{-2}$) and tilted with its backbone by 40°, we can find an upper limit for the effective intrinsic dipole moment of the molecules in the second layer using the Helmholtz equation [226],

$$\Delta\phi = \frac{ed \cdot \sin(40^\circ) N_{\text{dip}}}{\varepsilon_r \varepsilon_0} = 1.17/\varepsilon_r \text{ eV}, \quad (4.7)$$

where ε_r is the dielectric constant, which has been estimated to 1.22 for phtalocyanines [234]. The estimated $\Delta\phi$ is significantly larger than the experimental value of 0.4 eV, which indicates that the molecules might either be not densely packed and/or few molecules in the second layer might adapt opposite orientation. Nevertheless, we may relate the increase of the work function between 8 Å and 24 Å to aligned dipole moments pointing towards the surface that originate from molecules of the second layer.

Increasing the film thickness above 24 Å leads to a slight decrease of the work function, which will reach saturation for thick films. This indicates an arrangement of the molecules without preferential orientation, which on one hand does not provide a resulting dipole moment and at the same time slightly screens the dipole moment of the molecules in the second layer.

Our model is corroborated by the progression of the HIB, which is defined by the relative position of the HOMO onset closest to the Fermi level. Below 8 Å only one HOMO peak can be observed for which no clear trend can be identified (cf. Fig. 4.5(c) and Fig. 4.9(c)). This corresponds to disordered molecules in the first molecular layer. Between 16 Å and 20 Å the formerly mentioned second peak appears. This new peak can

be assigned to the HOMO of uniformly oriented molecules [213,218,220]. In our interpretation, the reason why we observe this peak only halfway through the formation of the second layer is that the intensity of this peak is too low to be observed below 16 Å. With increasing film thickness the position of the new peak is nearly constant but changes its intensity. Consistent with our model the new HOMO completely disappears for thicker films because the second layer gets more and more covered by higher layers without preferred molecular orientation that attenuate the signal from the new HOMO.

4.3.5 Concluding remarks

Concluding, we determined the electronic properties of PF-RUB and F₁₄-RUB thin films deposited on Au(111) and Ag(111). We determined the HIB of PF-RUB and F₁₄-RUB showing the tunability of the HIB of RUB by means of fluorination. The growth mode of the partially fluorinated F₁₄-RUB, which has a large dipole moment along its backbone, turns out to be more complex than for RUB or PF-RUB. We find stronger island growth and, importantly, evidence for a uniform molecular orientation in the second deposited layer for F₁₄-RUB. This leads to an essential modification of the work function and the HOMO level, depending on the film thickness. As a consequence, particularly the partially fluorinated F₁₄-RUB turns out to be a promising candidate for effective tuning of organic interfaces, which is of very high interest for organic optoelectronic devices.

CHAPTER 5

VIBRONIC EXCITATION OF RUB, F₁₄-RUB, AND PF-RUB

This chapter presents the vibrational properties of RUB, F₁₄-RUB, and PF-RUB, essentially following Ref. [142]. In particular, it compares and discusses experimental infrared (IR) and Raman spectra of the fluorinated compounds (F₁₄-RUB and PF-RUB) in thin films on native silicon and on SAM, and diluted in CH₂Cl₂ [235] with computed models. The vibrational modes are fundamental properties of a molecule that play an important role for the understanding of molecular charge carrier transport properties [62,92,110,236,237].

The findings are presented in different subsections. First, the computed and experimental IR and Raman spectra are shown and discussed (Secs. 5.1 and 5.2). Particularly for PF-RUB, spectra corresponding to molecules with a purely planar and a purely twisted tetracene backbone are extracted from the experimental data. Thereafter, we shortly focus on the correlation of morphology and conformation of the molecules [88,194,238]. Interestingly, we find a connection between dewetting and a change in the molecular conformation for the thin film on bare silicon. The results of this chapter are then briefly discussed and summarized.

The samples investigated in this chapter are moreover examined using grazing incidence X-ray diffraction (GIXD) techniques in Sec. 6.3.2. A connection between vibronic and structural properties can be established.

5.1 Computed vibrational modes

IR and Raman active vibrational modes of two conformations of the isolated PF-RUB (F₁₄-RUB) molecule that also occur for hydrogenated RUB [88, 146, 159, 239] (D_2 (C_2) and C_{2h} (C_s) symmetry with twisted and planar backbone, respectively) were computed with the B3LYP functional and TZVP basis set using TURBOMOLE 6.4 [166]. We find that the twisted D_2 (C_2) isomer of PF-RUB (F₁₄-RUB) is energetically favored by -0.34 eV (-0.24 eV) against the planar C_{2h} (C_s) conformation, which is roughly twice (one and a half) as much as in the case of RUB [87].

The values for the several types of vibration like in-plane bending, out-of-plane bending, and stretching (Tab. 5.1) correspond roughly to the classical harmonic oscillator model [240], $\hbar\omega \propto (k/\mu)^{\frac{1}{2}}$ (Eq. 2.16), with the reduced mass $\mu = (m_1 \cdot m_2)/(m_1 + m_2)$ of the involved atomic species with masses m_1 and m_2 . We find the strongest vibronic activity in the range $\tilde{\nu} \sim 1300 - 1600$ cm⁻¹, which agrees well with the spacing of the effective vibronic progression [92, 182, 240] of ~ 170 meV as observed in absorption and PL spectra of the three materials [87], Sec. 4.1. In order to account for the anharmonicity of the Morse potential (Sec. 2.3.1), the energy axis of the computed modes were scaled by a factor of 0.9915, which we found to yield a very good agreement between the theoretical model and experimental values for most modes [155]. Nevertheless, for particular modes like C-F stretching and few localized C-C stretching modes involving strong fluorine movement, a factor of 0.9860 could be more adequate. The particular type of vibration, which could be identified from the computed modes, is listed in Tab. 5.1. For better comparison of the computed model with the experimental spectra, in the following the intensity of each computed mode is represented by a Lorentzian with FWHM = 4 cm⁻¹.

5.1.1 Infrared (IR) modes

The computed oscillator strengths of all IR active vibrational modes of RUB, F₁₄-RUB, and PF-RUB are shown in Fig. 5.1, both for twisted and planar conformation of the respective molecule. The oscillator strength and thus the intensity of a specific IR active vibrational mode is proportional to its related transition dipole moment (see Sec. 2.3.1). Hence, in particular molecular bonds involving large amounts of mobile charges like they occur in fluorine atoms become relatively easily activated, whereas bonds including less mobile charges like in multiply bounded C or light H atoms with few electrons develop only poor IR activity. Having many C-F bonds, PF-RUB and F₁₄-RUB

Type of bonding	Type of vibrational mode	Abbreviation	Wavenumber $\tilde{\nu}$ [cm ⁻¹]
multiple C-C	skeletal	CCsk	0...250
C-F	out-of-plane bending	CFob	120...260
C-C	out-of-plane bending	CCob	280...810
C-H	out-of-plane bending	CHob	700...1000
C-F	in-plane bending	CFib	280...360
C-C	in-plane bending	CCib	400...1025
C-H	in-plane bending	CHib	1350...1650
C-F	stretching	CFs	900...1200
C-C	stretching	CCs	1040...1700
C-H	stretching	CHs	3150...3250

Table 5.1: Assignment of the vibrational modes of RUB, F₁₄-RUB, and PF-RUB. Due to the similar molecular geometry, the assignment is valid for all of the three derivatives. With H (F) being the lightest (heaviest) element participating in the bonds, the energy of the vibrational modes follows a classical harmonic oscillator model (C-F vibrations are excited at low energies compared to C-H vibrations). Note, that PF-RUB (RUB) contains no H (F) atoms and hence has no C-H (C-F) vibrations.

show strong IR activity in the C-F stretching region (900...1200 cm⁻¹), but also near to particular C-C stretching modes that are localized in the vicinity of fluorine atoms (1300...1700 cm⁻¹). RUB, on the other hand, exhibits much less IR activity, which basically occurs in the region of C-H stretching modes around 3150 cm⁻¹ and C-H/C-C bending modes around 750 cm⁻¹. Since the sensitivity of the IR spectrometer, which was used for the experiments, is most sensitive in the region of ~ 800–2000 cm⁻¹ (see Sec. 3.2.5), experimental IR spectra of RUB were too weak to be detected.

5.1.2 Raman modes

The computed intensities of all Raman active modes of RUB, F₁₄-RUB, and PF-RUB can be found in Fig. 5.2, both for twisted and planar conformation of the respective molecule. Involving a two-photon process the calculation of the Raman active modes is more complex than of IR active modes (see Sec. 3.1.6). As a result, the intensity of Raman modes can often not be predicted with the same precision as the intensity of IR modes.

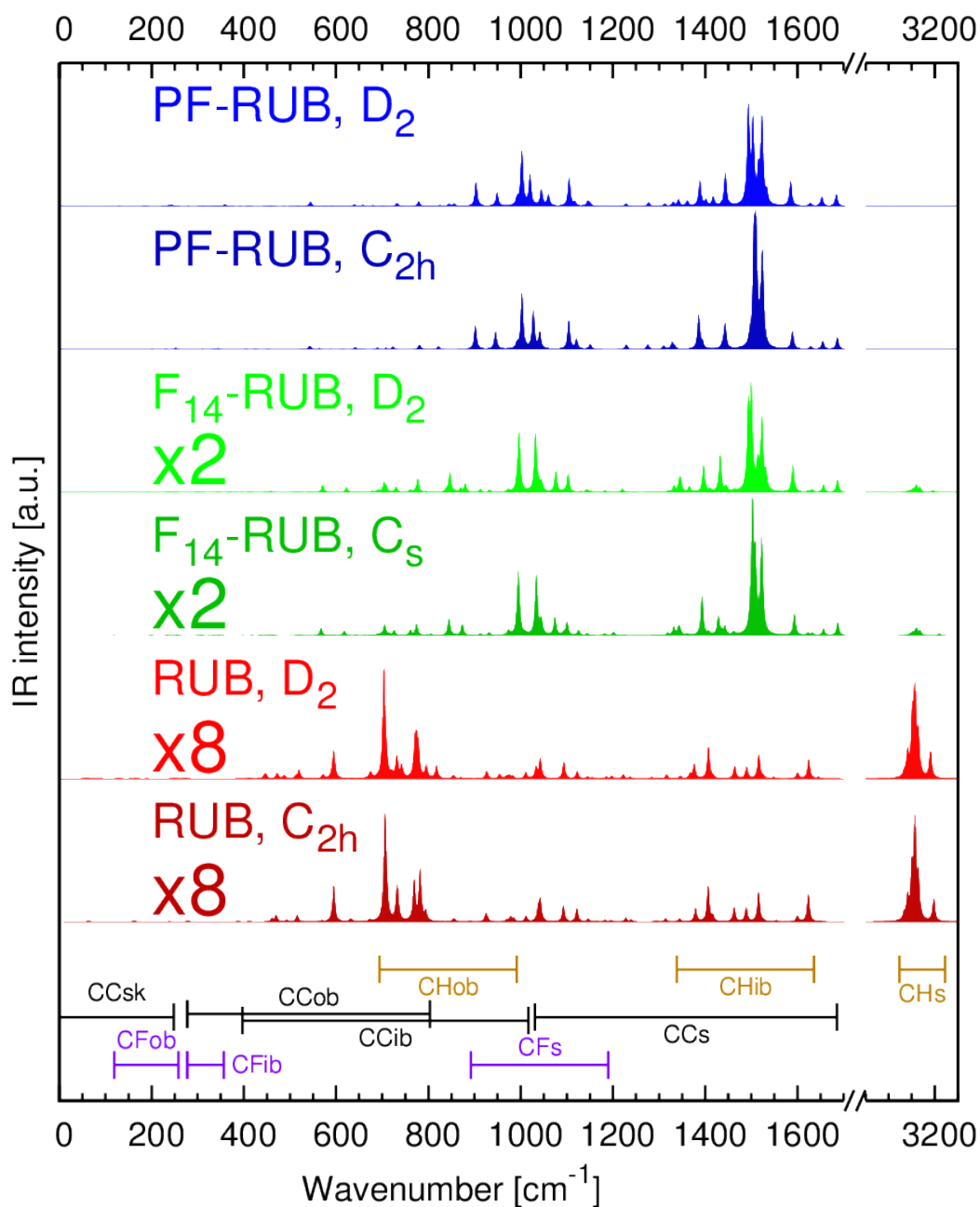


Figure 5.1: Computed IR spectra for PF-RUB, F₁₄-RUB, and RUB (from top to bottom) each for the twisted (D₂, C₂ geometry) and for the planar (C_{2h}, C_s geometry). Bars at the bottom mark the region of the type of vibrational mode (Compare Tab. 5.1). Note that the IR intensities for F₁₄-RUB and RUB are multiplied by ×2 and ×8, respectively. For further information, see text.

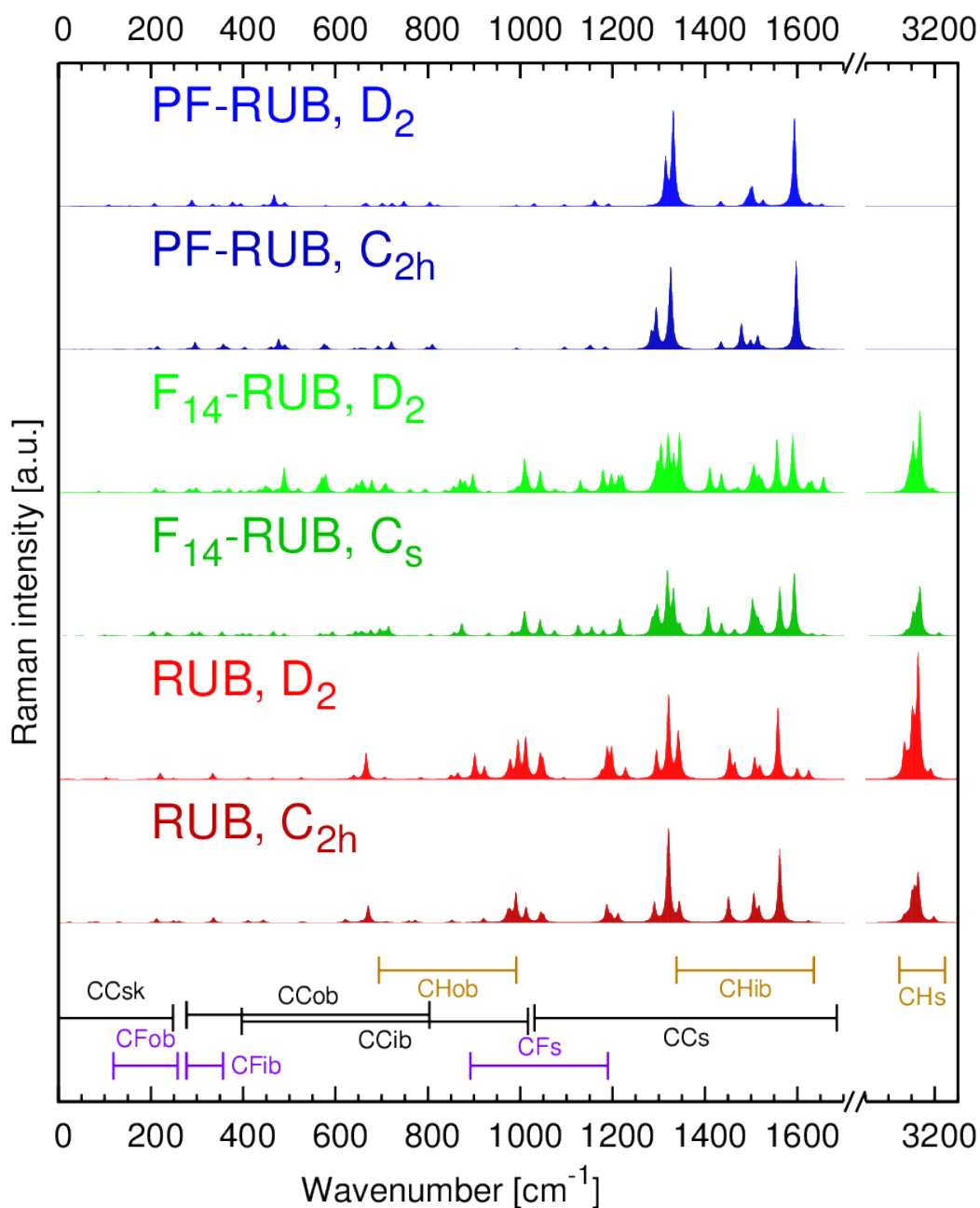


Figure 5.2: Computed Raman spectra for PF-RUB, F₁₄-RUB, and RUB (from top to bottom) each for the twisted (D₂, C₂ geometry) and for the planar (C_{2h}, C_s geometry). Bars at the bottom mark the region of the type of vibrational mode (Compare Tab. 5.1). For further information, see text.

This is in particular the case for the molecules studied in this work with their intricate three-dimensional geometry. Already slight deviations of the molecular geometry can lead to strong differences in the intensity of vibrational modes. As resonant and pre-resonant Raman spectra rely on elongations of internal vibrations in the relaxed excited geometry of the molecule, only modes of the highest symmetry contribute significantly [241]. Hence, particularly for PF-RUB, the number of strongly Raman-active modes remains far below the number of IR-active modes.

5.2 Experimental IR and Raman spectra

In this section, the experimentally obtained vibrational modes are presented. After a short description of the experimental setup, the IR and Raman spectra (acquired at 633 nm) of PF-RUB are shown and compared with the computed spectra. The spectra can be decomposed into peaks resulting from molecules with planar and twisted molecular backbone. Moreover, using Raman imaging techniques the sample morphology is investigated. This is finally followed by a subsection focusing on IR and Raman spectra (acquired at 633 nm) of F₁₄-RUB in comparison with computed spectra.

The experimental Raman spectra were acquired with our in-house spectrometer that is equipped with a He-Ne laser at 1.93 eV (Sec. 3.2.4), which is close to the HOMO-LUMO transition of the compounds. Since RUB, F₁₄-RUB, and PF-RUB show strong PL, it is not easy to separate the much weaker Raman peaks from the background, which is particularly for F₁₄-RUB a challenging task. Spectra of thin films with F₁₄-RUB and PF-RUB obtained at 785 nm can be found in the Appendix, p. 126. The same samples were examined with both Raman and IR spectroscopy. While the IR beam mediates over a spot of 1 mm (0.5 mm for solution), the beam for Raman spectroscopy is focused to a much smaller spot around 1 μ m.

5.2.1 Experimental conditions

Thin films were prepared, respectively, on silicon wafers with a native oxide layer and on silicon wafers covered with a self-assembled monolayer (SAM) [69] consisting of octadecyltrichlorosilane (OTS) [70]. For each material, the films were deposited on both substrates at the same time under ultra-high vacuum conditions [40,41]. During growth, the substrates were kept at room temperature (RT), and the film thickness was grown up to 100 nm at a growth rate of ~ 2 Å/min. Under these conditions fluorinated

rubrene thin films on native silicon substrates are supposed to grow amorphous [87]. Vibrational spectra of PF-RUB and F₁₄-RUB in diluted solution are obtained in Cl₂CH₂ with molar concentration of roughly 2 mol l⁻¹.

Raman spectra were acquired using an HORIBA JOBIN YVON LABRAM HR 800 spectrometer with a CCD-1024×256-OPEN-3S9 as detector (Sec. 3.2.4). Excitation for Raman was performed using a He-Ne laser at 633 nm with a spot size of $\sim 1 \mu\text{m}$. For the reduction of surface inhomogeneity effects of the samples, several spectra were acquired over a representative range and the spectra were integrated. Since the Raman peaks become sharper at low temperatures [184], the thin film samples were cooled down to 77 K during the measurement.

The IR spectra of the thin films and solution were obtained in transmission mode with a VERTEX 70 (BRUKER) Fourier transform infrared spectrometer with a PMA 50 detector unit attached (Sec. 3.2.5). In order to avoid back-reflection at the smooth side of the silicon wafer, p-polarized light was sent onto the substrate with an angle of incidence of 74° which is near to the Brewster angle of silicon. The diameter of the IR beam was $\sim 1 \text{ mm}$. The intensity I of the IR spectra was determined using $I = (I_{\text{Sample}} - I_0)/I_0$, where I_{Sample} describes the intensity of the thin film on the substrate (or the molecules dissolved in solution), and I_0 stands for the measured substrate (or the absorption of the solvent) only. Energy regions with strong IR absorption of the solvent CH₂Cl₂ could not be monitored [187].

5.2.2 IR and Raman spectra of PF-RUB

The samples were measured with IR and Raman spectroscopy within 4 hours after thin film growth. After one day we discovered a change in the IR and Raman spectra of the PF-RUB thin films deposited on the bare silicon wafers compared to the pristine film. Measurements on the following days thereafter did not reveal further changes in the IR and Raman spectra. From this we deduce that the thin films deposited on native silicon reached a stable state, about one day after thin film growth. Spectra of thin films on SAMs did not show changes over time. In the following, we will denote data obtained within 4 hours after film growth as 'pristine', data obtained after one day or later as 'late stage'. Interestingly, we observe a decrease of the PL background by a factor of 2 (not shown) for the sample on silicon from the pristine to its late stage. Such an increase in the PL quenching indicates a change of the exciton diffusion length [48, 83, 242]. For better evaluation of the spectra, the photoluminescence (PL) background of the Raman spectra was subtracted after acquisition.

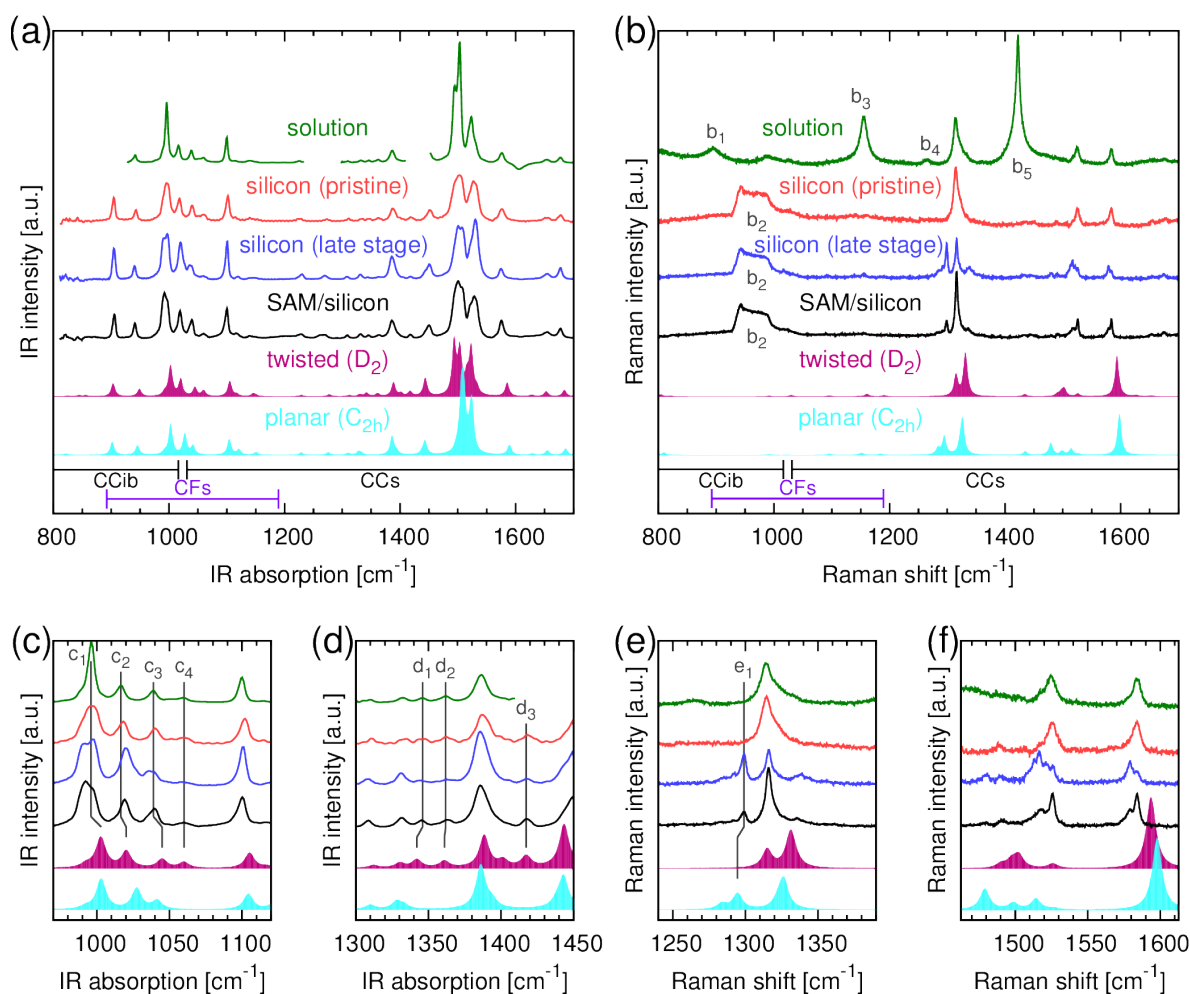


Figure 5.3: Experimental vibrational spectra of PF-RUB (lines) and spectra computed by DFT (filled curves). The experimental spectra are obtained from molecules dissolved in CH_2Cl_2 (green line, top), deposited on native silicon in 'pristine' (red line) and 'late stage' (blue line), as well as on SAM/silicon (black line, bottom). The theoretical spectra show Lorentzian-shaped modeled curves of the twisted (purple filled) and planar (cyan filled) conformation of the molecule. (a) FT-IR spectra in the fingerprint region of the PF-RUB molecule. (b) Raman spectra of the samples excited at 633 nm. (c) and (d) show a zoom into selected regions of the IR spectra, (e) and (f) of the Raman spectra, respectively. The bars at the bottom of (a) and (b) show the regions of the type of the vibrational mode ('CCib' = C-C in-plane bending, 'CCs' = C-C stretching, 'CFs' = C-F stretching). For explanation of the spectra, see text.

Fig. 5.3(a) shows the fingerprint region of the experimental IR spectra of PF-RUB dissolved in CH₂Cl₂, on native silicon (pristine and late), and on a SAM covered silicon in comparison with computed spectra (top to bottom). The peaks of the solution spectra are sharper than the peaks from the thin film spectra. Due to the high polarizability of the molecule caused by the large number of negative fluorine atoms, the spectra show strong IR peaks, particularly in the C-F and C-C stretching region. The computed IR spectra correspond remarkably well to the experimental spectra, and most of the vibrational modes can be identified.

Fig. 5.3(b) shows the fingerprint region of the experimental Raman spectra of PF-RUB in solution, on native silicon (pristine and late), and on SAM covered silicon in comparison with computed spectra (top to bottom). From a comparison of all samples, the Raman fingerprint of PF-RUB consists of prominent modes in the vicinity of 1315 cm⁻¹, 1520 – 1530 cm⁻¹, and 1590 cm⁻¹. Peaks in the spectrum of PF-RUB dissolved in CH₂Cl₂ at $\tilde{\nu} \sim 900$ cm⁻¹, ~ 1000 cm⁻¹, ~ 1160 cm⁻¹, ~ 1270 cm⁻¹, ~ 1425 cm⁻¹ (b₁, b₃-b₅) originate from the solvent [187]. In the thin film spectra a rather broad peak in the region of 900 – 1000 cm⁻¹ (b₂) is related to the silicon substrate [185].

Due to the very good agreement between theory and experiment, it is possible to distinguish small differences in the IR spectra. Figs. 5.3(c) and (d) show a zoom into the IR spectra. Since some of the peaks predicted by the theoretical model occur only either for the twisted or for the planar conformation of PF-RUB, it is possible to make an assignment of the spectra. Particularly, the spectrum of the computed twisted conformation shows peaks at 1060 cm⁻¹ (c₄), 1340 cm⁻¹ (d₁), 1360 cm⁻¹ (d₂), and 1420 cm⁻¹ (d₃) that do not exist in the spectrum for the planar conformation. Moreover, the computed spectrum for the twisted conformation, shows slightly different positions of the peaks c₂ and c₃, involving in particular a wider spacing than for the corresponding peaks in the computed spectrum of the planar conformation in the region of 1020 – 1050 cm⁻¹. Comparing the IR solution spectrum with the computed modes (Figs. 5.3(c) and (d)), we find a very good agreement of the peaks c₁–c₄ and d₁, d₂ with the twisted conformation [243, 244]. Also, the separation of the peaks c₂ and c₃ corresponds well to the respective computed twisted modes. This confirms the assumption that the majority of molecules in solution adopt an energetically favored twisted conformation [87].

A zoom of the Raman spectra (Fig. 5.3(e)) of PF-RUB in solution and thin film on silicon in pristine stage shows one peak at $\tilde{\nu} \sim 1315$ cm⁻¹ which has a slight shoulder at $\tilde{\nu} \sim 1325$ cm⁻¹. We can identify this peak with a corresponding peak in the computed twisted conformation at 1315 cm⁻¹. The second peak at roughly 1335 cm⁻¹ appearing in the theoretical model is obviously strongly suppressed and reduced to a shoulder in the experimental spectra. For the spectra on the SAM and on silicon in late stage

we observe an additional peak e_1 at 1299 cm^{-1} which is near to a computed peak of the planar conformation at 1295 cm^{-1} . Further Raman peaks around 1525 cm^{-1} and 1580 cm^{-1} also coincide roughly with peaks predicted by the computed model. Deviations between computed and measured Raman frequencies remain within the typical scatter of calculated modes obtained with the B3LYP hybrid functional with respect to observed values.

Comparing the Raman spectra of the pristine thin film on silicon with the solution spectra reveals an essentially identical spectrum (Figs. 5.3(b), (e), and (f)). This evidences that also in pristine thin films deposited on native silicon the PF-RUB molecules in the twisted molecular conformation prevail and are most likely disordered. Analogously, the IR spectrum of the PF-RUB thin film on silicon in the pristine stage is similar to the solution spectrum, albeit including a notable peak broadening for the thin film spectrum.

The IR and Raman spectra of PF-RUB molecules deposited on silicon in the late stage and on the SAM show slightly different signatures than the solution or pristine thin film spectra. The peak intensity observed in the IR spectra corresponding to the positions c_4 and d_1-d_3 are less pronounced than for the solution, and both pristine thin film spectra and the peak separation between c_2 and c_3 are different. A reason for this could be the presence of a fraction of molecules with a planar tetracene backbone [47, 196].

5.2.3 Molecular conformation of PF-RUB

In order to quantify the ratio of planar and twisted molecules in the respective samples, we perform a more detailed analysis including a decomposition of the spectra of the PF-RUB thin films deposited on SAM ($SAM(\tilde{\nu})$) and on silicon in the late stage ($SIL(\tilde{\nu})$). If the experimental spectra consist of molecules with a fraction α in the planar and another fraction β in the twisted conformation, which have different vibrational modes $A(\tilde{\nu})$ and $B(\tilde{\nu})$, respectively, the experimental spectra $SIL(\tilde{\nu})$ and $SAM(\tilde{\nu})$ are supposed to be a linear combination of both of them. Following this idea, we can describe the spectra of $SIL(\tilde{\nu})$ and $SAM(\tilde{\nu})$ in terms of the basis spectra $A(\tilde{\nu})$ and $B(\tilde{\nu})$ that correspond to the modes of purely planar and purely twisted conformation, respectively.

$$\begin{pmatrix} SIL(\tilde{\nu}) \\ SAM(\tilde{\nu}) \end{pmatrix} = \begin{pmatrix} \alpha_1 & \beta_1 \\ \alpha_2 & \beta_2 \end{pmatrix} \begin{pmatrix} A(\tilde{\nu}) \\ B(\tilde{\nu}) \end{pmatrix} \quad (5.1)$$

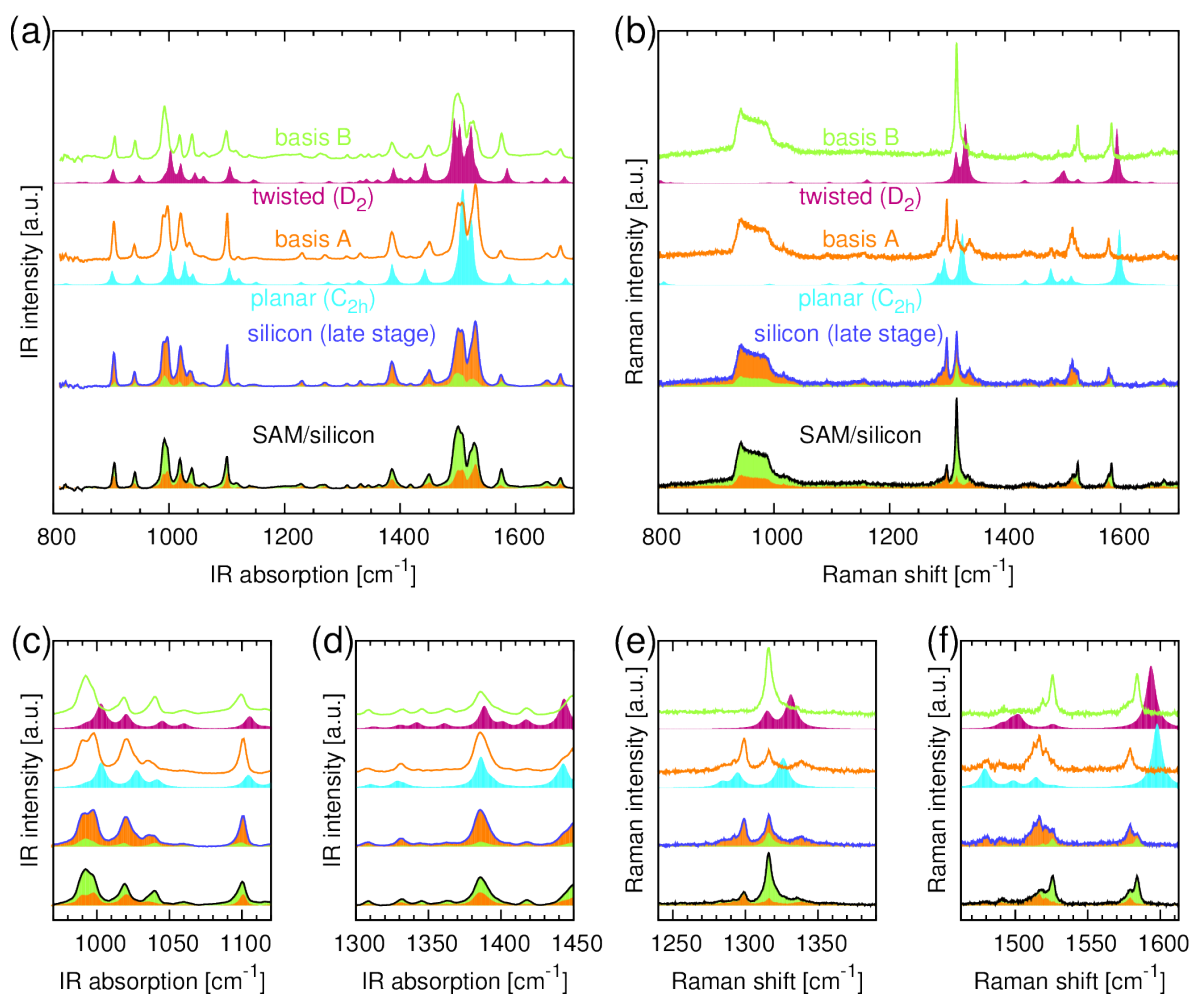


Figure 5.4: Decomposition of IR ((a), (c), and (d)) and Raman ((b), (e), and (f)) spectra of PF-RUB on silicon in the late stage (blue line) and on SAM (black line) into basis spectra basis A ($\tilde{\nu}$) (orange line) and basis B ($\tilde{\nu}$) (green line). While for IR basis A ($\tilde{\nu}$) agrees very well with the computed spectrum for the planar conformation (cyan, filled curve), basis B ($\tilde{\nu}$) corresponds to the computed spectrum for the twisted conformation (purple, filled curve). The Raman basis B ($\tilde{\nu}$) resembles the solution spectrum of PF-RUB (Fig. 5.3(b)) with slightly sharpened peaks.

On the other hand, the basis spectra $A(\tilde{\nu})$ and $B(\tilde{\nu})$ can be found by inversion of the matrix in Eq. (5.1),

$$\begin{pmatrix} A(\tilde{\nu}) \\ B(\tilde{\nu}) \end{pmatrix} = \frac{1}{\alpha_1\beta_2 - \alpha_2\beta_1} \begin{pmatrix} \beta_2 & -\beta_1 \\ -\alpha_2 & \alpha_1 \end{pmatrix} \begin{pmatrix} SIL(\tilde{\nu}) \\ SAM(\tilde{\nu}) \end{pmatrix}, \quad (5.2)$$

which is practically a projection of the spectra $SIL(\tilde{\nu})$ and $SAM(\tilde{\nu})$ onto each other. Note that Eqs. (5.1) and (5.2) effectively depend on only two parameters, since the total number of molecules, N , is identical for both films ($\alpha_i + \beta_i = N$) simultaneously deposited. For the same set of parameters ($\alpha_1/N = 0.79, \beta_1/N = 0.21, \alpha_2/N = 0.32, \beta_2/N = 0.68$) we find basis spectra $A(\tilde{\nu})$ and $B(\tilde{\nu})$ both for IR as well as for Raman under the constraint that different peaks in $A(\tilde{\nu})$ and $B(\tilde{\nu})$ become minimized but not negative, compare Fig. 5.4.

Remarkably, a comparison of the IR basis spectra $A(\tilde{\nu})$ and $B(\tilde{\nu})$ with the computed spectra for the planar (C_{2h}) and twisted (D_2) conformation of the free PF-RUB molecule (Fig. 5.4(a), (c), and (d)) reveals a very good agreement. From this finding we conclude that the modeled molecular geometries must be very close to the real conformations of the molecules. Obviously, basis $A(\tilde{\nu})$ corresponds to the planar conformation and basis $B(\tilde{\nu})$ to the twisted conformation, respectively. Analogously, the Raman basis spectrum $B(\tilde{\nu})$ coincides very well with the solution (and silicon pristine thin film) spectrum of PF-RUB, which is supposed to originate essentially from twisted molecules. Note that the Raman peaks of basis $B(\tilde{\nu})$ appear sharper than in the the solution spectrum, while maintaining the same peak area. An overview over the most important vibrational peaks is given in Tabs. 5.3 and 5.2.

This implies the following: (i) We can identify and assign the IR and Raman spectra of basis $A(\tilde{\nu})$ and $B(\tilde{\nu})$ to planar and twisted PF-RUB molecules, respectively. (ii) The intensity ratio of the basis spectra $A(\tilde{\nu})$ and $B(\tilde{\nu})$ can be associated with the fraction of planar to twisted molecules in the thin films. According to the values found for α_i and β_i , the ratio of planar:twisted PF-RUB molecules in the thin film deposited on bare silicon in the late stage corresponds to $\sim 4:1$ ($SIL(\tilde{\nu})$) whereas on SAM/silicon ($SAM(\tilde{\nu})$) this ratio changes to $\sim 1:2$.

Remarkably, the substrate apparently influences the molecular conformation still over a long distance through the entire thin film with a thickness of 100 nm. This behavior is unexpected, since molecular interaction usually happens on a much shorter length scale.

VIBRONIC EXCITATION OF RUB, F₁₄-RUB, AND PF-RUB

Vib. Mode		IR			Raman		
C _{2h}		Comp.	Basis A		Comp.	Basis A	
$\tilde{\nu}$ [cm ⁻¹]	Sym.	Int. [km/mol]	$\tilde{\nu}$ [cm ⁻¹]	Int. m, s	Int. \propto	$\tilde{\nu}$ [cm ⁻¹]	Int. m, s
214.3	A _g				0.04	215	m
476.9	A _g				0.12	486	m
901.9	A _u	247	905	s			
945.5	B _u	176	940	s			
992.3	A _u	48	990	s			
1002.9	B _u	578	998	s			
1027.4	A _u	395	1020	s			
1041.5	B _u	163	1035	m			
1104.4	A _u	296	1101	s			
1121.0	B _u	101	1120	m			
1228.8	A _u	48	1230	m			
1275.5	A _u	47	1270	m			
1283.8	A _g				0.16	1285	m
1294.6	A _g				0.44	1299	s
1310.1	B _u	35	1308	m			
1322.4	A _g				0.19	1316	s
1326.4	A _g				0.82	1339	s
1328.2	A _u	63	1331	m			
1386.1	A _u	355	1386	s			
1443.1	A _u	258	1450	s			
1479.0	A _g				0.29	1480	m
1506.0	B _u	1022	1501	s			
1510.3	B _u	1051	1507	s			
1514.2	A _g				0.15	1516	s
1522.9	A _u	303	1522	s			
1524.5	A _u	670	1531	s			
1526.6	A _g				0.02	1521	s
1589.2	B _u	184	1574	m			
1597.8	A _g				1.00	1579	s
1654.4	A _u	63	1654	m			
1686.4	A _u	124	1677	s			

Table 5.2: Detailed overview over the most prominent experimentally observed IR and Raman peaks of the basis spectra $A(\tilde{\nu})$ in association with the computed IR and Raman modes for the C_{2h} geometry of the free PF-RUB molecule. Observed peaks have strong (s) or medium (m) intensity. The energies of the computed modes are multiplied by 0.9915. Raman intensities are normalized to the strongest mode of the isomer.

VIBRONIC EXCITATION OF RUB, F₁₄-RUB, AND PF-RUB

Vib. Mode		IR			Raman		
D ₂		Comp.	Basis B		Comp.	Basis B	
$\tilde{\nu}$ [cm ⁻¹]	Sym.	Int. [km/mol]	$\tilde{\nu}$ [cm ⁻¹]	Int. m, s	Int. \propto	$\tilde{\nu}$ [cm ⁻¹]	Int. m, s
169.9	A				0.01	236	m
207.9	A				0.04	244	m
289.0	A				0.07	284	m
377.3	A				0.05	398	m
394.5	A				0.03	405	m
467.0	A				0.13	463	s
903.4	B ₃	247	906	s			
948.8	B ₁	137	941	s			
1003.0	B ₂	529	992	s			
1020.3	B ₃	314	1019	s			
1045.0	B ₁	168	1040	s			
1060.1	B ₂	110	1060	m			
1105.3	B ₃	290	1099	s			
1277.4	B ₃	37	1261	m			
1312.2	B ₁	22	1309	m			
1330.4	B ₃	39	1332	m			
1331.1	A				0.99	1316	s
1334.2	A				0.12	1336	m
1342.0	B ₁	67	1345	m			
1361.0	B ₂	53	1363	m			
1388.5	B ₃	261	1386	s			
1417.4	B ₂	89	1418	m			
1443.5	B ₃	327	1449	s			
1493.3	B ₁	948	1500	s			
1502.4	A				0.18	1519	m
1503.5	B ₂	694	1507	s			
1515.4	B ₂	290	1521	s			
1523.1	B ₃	855	1527	s			
1526.0	A				0.07	1526	s
1533.3	B ₃	112	1533	s			
1585.2	B ₁	259	1576	s			
1593.6	A				1.00	1584	s
1627.0	A				0.03	1653	m
1652.6	B ₃	75	1654	m			
1652.9	A				0.02	1675	m
1684.6	B ₃	85	1677	m			

Table 5.3: Detailed overview over the most prominent experimentally observed IR and Raman peaks of the basis spectrum $B(\tilde{\nu})$ in association with the computed IR and Raman modes for the D₂ geometry of the free PF-RUB molecule. Observed peaks have strong (s) or medium (m) intensity. The energies of the computed modes are multiplied by 0.9915. Raman intensities are normalized to the strongest mode of the isomer.

5.2.4 Raman imaging of PF-RUB thin films

In a further step we analyze microscopically resolved Raman imaging spectra of the sample with PF-RUB deposited on SAM and on silicon in the late stage. Fig. 5.5 shows optical microscopy and Raman imaging pictures of the samples.

The optical microscopy picture of PF-RUB on silicon (Figs. 5.5(a) and (c)) shows a mostly homogeneous surface, with few differently patterned speckles of $5 - 20 \mu\text{m}$ in diameter. For the sample on the SAM we find islands as observed in the AFM picture. In order to obtain information about the local molecular conformation and a possible correlation with the morphology, we provide a zoom (red square) into the optical microscopy pictures for both substrates, where we performed Raman imaging. The Raman region of $1250 - 1400 \text{ cm}^{-1}$ is modeled with several Lorentzians, so the empirically found Raman signature of the twisted and planar conformation can be described. After that, each of the mapped spectra is fitted according to the intensity α_i and β_i for the modeled signature of the twisted and planar conformation, respectively. The resulting fraction $(\alpha_i - \beta_i)/(\alpha_i + \beta_i)$ of the local parameters determines the color coding. While red, blue, and green stands for domains of purely twisted, purely planar, and mixed molecules, respectively, the pixel brightness corresponds to the overall Raman peak intensity $(\alpha_i + \beta_i)$ at a given spot i . As a result of the comparison of Raman imaging with the optical microscopy pictures, we find a correlation between the observed thin film morphology and the conformation of the molecules.

For the thin film deposited on silicon in the late stage we observe a sharp Gaussian distribution ($\text{FWHM} = 0.16$) with center around 4:1 for the planar:twisted ratio. There are only few speckles with $5 - 20 \mu\text{m}$ in diameter that show clear predominance of twisted molecules. This is in sharp contrast to the pristine film, where we observe exclusively molecules in twisted conformation (no imaging provided).

For the thin film on the SAM, we find that the bigger grains surrounded by a feeding zone mostly consist of twisted molecules (red). In contrast to the bigger grains, most of the coarse grained (smaller) islands contain more or less equally (green) blended regions of the two conformations. The ratio of the molecules in twisted and planar conformation follows a Gaussian distribution centered around 2:1, but with much bigger FWHM (0.88) than for the film on bare silicon in the late stage.

Both samples are analyzed and discussed further using grazing incidence X-ray diffraction (GIXD) in Sec. 6.3.2. It can be shown that both samples contain crystallites belonging to at least two different unit cells.

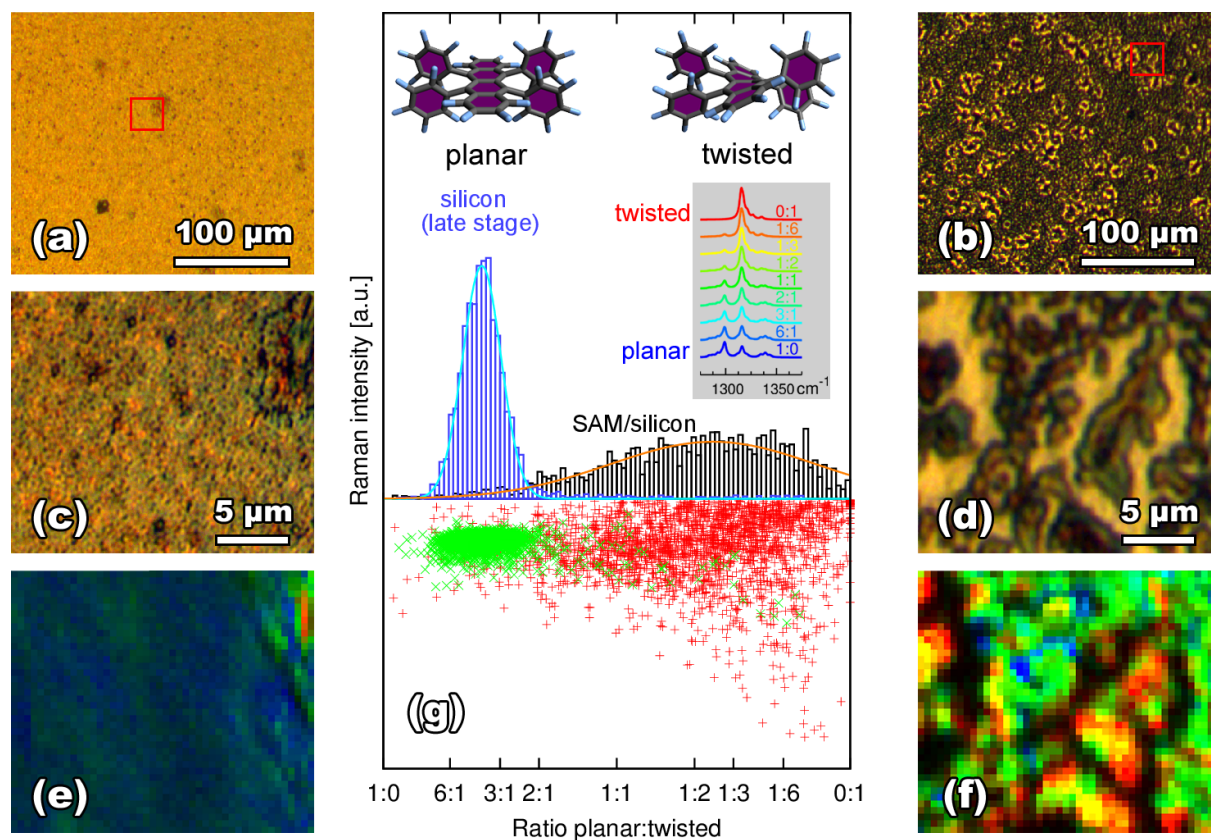


Figure 5.5: Microscopic analysis of the distribution of the ratio of planar and twisted PF-RUB molecules in the film on silicon (late stage) and on SAM/silicon. (a) and (b) Light microscope picture of PF-RUB on silicon (late stage) and on SAM/silicon, respectively. Panels (c) and (d) provide a zoom into the region selected by a red frame in (a) and (b), respectively. (e) and (f) Raman imaging (matrix of 46 px × 40 px) pictures of the peak signature around 1320 cm⁻¹ of PF-RUB on silicon (late stage) and on SAM/silicon, respectively. The images (e) and (f) correspond to the zoom of the light microscopy pictures, (c) and (d), respectively. While blue pixels stand for areas of purely planar molecules, red pixels visualize twisted molecules, and green regions are mixtures of both. (g) Evaluation of the Raman imaging pictures. While the distribution of the ratio of planar:twisted molecules of the sample in late stage (blue) is rather narrow, the histogram is broader for the sample on the SAM. Both histograms can be fitted well with a Gaussian. Green 'x' and red '+' (bottom) represent the individual pixel intensities from the imaging of silicon late stage and SAM/silicon, respectively, plotted on the negative y-axis. Gray box: Color coding for the ratio of planar:twisted molecules as used for the imaging pictures.

5.2.5 IR and Raman spectra of F₁₄-RUB

The samples were measured with IR and Raman spectroscopy within 1 day after thin film growth. In contrast to PF-RUB, no notable postgrowth changes in the vibrational spectra were observed for F₁₄-RUB thin films. For better evaluation of the spectra, the photoluminescence (PL) background of the Raman spectra was subtracted after acquisition.

Fig. 5.6(a) shows the fingerprint region of the experimental IR spectra of F₁₄-RUB dissolved in CH₂Cl₂, on native silicon, and on a SAM covered silicon in comparison with computed spectra (top to bottom). The peaks of the solution spectra are slightly sharper than the peaks from the thin film spectra. Similarly to PF-RUB, there are pronounced IR peaks in the C-F and C-C stretching region due to the high polarizability of the molecule. H-C modes result in much weaker peaks, since hydrogen carries far less charges than F or C, and are thus less pronounced. The computed IR modes correspond remarkably well to the experimental spectra, and most modes can be identified. In contrast to PF-RUB, the spectra of the computed modes for the planar (*C_s*) and twisted (*C₂*) conformation do not differ notably, which makes an assignment of the experimental spectra of F₁₄-RUB to particular molecular conformations (in analogy to PF-RUB) difficult.

Fig. 5.6(b) shows the fingerprint region of the experimental Raman spectra of F₁₄-RUB in solution, on native silicon, and on a SAM covered silicon in comparison with computed spectra (top to bottom). The Raman spectra are superimposed by a strong PL background (not shown), since the samples are excited at 633 nm (1.96 eV), which is close to the HOMO-LUMO transition of the molecule (compare Sec. 4.1). As a result, only the most prominent Raman active vibrational modes at $\sim 1300 - 1350 \text{ cm}^{-1}$ can be observed. Peaks in the spectrum of F₁₄-RUB dissolved in CH₂Cl₂ at $\tilde{\nu} \sim 1160 \text{ cm}^{-1}$ (*b₃*) and $\tilde{\nu} \sim 1425 \text{ cm}^{-1}$ (*b₅*) originate from the solvent [187]. In the thin film spectra a rather broad peak in the region of $900 - 1000 \text{ cm}^{-1}$ (*b₂*) is related to the silicon substrate [185]. Between the spectra of the different samples (thin film on silicon, thin film on SAM, and in solution), no significant dissimilarities can be distinguished. The computed Raman spectra show several peaks with comparable intensity in the fingerprint region, corresponding to either C-C or C-F stretching or C-H or C-C bending modes. In addition, off-resonant Raman spectra with reduced PL background were obtained at an excitation energy of 785 nm (see Appendix, p. 126). The peaks of those spectra are more pronounced, but nevertheless it remains impossible to assign the spectra to either the planar or twisted species as performed for PF-RUB.

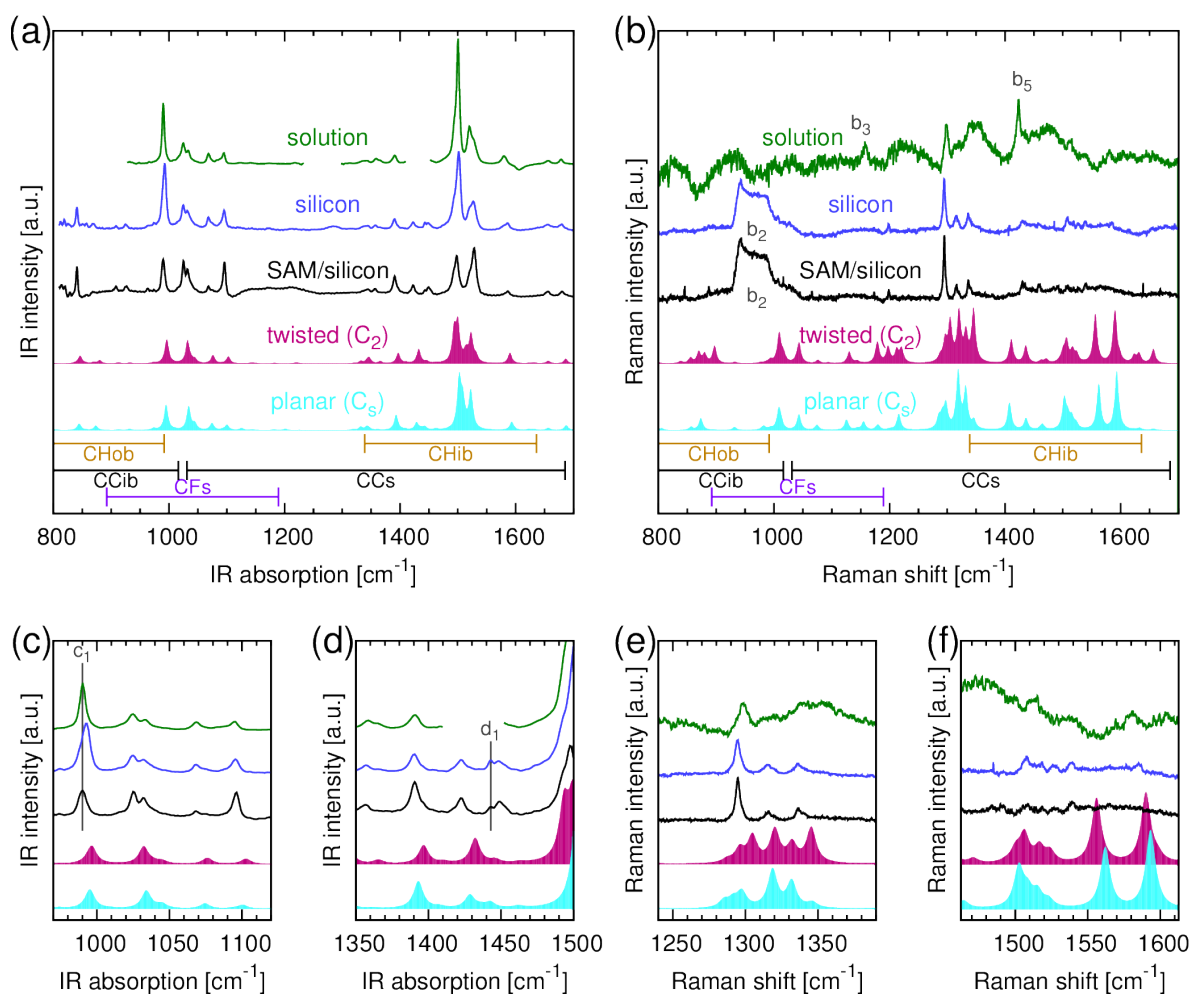


Figure 5.6: Experimental vibrational spectra of F_{14} -RUB (lines) and spectra computed by DFT (filled curves). The experimental spectra are obtained from molecules dissolved in CH_2Cl_2 (green line, top), deposited on native silicon in 'pristine' (red line) and 'late stage' (blue line), as well as on SAM/silicon (black line, bottom). The theoretical spectra show Lorentzian-shaped modeled curves of the twisted (purple filled) and planar (cyan filled) conformation of the molecule. (a) FT-IR spectra in the fingerprint region of the F_{14} -RUB molecule. (b) Raman spectra of the samples excited at 633 nm. (c) and (d) show a zoom into selected regions of the IR spectra, (e) and (f) of the Raman spectra, respectively. The bars at the bottom of (a) and (b) show the regions of the type of the vibrational mode ('CCib' = C-C in-plane bending, 'CCs' = C-C stretching, 'CFs' = C-F stretching). For explanation of the spectra, see text.

The IR spectrum of F₁₄-RUB deposited on silicon shows predominantly similarities with the solution spectrum. The IR peak signature (*i. e.* relative intensities) in the region of $\sim 1000 - 1100 \text{ cm}^{-1}$ (Fig. 5.6(c)) and also in the region of $\sim 1450 - 1550 \text{ cm}^{-1}$ resembles roughly the signatures of the solution spectrum within these ranges. This is in contrast to the spectrum of the thin film on the SAM, which shows different relative peak intensities in these regions. The peak c_1 of the silicon sample, however, is shifted by 2.5 cm^{-1} away from the solution peak, whereas the position of a corresponding c_1 peak in the thin film on the SAM coincides very well with the solution spectrum. The spectra of the thin film on silicon and on SAM differ particularly in the region of $\sim 1450 - 1550 \text{ cm}^{-1}$ and also, a peak at 1443 cm^{-1} (d_1) is more pronounced in the spectrum of the thin film on silicon against the spectrum of the film on SAM.

In summary, the comparison of the thin film spectra with the solution spectra suggests that the F₁₄-RUB molecules deposited in thin films on native silicon predominantly adopt a conformation with a twisted tetracene backbone. The exact molecular geometry, however, could not be determined from this set of data. An overview over the most prominent vibrational modes as experimentally observed in comparison with the computed values for the twisted C_2 and the planar C_s isomer can be found in Tab. 5.4.

5.3 Concluding remarks

In summary, we obtained both Raman as well as IR spectra of PF-RUB and F₁₄-RUB thin films on bare silicon wafers, SAM covered wafers, and in solution. We identified and assigned the experimental vibrational peaks in detail to computed modes of isomers with planar and twisted tetracene backbones. Similarly to unsubstituted RUB we find that free PF-RUB and F₁₄-RUB molecules with twisted backbone are energetically favored compared to the planarized isomer.

Moreover, for PF-RUB we could show that not only particular vibrational modes of the experimental spectra correspond to either the planar or twisted conformation of the molecule, but we could decompose the experimental spectra into fractions derived from planar and twisted molecules. Using Raman imaging, we distinguished different regions of the thin films with respect to the ratio of planar and twisted molecules on a micrometer scale and found significant differences between PF-RUB on silicon and PF-RUB on SAM/silicon.

The PF-RUB thin film deposited on native SiO₂ is disordered and very smooth directly after growth (see Chap. 6), and nearly all molecules exhibit a twisted backbone. Within

VIBRONIC EXCITATION OF RUB, F₁₄-RUB, AND PF-RUB

Experimental				Computed C ₂				Computed C _s			
Raman		IR		Vib. Mode		Raman	IR	Vib. Mode		Raman	IR
$\tilde{\nu}$ [cm ⁻¹]	Int. m, s	$\tilde{\nu}$ [cm ⁻¹]	Int. m, s	$\tilde{\nu}$ [cm ⁻¹]	Sym.	Int. \propto	Int. [km/mol]	$\tilde{\nu}$ [cm ⁻¹]	Sym.	Int. \propto	Int. [km/mol]
365	m			369.4	A	0.06	4	354.3	A'	0.07	1
703	m			703.9	A	0.05	46	704.9	A'	0.04	56
		841 [†]	s	846.3	B		101	844.6	A''		88
		869 [†]	m	869.9	A	0.15	19	873.5	A'	0.21	61
887	m			897.3	A	0.24		895.2	A'	0.01	1
		908 [†]	m	912.8	B		15	912.8	A''		9
		926 [†]	m	932.3	A	0.02	8	931.8	A'	0.05	9
		990* 993 [‡]	s	996.6	B		289	995.2	A'	0.02	315
1006	m			1009.2	A	0.41		1008.3	A'	0.33	4
1026	m			1016.6	A	0.11	3	1011.9	A'	0.12	3
		1025	s	1032.3	B		300	1034.1	A''		310
		1033	s	1039.1	A	0.03	26	1043.2	A'	0.25	20
1066	m			1043.4	A	0.27	3	1044.7	A'	0.01	18
		1069	m/s	1045.0	B		44	1045.4	A''		43
		1084	m	1076.2	A	0.04	109	1074.5	A'	0.09	92
		1095	s	1102.8	B		91	1100.4	A''		68
1173	m			1179.3	A	0.22	0	1180.3	A'	0.07	0
1198	m			1197.6	A	0.22	0	1197.8	A'	0.01	0
1209	m			1212.5	A	0.17	2	1215.9	A'	0.28	2
1295	s			1296.0	A	0.28	1	1297.5	A'	0.40	1
1316	s			1320.3	A	0.68	5	1318.7	A'	0.96	10
1338	s	1336	m	1332.2	A	0.38	31	1331.9	A'	0.68	40
		1344	m	1345.4	A	0.60	40	1342.5	A''		43
		1357	m	1347.1	B		36	1346.2	A''		17
		1365*	w/m	1365.6	B		29	1361.4	A''		7
		1391	s	1396.7	B		138	1393.1	A''		203
1430	m	1423 [†]	m	1410.6	A	0.33	13	1407.6	A'	0.47	14
		1443 [†]	m	1432.2	B		188	1428.6	A''		97
1435	m			1435.9	A	0.24	0	1436.2	A'	0.20	16
		1449 [†]	m	1445.8	B		26	1442.7	A''		40
1459	m			1462.3	A	0.03	2	1461.8	A'	0.03	15
1485	m			1471.1	A	0.05	1	1464.8	A'	0.08	1
1492	m	1498*	s	1493.4	A	0.02	411	1502.0	A'	0.23	283
		1501 [#]	s	1499.9	B		430	1502.8	A'	0.30	348
1508	m			1506.3	A	0.29	4	1508.7	A'	0.19	326
		1520	s	1522.8	B		353	1522.1	A''		401
		1528	s	1531.5	B		81	1524.9	A''		50
1540	m			1556.1	A	0.67		1562.1	A'	0.79	0
		1586	m	1590.1	A	0.73	139	1593.2	A'	1.00	108
		1655	m	1656.3	B		37	1656.3	A''		26
		1679	m	1686.6	B		64	1687.5	A''		67
				3145.9	A	0.24	0	3145.3	A'	0.03	0
				3153.4	A	0.53		3152.8	A'	0.30	7
				3160.8	A	0.03	14	3161.1	A'	0.25	16
				3167.9	A	1.00	0	3168.0	A'	0.73	6

Table 5.4: Detailed overview over the most prominent experimentally observed IR and Raman peaks in association with the computed modes for the two isomers (C_s and C₂ geometries) considered for the free F₁₄-RUB molecule. Observed peaks have strong (s) or medium (m) intensity. The energies of the computed modes are multiplied by 0.9915, computed Raman intensities are normalized to the respective strongest mode.

24 hours after growth, we observe a dewetting of the film and approximately two-thirds of the molecules change their conformation to a planar backbone and the film roughens (see Chap. 6). In fact, the relatively low evaporation temperature of PF-RUB molecules from our Knudsen cell in comparison to RUB suggests that a reorientation of the PF-RUB molecules in the thin film is promoted already at RT without further annealing. However, directly after growth, the PF-RUB thin film on SAM already contains both conformations of the molecule forming stable clusters on a micrometer scale. Obviously, the SAM leads to a modification in the surface energy which enhances the diffusion of the PF-RUB molecules so that stable crystallite nuclei can be formed (see Chap. 6). The exploration of the vibrational properties of PF-RUB and F₁₄-RUB is of fundamental interest and will contribute to a more general understanding of the charge carrier mobility in fluorinated rubrene derivatives.

CHAPTER 6

STRUCTURE AND MORPHOLOGY OF F₁₄-RUB AND PF-RUB THIN FILMS

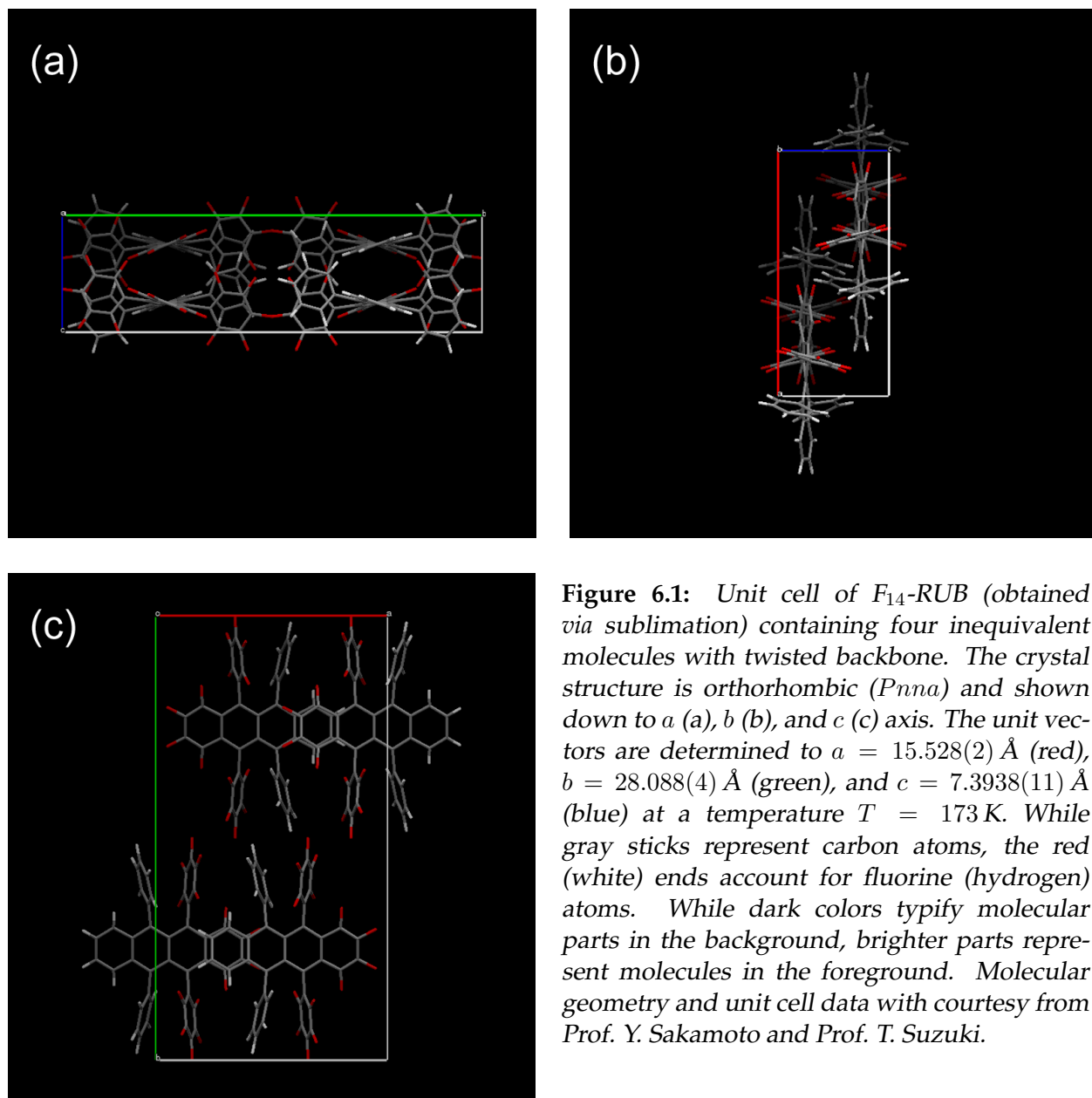
This chapter reports on crystal and thin film structures of the fluorinated rubrenes. The nucleation of rubrene (RUB) and its derivatives is in many cases very complex. Nevertheless, it has strong influence on the electronic and vibronic properties of the materials in thin films. The first section (Sec.6.1) reports on the crystal structures and unit cells of the fluorinated compounds that were found by Y. Sakamoto and T. Suzuki from crystals grown from sublimation and solution. The next section (Sec.6.2) discusses pristine thin films that were produced during this work and their morphological stability. All compounds show a strong and complex dewetting behavior [245], which is facilitated by the intricate molecular geometry. In the third and last section (Sec. 6.3), the morphology and structure of matured PF-RUB and F₁₄-RUB thin films on silicon and on a self assembled monolayer (SAM) are examined. The samples in this section are identical to the ones that were investigated in Chap. 5 with respect to their vibronic properties. The crystallinity of the respective thin films using grazing incidence X-ray diffraction (GIXD) is discussed.

6.1 Crystal structures of fluorinated rubrene

For RUB, different single crystal structures formed by molecules with planar tetracene backbone (C_{2h} symmetry) have been found, for which the commonly reported orthorhombic unit cell turned out to be most efficient in terms of charge carrier mobility [88, 146, 239, 246, 247]. But also monoclinic [248] and triclinic packing structures have been observed [249], and in general a polymorphism of different unit cells and/or disordered phases are found in an aggregation of RUB molecules. In the orthorhombic crystal structure, which shows high anisotropic mobilities [84], the molecules are ordered in a herringbone pattern, that is the preferred crystal structure of many small molecule OSCs [250], particularly in the acene group [30]. While thin films of RUB are usually amorphous [195] and contain a majority of twisted molecules [127], RUB molecules in crystals nevertheless adopt a planar conformation due to a more efficient packing in the crystalline phase [88, 146, 239, 249]. This can be different for RUB derivatives, where crystallization of substituted RUB molecules with a twisted molecular backbone has been observed recently [43, 44].

In analogy to the RUB molecule [47, 196] there are also two stable molecular conformations for newly synthesized fluorinated rubrenes in free space, either with a planar or with a twisted tetracene backbone that result in different optical properties and polaron binding energies [157]. However, it is not *a priori* clear which molecular conformation prevails for PF-RUB and F₁₄-RUB in thin films or crystals.

One approach to obtain RUB single crystals is the growth from solution [112, 249, 251–254], which, however, not always results in satisfying crystal qualities. A more controlled technique is the so-called *hot wall* deposition [88, 139, 255], which allows to create even large crystals from the gaseous phase at high temperature and high pressure. Yet it is expensive to perform and also requires a lot of material. After the synthesis of the fluorinated rubrene by Prof. Y. Sakamoto and Prof. T. Suzuki, X-ray powder diffraction of F₁₄-RUB and PF-RUB was performed. It turned out that F₁₄-RUB molecules adopt an orthorhombic crystal structure and a twisted backbone, when crystallized *via* sublimation (Fig. 6.1). For PF-RUB two different monoclinic (albeit both very close to orthorhombic) unit cells are reported by Prof. Y. Sakamoto and Prof. T. Suzuki, depending on whether the crystals were created from solution (Fig. 6.2) or from sublimation (Fig. 6.3). While the PF-RUB molecules precipitated from solution adopt a nearly planar backbone, the molecules crystallized *via* sublimation obtain a twisted backbone. A list containing the respective crystal parameters (Tab. 6.1) can be found in Sec. 6.3.2.



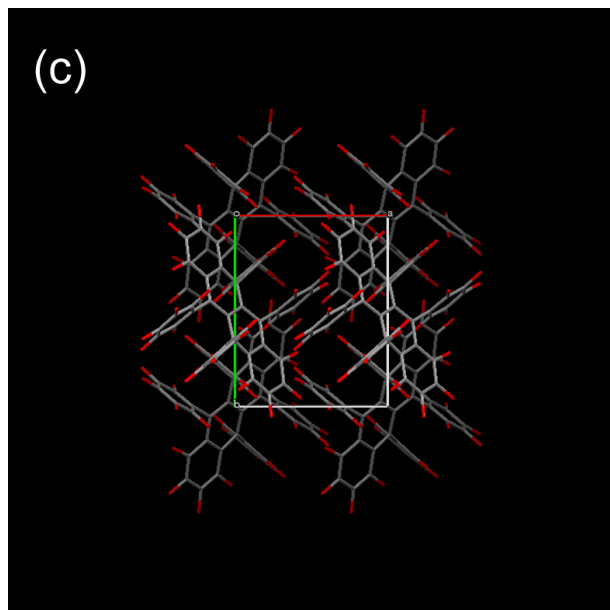
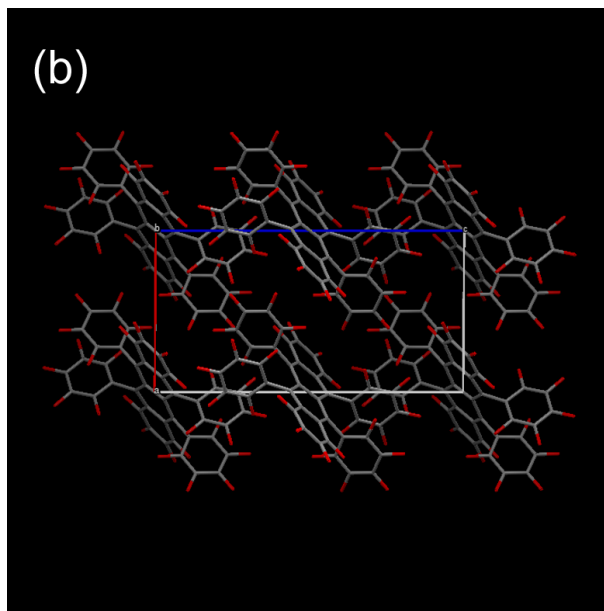
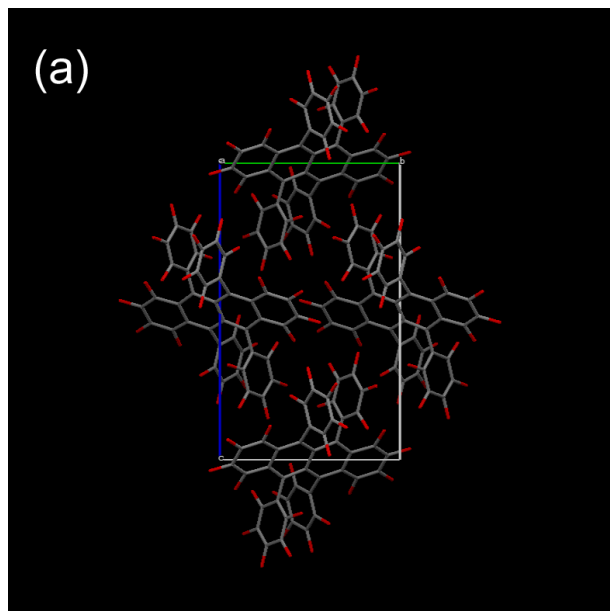
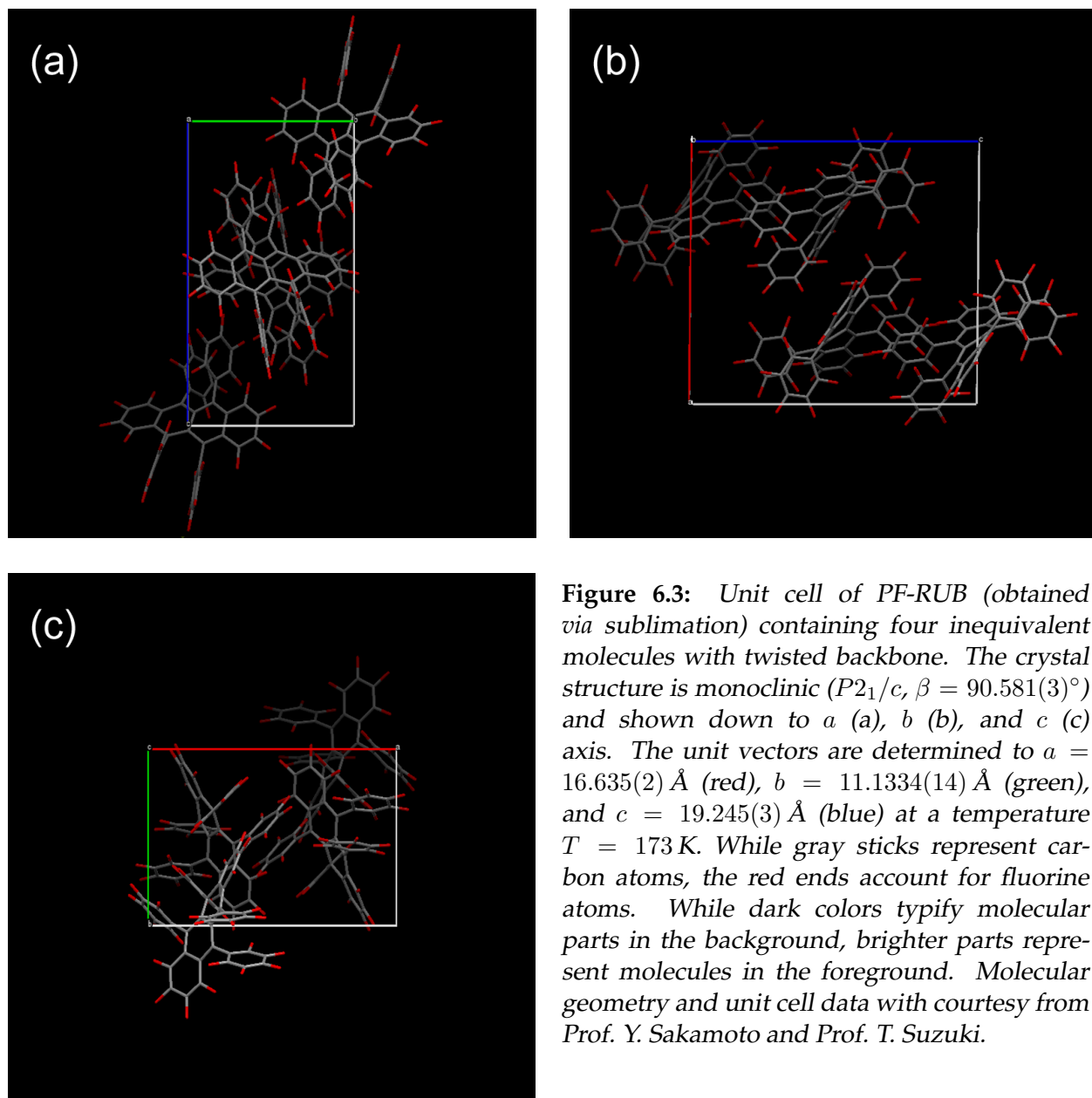


Figure 6.2: Unit cell of PF-RUB (obtained via solution) containing two inequivalent molecules with nearly planar backbone. The crystal structure is monoclinic ($P2_1/c$, $\beta = 90.408(8)^\circ$) and shown down to a (a), b (b), and c (c) axis. The unit vectors are determined to $a = 8.9017(17) \text{ \AA}$ (red), $b = 10.527(2) \text{ \AA}$ (green), and $c = 17.992(4) \text{ \AA}$ (blue) at a temperature $T = 173 \text{ K}$. While gray sticks represent carbon atoms, the red ends account for fluorine atoms. While dark colors typify molecular parts in the background, brighter parts represent molecules in the foreground. Molecular geometry and unit cell data with courtesy from Prof. Y. Sakamoto and Prof. T. Suzuki.



6.2 Pristine thin films

Self assembling of molecules is a very complex process depending strongly on the properties of the substrates. Organic thin films do not grow always in crystalline form, since the molecules not necessarily have sufficient opportunities to orient and align themselves to be incorporated into a crystal structure. Thin films of some complex molecules, however, dewet and reorient themselves even days after deposition in order to adopt an energetically more favored assembling. The reason for this complicated behavior can often be found in the intricate molecular structure and in the case of RUB, which can adopt several conformations, also in the chirality of the twisted isomer of the RUB molecule [68,218,228,229,256,257].

6.2.1 Thin film growth

A flexible and cheap way to produce organic structures, and hence preferred in many situations to *hot-wall* deposition or precipitation from solution, is thin film growth using organic molecular beam deposition (OMBD, see Sec. 3.2.1). The OMBD technique can be easily employed for the growth of organic layers on another material (metal, silicon wafer, other organics, etc.), regardless of its roughness or shape.

The crystallization process of molecules becomes more difficult with increasing degree of molecular complexity, which particularly in the case of RUB, F₁₄-RUB, and PF-RUB leads to usually amorphous thin film growth. Due to their intricate three-dimensional molecular structure that is mainly caused by the phenylrings, there are additional degrees of freedom, *i. e.* the molecules can adopt different conformations. As a consequence, thin film growth of RUB, F₁₄-RUB, and PF-RUB is a very complex process and depends strongly on different growth parameters, e. g. deposition rate, substrate temperature, surface energy of the substrate, and pressure [111,245]. In spite of several attempts to produce (poly)crystalline RUB films using OMBD techniques, it remains a challenging task.

Similarly to RUB, we find that free F₁₄-RUB and PF-RUB molecules with twisted backbone are energetically preferred to the planarized isomer (Sec. 4.1) and that the twisted conformation prevails directly after growth on silicon substrates [87,159]. In contrast to the disordered growth on silicon, different polymorphs of superstructures (e. g. five-fold symmetry) are observed for RUB on clean metal single crystal surfaces [218,230], which is unusual for organics [231]. It has been shown that annealing of RUB thin films on silicon [113,194] can help in parts to overcome the energy barrier needed for a

reorientation of the molecules and can stabilize the film by an increase in the degree of crystallization [249]. Another possibility to influence the thin film growth and also the molecular conformation is the modification of the substrate e. g. with a self-assembled monolayer (SAM) [116,258,259]. On many organic substrates [258,260,261] coexist the twisted and the planar conformation already from the first monolayer on [142,157].

6.2.2 Postgrowth dewetting

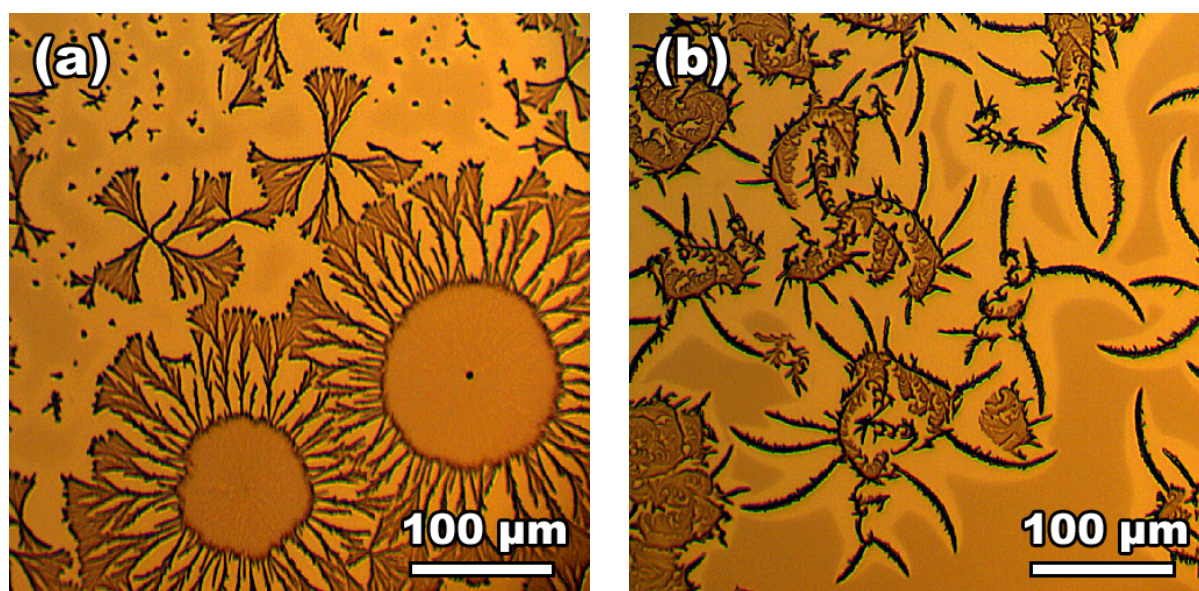


Figure 6.4: Light microscopy picture of thin films of (a) F₁₄-RUB (20 nm) and (b) PF-RUB (55 nm), each roughly one month after deposition on a silicon wafer at room temperature. While the left image shows a typical spherulitic dewetting pattern of F₁₄-RUB, which is similar to what has been observed for RUB, this seems to be different for PF-RUB with rather bent islands prevailing as suggested by the picture on the right. Brighter regions surrounding the islands demarcate feeding zones that presumably contributed molecules to the island growth. Note that the particular dewetting process strongly depends on the growth parameters (substrate, growth rate, pressure, etc.) and storage conditions (absence/presence of light, level of oxygen, humidity, etc.). As a consequence, a magnitude of different dewetting patterns can be observed [245].

Postgrowth dewetting [65] of RUB thin films is a well-known phenomenon [194,200,238,251,262–268]. Three-dimensional molecules such as RUB, F₁₄-RUB, and PF-RUB

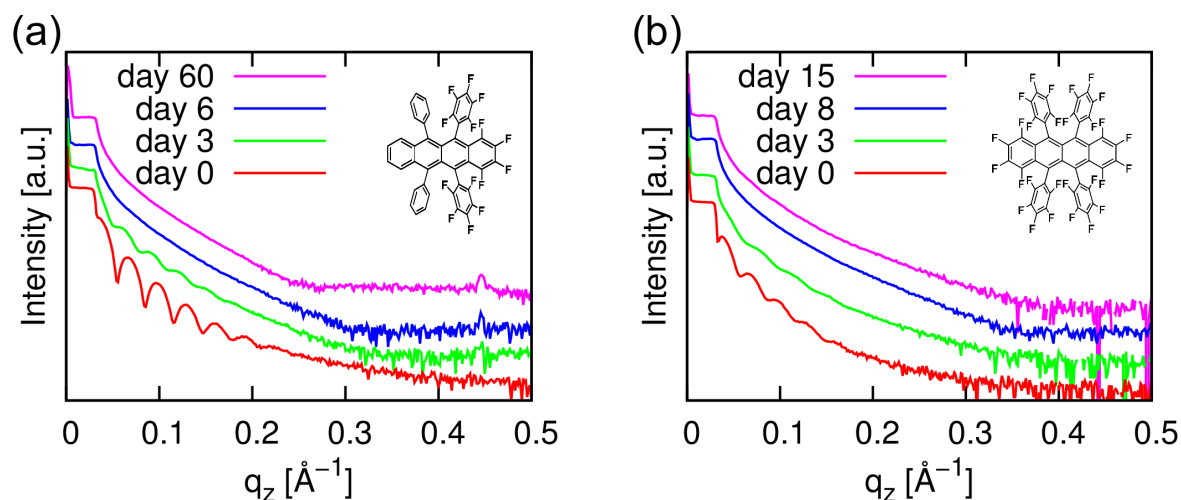


Figure 6.5: X-ray reflectivity (XRR) scans of thin films of (a) F₁₄-RUB and (b) PF-RUB, directly after deposition and after some days. As evidenced by the vanishing of the Kiessig fringes that are still present for the pristine films (day 0) in the vicinity of $q_z \approx 0.1 \text{ \AA}^{-1}$ and thus indicating a smooth sample surface, the samples roughen significantly during the time after thin film growth. Interestingly, a relatively weak Bragg peak appears at $q_z = 0.44 \text{ \AA}^{-1}$ for the partially fluorinated compound, which corresponds to a real space distance $d_z = 14.05 \text{ \AA}$. This value agrees well with the (020) orientation of the F₁₄-RUB crystal structure (Sec. 6.1), for RUB [194] thin films the (200) orientation has been observed by XRR after annealing. The thin films with a thickness of 20 nm were stored in absence of light and oxygen.

are only weakly bound to the substrate [88,264] and diffuse on its surface much more freely than two-dimensional molecules [264]. Moreover, the molecules can adopt different conformations with similar energies that can easily be transformed into each other [218], which facilitates restructuring of the thin films. Fig. 6.4 shows light microscopy pictures of typical patterns of F₁₄-RUB and PF-RUB thin films on silicon after dewetting. While F₁₄-RUB in many cases forms spherulites, which is similar to RUB [194, 200, 262, 263, 267, 268], PF-RUB usually shows a different pattern. Accompanied with the dewetting process of the thin films is often a roughening of the thin film that can be observed with X-ray reflectivity (Fig. 6.5). In particular cases weak Bragg peaks can be observed after dewetting, which evidences the existence of crystallinity. The considerably lower evaporation temperature of the (per)fluorinated rubrene derivative is supposed to increase the probability of postgrowth dewetting.

6.3 Morphology and structure of matured thin films

This section focuses on the thin film samples of PF-RUB and F₁₄-RUB that are examined in Chap. 5 with infrared (IR) and Raman spectroscopy. It reports on the morphology and structure of the samples deposited on silicon in late stage and on SAM.

6.3.1 Thin film morphology

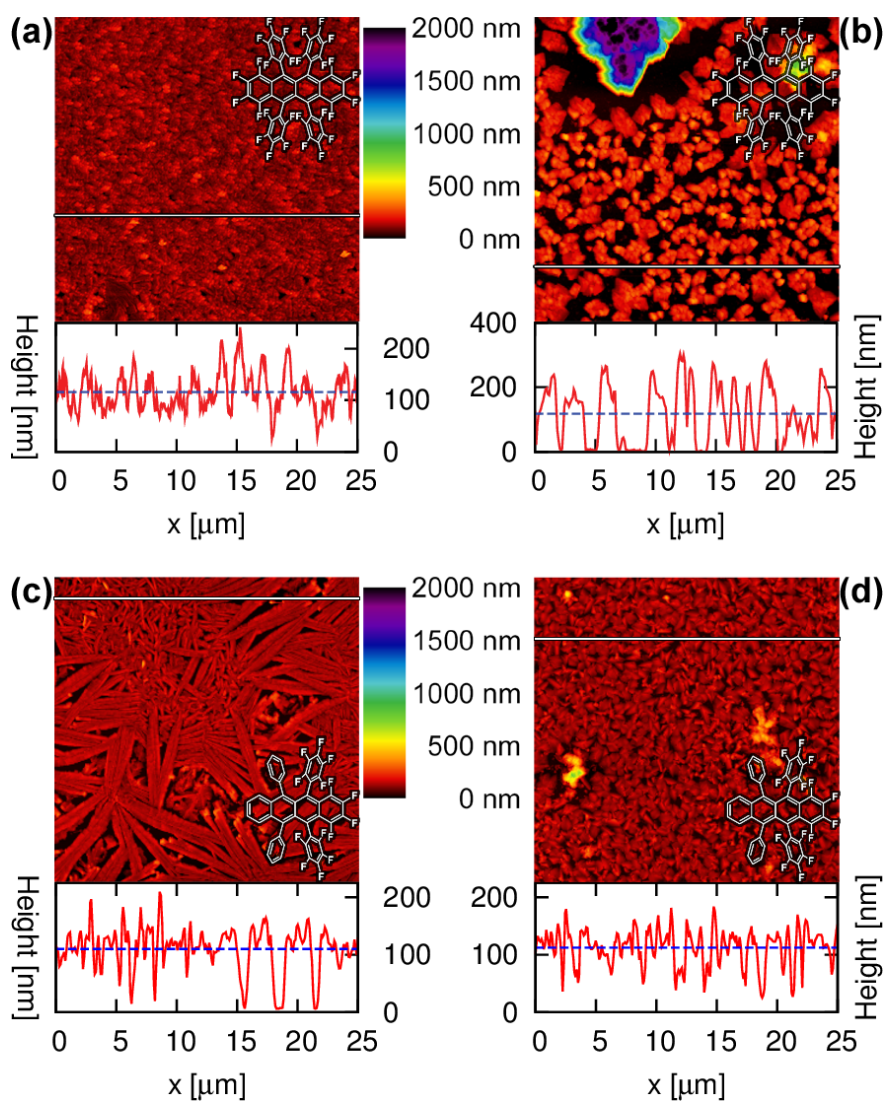


Figure 6.6: Representative atomic force microscope (AFM) picture of PF-RUB and F₁₄-RUB deposited on silicon in the late stage ((a) and (c), respectively) and on SAM ((b) and (d), respectively). While the surface is roughened for the PF-RUB film on silicon in the late stage, steep islands can be observed for the PF-RUB sample on the SAM. All films have a thickness of ~ 100 nm and the samples with identical molecules were deposited at the same time under the same conditions. The height profiles below the pictures follow the white line in the respective AFM acquisitions.

Figs. 6.6(a) and (b) show an atomic force microscope (AFM) picture of a representative area of the sample with PF-RUB deposited on silicon in the late stage and on SAM, respectively. The sample with PF-RUB deposited on silicon in the late stage reveals a large surface roughening of $\sigma = 35$ nm. This is different for the pristine thin film deposited on silicon, which is very smooth with $\sigma < 1$ nm (not shown) [194, 195]. The PF-RUB film on SAM exhibits a very different surface morphology [258]. Most of the sample is covered with a coarse-grained pattern, which under the AFM turns out to consist of steep islands with a height of 200 – 300 nm and a diameter of up to 5 μ m. Between these islands, there is no or only a very thin film coverage, probably only a wetting layer. Within the coarse-grained pattern we observe several even bigger grains (height up to 2 μ m) that are surrounded by an emptied feeding zone.

Fig. 6.6(c) and (d) visualize an AFM picture of a representative area of the sample with F₁₄-RUB deposited on silicon and on SAM, respectively. Both films show a similar roughening of $\sigma = 45$ nm. At the surface of the sample deposited on bare silicon, we observe needles of different sizes in the range of 1 . . . 10 μ m that have an approximate length to width ratio of ~ 10 . This is contrasted by the F₁₄-RUB sample on SAM, which shows a pattern of clusters with a height of ~ 100 nm and a diameter of ~ 1 μ m. These clusters formed by F₁₄-RUB on SAM are smaller and have less sharp edges than the islands of PF-RUB on SAM. In contrast to PF-RUB, the vibrational properties of the two F₁₄-RUB samples do not differ significantly within different spots (see Chap. 5).

6.3.2 Grazing incidence X-ray diffraction

This section presents grazing incidence X-ray diffraction (GIXD) data of the PF-RUB and F₁₄-RUB thin films that are discussed in Chap. 5. GIXD data can give information about the (poly)crystallinity of a sample. The spectra were obtained at the SWISS LIGHT SOURCE (MS-X04SA/SURFACE DIFFRACTION beamline) [193] at 13.996 keV using a PILATUS detector. During measurement the samples were kept at room temperature under protective atmosphere. The incidence angle $\alpha = 0.12^\circ$ of the beam was below the critical angle of SiO₂. For three of the samples (PF-RUB on SAM and native silicon in late stage, and F₁₄-RUB on native silicon) additional reciprocal space maps were recorded (Fig. 6.7).

Figs. 6.8 and 6.9 show grazing incidence X-ray diffraction (GIXD) data for each of the two PF-RUB and F₁₄-RUB thin films in comparison with calculated spectra. The two samples of each PF-RUB and F₁₄-RUB that differ in their respective substrate (native silicon dioxide (late stage) and SAM deposited on native silicon dioxide) show pro-

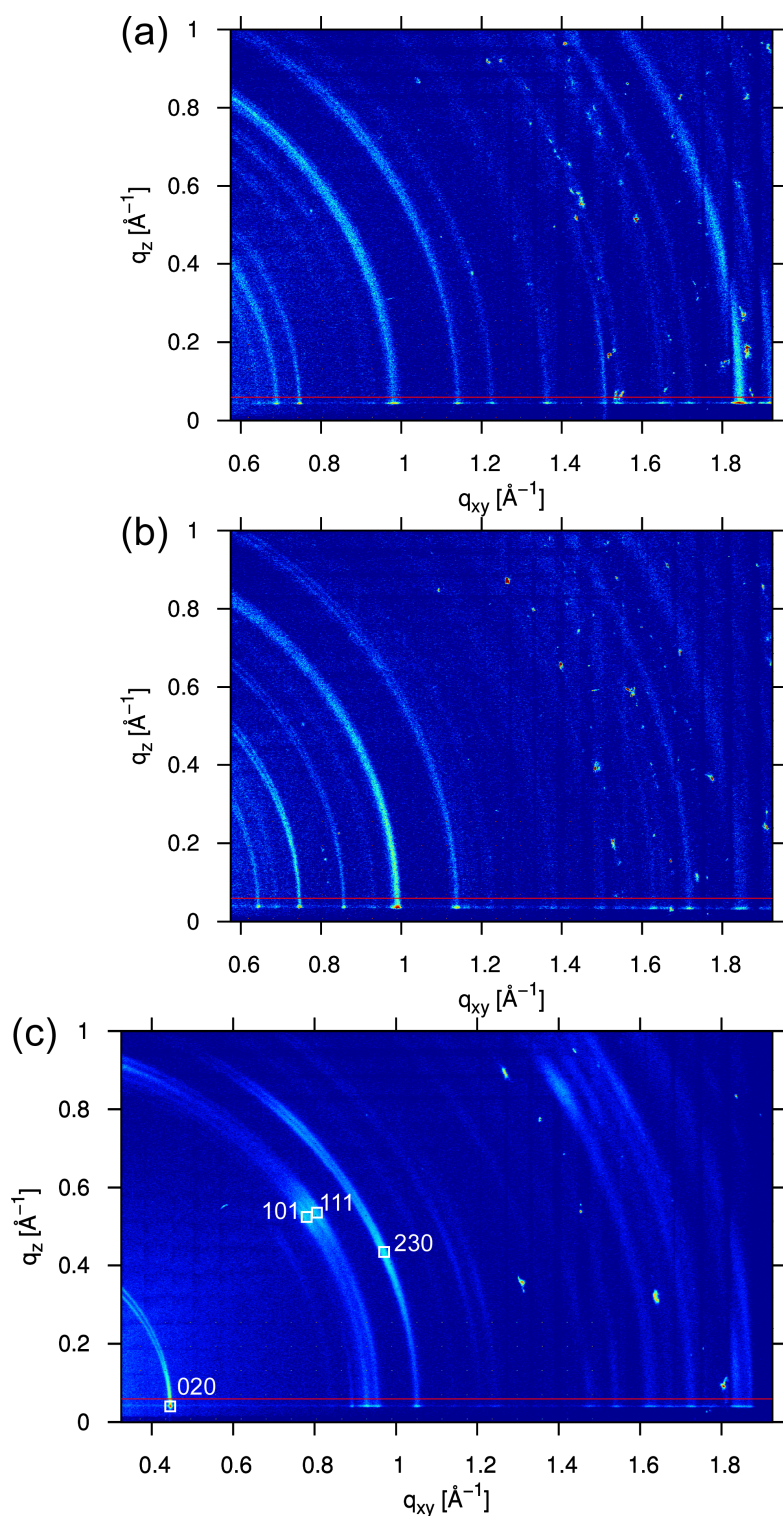


Figure 6.7: Reciprocal space maps of (a) the PF-RUB thin deposited on native silicon (late stage), (b) the PF-RUB thin deposited on SAM, and (c) the F_{14} -RUB thin deposited on native silicon obtained in the GIXD regime. The diffraction pattern of all samples show concentric rings that evidence the polycrystalline structure of the thin films. The rings observed in the reciprocal spacemaps of the PF-RUB thin films (a) and (b) do not vary notably in intensity, which indicates no distinguished preferential orientation of the molecules on both substrates. This is different for the map of the F_{14} -RUB thin film on SiO_2 (c) that shows maxima (white boxes) within its respective ring patterns that rely on a preferred orientation of the molecules. The red line at $q_z \approx 0.06 \text{ \AA}^{-1}$ in each panel denotes the position of the GIXD scans provided in Figs. 6.8 and 6.9. Horizontal and vertical stripes in the pictures at particularly larger q values originate from the compilation of several acquisition windows with different background and have no physical meaning.

	F₁₄-RUB (sublimation)	PF-RUB (solution)	PF-RUB (sublimation)
Lattice system	orthorhombic	monoclinic	monoclinic
Space group	<i>Pnna</i>	<i>P2₁/c</i> , $\beta = 90.408(8)^\circ$	<i>P2₁/c</i> , $\beta = 90.581(3)^\circ$
Molecules / unit cell	4	2	4
<i>a</i> [Å]	15.528(2)	8.9017(17)	16.635(2)
<i>b</i> [Å] (173 K)	28.088(4)	10.527(2)	11.1334(14)
<i>c</i> [Å]	7.3938(11)	17.992(4)	19.245(3)
Unit cell volume [Å ³]	3224.8(8)	1685.9(6)	3564.0(8)
<i>a</i> [Å]	15.436 (-0.6%)	9.099 (+2.2%)	16.797 (+1.0%)
<i>b</i> [Å] (RT)	28.207 (+0.4%)	10.661 (+1.3%)	11.255 (+1.1%)
<i>c</i> [Å]	7.542 (+2.0%)	18.102 (+0.6%)	19.289 (+0.2%)
Unit cell volume [Å ³]	3283.8 (+1.8%)	1756.0 (+4.2%)	3646.6 (+2.3%)

Table 6.1: Overview over the unit cell properties of F₁₄-RUB and PF-RUB that were introduced in Sec. 6.1. While the values supplied by Y. Sakamoto and T. Suzuki apply for unit cells at 173 K, slightly modified axial distances *a*, *b*, and *c* (fixed angles) appear to be more adequate when comparing to the GIXD spectra of the thin films obtained at RT. Percentage values in parenthesis designate the relative change of the respective axial distance at RT with reference to the unit cell size at 173 K.

nounced diffraction peaks in q_{xy} direction indicating a (poly)crystalline structure of the film, which is confirmed by the reciprocal space maps. The respective peak positions are identical for the two films of each PF-RUB and F₁₄-RUB, however, the respective peak intensities vary between the films which probably refers to the different texture of the films on those substrates.

The experimental GIXD spectra are shown in comparison with calculated spectra that are derived from the unit cells of PF-RUB and F₁₄-RUB provided in Sec. 6.1. However, since the GIXD spectra of the thin films were acquired at RT but the original unit cells presented in Sec. 6.1 correspond to crystallites measured at $T = 173$ K, the unit cell parameters that apply for the thin films may differ slightly from the values introduced in Sec. 6.1. In order to account for this deformation of the unit cells the axial distances *a*, *b*, and *c* were modified while the other parameters of the unit cell were left constant (Tab. 6.1).

In the case of PF-RUB, two different modified unit cells (from sublimation and from solution) are considered, whose calculated spectra are shown in Fig. 6.8 (purple and yellow, respectively). Using the parameters α_i and β_i that determine the ratio of planar

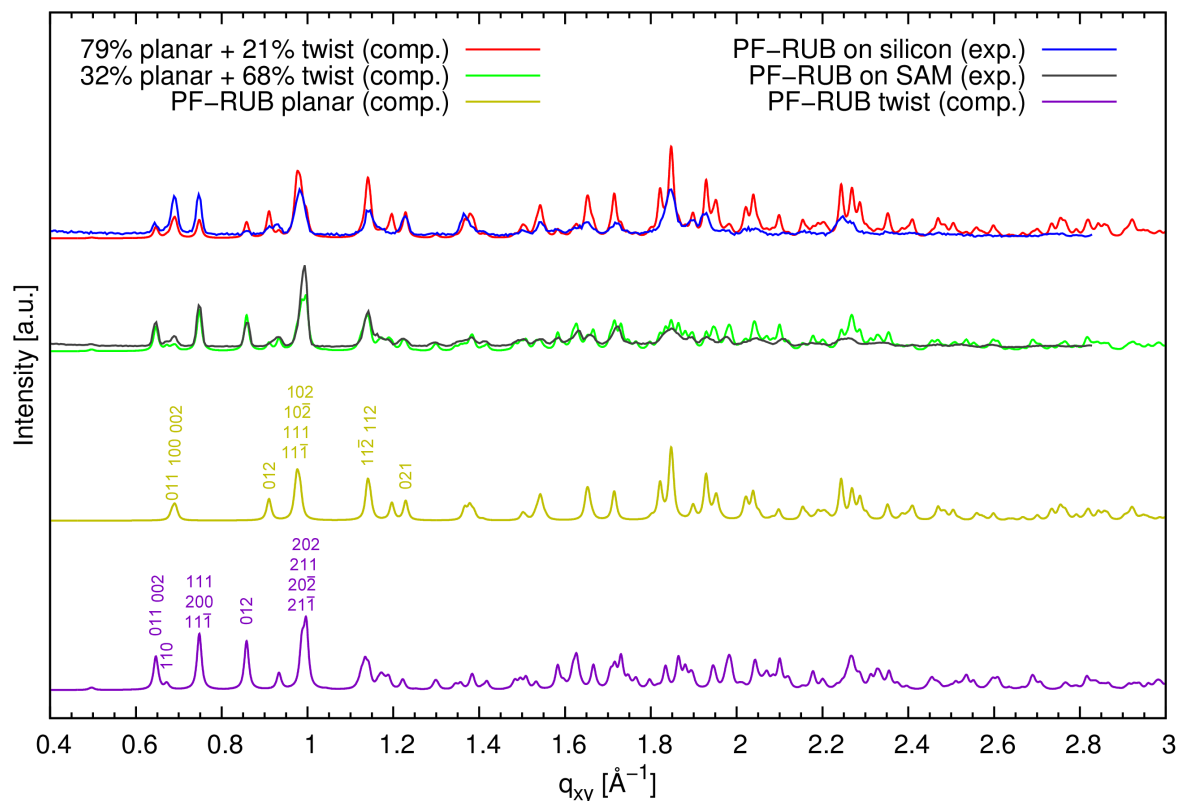


Figure 6.8: Grazing incidence X-ray diffraction (GIXD) data of the PF-RUB thin films deposited on a silicon wafer with native oxide layer (blue) and on SAM (gray) in comparison with computed spectra. The computed spectrum in yellow (purple) was obtained from the unit cell formed by PF-RUB molecules from solution (sublimation), see Sec. 6.1. Red and green spectra represent a superposition of the computed spectra using the ratio of planar to twisted molecules, which was found with vibrational spectroscopy (Sec. 5.2.2) for the thin films on silicon (late stage) and on SAM, respectively. Since GIXD was obtained at RT, the length axes of the respective unit cells were slightly modified (see text).

to twisted molecules (found in Sec. 5.2.2) and the fact that molecules in the unit cell from solution (from sublimation) correspond to the planar (twisted) conformation, calculated spectra (respective red and green) with a ratio of planar to twisted molecules can be modeled in a way that they correspond to the ratio of the spectra of the thin films on native silicon in late stage (blue) and on SAM (gray). A comparison of the modeled spectrum with 79 % (32 %) planar and 21 % (68 %) twisted molecules that are

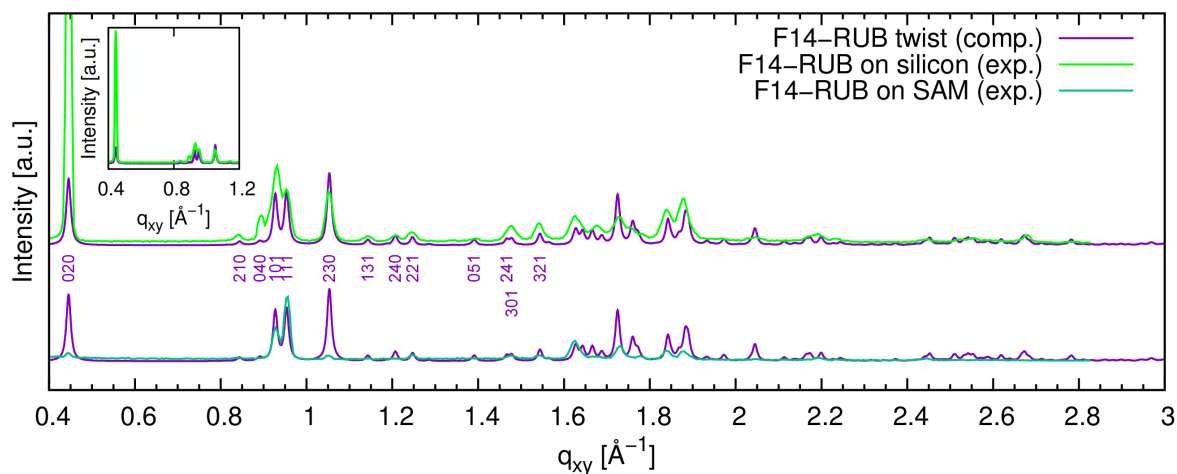


Figure 6.9: Grazing incidence X-ray diffraction (GIXD) scans of the F₁₄-RUB thin films deposited on a silicon wafer with native oxide layer (green) and on SAM (cyan) in comparison with a computed spectrum. The computed spectrum in purple was obtained from the unit cell formed by F₁₄-RUB molecules from sublimation, see Sec. 6.1. Since GIXD was obtained at RT, the length axes of the unit cell was slightly modified (see text).

featured by the red (green) line shows a satisfying agreement with the experimental spectrum of the thin film on native silicon in late stage (on SAM) with the blue (gray) line. This finding corroborates the results found in Sec. 5.2.2. The peak intensities in the reciprocal space maps of the two films (Fig. 6.7(a) and (b)) vary for both films only very weakly with changing orientation, which indicates that the molecules in both films have essentially no preferential orientation.

The new parameters suggested in Tab. 6.1 for F₁₄-RUB lead to a satisfying agreement of the modeled unit cell with the experimental GIXD peaks (Fig. 6.9), so it can be concluded that this modified unit cell yields a rough estimate of the real unit cells. The difference in the peak intensity between the GIXD peaks of the two films can be attributed to a variation in orientation and/or occurrence of the particular unit cells within the thin film structures induced by the substrate. The reciprocal space map (Fig. 6.7(c)) of the F₁₄-RUB thin film on native silicon indicates a preferential orientation of the molecules in the sample. While the (020) reflex is most pronounced for $q_z^{020} = 0 \text{ \AA}^{-1}$, we find a maximum of the (101) and (111) reflex at $q_z^{101} = 0.53 \text{ \AA}^{-1}$ and $q_z^{111} = 0.54 \text{ \AA}^{-1}$, and at $q_{xy}^{101} = 0.78 \text{ \AA}^{-1}$ and $q_{xy}^{111} = 0.80 \text{ \AA}^{-1}$, respectively. From this, we deduce a preferred alignment of the F₁₄-RUB molecules with their backbone inclined

Compound/ substrate	Peak position [Å ⁻¹]	FWHM [Å ⁻¹]	$d_{\text{coh}, }$ [nm]	Peak assignment to molecular conformation
PF-RUB/SiO ₂	0.747	0.0143	41.3	twisted
	0.690	0.0160	36.9	planar
PF-RUB/SAM	0.747	0.0125	47.2	twisted
	0.690	0.0120	49.2	planar
F ₁₄ -RUB/SiO ₂	0.445	0.0132	44.72	twisted
F ₁₄ -RUB/SAM	0.445	0.0126	46.9	twisted

Table 6.2: Analysis of the average in-plane diameter of crystallite grains consisting of molecules with planar and twisted conformation in the thin films of PF-RUB and F₁₄-RUB on native silicon (SiO₂) and on SAM, based on the GIXD data. Note that the values evaluated are a rough estimate providing a lower limit of the average in-plane grain size.

under an angle of roughly 35° against the surface, which is remarkably similar to the molecular arrangement observed on highly ordered metal surfaces using photoelectron spectroscopy (PES), see Sec. 4.3. The orientation is different for the thin film on the SAM (no reciprocal spacemap provided), which is indicated by a difference in the relative peak intensities in the GIXD scan (Fig. 6.9). The (020) peak, for instance, is for the thin film on the SAM much less pronounced in comparison to the other peaks than for the thin film on native silicon.

In order to obtain a rough estimate for the in-plane coherent crystallite size $d_{\text{coh},||}$ within the thin films of PF-RUB and F₁₄-RUB, selected peaks of the GIXD data provided in Figs. 6.8 and 6.9 were analyzed using the Scherrer formula [269,270]

$$d_{\text{coh},||} = \frac{2\pi K}{\text{FWHM}}, \quad (6.1)$$

where FWHM denotes the full width half maximum of the peaks and $K = 0.94$ is Scherrer's constant for spherically shaped grains. The resulting in-plane grain sizes are listed in Tab. 6.2. The found crystallite grain sizes are much smaller than the particularly for PF-RUB discovered areas (Sec. 5.2.4) with identical molecular conformation using Raman imaging. Note, however, that the values listed in Tab. 6.2 can yield merely a lower limit of the real island size and instrumental factors were not considered. These findings indicate that the regions of identical molecular conformation found in Sec. 5.2.4 most likely are strongly fragmented into smaller crystallite subunits.

6.4 Concluding remarks

Dewetting of RUB thin films is a well-known phenomenon, which is facilitated by the three-dimensional geometry of the molecule [88, 264]. While thin films of RUB are usually amorphous [195] and contain a majority of energetically favored twisted molecules [127], RUB molecules in crystals nevertheless adopt a planar conformation due to a more efficient packing in the crystalline phase [88, 146, 239, 249]. This can be different for RUB derivatives, where crystallization of substituted RUB molecules with twisted molecular backbone has been observed recently [43, 44]. It has been shown that annealing of rubrene thin films on SiO₂ [113, 194] or film growth on organics [258, 260, 261] can help in parts to overcome the energy barrier needed for a reorientation of the RUB molecules and stabilize the film by an increase in the degree of crystallization [249].

The PF-RUB and F₁₄-RUB thin films deposited on native SiO₂ are disordered and very smooth directly after growth and nearly all PF-RUB molecules exhibit a twisted backbone (see Chap. 5). Within several hours after growth, we observe a dewetting of the films, the films roughen and a large number of the PF-RUB molecules change their conformation to a planar backbone (see Chap. 5). In fact, the relatively low evaporation temperature of particularly PF-RUB molecules from our Knudsen cell in comparison to RUB suggests that a reorientation of the PF-RUB molecules in the thin film is promoted already at RT without further annealing. However, directly after growth, the PF-RUB thin film on SAM already contains both conformations of the molecule (see Chap. 5) forming stable clusters on a micrometer scale. Obviously, the SAM leads to a modification in the surface energy which enhances the diffusion of the PF-RUB molecules so that stable crystallite nuclei can be formed.

Grazing incidence X-ray diffraction (GIXD) measurements of the two PF-RUB and the two F₁₄-RUB thin films both on SiO₂ in late stage and on SAM (compare Chap. 5) suggest a polycrystalline structure of the thin films. This indicates that the driving force behind the planarization of the PF-RUB molecules occurring in the thin film on SiO₂ is most likely governed by an energy gain due to a more efficient crystal packing. As we find from the analysis of reciprocal space maps, the molecules in the PF-RUB thin films do not show any preferred orientation. This is contrasted by the reciprocal space maps of the F₁₄-RUB thin films on native silicon that indicate a prevailing of molecules that are tilted by approximately 35° against the substrate. This corresponds to the arrangement observed for the same material on highly ordered metal in Sec. 4.3 using PES techniques.

CHAPTER 7

SUMMARY AND OUTLOOK

The aim of this thesis was the characterization and study of two rubrene (RUB) derivatives, namely perfluoro-5,6,11,12-tetraphenyltetracene ($C_{42}F_{28}$, PF-RUB) and 1,2,3,4-tetrafluoro-5,12-bis(2,3,4,5,6-pentafluorophenyl)-6,11-diphenyltetracene ($C_{42}F_{14}H_{14}$, F_{14} -RUB). The two compounds have a molecular structure that is very similar to RUB, but can be chemically distinguished in an essential manner from RUB due to their fluorination (Fig. 7.1). Note that the partially fluorinated F_{14} -RUB differs clearly from the two other compounds in a large dipole moment along its molecular backbone. Not at least due to their similarity to RUB, which has a high hole mobility and large exciton diffusion length, the new materials are of great interest for applications.

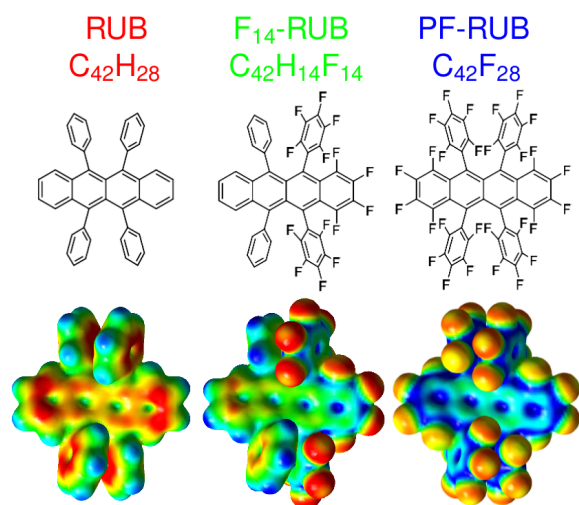


Figure 7.1: Molecular structure and molecular electrostatic potential of rubrene (RUB, left), partially fluorinated rubrene (F_{14} -RUB, middle), and perfluororubrene (PF-RUB, right) that were studied in this work. RUB is known for its high charge carrier mobility and large exciton diffusion length in crystals. The molecules show a systematic increase in fluorination, which has strong impact especially on the electronic properties of the compounds. Note that F_{14} -RUB differs from RUB and PF-RUB in its lower symmetry and associated strong dipole moment. All three compounds are red colored dyes.

7.1 Rubrene with different degree of fluorination: Molecules in solution, pristine thin films on SiO₂, and DFT computations in free space

The influence of partial and full fluorination on the rubrene molecule can be studied most efficiently in systems containing isolated molecules without or with only weak molecular interactions. Obviously, diluted molecules in solution do not interact strongly with each other. Moreover, also pristine thin films on SiO₂, *i. e.* films that were deposited only few hours prior to measurement and have not changed considerably since then, were in this work shown to be disordered. In addition to the experimental measurements, density functional theory (DFT) computations for isolated molecules of the three compounds were performed. In fact, the DFT models describe systems with properties that are very similar to the diluted molecules or molecules in pristine thin films on SiO₂.

Measurements of the optical properties, vibrational spectra, and X-ray diffraction revealed that pristine films of the three compounds on SiO₂ are essentially disordered. Thin films of the three compounds grow with a rate of few Å/min usually smooth on SiO₂ at room temperature (RT), as confirmed by X-ray reflectivity (XRR) measurements of the thin films. There have been no Bragg peaks observed directly after growth, which confirms that there is no preferred molecular orientation in the *z*-direction. This is in contrast to many other small-molecule organic semiconductors (OSCs) as *e. g.* from the acene or rylene group that evolve ordered structures much more readily. One reason for this difference is the intricate three-dimensional molecular structure of RUB, F₁₄-RUB, and PF-RUB, which is caused by the (perfluoro)phenyl wings.

As it can be shown by DFT computations in free space there are at least two stable conformations for all compounds, one with twisted and one with planar molecular backbone that correspond respectively to *D*₂ and *C*_{2*h*} for RUB and PF-RUB and to *C*₂ and *C*_{*s*} symmetry for F₁₄-RUB. In each case, the twisted conformation is energetically favored ($\Delta E = 0.17$ eV, 0.24 eV, and 0.34 eV for RUB, F₁₄-RUB, and PF-RUB, respectively). Particularly for PF-RUB, the experimental vibrational (*i. e.* infrared (IR) and Raman) peaks could be assigned to computed modes of the two isomers and it could be shown that indeed the twisted isomer prevails in solution and in pristine thin films of PF-RUB. For the partially fluorinated F₁₄-RUB an assignment to either twisted or planar conformation is more ambiguous. This can *inter alia* be traced back to its reduced molecular symmetry that permits a larger number of Raman and IR active vibrational modes than RUB or PF-RUB, which results in more intricate spectra. Nevertheless,

it was shown that F₁₄-RUB molecules in solution and pristine thin films have a very similar vibrational fingerprint, which is in analogy to PF-RUB and RUB.

All three compounds show pronounced absorption and photoluminescence (PL) spectra that are very similar in solution and thin films, and are superimposed by an almost mirrorsymmetric vibronic progression with a spacing of ~ 170 meV. The similarity of solution and thin film spectra corroborates the presence of disordered molecules in the pristine thin films. Interestingly, the optical properties in solution and pristine thin film are very similar for all materials (optical gap in absorption and PL at ~ 2.50 eV and ~ 2.10 eV, respectively). Merely the HOMO-LUMO transition of F₁₄-RUB is slightly red-shifted by ~ 0.05 eV against the other two compounds. Obviously, the optical gaps of most RUB derivatives reported so far do not deviate strongly from the optical gap of RUB [43, 47, 120]. This can be explained by the fact that for all these derivatives including the strongly fluorinated compounds examined in this work, the majority of the electron density is located at the backbone of the molecule and not at the phenyl wings, which are often substituted. This is true for both the HOMO as well as the LUMO. Note, however, that the optical band gap of small-molecule OSCs can indeed become modified upon (per)fluorination. For instance, the optical band gaps of the related compounds pentacene and tetracene [137] become smaller upon perfluorination. In contrast to the DFT computations, both solution (in Cl₂CH₂) and disordered pristine thin film spectra of the three materials are influenced by the dielectric function of the solvent. In the case of the thin films, the solvent consists of the material itself. Nevertheless, the DFT computations of the free molecules reproduce the optical properties qualitatively well and, moreover, under the consideration of the dielectric function of the solvent, they can also be quantitatively well understood.

As it turns out from real-time absorption measurements of thin films of the three materials that were exposed to air, the fluorinated compounds are much more stable against oxidation than RUB. In particular for PF-RUB no measurable influences by oxygen could be observed at all. This can be explained by the ionization potential (IP) of the compounds that increases with the degree of fluorination, which is caused by the very large electronegativity of the fluorine. Moreover, the newly synthesized compounds F₁₄-RUB and PF-RUB are also more stable against oxidation than most known RUB derivatives. Using cyclic voltammetry (CV) in solution and ultra-violet photoelectron spectroscopy (UPS) in pristine thin films, the ionization (and with CV also the reduction) potential (IP) of the three materials was determined experimentally (5.4 eV (5.2 eV) to 7.0 eV (6.7 eV) from RUB to PF-RUB in solution (thin films on Au(111)). Under consideration of the polarization energies caused by the solvent, DFT computations basing on the anion and cation of the compounds were able to reproduce and

explain the values of the ionization (5.1 eV to 6.9 eV from RUB to PF-RUB) and reduction (2.1 eV to 3.9 eV from RUB to PF-RUB) potential well. Good knowledge of the IP and hole injection barrier (HIB) of an organic compounds plays a crucial role for constructing devices of the respective material.

7.2 Ordered structures of fluorinated rubrene molecules in thin films

Beside the characterization of isolated fluorinated rubrene, condensed molecules in thin films or in even crystalline form are particularly relevant for applications. However, directly after deposition, the molecular order in thin films grown with OMBD techniques is often not yet fully equilibrated.

This is of particular relevance for RUB, which is known for its complicated growth behavior including dewetting that depends strongly on different growth parameters and choice of the substrate. As it has turned out, thin films of the fluorinated compounds seem to dewet even more readily than RUB, yet they have lower sublimation temperatures (the temperature sensor attached to the crucible in our system reports $\sim 155^\circ\text{C}$, $\sim 135^\circ\text{C}$, and $\sim 96^\circ\text{C}$ for evaporation of RUB, F_{14} -RUB, and PF-RUB, respectively). In particular the evaporation temperatures found for PF-RUB are remarkably low in comparison to most other small-molecule OSCs of similar size, which often sublime at temperatures that are by $\sim 100^\circ\text{C}$ larger. The timescale of the dewetting process of the thin film on SiO_2 could be observed by X-ray reflectivity (XRR) and vibrational spectroscopy. XRR scans show a roughening of the primarily smooth (and disordered) thin film and we observe particularly for F_{14} -RUB the growth of a Bragg peak. This indicates a molecular order in the z -direction after several days of dewetting. Using IR and Raman spectroscopy it has turned out that within one day PF-RUB molecules undergo a transition from their original conformation with twisted backbone to a conformation with planar backbone. Minor postgrowth reordering of thin films is indeed known for many OSCs. However, most thin films of OSCs remain fairly stable after deposition and such strong dewetting behavior as it is observed for RUB and its derivatives, including a change in molecular conformation as in the case of PF-RUB, is unusual.

A crystalline arrangement can be the preferred structure particularly for applications, which is not always easy to obtain. One reason for the complex nucleation process of the (fluorinated) rubrenes is their intricate and bulky molecular structure, but also

the chirality in the twisted conformation plays an important role. For all three compounds, the twisted isomer is energetically favored, but RUB nevertheless crystallizes with a planar backbone. This seems to be different for most known RUB derivatives that form crystalline phases with twisted backbones as it is also the case for the fluorinated rubrenes. However, for PF-RUB also a crystal structure with planar molecular backbone has been observed. The chirality of the molecules makes assembling the twisted molecules into a single crystalline structure more difficult since crystallites of each of the two inequivalent twisted molecules can start to nucleate. This is in contrast to most other small molecular OSCs that are often rod-shaped (e. g. acenes, rylenes) or discoidal (e. g. phtalocyanines). Only in few cases small-molecule OSCs have a three-dimensional structure (the most prominent example is the spherical C_{60} (fullerene)) but are not necessarily able to adopt a chiral conformation.

The polycrystallinity of the thin films of both fluorinated rubrenes was confirmed by grazing incidence X-ray diffraction (GIXD) measurements that were performed several weeks after growth. Particularly in the case of PF-RUB, the GIXD data points towards at least two different unit cells, that most probably correspond to molecules with planar and twisted molecular backbone. While thin films of fluorinated rubrene grow disordered on SiO_2 and dewet afterwards, it could be shown in this work that the modification of the wafer with SAMs leads to more stable thin films and different growth behavior including a higher degree in crystallinity. Employing Raman imaging techniques it was possible to detect clusters of PF-RUB molecules with planar and twisted molecular backbone on a micrometer scale and investigate the unlike molecular conformation on the different substrates. GIXD space maps evidence a polycrystalline structure of the investigated thin films of PF-RUB and F_{14} -RUB.

Importantly, the partially fluorinated F_{14} -RUB differs fundamentally from the two other compounds in its lower symmetry and associated dipole moment, which is oriented along its molecular axis and was computed in this work using DFT to $\sim 4.2D$. In fact, small-molecules OSCs with associated dipole moment have been synthesized before e. g. in form of nonplanar phtalocyanines with properly chosen center occupation. However, such a strong dipole moment as it occurs in F_{14} -RUB and that, moreover, is located on a single molecule, is seldom. While its effect is small in disordered molecular systems (solution, pristine thin film), it can have consequences in thin films with molecular order. Interestingly, using photoelectron spectroscopy (PES) it has turned out that the partially fluorinated compound F_{14} -RUB shows evidence for a uniform molecular orientation in the second deposited layer of thin films deposited on highly-oriented metal substrates (Au(111) and Ag(111)). As we observe, it has strong influence on the work function and the HOMO level. This is of very high interest for applica-

tions since the employment of strong molecular dipole moments allow for effective modification of the work function at interfaces.

7.3 Application potential of fluorinated rubrene and outlook

RUB is one of the most investigated OSCs so far and has a very high application potential in optoelectronic devices. Nevertheless, besides of a large number of advantageous properties, like a very high hole mobility and exciton diffusion length in crystals, there are reasons why a modification of some of its properties can be desired. The materials F₁₄-RUB and PF-RUB have a very similar molecular structure, but behave chemically very different from RUB. Although this study provides a rather comprehensive examination of the two compounds, there are still open questions.

The identical molecular geometry of the fluorinated molecules and the RUB molecule should allow F₁₄-RUB and PF-RUB to adsorb well onto crystals or thin films of RUB. Thus, they can be used as an interface to modify e. g. the surface of RUB crystals in order to align the electronic properties with a contact material. On the other hand, the fluorinated rubrene molecules are ideally suited for doping RUB thin films or single crystals, which offers possibly a way to continuously tune the electronic properties of the RUB bulk. Also, this may offer a way to modify the charge carrier mobility. However, it is not *a priori* clear whether the three compounds intermix or phase separate. There is a wide field still to be explored of potential applications for the use of F₁₄-RUB and PF-RUB, also in combination with other organic materials. This outlook can discuss only some aspects that are of relevance for possible applications of fluorinated rubrene.

1. Fluorinated rubrene can be used in special cases as 'improved' RUB. This applies in particular for situations, in which a material with very similar properties to RUB but at the same time enhanced in some other respect is needed. However, despite of a large number of similarities to RUB (*inter alia* optical properties and molecular geometry), it must be pointed out that there are serious differences between RUB, F₁₄-RUB, and PF-RUB.
2. Heterostructures with fluorinated rubrene: It is a key point for the application in organic devices to combine good charge carrier properties of a material with a

suitable energy level alignment at its interface [271,272]. Manipulating the semiconductor interface in a controlled manner by orienting the molecular dipoles – as possible with F₁₄-RUB – is of very high interest [212,233,273,274].

3. Molecular mixtures: For some applications, a combination of fluorinated and unsubstituted derivative of a compound can be the right choice in order to achieve particular functionalities. This is especially favored e. g. in the functional layer of organic photovoltaics (OPVs). Sterically similar materials favor good intermixing, but the fluorinated materials can also, in principle, be used in combination with any other organic material [52].

One of the obvious advantages of the fluorinated rubrenes over RUB is their enhanced stability against oxygen. In applications that require a material with optical and sterical properties similar to RUB, but with enhanced stability against oxidation, (per)fluorinated rubrene could be a suitable solution. Beside having nearly identical optical properties, though a very different electronic structure, the fluorinated materials are sterically very similar to RUB.

Despite many analogies between RUB and the fluorinated derivatives studied in this work, there are significant differences between the three materials that make a naive exchange of one material by the other impossible. One of the big advantages of RUB over other OSCs is its high hole mobility in crystals. However, the charge carrier properties of F₁₄-RUB and PF-RUB are hard to predict *a priori* and are yet to be determined experimentally. In fact, the unit cells found for F₁₄-RUB and PF-RUB up to now do not point towards the same π -stacking behavior as occurs in the orthorhombic phase of RUB and which is essentially responsible for the high mobility values in the case of RUB crystals.

At present the synthesis of fluorinated rubrenes is a very complex and expensive process. Hence, it is to expect that in the near future the incorporation of large amounts of (per)fluorinated OSCs into devices could raise their costs due to both the production and the recycling of the raw material. Note that for some applications that are exposed to elevated temperatures, as is not unusual for OPVs, the low sublimation temperature particularly of the fully fluorinated PF-RUB might be a challenge.

An important and in fact very advantageous difference between all three compounds is certainly their different IP. It is a key point for application in organic devices to combine good charge carrier properties of a material with a suitable energy level alignment at its interface. In this respect, both of the fluorinated rubrenes represent alternative materials to RUB opening a way to better adapted device architectures. Due to their

steric similarity, the fluorinated rubrenes can be employed in particular in combination with RUB but also with other OSCs available. To this end, employing of fluorinated materials opens new choices for contact materials.

The fluorinated rubrenes can also be applied at the interface of heterostructures between arbitrary organic materials, as has been done with RUB in OPVs [101] or OLEDs [102]. Importantly, this very general field of application is of high relevance for partially fluorinated F_{14} -RUB since it has a large dipole moment along its backbone, thus allowing for effective modification of the interface. In fact, this property receives special attention, because there are not many small-molecule OSCs with a comparably strong dipole moment that could be synthesized. As it has been shown in this work, F_{14} -RUB molecules deposited on highly ordered noble metals align themselves in the second molecular layer with a fraction of their dipole moment along the surface normal. More detailed knowledge on the molecular orientation on different substrates including organic material is needed for a better understanding and exploitation of the dipole moment in functional materials. In this context, measurements involving scanning tunneling microscopy (STM) as performed for RUB [68] or comparable techniques could be helpful and shed more light on the orientation and order of F_{14} -RUB molecules at surfaces.

Another topic that has gained increased attention during the recent past is the blending of OSCs [52]. The investigation of bulk heterojunctions is a wide field that plays an important role e. g. for the active layer in OPVs. Herein, the mixture of hydrocarbons with their (per)fluorinated counterpart is of particular interest. It is not *a priori* clear if e. g. PF-RUB and RUB mix on a molecular level, or if phase separation occurs. Other small-molecule OSCs were shown to form indeed equimolar blends with their sterically compatible perfluorinated counterpart as for instance pentacene and perfluoropentacene resulting in an alternating molecular order. However, phase separation of RUB and PF-RUB could be promoted by the intricate molecular structure and the different unit cells of the pure materials. Blending fluorinated rubrenes with RUB or other organics is a wide spread field that remains to be explored. Intermixing RUB with e. g. PF-RUB on a molecular level could open up the possibility of continuous tuning of the electronic properties of RUB crystals by including foreign PF-RUB molecules.

APPENDIX

A Extended cyclic voltammograms

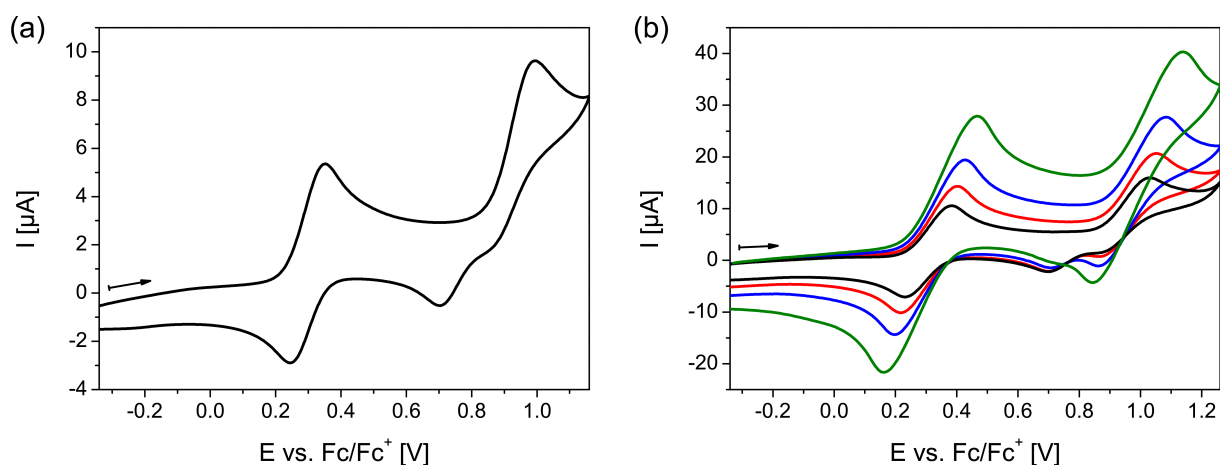


Figure 2: Anodic cyclic voltammograms of RUB ($c = 2.6 \text{ mM}$) in $0.1 \text{ M NBu}_4\text{PF}_6/\text{CH}_2\text{Cl}_2$ at Pt recorded with different scan rates in a potential window of -0.34 to $+1.26 \text{ V}$. (a) black line = 100 mV s^{-1} . (b) black line = 500 mV s^{-1} , red line = 1000 mV s^{-1} , blue line = 2000 mV s^{-1} and green line = 5000 mV s^{-1} . The voltammograms are not background corrected.

At potentials above 0.5 V , a second chemically irreversible oxidation wave located at around $+1.0 \text{ V}$ is observed for RUB (Fig. 2(a)). In the backward scan a weak reduction signal at $\sim +0.7 \text{ V}$ appears. We attribute this peak to the reduction of products formed in follow up reactions that are coupled to the second oxidation. At higher scan rates ($v \geq 1000 \text{ mV s}^{-1}$) the peak current of the signal at $+0.7 \text{ V}$ decreases and the second

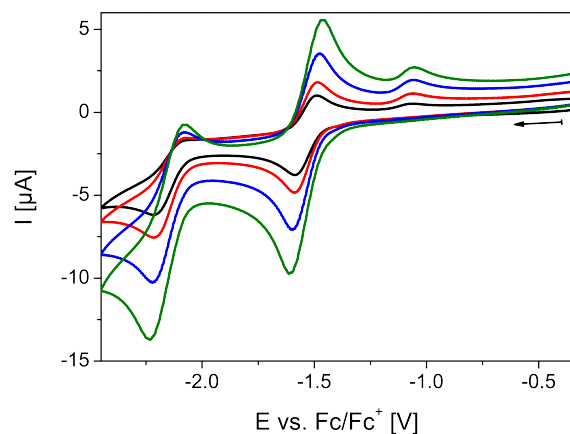


Figure 3: Cathodic cyclic voltammograms of F_{14} -RUB ($c = 1.4 \text{ mM}$) in $0.1 \text{ M NBu}_4\text{PF}_6/\text{CH}_2\text{Cl}_2$ at Pt recorded in a potential window of -0.35 to -2.45 V with different scan rates. Black line = 100 mV s^{-1} , red line = 200 mV s^{-1} , blue line = 500 mV s^{-1} and green line = 1000 mV s^{-1} . The voltammograms are not background corrected.

oxidation becomes chemically reversible (Fig. 2(b)). Thus, the follow up reactions seem to be slow and within the time scale of the cyclic voltammetric experiment.

For F_{14} -RUB the electron transfer reaction at -2.15 V becomes chemically reversible for scan rates $v \geq 500 \text{ mV s}^{-1}$ (Fig. 3). Nevertheless, the corresponding peak current of the re-oxidation peak in the backward scan remains low. We observe a weak oxidation wave at around -1.2 V which indicates products from follow up reactions that are coupled to the second reduction.

B Raman spectra of PF-RUB and F_{14} -RUB thin films acquired at 785 nm

Fig. 4 shows Raman spectra of thin films of F_{14} -RUB and PF-RUB (thickness 20 nm) deposited on native silicon at room temperature. Since the spectra are excited off-resonantly at 785 nm , the photoluminescence (PL) background of the spectra is less pronounced than at 633 nm and can thus be subtracted more easily. This results particularly for F_{14} -RUB in more distinct Raman spectra. For discussion of the spectra, see Chap. 5.

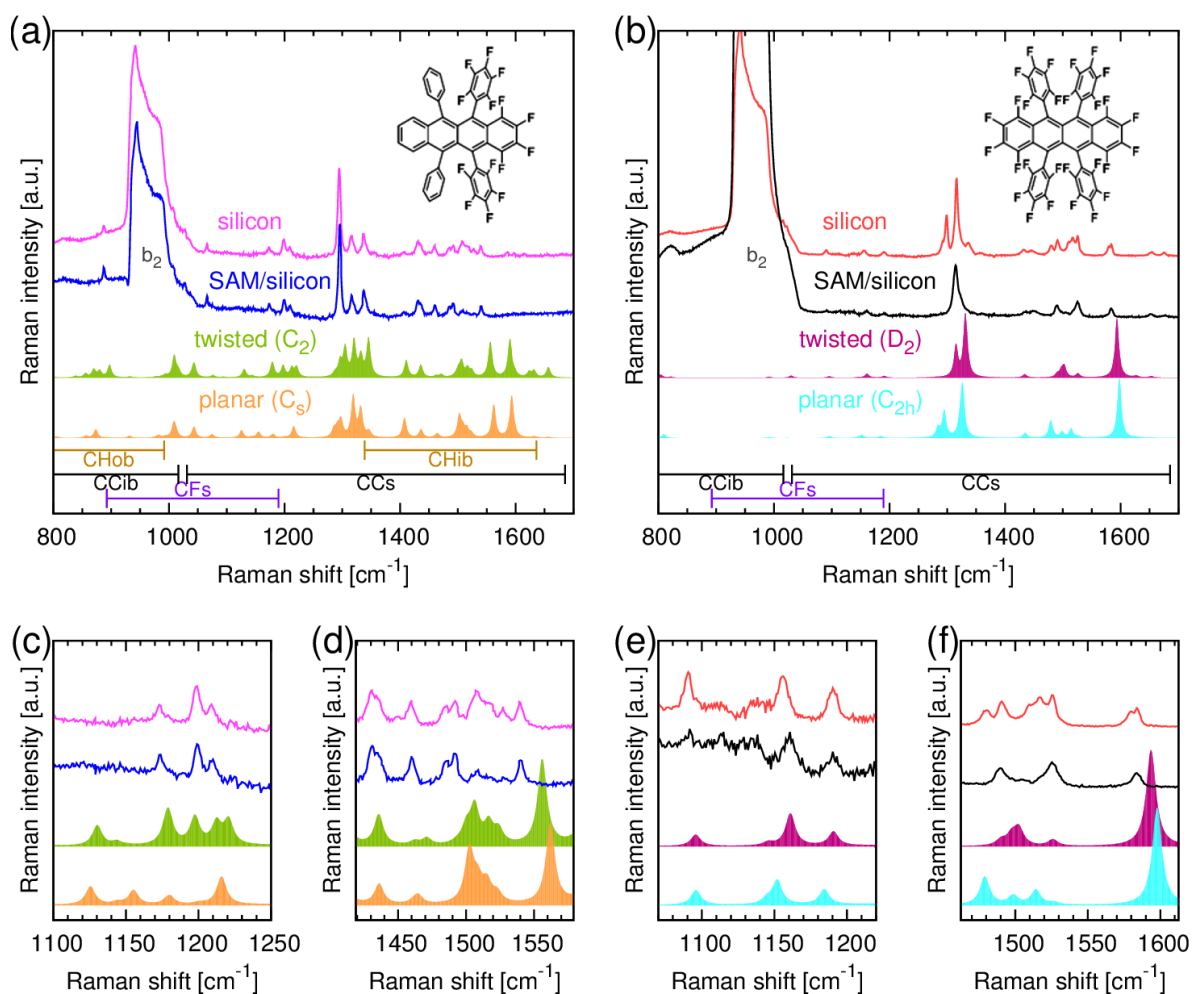


Figure 4: Experimental vibrational spectra of F_{14} -RUB (lines) ((a), (c), (d)) and PF-RUB ((b), (e), (f)), each together with the respective spectra computed by DFT (filled curves). The experimental spectra are obtained from molecules deposited on native silicon (top line) as well as on SAM/silicon (bottom line). The spectra were acquired only few hours after deposition, particularly the thin films of PF-RUB correspond to the 'pristine stage'. The theoretical spectra show Lorentzian-shaped modeled curves of the twisted (top filled curve) and planar (bottom filled curve) conformation of the molecule. (c) and (d) provide a zoom into selected regions of (a), analogously provide (e) and (f) a zoom into selected regions of (b). The samples (at 173 K) were excited at 785 nm using a Renishaw InVIA Raman spectrometer. The bars at the bottom of (a) and (b) show the regions of the type of the vibrational mode ('CCib' = C-C in-plane bending, 'CCs' = C-C stretching, 'CFs' = C-F stretching). For explanation of the spectra, see text. The spectra were acquired in cooperation with Melanie Keuper, Christoph Berthold, and Klaus Georg Nickel.

LIST OF FIGURES

1.1	Chemical structure of RUB, F ₁₄ -RUB, and PF-RUB	6
1.2	RUB, F ₁₄ -RUB, and PF-RUB diluted in CH ₂ Cl ₂	9
2.1	Real and imaginary part of the dielectric function	14
2.2	Diffraction of an electromagnetic wave at a continuous interface	16
2.3	Brewster's angle condition	17
2.4	Molecular symmetry of the RUB molecule	19
2.5	Vibrational excitation: Infrared (IR) and Raman	21
2.6	Displaced harmonic oscillator model	23
2.7	Schematic photoelectron spectrum with relevant energies.	26
3.1	Scheme for quantum chemical computation using TURBOMOLE 6.4	33
3.2	Fabrication procedure of a self assembled monolayer (SAM)	35
3.3	Knudsen cell used for evaporation of F ₁₄ -RUB and PF-RUB.	37
3.4	UHV-system used for thin film preparation.	38
3.5	Cyclic voltammetry setup.	39
3.6	Schematic of spectroscopic ellipsometry.	40
3.7	Layer model used during real-time acquisition of <i>in situ</i> ellipsometry measurements.	41
3.8	Schematic of the beam path of the confocal Raman spectrometer.	43

LIST OF FIGURES

3.9	Beam path of the FT-IR Spectrometer	44
3.10	Schematic of the A145 liquid cell from Bruker used for IR spectroscopy. .	45
3.11	Principle of photoelectron spectroscopy (PES).	46
3.12	X-ray photoelectron spectrum and ultraviolet photoelectron spectrum of Au(111) showing region of the binding energies of the molecular orbitals.	47
3.13	Principle of an atomic force microscope (AFM).	48
3.14	XRR and GIXD scattering geometry	49
4.1	PL and absorption spectra of RUB, F ₁₄ -RUB, and PF-RUB in thin films and solution	53
4.2	Molecular electrostatic potential (MEP) of RUB, F ₁₄ -RUB, and PF-RUB, mapped on the electron density surface.	56
4.3	Real time observation of the optical properties of RUB, F ₁₄ -RUB, and PF-RUB thin films using spectroscopic ellipsometry during oxidation. .	61
4.4	CV of RUB, F ₁₄ -RUB, and PF-RUB diluted in CH ₂ Cl ₂	64
4.5	Valence spectra of PF-RUB and of F ₁₄ -RUB, each on Au(111) and Ag(111).	68
4.6	Energy alignment of PF-RUB, F ₁₄ -RUB, and RUB on Au(111) and Ag(111)	70
4.7	Core-level spectra of PF-RUB and F ₁₄ -RUB, each on Au(111) and Ag(111).	72
4.8	Molecular stoichiometry of F ₁₄ -RUB and PF-RUB studied by XPS	73
4.9	Work function, HIB and core-levels depending on film thickness	74
4.10	Proposed growth model for F ₁₄ -RUB on Au(111) and Ag(111).	76
5.1	Computed IR spectra of RUB, F ₁₄ -RUB, and PF-RUB	82
5.2	Computed Raman spectra of RUB, F ₁₄ -RUB, and PF-RUB	83
5.3	IR and Raman (633 nm) spectra of PF-RUB in solution and thin films on silicon ('pristine' and 'late stage') and on SAM.	86
5.4	Decomposition of IR and Raman spectra of PF-RUB of thin films on silicon in 'late stage' and on SAM into twisted and planar isomer.	89
5.5	Raman imaging of PF-RUB showing regions of molecules with planar and twisted molecular backbone.	94
5.6	IR and Raman (633 nm) spectra of F ₁₄ -RUB in solution and thin films on silicon and on SAM.	96

6.1	Unit cell of F ₁₄ -RUB (obtained <i>via</i> sublimation) containing four inequivalent molecules with twisted backbone.	103
6.2	Unit cell of PF-RUB (obtained <i>via</i> solution) containing two inequivalent molecules with nearly planar backbone.	104
6.3	Unit cell of PF-RUB (obtained <i>via</i> sublimation) containing four inequivalent molecules with twisted backbone.	105
6.4	Light microscopy picture of thin films of F ₁₄ -RUB (20 nm) and PF-RUB (55 nm) one month after deposition on a silicon wafer.	107
6.5	X-ray reflectivity (XRR) scans of thin films of F ₁₄ -RUB and PF-RUB.	108
6.6	AFM picture of PF-RUB and F ₁₄ -RUB deposited on silicon in the and on SAM.	109
6.7	Reciprocal space maps of PF-RUB and F ₁₄ -RUB thin films in the GIXD regime	111
6.8	GIXD scans of PF-RUB thin films on silicon and on SAM	113
6.9	GIXD scans of F ₁₄ -RUB thin films on silicon and on SAM	114
7.1	Molecular structure of RUB, F ₁₄ -RUB, and PF-RUB.	117
2	Extended Cyclic voltammetry spectra of RUB with irreversible oxidation.	125
3	Extended Cyclic voltammetry spectra of F ₁₄ -RUB with irreversible reduction.	126
4	Raman spectra of F ₁₄ -RUB and PF-RUB in thin films on silicon and on SAM excited at 785 nm.	127

LIST OF TABLES

1.1	Evaporation temperatures of RUB, F ₁₄ -RUB, and PF-RUB from the Knudsen cell	9
2.1	Possible point groups of the RUB, F ₁₄ -RUB, and PF-RUB molecules . . .	20
4.1	Fitted values of RUB, F ₁₄ -RUB, and PF-RUB absorption and emission spectra of the thin films and solution.	55
4.2	Half wave potential values derived from cyclic voltammetric experiments in comparison with DFT computed values.	65
5.1	Assignment of the vibrational modes of RUB, F ₁₄ -RUB, and PF-RUB. . .	81
5.2	Detailed overview over the most prominent experimentally observed IR and Raman peaks of the basis spectra $A(\tilde{\nu})$ in association with the computed IR and Raman modes for the C_{2h} geometry of the free PF-RUB molecule.	91
5.3	Detailed overview over the most prominent experimentally observed IR and Raman peaks of the basis spectrum $B(\tilde{\nu})$ in association with the computed IR and Raman modes for the D_2 geometry of the free PF-RUB molecule.	92
5.4	Detailed overview over the most prominent experimentally observed IR and Raman peaks in association with the computed modes for the two isomers (C_s and C_2 geometries) considered for the free F ₁₄ -RUB molecule.	98

LIST OF TABLES

6.1	Unit cell parameters of F ₁₄ -RUB and PF-RUB at 173 K and estimated values for thin films at RT.	112
6.2	Average in-plane diameters of grains with planar and twisted molecular backbone in PF-RUB and F ₁₄ -RUB thin films	115

LIST OF ABBREVIATIONS

Device structure

BHJ	Bulk heterojunction
CCD	Charge-coupled device
OFET	Organic field-effect transistor
LCD	Liquid crystal display
OLED	Organic light emitting device
OPV	Organic photovoltaic
OTFT	Organic thin film transistor

Experimental

AFM	Atomic force microscopy
CV	Cyclic voltammetry
EDC	Energy distribution curve
FT-IR	Fourier-transform infrared
GIXD	Grazing incidence X-ray diffraction
HV	High vacuum
OMBD	Organic molecular beam deposition
PES	Photoelectron spectroscopy
PL	Photoluminescence
QCM	Quartz crystal microbalance
RT	Room temperature
SECO	Secondary electron cutoff
STM	Scanning tunneling microscopy
UHV	Ultrahigh vacuum
UPS	Ultraviolet photoelectron spectroscopy
XPS	X-ray photoelectron spectroscopy
XRR	X-ray reflectivity

LIST OF ABBREVIATIONS

Materials

Alq ₃	Tris(8-hydroxyquinolino)aluminium	C ₂₇ H ₁₈ AlN ₃ O ₃
α-NPD	4,4'-bis[N-(1-naphthyl)-N-phenylamion]biphenyl	C ₄₄ H ₃₂ N ₂
F ₁₄ -RUB	1,2,3,4-Tetrafluoro-5,12-bis(2,3,4,5,6-pentafluorophenyl)-6,11-di-phenyltetracene	C ₄₂ F ₁₄ H ₁₄
ITO	Indium tin oxide	
OSC	Organic semiconductor	
OTS	Octadecyltrichlorosilane	C ₁₈ H ₃₇ Cl ₃ Si
PF-RUB	Perfluororubrene	C ₄₂ F ₂₈
	(perfluoro-5,6,11,12-tetraphenyltetracene)	C ₄₂ F ₂₈
RUB	Rubrene (5,6,11,12-tetraphenyltetracene)	C ₄₂ H ₂₈
SAM	Self-assembled monolayer	
TCNQ	Tetracyanoquinodimethane	C ₁₂ H ₄ N ₄

Energies/potentials

EA	Electron affinity
HIB	Hole injection barrier
IP	Ionization potential
MEP	Molecular electrostatic potential
VL	Vacuum level

Theory

B3LYP	Becke, three parameter, Lee-Yang-Parr
DFT	Density functional theory
GGA	Generalized gradient approximation
GTO	Gaussian-type orbital
HF	Hartree Fock
HOMO	Highest occupied molecular orbital
KS	Kohn-Sham
LDA	Local density approximation
LUMO	Lowest unoccupied molecular orbital
SCF	Self-consistent field
STO	Slater-type orbital
TD-DFT	Time dependent density functional theory
TZVP	Triple-zeta valence plus polarization

Miscellaneous

IR	Infrared
FWHM	Full width at half maximum
UV	Ultraviolet

BIBLIOGRAPHY

- [1] M. Pope and C. E. Swenberg, *Electronic Processes in Organic Crystals and Polymers* (1999), Oxford University Press (New York).
- [2] J. E. Greene, *Appl. Phys. Rev.* **2**, 011101 (2015): *Tracing the 4000 Year History of Organic Thin Films: From Monolayers on Liquids to Multilayers on Solids.*
- [3] W. Brütting and C. Adachi, in *Physics of Organic Semiconductors*, 2nd ed., edited by W. Brütting (2012), Wiley-VCH (Weinheim).
- [4] S. Ahmad, *Journal of Polymer Engineering* **34**, 279 (2014): *Organic Semiconductors for Device Applications: Current Trends and Future Prospects.*
- [5] T. W. Kelley, P. F. Baude, C. Gerlach, D. E. Ender, D. Muires, M. A. Haase, D. E. Vogel, and S. D. Theiss, *Chem. Mater.* **16**, 4413 (2004): *Recent Progress in Organic Electronics: Materials, Devices, and Processes.*
- [6] C. Liu, Y. Xu, and Y.-Y. Noh, *Materials Today* **18**, 79 (2015): *Contact Engineering in Organic Field-effect Transistors.*
- [7] N. Thejo Kalyani and S. Dhoble, *Renew. Sustainable Energy Rev.* **16**, 2696 (2012): *Organic Light Emitting Diodes: Energy Saving Lighting Technology – A Review.*
- [8] J. C. Bernède, *J. Chil. Chem. Soc.* **53**, 1549 (2008): *Organic Photovoltaic Cells: History, Principle and Techniques.*
- [9] A. Pivrikas, N. S. Sariciftci, G. Juška, and R. Österbacka, *Prog. Photovolt: Res. Appl.* **15**, 677 (2007): *A Review of Charge Transport and Recombination in Polymer/fullerene Organic Solar Cells.*

BIBLIOGRAPHY

- [10] C. Deibel and V. Dyakonov, Rep. Prog. Phys. **73**, 096401 (2010): *Polymer-fullerene Bulk Heterojunction Solar Cells*.
- [11] Q. Gan, F. J. Bartoli, and Z. H. Kafafi, Adv. Mater. **25**, 2385 (2013): *Plasmonic-Enhanced Organic Photovoltaics: Breaking the 10% Efficiency Barrier*.
- [12] N. C. Greenham, Phil. Trans. R. Soc. A **371**, 20110414 (2013): *Polymer Solar Cells*.
- [13] B. Kippelen and J.-L. Brédas, Energy Environ. Sci. **2**, 251 (2009): *Organic Photovoltaics*.
- [14] P. Peumans, S. Uchida, and S. R. Forrest, Nature **425**, 158 (2003): *Efficient Bulk Heterojunction Photovoltaic Cells Using Small-molecular-weight Organic Thin Films*.
- [15] M. D. McGehee and M. A. Topinka, Nat. Mater. **5**, 675 (2006): *Solar Cells: Pictures from the Blended Zone*.
- [16] R. R. Lunt, J. B. Benziger, and S. R. Forrest, Adv. Mater. **19**, 4229 (2007): *Growth of an Ordered Crystalline Organic Heterojunction*.
- [17] J. Roncali, Acc. Chem. Res. **42**, 1719 (2009): *Molecular Bulk Heterojunctions: An Emerging Approach to Organic Solar Cells*.
- [18] M. K. Siddiki, J. Li, D. Galipeau, and Q. Qiao, Energy Environ. Sci. **3**, 867 (2010): *A Review of Polymer Multijunction Solar Cells*.
- [19] J. Yu, Y. Zheng, and J. Huang, Polymers **6**, 2473 (2014): *Towards High Performance Organic Photovoltaic Cells: A Review of Recent Development in Organic Photovoltaics*.
- [20] T. Mori, J. Phys.: Condens. Matter **20**, 184010 (2008): *Molecular Materials for Organic Field-effect Transistors*.
- [21] C. R. Newman, C. D. Frisbie, D. A. da Silva Filho, J.-L. Brédas, P. C. Ewbank, and K. R. Mann, Chem. Mater. **16**, 4436 (2004): *Introduction to Organic Thin Film Transistors and Design of n-Channel Organic Semiconductors*.
- [22] C. D. Dimitrakopoulos and D. J. Mascaro, IBM J. Res. & Dev. **45**, 11 (2001): *Organic Thin-film Transistors: A Review of Recent Advances*.
- [23] J. Mabeck and G. Malliaras, Anal. Bioanal. Chem. **384**, 343 (2006): *Chemical and Biological Sensors Based on Organic Thin-film Transistors*.

- [24] Y. Wakayama, R. Hayakawa, and H.-S. Seo, *Sci. Technol. Adv. Mater.* **15**, 024202 (2014): *Recent Progress in Photoactive Organic Field-effect Transistors*.
- [25] P. Heremans, G. H. Gelinck, R. Müller, K.-J. Baeg, D.-Y. Kim, and Y.-Y. Noh, *Chem. Mater.* **23**, 341 (2011): *Polymer and Organic Nonvolatile Memory Devices*.
- [26] R. C. G. Naber, C. Tanase, P. W. M. Blom, G. H. Gelinck, A. W. Marsman, F. J. Touwslager, S. Setayesh, and D. M. de Leeuw, *Nat Mater* **4**, 243 (2005): *High-performance Solution-processed Polymer Ferroelectric Field-effect Transistors*.
- [27] Q.-D. Ling, D.-J. Liaw, C. Zhu, D. S.-H. Chan, E.-T. Kang, and K.-G. Neoh, *Prog. Polym. Sci.* **33**, 917 (2008): *Polymer Electronic Memories: Materials, Devices and Mechanisms*.
- [28] Y. Yang, J. Ouyang, L. Ma, R.-H. Tseng, and C.-W. Chu, *Adv. Funct. Mater.* **16**, 1001 (2006): *Electrical Switching and Bistability in Organic/Polymeric Thin Films and Memory Devices*.
- [29] T. Tsutsui and K. Fujita, *Adv. Mater.* **14**, 949 (2002): *The shift from “hard” to “soft” electronics*.
- [30] J. E. Anthony, *Chem. Rev.* **106**, 5028 (2006): *Functionalized Acenes and Heteroacenes for Organic Electronics*.
- [31] J. E. Anthony, *Angew. Chem. Int. Ed.* **47**, 452 (2008): *The Larger Acenes: Versatile Organic Semiconductors*.
- [32] R. Rieger and K. Müllen, *J. Phys. Org. Chem.* **23**, 315 (2010): *Forever Young: Polycyclic Aromatic Hydrocarbons as Model Cases for Structural and Optical Studies*.
- [33] C. Moureu, C. Dufraisse, and P. M. Dean, *Compt. Rend.* **182**, 1440 (1926): *Sur un hydrocarbure coloré: le rubrène*.
- [34] P. Heremans, *Nature* **444**, 828 (2006): *Organic Crystals at Large*.
- [35] J. Lewis, *Mater. Today* **9**, 38 (2006): *Material Challenge for Flexible Organic Devices*.
- [36] A. L. Briseno, S. C. B. Mannsfeld, M. M. Ling, S. Liu, R. J. Tseng, C. Reese, M. E. Roberts, Y. Yang, F. Wudl, and Z. Bao, *Nature* **444**, 913 (2006): *Patterning Organic Single-crystal Transistor Arrays*.

- [37] D. J. Gundlach, *Nat. Mater.* **6**, 173 (2007): *Organic Electronics: Low Power, High Impact*.
- [38] S. Möller, C. Perlov, W. Jackson, C. Taussig, and S. R. Forrest, *Nature* **426**, 166 (2003): *A Polymer/semiconductor Write-once Read-many-times Memory*.
- [39] H. Minemawari, T. Yamada, H. Matsui, J. Tsutsumi, S. Haas, R. Chiba, R. Kumai, and T. Hasegawa, *Nature* **475**, 364 (2011): *Inkjet Printing of Single-crystal Films*.
- [40] F. Schreiber, *phys. stat. sol. (a)* **201**, 1037 (2004): *Organic Molecular Beam Deposition: Growth Studies Beyond the First Monolayer*.
- [41] G. Witte and C. Wöll, *J. Mater. Res.* **19**, 1889 (2004): *Growth of Aromatic Molecules on Solid Substrates for Applications in Organic Electronics*.
- [42] H. Cao, W. He, Y. Mao, X. Lin, K. Ishikawa, J. H. Dickerson, and W. P. Hess, *J. Power Sources* **264**, 168 (2014): *Recent Progress in Degradation and Stabilization of Organic Solar Cells*.
- [43] K. A. McGarry, W. Xie, C. Sutton, C. Risko, Y. Wu, V. G. Young, J.-L. Brédas, C. D. Frisbie, and C. J. Douglas, *Chem. Mater.* **25**, 2254 (2013): *Rubrene-Based Single-Crystal Organic Semiconductors: Synthesis, Electronic Structure, and Charge-Transport Properties*.
- [44] M. Mamada, H. Katagiri, T. Sakanoue, and S. Tokito, *Cryst. Growth Des.* **15**, 442 (2015): *Characterization of New Rubrene Analogues with Heteroaryl Substituents*.
- [45] S. Uttiya, L. Miozzo, E. M. Fumagalli, S. Bergantin, R. Ruffo, M. Parravicini, A. Papagni, M. Moret, and A. Sassella, *J. Mater. Chem. C* **2**, 4147 (2014): *Connecting Molecule Oxidation to Single Crystal Structural and Charge Transport Properties in Rubrene Derivatives*.
- [46] X. Zhang, J. K. Sørensen, X. Fu, Y. Zhen, G. Zhao, L. Jiang, H. Dong, J. Liu, Z. Shuai, H. Geng, T. Bjørnholm, and W. Hu, *J. Mater. Chem. C* **2**, 884 (2014): *Rubrene Analogues with the Aggregation-induced Emission Enhancement Behaviour*.
- [47] A. S. Paraskar, A. R. Reddy, A. Patra, Y. H. Wijsboom, O. Gidron, L. J. W. Shimon, G. Leitus, and M. Bendikov, *Chem. Eur. J.* **14**, 10639 (2008): *Rubrenes: Planar and Twisted*.

- [48] T. K. Mullenbach, K. A. McGarry, W. A. Luhman, C. J. Douglas, and R. J. Holmes, *Adv. Mater.* **25**, 3689 (2013): *Connecting Molecular Structure and Exciton Diffusion Length in Rubrene Derivatives*.
- [49] J. B. Birks, *Photophysics of Aromatic Molecules* (1970), Wiley-Interscience (London, New York).
- [50] M. Schwoerer and H. C. Wolf, *Organic Molecular Solids* (2005), Wiley-VCH (Weinheim).
- [51] F. C. Spano, *Annu. Rev. Phys. Chem.* **57**, 217 (2006): *Excitons in Conjugated Oligomer Aggregates, Films, and Crystals*.
- [52] A. Hinderhofer and F. Schreiber, *ChemPhysChem* **13**, 628 (2012): *Organic-organic Heterostructures: Concepts and Applications*.
- [53] W. Cao and J. Xue, *Energy Environ. Sci.* **7**, 2123 (2014): *Recent Progress in Organic Photovoltaics: Device Architecture and Optical Design*.
- [54] A. Kahn, N. Koch, and W. Gao, *J. Polym. Sci. B Polym. Phys.* **41**, 2529 (2003): *Electronic Structure and Electrical Properties of Interfaces between Metals and π -Conjugated Molecular Films*.
- [55] N. Koch, *J. Phys.: Condens. Matter* **20**, 184008 (2008): *Energy Levels at Interfaces Between Metals and Conjugated Organic Molecules*.
- [56] R. Steim, F. R. Kogler, and C. J. Brabec, *J. Mater. Chem.* **20**, 2499 (2010): *Interface Materials for Organic Solar Cells*.
- [57] N. Koch, *Phys. Status Solidi RRL* **6**, 277 (2012): *Electronic Structure of Interfaces with Conjugated Organic Materials*.
- [58] Y. Gao, *Mater. Sci. Eng. R* **68**, 39 (2010): *Surface Analytical Studies of Interfaces in Organic Semiconductor Devices*.
- [59] A. Zhugayevych and S. Tretiak, *Annu. Rev. Phys. Chem.* **66**, 305 (2015): *Theoretical Description of Structural and Electronic Properties of Organic Photovoltaic Materials*.
- [60] D. Hertel and H. Bässler, *ChemPhysChem* **9**, 666 (2008): *Photoconduction in Amorphous Organic Solids*.

- [61] D. R. T. Zahn, G. N. Gavrilă, and G. Salvani, *Chem. Rev.* **107**, 1161 (2007): *Electronic and Vibrational Spectroscopies Applied to Organic/Inorganic Interfaces.*
- [62] A. Troisi, *Adv. Mater.* **19**, 2000 (2007): *Prediction of the Absolute Charge Mobility of Molecular Semiconductors: the Case of Rubrene.*
- [63] A. Troisi, *Chem. Soc. Rev.* **40**, 2347 (2011): *Charge Transport in High Mobility Molecular Semiconductors: Classical Models and New Theories.*
- [64] N. Ueno and S. Kera, *Prog. Surf. Sci.* **83**, 490 (2008): *Electron Spectroscopy of Functional Organic Thin Films: Deep Insights into Valence Electronic Structure in Relation to Charge Transport Property.*
- [65] L. Gránásy, T. Pusztai, T. Börzsönyi, G. Tóth, G. Tegze, J. Warren, and J. Douglas, *J. Mater. Res.* **21**, 309 (2011): *Phase Field Theory of Crystal Nucleation and Polycrystalline Growth: A Review.*
- [66] S. Kowarik, A. Gerlach, and F. Schreiber, *J. Phys.: Condens. Matter* **20**, 184005 (2008): *Organic Molecular Beam Deposition: Fundamentals, Growth Dynamics, and in-situ Studies.*
- [67] A. A. Virkar, S. Mannsfeld, Z. Bao, and N. Stingelin, *Adv. Mater.* **22**, 3857 (2010): *Organic Semiconductor Growth and Morphology Considerations for Organic Thin-Film Transistors.*
- [68] M.-C. Blüm, Ph.D. thesis, École Polytechnique Fédérale de Lausanne, (2006): *Supramolecular Assembly, Chirality, and Electronic Properties of Rubrene Studied by STM and STS.*
- [69] F. Schreiber, *Prog. Surf. Sci.* **65**, 151 (2000): *Structure and Growth of Self-Assembling Monolayers.*
- [70] F. Schreiber, *J. Phys. Condens. Matter.* **16**, R881 (2004): *Self-assembled monolayers: From 'Simple' Alkanethiols to Bio-functionalised Interfaces.*
- [71] O. Mitrofanov, D. V. Lang, C. Kloc, J. M. Wikberg, T. Siegrist, W.-Y. So, M. A. Sergent, and A. P. Ramirez, *Phys. Rev. Lett.* **97**, 166601 (2006): *Oxygen-Related Band Gap State in Single Crystal Rubrene.*
- [72] C. Krellner, S. Haas, C. Goldmann, K. P. Pernstich, D. J. Gundlach, and B. Batlogg, *Phys. Rev. B* **75**, 245115 (2007): *Density of Bulk Trap States in Organic Semiconductor Crystals: Discrete Levels Induced by Oxygen in Rubrene.*

-
- [73] O. Mitrofanov, C. Kloc, T. Siegrist, D. V. Lang, W.-Y. So, and A. P. Ramirez, *Appl. Phys. Lett.* **91**, 212106 (2007): *Role of Synthesis for Oxygen Defect Incorporation in Crystalline Rubrene.*
- [74] H. Najafov, B. Lyu, I. Biaggio, and V. Podzorov, *Appl. Phys. Lett.* **96**, 183302 (2010): *Two Mechanisms of Exciton Dissociation in Rubrene Single Crystals.*
- [75] X. Song, L. Wang, Q. Fan, Y. Wu, H. Wang, C. Liu, N. Liu, J. Zhu, D. Qi, X. Gao, and A. T. S. Wee, *Appl. Phys. Lett.* **97**, 032106 (2010): *Role of Oxygen Incorporation in Electronic Properties of Rubrene Films.*
- [76] H. Najafov, D. Mastrogiovanni, E. Garfunkel, L. C. Feldman, and V. Podzorov, *Adv. Mater.* **23**, 981 (2011): *Photon-Assisted Oxygen Diffusion and Oxygen-Related Traps in Organic Semiconductors.*
- [77] Y. Chen, B. Lee, D. Fu, and V. Podzorov, *Adv. Mater.* **23**, 5370 (2011): *The Origin of a 650 nm Photoluminescence Band in Rubrene.*
- [78] V. Podzorov, E. Menard, A. Borissov, V. Kiryukhin, J. A. Rogers, and M. E. Gershenson, *Phys. Rev. Lett.* **93**, 086602 (2004): *Intrinsic Charge Transport on the Surface of Organic Semiconductors.*
- [79] V. C. Sundar, J. Zaumseil, V. Podzorov, E. Menard, R. L. Willett, T. Someya, M. E. Gershenson, and J. A. Rogers, *Science* **303**, 1644 (2004): *Elastomeric Transistor Stamps: Reversible Probing of Charge Transport in Organic Crystals.*
- [80] J. Takeya, M. Yamagishi, Y. Tominari, R. Hirahara, Y. Nakazawa, T. Nishikawa, T. Kawase, T. Shimoda, and S. Ogawa, *Appl. Phys. Lett.* **90**, 102120 (2007): *Very High-Mobility Organic Single-Crystal Transistors with in-Crystal Conduction Channels.*
- [81] J. Takeya, J. Kato, K. Hara, M. Yamagishi, R. Hirahara, K. Yamada, Y. Nakazawa, S. Ikehata, K. Tsukagoshi, Y. Aoyagi, T. Takenobu, and Y. Iwasa, *Phys. Rev. Lett.* **98**, 196804 (2007): *In-Crystal and Surface Charge Transport of Electric-Field-Induced Carriers in Organic Single-Crystal Semiconductors.*
- [82] G. Witte and C. Wöll, *phys. stat. sol. (a)* **205**, 497 (2008): *Molecular Beam Deposition and Characterization of Thin Organic Films on Metals for Applications in Organic Electronics.*

- [83] H. Najafov, B. Lee, Q. Zhou, L. C. Feldman, and V. Podzorov, *Nat. Mater.* **9**, 938 (2010): *Observation of Long-range Exciton Diffusion in Highly Ordered Organic Semiconductors.*
- [84] P. Irkhin and I. Biaggio, *Phys. Rev. Lett.* **107**, 017402 (2011): *Direct Imaging of Anisotropic Exciton Diffusion and Triplet Diffusion Length in Rubrene Single Crystals.*
- [85] B. Verreet, P. Heremans, A. Stesmans, and B. P. Rand, *Adv. Mater.* **25**, 5504 (2013): *Microcrystalline Organic Thin-Film Solar Cells.*
- [86] G. Schweicher, Y. Olivier, V. Lemaury, and Y. H. Geerts, *Isr. J. Chem.* **54**, 595 (2014): *What Currently Limits Charge Carrier Mobility in Crystals of Molecular Semiconductors?*
- [87] F. Anger, R. Scholz, E. Adamski, K. Broch, A. Gerlach, Y. Sakamoto, T. Suzuki, and F. Schreiber, *Appl. Phys. Lett.* **102**, 013308 (2013): *Optical Properties of Fully and Partially Fluorinated Rubrene in Films and Solution.*
- [88] D. Käfer and G. Witte, *Phys. Chem. Chem. Phys.* **7**, 2850 (2005): *Growth of Crystalline Rubrene Films with Enhanced Stability.*
- [89] E. Fumagalli, L. Raimondo, L. Silvestri, M. Moret, A. Sassella, and M. Campione, *Chem. Mater.* **23**, 3246 (2011): *Oxidation Dynamics of Epitaxial Rubrene Ultrathin Films.*
- [90] J. Y. Lee, S. Roth, and Y. W. Parka, *Appl. Phys. Lett.* **88**, 252106 (2006): *Anisotropic Field Effect Mobility in Single Crystal Pentacene.*
- [91] D. J. Gundlach, Y. Y. Lin, T. N. Jackson, S. F. Nelson, and D. G. Schlom, *IEEE Electron Device Lett.* **18**, 87 (1997): *Pentacene Organic Thin-Film Transistors-Molecular Ordering and Mobility.*
- [92] D. A. da Silva Filho, E.-G. Kim, and J.-L. Brédas, *Adv. Mater.* **17**, 1072 (2005): *Transport Properties in the Rubrene Crystal: Electronic Coupling and Vibrational Reorganization Energy.*
- [93] H. Morisaki, T. Koretsune, C. Hotta, J. Takeya, T. Kimura, and Y. Wakabayashi, *Nat Comms* **5**, 5400 (2014): *Large Surface Relaxation in the Organic Semiconductor Tetracene.*

-
- [94] V. Stehr, J. Pfister, R. Fink, B. Engels, and C. Deibel, *Phys. Rev. B* **83**, 155208 (2011): *First-principles Calculations of Anisotropic Charge-carrier Mobilities in Organic Semiconductor Crystals*.
- [95] S. Machida, Y. Nakayama, S. Duhm, Q. Xin, A. Funakoshi, N. Ogawa, S. Kera, N. Ueno, and H. Ishii, *Phys. Rev. Lett.* **104**, 156401 (2010): *Highest-Occupied-Molecular-Orbital Band Dispersion of Rubrene Single Crystals as Observed by Angle-Resolved Ultraviolet Photoelectron Spectroscopy*.
- [96] N. Sato, K. Seki, and H. Inokuchi, *J. Chem. Soc., Faraday Trans.* **77**, 1621 (1981): *Polarization Energies of Organic Solids Determined by Ultraviolet Photoelectron Spectroscopy*.
- [97] R. M. Pinto, *J. Phys. Chem. C* **118**, 2287 (2014): *Photocurrent Generation in Bulk vs Bilayer Devices: Quantum Treatment of Model Rubrene/7,7,8,8-Tetracyanoquinodimethane Heterojunctions for Organic Solar Cells*.
- [98] A. M. C. Ng, A. B. Djurišić, W.-K. Chan, and J.-M. Nunzi, *Chem. Phys. Lett.* **474**, 141 (2009): *Near Infrared Emission in Rubrene:fullerene Heterojunction Devices*.
- [99] W. Mou, S. Ohmura, S. Hattori, K.-i. Nomura, F. Shimojo, and A. Nakano, *J. Chem. Phys.* **136**, 184705 (2012): *Enhanced Charge Transfer by Phenyl Groups at a Rubrene/C60 Interface*.
- [100] A. K. Pandey and J.-M. Nunzi, *Adv. Mater.* **19**, 3613 (2007): *Rubrene/Fullerene Heterostructures with a Half-gap Electroluminescence Threshold and Large Photovoltage*.
- [101] J. Huang, J. Yu, W. Wang, and Y. Jiang, *Appl. Phys. Lett.* **98**, 023301 (2011): *Organic Solar Cells with a Multicharge Separation Structure Consisting of a Thin Rubrene Fluorescent Dye for Open Circuit Voltage Enhancement*.
- [102] K. Cho, S. W. Cho, C.-N. Whang, K. Jeong, S. J. Kang, and Y. Yi, *Appl. Phys. Lett.* **91**, 152107 (2007): *The Origin of Electron Injection Improvement in Organic Light-emitting Devices with an Organic Oxide/rubrene Electron Injection Layer*.
- [103] Z. Liu, H. Wang, Q. Yang, T. W. Ng, M. F. Lo, N. B. Wong, S. T. Lee, and C. S. Lee, *Appl. Surf. Sci.* **257**, 8462 (2011): *Effects of Rubrene Mixing on the Electronic Structures of Donor/acceptor Interface in Organic Photovoltaic Device*.
- [104] Z. Wang, S. Naka, and H. Okada, *Appl. Phys. A* **100**, 1103 (2010): *Performance Improvement of Rubrene-based Organic Light Emitting Devices with a Mixed Single Layer*.

- [105] R. Uchida, H. Yada, M. Makino, Y. Matsui, K. Miwa, T. Uemura, J. Takeya, and H. Okamoto, *Appl. Phys. Lett.* **102**, 093301 (2013): *Charge Modulation Infrared Spectroscopy of Rubrene Single-crystal Field-effect Transistors.*
- [106] W. Xie and C. D. Frisbie, *J. Phys. Chem. C* **115**, 14360 (2011): *Organic Electrical Double Layer Transistors Based on Rubrene Single Crystals: Examining Transport at High Surface Charge Densities above 10^{13} cm^{-2} .*
- [107] Y. Okada, K. Sakai, T. Uemura, Y. Nakazawa, and J. Takeya, *Phys. Rev. B* **84**, (2011): *Charge Transport and Hall Effect in Rubrene Single-crystal Transistors under High Pressure.*
- [108] D. Braga, M. Campione, A. Borghesi, and G. Horowitz, *Adv. Mater.* **22**, 424 (2010): *Organic Metal-Semiconductor Field-Effect Transistor (OMESFET) Fabricated on a Rubrene Single Crystal.*
- [109] H. L. Kwok, *J Mater Sci: Mater Electron* **21**, 535 (2010): *The Roles of "Free" and "Trapped" Charges in Single-crystal Rubrene Organic Field-effect Transistors.*
- [110] M. Fischer, M. Dressel, B. Gompf, A. K. Tripathi, and J. Pflaum, *Appl. Phys. Lett.* **89**, 182103 (2006): *Infrared Spectroscopy on the Charge Accumulation Layer in Rubrene Single Crystals.*
- [111] V. Podzorov, E. Menard, S. Pereversev, B. Yakshinsky, T. Madey, J. A. Rogers, and M. E. Gershenson, *Appl. Phys. Lett.* **87**, 093505 (2005): *Interaction of Organic Surfaces with Active Species in the High-vacuum Environment.*
- [112] N. Stingelin-Stutzmann, E. Smits, H. Wondergem, C. Tanase, P. Blom, P. Smith, and D. De Leeuw, *Nat Mater* **4**, 601 (2005): *Organic Thin-film Electronics from Vitreous Solution-processed Rubrene Hypereutectics.*
- [113] M. Nothaft and J. Pflaum, *phys. stat. sol. (b)* **245**, 788 (2008): *Thermally and Seed-layer Induced Crystallization in Rubrene Thin Films.*
- [114] S. Seo, B.-N. Park, and P. G. Evansa, *Appl. Phys. Lett.* **88**, 232114 (2006): *Ambipolar Rubrene Thin Film Transistors.*
- [115] J. H. Seo, D. S. Park, S. W. Cho, C. Y. Kim, W. C. Jang, C. N. Whang, K. H. Yoo, G. S. Chang, T. Pedersen, A. Moewes, K. H. Chae, and S. J. Cho, *Appl. Phys. Lett.* **89**, 163505 (2006): *Buffer Layer Effect on the Structural and Electrical Properties of Rubrene-based Organic Thin-film Transistors.*

- [116] Z. Li, J. Du, Q. Tang, F. Wang, J.-B. Xu, J. C. Yu, and Q. Miao, *Adv. Mater.* **22**, 3242 (2010): *Induced Crystallization of Rubrene in Thin-Film Transistors.*
- [117] J.-M. Choi and S. Im, *Appl. Phys. Lett.* **93**, 043309 (2008): *Optimum Channel Thickness of Rubrene Thin-film Transistors.*
- [118] X. Zhang, Q. Meng, Y. He, C. Wang, H. Dong, and W. Hu, *Sci. China Chem.* **54**, 631 (2011): *A New Pseudo Rubrene Analogue with Excellent Film Forming Ability.*
- [119] H. Fong, S. So, W. Sham, C. Lo, Y. Wu, and C. Chen, *Chem. Phys.* **298**, 119 (2004): *Effects of Tertiary Butyl Substitution on the Charge Transporting Properties of Rubrene-based Films.*
- [120] S. Uttiya, L. Raimondo, M. Campione, L. Miozzo, A. Yassar, M. Moret, E. Fumagalli, A. Borghesi, and A. Sassella, *Synth. Met.* **161**, 2603 (2012): *Stability to Photo-Oxidation of Rubrene and Fluorine-Substituted Rubrene.*
- [121] C. Sutton, M. S. Marshall, C. D. Sherrill, C. Risko, and J.-L. Brédas, *J. Am. Chem. Soc.* **137**, 8775 (2015): *Rubrene: The Interplay between Intramolecular and Intermolecular Interactions Determines the Planarization of Its Tetracene Core in the Solid State.*
- [122] E. A. Meyer, R. K. Castellano, and F. Diederich, *Angew. Chem. Int. Ed.* **42**, 1210 (2003): *Interactions with Aromatic Rings in Chemical and Biological Recognition.*
- [123] M. C. R. Delgado, K. R. Pigg, D. A. da Silva Filho, N. E. Gruhn, Y. Sakamoto, T. Suzuki, R. M. Osuna, J. Casado, V. Hernández, J. Teodomiro, L. Navarrete, N. G. Martinelli, J. Cornil, R. S. Sánchez-Carrera, V. Coropceanu, and J.-L. Brédas, *J. Am. Chem. Soc.* **131**, 1502 (2009): *Impact of Perfluorination on the Charge-Transport Parameters of Oligoacene Crystals.*
- [124] D. G. de Oteyza, Y. Wakayama, X. Liu, W. Yang, P. L. Cook, F. J. Himpsel, and J. E. Ortega, *Chem. Phys. Lett.* **490**, 54 (2010): *Effect of Fluorination on the Molecule-Substrate Interactions of Pentacene/Cu(100) Interfaces.*
- [125] S. Kera, S. Hosoumi, K. Sato, H. Fukagawa, S.-i. Nagamatsu, Y. Sakamoto, T. Suzuki, H. Huang, W. Chen, A. T. S. Wee, V. Coropceanu, and N. Ueno, *J. Phys. Chem. C* **117**, 22428 (2013): *Experimental Reorganization Energies of Pentacene and Perfluoropentacene: Effects of Perfluorination.*
- [126] Y. Yamaguchi, *J. Chem. Phys.* **122**, 184702 (2005): *Effects of Fluorination on Electronic and Excited States of Fused Zinc Oligoporphyrins.*

- [127] M. Kytka, A. Gerlach, J. Kováč, and F. Schreiber, *Appl. Phys. Lett.* **90**, 131911 (2007): *Real-time Observation of Oxidation and Photo-oxidation of Rubrene Thin Films by Spectroscopic Ellipsometry.*
- [128] A. Hinderhofer, U. Heinemeyer, A. Gerlach, S. Kowarik, R. M. J. Jacobs, Y. Sakamoto, T. Suzuki, and F. Schreiber, *J. Chem. Phys.* **127**, 194705 (2007): *Optical Properties of Pentacene and Perfluoropentacene Thin Films.*
- [129] A. Hinderhofer, C. Frank, T. Hosokai, A. Resta, A. Gerlach, and F. Schreiber, *J. Chem. Phys.* **134**, 104702 (2011): *Structure and Morphology of Coevaporated Pentacene-perfluoropentacene Thin Films.*
- [130] K. Broch, U. Heinemeyer, A. Hinderhofer, F. Anger, R. Scholz, A. Gerlach, and F. Schreiber, *Phys. Rev. B* **83**, 245307 (2011): *Optical Evidence for Intermolecular Coupling in Mixed Films of Pentacene and Perfluoropentacene.*
- [131] F. Anger, J. O. Ossó, U. Heinemeyer, K. Broch, R. Scholz, A. Gerlach, and F. Schreiber, *J. Chem. Phys.* **136**, 054701 (2012): *Photoluminescence Spectroscopy of Pure Pentacene, Perfluoropentacene, and Mixed Thin Films.*
- [132] B. Milián Medina, D. Beljonne, H.-J. Egelhaaf, and J. Gierschner, *J. Chem. Phys.* **126**, 111101 (2007): *Effect of Fluorination on the Electronic Structure and Optical Excitations of π -conjugated Molecules.*
- [133] S. M. Ryno, S. R. Lee, J. S. Sears, C. Risko, and J.-L. Brédas, *J. Phys. Chem. C* **117**, 13853 (2013): *Electronic Polarization Effects upon Charge Injection in Oligoacene Molecular Crystals: Description via a Polarizable Force Field.*
- [134] R. C. Wheland and E. L. Martin, *J. Org. Chem.* **40**, 3101 (1975): *Synthesis of Substituted 7,7,8,8-tetracyanoquinodimethanes.*
- [135] H. Peisert, M. Knupfer, T. Schwieger, G. G. Fuentes, D. Olligs, J. Fink, and T. Schmidt, *J. Appl. Phys.* **93**, 9683 (2003): *Fluorination of Copper Phthalocyanines: Electronic Structure and Interface Properties.*
- [136] Y. Sakamoto, T. Suzuki, M. Kobayashi, Y. Gao, Y. Fukai, Y. Inoue, F. Sato, and S. Tokito, *J. Am. Chem. Soc.* **126**, 8138 (2004): *Perfluoropentacene: High-Performance p-n Junctions and Complementary Circuits with Pentacene.*
- [137] Y. Sakamoto, T. Suzuki, M. Kobayashi, Y. Gao, Y. Inoue, and S. Tokito, *Mol. Cryst. Liq. Cryst.* **444**, 225 (2006): *Perfluoropentacene and Perfluorotetracene: Syntheses, Crystal Structures, and FET Characteristics.*

-
- [138] Y. Sakamoto, S. Komatsu, and T. Suzuki, *J. Am. Chem. Soc.* **123**, 4643 (2001): *Tetradecafluorosexithiophene: The First Perfluorinated Oligothiophene*.
- [139] R. Laudise, C. Kloc, P. Simpkins, and T. Siegrist, *J. Cryst. Growth* **187**, 449 (1998): *Physical Vapor Growth of Organic Semiconductors*.
- [140] E. Frankevich, B. Romyantsev, and V. Lesin, *J. Lumin.* **11**, 91 (1975): *Magnetic Field Effect on the Thermostimulated Chemiluminescence of Photoperoxidized Rubrene*.
- [141] F. Anger, H. Glowatzki, A. Franco-Cañellas, C. Bürker, A. Gerlach, R. Scholz, Y. Sakamoto, T. Suzuki, N. Koch, and F. Schreiber, *J. Phys. Chem. C* **119**, 6769 (2015): *Interface Dipole and Growth Mode of Partially and Fully Fluorinated Rubrene on Au(111) and Ag(111)*.
- [142] F. Anger, R. Scholz, A. Gerlach, and F. Schreiber, *J. Chem. Phys.* **142**, 224703 (2015): *Vibrational Modes and Changing Molecular Conformation of Perfluororubrene in Thin Films and Solution*.
- [143] F. Anger, T. Breuer, A. Ruff, M. Klues, A. Gerlach, R. Scholz, S. Ludwigs, and F. Schreiber, *J. Phys. Chem. C* *accepted*: *Enhanced Stability of Rubrene against Oxidation by Partial and Complete Fluorination*.
- [144] E. J. Bowen and F. Steadman, *J. Chem. Soc.* 1098 (1934): 233. *The Photo-oxidation of Rubrene*.
- [145] Y. Nakayama, S. Machida, T. Minari, K. Tsukagishi, Y. Noguchi, and H. Ishii, *Appl. Phys. Lett.* **93**, 173305 (2008): *Direct Observation of the Electronic States of Single Crystalline Rubrene under Ambient Condition by Photoelectron Yield Spectroscopy*.
- [146] M. E. Helou, O. Medenbach, and G. Witte, *Cryst. Growth Des.* **10**, 3496 (2010): *Rubrene Microcrystals: A Route to Investigate Surface Morphology and Bulk Anisotropies of Organic Semiconductors*.
- [147] WIKIPEDIA contributors, "Permittivity" — *Wikipedia, The Free Encyclopedia*, <https://en.wikipedia.org/w/index.php?title=Permittivity&oldid=704328006> (accessed June 1, 2015).
- [148] I. Renge, *Chem. Phys.* **167**, 173 (1992): *On the Determination of Molecular Polarizability Changes upon Electronic Excitation from the Solvent Shifts of Absorption Band Maxima*.

BIBLIOGRAPHY

- [149] P. Suppan, *J. Photochem. Photobiol. A* **50**, 293 (1990): *Invited Review Solvatochromic Shifts: The Influence of the Medium on the Energy of Electronic States*.
- [150] U. Heinemeyer, Ph.D. thesis, Eberhard Karls Universität Tübingen (2009): *Optical Properties of Organic Semiconductor Thin Films: Static Spectra and Real-time Growth Studies*.
- [151] P. Atkins and R. Friedman, *Molecular Quantum Mechanics*, 4 ed. (2005), Oxford University Press (New York).
- [152] C. V. Raman, *Proc. Indian Acad. Sci. A* **29**, 381 (1949): *The Theory of the Christiansen Experiment*.
- [153] F. A. Cotton, *Chemical Applications of Group Theory* (1990), John Wiley & Sons (New York).
- [154] *Organic Molecular Photophysics*, edited by J. B. Birks (1975), Vol. 2, Wiley-Interscience (London).
- [155] Y. Yamakita, J. Kimura, and K. Ohno, *J. Chem. Phys.* **126**, 064904 (2007): *Molecular Vibrations of [n]oligoacenes (n = 2-5 and 10) and Phonon Dispersion Relations of Polyacene*.
- [156] L. Gisslén, Ph.D. thesis, Walter Schottky Institut, Technische Universität München (2009): *Influence of Frenkel Excitons and Charge Transfer States on the Spectroscopic Properties of Organic Molecular Crystals*.
- [157] S. Duhm, Q. Xin, S. Hosoumi, H. Fukagawa, K. Sato, N. Ueno, and S. Kera, *Adv. Mater.* **24**, 901 (2012): *Charge Reorganization Energy and Small Polaron Binding Energy of Rubrene Thin Films by Ultraviolet Photoelectron Spectroscopy*.
- [158] A. K. Dutta, T. N. Misra, and A. J. Pal, *Solid State Commun.* **99**, 767 (1996): *Two photon Delayed Fluorescence Emission from Aggregates of Rubrene in Langmuir-Blodgett films at 77 K*.
- [159] M. Kytka, L. Gisslén, A. Gerlach, U. Heinemeyer, J. Kováč, R. Scholz, and F. Schreiber, *J. Chem. Phys.* **130**, 214507 (2009): *Optical Spectra Obtained from Amorphous Films of Rubrene: Evidence for Predominance of Twisted Isomer*.
- [160] R. A. Marcus, *J. Chem. Phys.* **24**, 966 (1956): *On the Theory of Oxidation-Reduction Reactions Involving Electron Transfer. I*.

- [161] R. Scholz, R. Luschtinetz, G. Seifert, T. Jägeler-Hoheisel, C. Körner, K. Leo, and M. Rapacioli, *J. Phys.: Condens. Matter* **25**, 473201 (2013): *Quantifying Charge Transfer Energies at Donor-acceptor Interfaces in Small-molecule Solar Cells with Constrained DFTB and Spectroscopic Methods*.
- [162] L. E. Lyons, *J. Chem. Soc.* 5001 (1957): *Photo- and Semi-conductance in Organic Crystals. Part V. Ionized States in Molecular Crystals*.
- [163] A. Einstein, *Ann. Phys.* **322**, 132 (1905): *Über einen die Erzeugung und Verwandlung des Lichtes betreffenden heuristischen Gesichtspunkt*.
- [164] H. Ishii, K. Sugiyama, E. Ito, and K. Seki, *Adv. Mater.* **11**, 605 (1999): *Energy Level Alignment and Interfacial Electronic Structures at Organic/Metal and Organic/Organic Interfaces*.
- [165] C. Bürker, Ph.D. thesis, Eberhard Karls Universität Tübingen (2014): *Adsorption Geometry of π -conjugated Organic Molecules on Metal Surfaces Studied with the X-ray Standing Wave Technique*.
- [166] TURBOMOLE V6.4 2012, a development of University of Karlsruhe and Forschungszentrum Karlsruhe GmbH, 1989-2007, TURBOMOLE GMBH, since 2007; available from <http://www.turbomole.com>.
- [167] BWGRID (<http://www.bw-grid.de>), member of the German D-Grid initiative, funded by the Ministry for Education and Research (Bundesministerium für Bildung und Forschung) and the Ministry for Science, Research and Arts Baden-Württemberg (Ministerium für Wissenschaft, Forschung und Kunst Baden-Württemberg).
- [168] M. J. Frisch, G. W. Trucks, H. B. Schlegel, G. E. Scuseria, M. A. Robb, J. R. Cheeseman, J. A. Montgomery, Jr., T. Vreven, K. N. Kudin, J. C. Burant, J. M. Millam, S. S. Iyengar, J. Tomasi, V. Barone, B. Mennucci, M. Cossi, G. Scalmani, N. Rega, G. A. Petersson, H. Nakatsuji, M. Hada, M. Ehara, K. Toyota, R. Fukuda, J. Hasegawa, M. Ishida, T. Nakajima, Y. Honda, O. Kitao, H. Nakai, M. Klene, X. Li, J. E. Knox, H. P. Hratchian, J. B. Cross, V. Bakken, C. Adamo, J. Jaramillo, R. Gomperts, R. E. Stratmann, O. Yazyev, A. J. Austin, R. Cammi, C. Pomelli, J. W. Ochterski, P. Y. Ayala, K. Morokuma, G. A. Voth, P. Salvador, J. J. Dannenberg, V. G. Zakrzewski, S. Dapprich, A. D. Daniels, M. C. Strain, O. Farkas, D. K. Malick, A. D. Rabuck, K. Raghavachari, J. B. Foresman, J. V. Ortiz, Q. Cui, A. G. Baboul, S. Clifford, J. Cioslowski, B. B. Stefanov, G. Liu, A. Liashenko, P. Piskorz, I. Komaromi, R. L.

BIBLIOGRAPHY

- Martin, D. J. Fox, T. Keith, M. A. Al-Laham, C. Y. Peng, A. Nanayakkara, M. Challacombe, P. M. W. Gill, B. Johnson, W. Chen, M. W. Wong, C. Gonzalez, and J. A. Pople, GAUSSIAN 03, Revision D.01 (Gaussian, Inc., Wallingford, CT, 2004).
- [169] G. Schaftenaar and J. Noordik, *J. Comput.-Aided Mol. Design* **14**, 123 (2000): *Molden: A Pre- and Post-processing Program for Molecular and Electronic Structures*.
- [170] W. Kohn, *Rev. Mod. Phys.* **71**, 1253 (1999): *Nobel Lecture: Electronic Structure of Matter - Wave Functions and Density Functionals*.
- [171] A. D. Becke, *J. Chem. Phys.* **98**, 1372 (1993): *A New Mixing of Hartree-Fock and Local Density-functional Theories*.
- [172] C. Lee, W. Yang, and R. G. Parr, *Phys. Rev. B* **37**, 785 (1988): *Development of the Colle-Salvetti Correlation-energy Formula into a Functional of the Electron Density*.
- [173] S. F. Boys, *Proceedings of the Royal Society A: Mathematical, Physical and Engineering Sciences* **200**, 542 (1950): *Electronic Wave Functions. I. A General Method of Calculation for the Stationary States of Any Molecular System*.
- [174] O. Treutler and R. Ahlrichs, *J. Chem. Phys.* **102**, 346 (1995): *Efficient Molecular Numerical Integration Schemes*.
- [175] K. Eichkorn, F. Weigend, O. Treutler, and R. Ahlrichs, *Theor. Chem. Acc.* **97**, 119 (1997): *Auxiliary Basis Sets for Main Row Atoms and Transition Metals and Their Use to Approximate Coulomb Potentials*.
- [176] M. Kytka, Ph.D. thesis, Slovak University of Technology in Bratislava (2008): *Characterization of Rubrene Thin Films by Optical Techniques*.
- [177] J. Heinze, *Angew. Chem. Int. Ed. Engl.* **23**, 831 (1984): *Cyclic Voltammetry—“Electrochemical Spectroscopy”*.
- [178] G. Gritzner and J. Kuta, *Pure Appl. Chem.* **56**, 461 (1984): *Recommendations on Reporting Electrode Potentials in Nonaqueous Solvents (Recommendations 1983)*.
- [179] C. M. Cardona, W. Li, A. E. Kaifer, D. Stockdale, and G. C. Bazan, *Adv. Mater.* **23**, 2367 (2011): *Electrochemical Considerations for Determining Absolute Frontier Orbital Energy Levels of Conjugated Polymers for Solar Cell Applications*.
- [180] A. Rothen, *Rev. Sci. Instrum.* **16**, 26 (1945): *The Ellipsometer, an Apparatus to Measure Thicknesses of Thin Surface Films*.

-
- [181] K. Vedam, *Thin Solid Films* **313-314**, 1 (1998): *Spectroscopic Ellipsometry: A Historical Overview*.
- [182] U. Heinemeyer, R. Scholz, L. Gisslén, M. I. Alonso, J. O. Ossó, M. Garriga, A. Hinderhofer, M. Kytka, S. Kowarik, A. Gerlach, and F. Schreiber, *Phys. Rev. B* **78**, 085210 (2008): *Exciton-phonon Coupling in Diindenoperylene Thin Films*.
- [183] F. Anger, Diplomarbeit, Eberhard-Karls-Universität zu Tübingen (2010): *Photoluminescence and Raman Spectroscopy of Pentacene/perfluoropentacene Mixed Thin Films*.
- [184] Z. Q. Ren, L. E. McNeil, S. Liu, and C. Kloc, *Phys. Rev. B* **80**, 245211 (2009): *Molecular Motion and Mobility in an Organic Single Crystal: Raman Study and Model*.
- [185] P. A. Temple and C. E. Hathaway, *Phys. Rev. B* **7**, 3685 (1973): *Multiphonon Raman Spectrum of Silicon*.
- [186] S. Zorn, Ph.D. thesis, Eberhard-Karls-Universität zu Tübingen (2010): *In-situ Studies of Protein-resistant Self-assembling Monolayers*.
- [187] *Infrared and Raman Spectra of Polyatomic Molecules*, edited by G. Herzberg (1945), D. Van Nostrand Company, Inc. Princeton, New Jersey (New York).
- [188] G. Hansson and S. Flodström, *Phys. Rev. B* **18**, 1572 (1978): *Photoemission Study of the Bulk and Surface Electronic Structure of Single Crystals of Gold*.
- [189] M. Chelvayohan and C. H. B. Mee, *J. Phys. C: Solid State Phys.* **15**, 2305 (1982): *Work Function Measurements on (110), (100) and (111) Surfaces of Silver*.
- [190] D. Nečas and P. Klapetek, *Cent. Eur. J. Phys.* **10**, 181 (2012): *Gwyddion: An Open-source Software for SPM Data Analysis*.
- [191] J. Instruments, *The NanoWizard AFM Handbook*, 1.3 ed., JPK Instruments (2005).
- [192] J. Als-Nielsen and D. McMorrow, *Elements of Modern X-ray Physics*, 2nd ed. (2011), John Wiley & Sons, Ltd (Chichester).
- [193] P. R. Willmott, D. Meister, S. J. Leake, M. Lange, A. Bergamaschi, M. Böge, M. Calvi, C. Cancellieri, N. Casati, A. Cervellino, Q. Chen, C. David, U. Flechsig, F. Gozzo, B. Henrich, S. Jäggi-Spielmann, B. Jakob, I. Kalichava, P. Karvinen, J. Krempasky, A. Lüdeke, R. Lüscher, S. Maag, C. Quitmann, M. L. Reinle-Schmitt, T. Schmidt, B. Schmitt, A. Streun, I. Vartiainen, M. Vitins, X. Wang, and

- R. Wullschleger, J. Synchrotron Radiat. **20**, 667 (2013): *The Materials Science Beamline Upgrade at the Swiss Light Source*.
- [194] S.-W. Park, J.-M. Choi, K. H. Lee, H. W. Yeom, S. Im, and Y. K. Lee, J. Phys. Chem. B **114**, 5661 (2010): *Amorphous-to-Crystalline Phase Transformation of Thin Film Rubrene*.
- [195] S. Kowarik, A. Gerlach, S. Sellner, F. Schreiber, J. Pflaum, L. Cavalcanti, and O. Kononov, Phys. Chem. Chem. Phys. **8**, 1834 (2006): *Anomalous Roughness Evolution of Rubrene Thin Films Observed in Real Time during Growth*.
- [196] D. Käfer, L. Ruppel, G. Witte, and C. Wöll, Phys. Rev. Lett. **95**, 166602 (2005): *Role of Molecular Conformations in Rubrene Thin Film Growth*.
- [197] R. Loudon, *The Quantum Theory of Light*, 3 ed. (2000), Oxford University Press (New York).
- [198] Y. Harada, T. Takahashi, S. Fujisawa, and T. Kajiwara, Chem. Phys. Lett. **62**, 283 (1979): *Application of Photoelectron Spectroscopy to the Study of Photochemical Reactions of Solids. Photooxidation of Rubrene (5,6,11,12-tetraphenylanthracene)*.
- [199] H. Najafov, I. Biaggio, V. Podzorov, M. F. Calhoun, and M. E. Gershenson, Phys. Rev. Lett. **96**, 056604 (2006): *Primary Photoexcitations and the Origin of the Photocurrent in Rubrene Single Crystals*.
- [200] S.-W. Park, J. M. Hwang, J.-M. Choi, D. K. Hwang, M. S. Oh, J. H. Kim, and S. Im, Appl. Phys. Lett. **90**, 153512 (2007): *Rubrene Thin-film Transistors with Crystalline and Amorphous Channels*.
- [201] M. Müller, A. Langner, O. Krylova, E. L. Moal, and M. Sokolowski, Appl. Phys. B **105**, 67 (2011): *Fluorescence Spectroscopy of Ultrathin Molecular Organic Films on Surfaces*.
- [202] A. Karpfen, C. H. Choi, and M. Kertesz, J. Phys. Chem. A **101**, 7426 (1997): *Single-Bond Torsional Potentials in Conjugated Systems: A Comparison of and Density Functional Results*.
- [203] S. Grimme and M. Parac, ChemPhysChem **4**, 292 (2003): *Substantial Errors from Time-Dependent Density Functional Theory for the Calculation of Excited States of Large π Systems*.

-
- [204] U. Weiler, T. Mayer, W. Jaegermann, C. Kelting, D. Schlettwein, S. Makarov, and D. Wöhrle, *J. Phys. Chem. B* **108**, 19398 (2004): *Electronic Energy Levels of Organic Dyes on Silicon: A Photoelectron Spectroscopy Study of ZnPc, F₁₆ZnPc, and ZnTPP on p-Si(111):H.*
- [205] T. Mayer, U. Weiler, C. Kelting, D. Schlettwein, S. Makarov, D. Wöhrle, O. Abdallah, M. Kunst, and W. Jaegermann, *Solar Energy Materials and Solar Cells* **91**, 1873 (2007): *Silicon-organic Pigment Material Hybrids for Photovoltaic Application.*
- [206] N. S. Bayliss, *J. Chem. Phys.* **18**, 292 (1950): *The Effect of the Electrostatic Polarization of the Solvent on Electronic Absorption Spectra in Solution.*
- [207] A. Kapturkiewicz, *J. Electroanal. Chem.* **372**, 101 (1994): *Solvent and Temperature Control of the Reaction Mechanism and Efficiency in the Electrogenenerated Chemiluminescence of Rubrene.*
- [208] S. Hofmann, M. Hummert, R. Scholz, R. Luschtinetz, C. Murawski, P.-A. Will, S. I. Hintschich, J. Alex, V. Jankus, A. P. Monkman, B. Lüssem, K. Leo, and M. C. Gather, *Chem. Mater.* **26**, 2414 (2014): *Engineering Blue Fluorescent Bulk Emitters for OLEDs: Triplet Harvesting by Green Phosphors.*
- [209] L. Wang, S. Chen, L. Liu, D. Qi, X. Gao, and A. T. S. Wee, *Appl. Phys. Lett.* **90**, 132121 (2007): *Thickness-Dependent Energy Level Alignment of Rubrene Adsorbed on Au(111).*
- [210] H. Ding and Y. Gao, *Appl. Phys. A* **95**, 89 (2009): *Electronic Structure at Rubrene Metal Interfaces.*
- [211] S. Sinha and M. Mukherjee, *J. Appl. Phys.* **114**, 083709 (2013): *Thickness Dependent Electronic Structure and Morphology of Rubrene Thin Films on Metal, Semiconductor, and Dielectric Substrates.*
- [212] H. Fukagawa, S. Hosoumi, H. Yamane, S. Kera, and N. Ueno, *Phys. Rev. B* **83**, 085304 (2011): *Dielectric Properties of Polar-Phthalocyanine Monolayer Systems with Repulsive Dipole Interaction.*
- [213] H. Ding, C. Reese, A. J. Mäkinen, Z. Bao, and Y. Gao, *Appl. Phys. Lett.* **96**, 222106 (2010): *Band Structure Measurement of Organic Single Crystal with Angle-Resolved Photoemission.*

- [214] R. Ahlrichs, M. Bär, M. Häser, H. Horn, and C. Kölmel, *Chem. Phys. Lett.* **162**, 165 (1989): *Electronic Structure Calculations on Workstation Computers: The Program System Turbomole.*
- [215] R. Scholz and A. Abbasi, *Phys. Status Solidi (c)* **7**, 236 (2010): *Influence of Dispersion Interactions on The Adsorption of PTCDA on Ag(110).*
- [216] C. J. Powell and A. Jablonski, *NIST Electron Effective-Attenuation-Length Database - Version 1.0* (2001), National Institute of Standards and Technology (Gaithersburg, MD).
- [217] X.-Q. Liu, H.-H. Kong, X. Song, L. Liu, and L. Wang, *Surf. Interface Anal.* **43**, 1494 (2011): *Ultrathin Monolayer of Rubrene on Au(111) Induced by Charge Transfer.*
- [218] M.-C. Blüm, M. Pivetta, F. Patthey, and W.-D. Schneider, *Phys. Rev. B* **73**, 195409 (2006): *Probing and Locally Modifying the Intrinsic Electronic Structure and the Conformation of Supported Nonplanar Molecules.*
- [219] M. Lan, Z.-H. Xiong, G.-Q. Li, T.-N. Shao, J.-L. Xie, X.-F. Yang, J.-Z. Wang, and Y. Liu, *Phys. Rev. B* **83**, 195322 (2011): *Strain-Driven Formation of Rubrene Crystalline Films on Bi(001).*
- [220] H. Glowatzki, G. Gavrilă, S. Seifert, R. Johnson, J. Räder, K. Müllen, D. Zahn, J. Rabe, and N. Koch, *J. Phys. Chem. C* **112**, 1570 (2008): *Hexa-perihexabenzocoronene on Ag(111): Monolayer/Multilayer Transition of Molecular Orientation and Electronic Structure.*
- [221] S. Duhm, H. Glowatzki, V. Cimpeanu, J. Klankermayer, J. P. Rabe, R. L. Johnson, and N. Koch, *J. Phys. Chem. B* **110**, 21069 (2006): *Weak Charge Transfer between an Acceptor Molecule and Metal Surfaces Enabling Organic/Metal Energy Level Tuning.*
- [222] G. Witte, K. Hänel, S. Söhnchen, and C. Wöll, *Appl. Phys. A* **82**, 447 (2006): *Growth and Morphology of Thin Films of Aromatic Molecules on Metals: The Case of Perylene.*
- [223] G. Witte, S. Lukas, P. S. Bagus, and C. Wöll, *Appl. Phys. Lett.* **87**, 263502 (2005): *Vacuum Level Alignment at Organic/Metal Junctions: "Cushion" Effect and the Interface Dipole.*
- [224] E. Ito, H. Oji, H. Ishii, K. Oichi, Y. Ouchi, and K. Seki, *Chem. Phys. Lett.* **287**, 137 (1998): *Interfacial Electronic Structure of Long-Chain Alkane/Metal Systems Studied by UV-Photoelectron and Metastable Atom Electron Spectroscopies.*

- [225] N. Koch, A. Vollmer, S. Duhm, Y. Sakamoto, and T. Suzuki, *Adv. Mater.* **19**, 112 (2007): *The Effect of Fluorination on Pentacene/Gold Interface Energetics and Charge Reorganization Energy.*
- [226] N. Koch, A. Gerlach, S. Duhm, H. Glowatzki, G. Heimel, A. Vollmer, Y. Sakamoto, T. Suzuki, J. Zegenhagen, J. P. Rabe, and F. Schreiber., *J. Am. Chem. Soc.* **130**, 7300 (2008): *Adsorption Induced Intramolecular Dipole: Correlating Molecular Conformation and Interface Electronic Structure.*
- [227] I. G. Hill, A. J. Mäkinen, and Z. H. Kafafi, *J. Appl. Phys.* **88**, 889 (2000): *Initial Stages of Metal/Organic Semiconductor Interface Formation.*
- [228] M. Pivetta, M.-C. Blüm, F. Patthey, and W.-D. Schneider, *Chem. Eur. J. of Chem. Phys.* **11**, 1558 (2010): *Coverage-Dependent Self-Assembly of Rubrene Molecules on Noble Metal Surfaces Observed by Scanning Tunneling Microscopy.*
- [229] M. Pivetta, M.-C. Blüm, F. Patthey, and W.-D. Schneider, *J. Phys. Chem. B* **113**, 4578 (2009): *Three-Dimensional Chirality Transfer in Rubrene Multilayer Islands on Au(111).*
- [230] J. A. Miwa, F. Cicoira, J. Lipton-Duffin, D. F. Perepichka, C. Santato, and F. Rosei, *Nanotechnology* **19**, 424021 (2008): *Self-Assembly of Rubrene on Cu(111).*
- [231] G. Tomba, M. Stengel, W.-D. Schneider, A. Baldereschi, and A. De Vita, *ACS Nano* **4**, 7545 (2010): *Supramolecular Self-Assembly Driven by Electrostatic Repulsion: The 1D Aggregation of Rubrene Pentagons on Au(111).*
- [232] L. Wang, S. Chen, L. Liu, D. Qi, X. Gao, J. Subbiah, S. Swaminathan, and A. T. S. Wee, *J. Appl. Phys.* **102**, 063504 (2007): *Conformational Degree and Molecular Orientation in Rubrene Film by in Situ X-ray Absorption Spectroscopy.*
- [233] S. Kera, Y. Yabuuchi, H. Yamane, H. Setoyama, K. K. Okudaira, A. Kahn, and N. Ueno, *Phys. Rev. B* **70**, 085304 (2004): *Impact of an Interface Dipole Layer on Molecular Level Alignment at an Organic-Conductor Interface Studied by Photoemission Spectroscopy.*
- [234] H. Fukagawa, H. Yamane, S. Kera, K. K. Okudaira, and N. Ueno, *Phys. Rev. B* **73**, 041302 (2006): *Experimental Estimation of the Electric Dipole Moment and Polarizability of Titanyl Phthalocyanine Using Ultraviolet Photoelectron Spectroscopy.*

- [235] T. Breuer, M. A. Celik, P. Jakob, R. Tonner, and G. Witte, *J. Phys. Chem. C* **116**, 14491 (2012): *Vibrational Davydov Splittings and Collective Mode Polarizations in Oriented Organic Semiconductor Crystals*.
- [236] A. Girlando, L. Grisanti, M. Masino, I. Bilotti, A. Brillante, R. G. Della Valle, and E. Venuti, *Phys. Rev. B* **82**, 035208 (2010): *Peierls and Holstein Carrier-phonon Coupling in Crystalline Rubrene*.
- [237] E. Venuti, I. Bilotti, R. G. Della Valle, A. Brillante, P. Ranzieri, M. Masino, and A. Girlando, *J. Phys. Chem. C* **112**, 17416 (2008): *Polarized Raman Spectra of a Rubrene Single Crystal*.
- [238] R. J. Thompson, B. Yadin, Z. J. Grout, S. Hudziak, C. L. Kloc, O. Mitrofanov, and N. J. Curson, *Appl. Phys. Lett.* **98**, 053302 (2011): *Evolution of the Surface Morphology of Rubrene under Ambient Conditions*.
- [239] T. Matsukawa, M. Yoshimura, M. Uchiyama, M. Yamagishi, A. Nakao, Y. Takahashi, J. Takeya, Y. Kitaoka, Y. Mori, and T. Sasaki, *Jpn. J. Appl. Phys.* **49**, 085502 (2010): *Polymorphs of Rubrene Crystal Grown from Solution*.
- [240] T. Petrenko, O. Krylova, F. Neese, and M. Sokolowski, *New J. Phys.* **11**, 015001 (2009): *Optical Absorption and Emission Properties of Rubrene: Insight from a Combined Experimental and Theoretical Study*.
- [241] R. Scholz, L. Gisslén, B.-E. Schuster, M. B. Casu, T. Chassé, U. Heinemeyer, and F. Schreiber, *J. Chem. Phys.* **134**, 014504 (2011): *Resonant Raman Spectra of Diindenoperylene Thin Films*.
- [242] P. Irkhin, A. Ryasnyanskiy, M. Koehler, and I. Biaggio, *Phys. Rev. B* **86**, 085143 (2012): *Absorption and Photoluminescence Spectroscopy of Rubrene Single Crystals*.
- [243] C. H. Choi and M. Kertesz, *Macromolecules* **30**, 620 (1997): *Conformational Studies of Vibrational Properties and Electronic States of Leucoemeraldine Base and Its Oligomers*.
- [244] L. Cuff and M. Kertesz, *Macromolecules* **27**, 762 (1994): *Ab Initio Oligomer Approach to Vibrational Spectra of Polymers: Comparison of Helical and Planar Poly(p-phenylene)*.
- [245] E. Adamski, Diplomarbeit, Eberhard-Karls-Universität zu Tübingen (2012): *Wachstum und Morphologie von perfluorierten und halbfluorierten Rubren-Dünnschichten*.

- [246] D. E. Henn, W. G. Williams, and D. J. Gibbons, *J Appl Crystallogr* **4**, 256 (1971): *Crystallographic Data for an Orthorhombic Form of Rubrene*.
- [247] O. D. Jurchescu, A. Meetsma, and T. T. M. Palstra, *Acta Cryst.* **B62**, 330 (2006): *Low-temperature Structure of Rubrene Single Crystals Grown by Vapor Transport*.
- [248] W. H. Taylor, *Z. Kristallogr.* **93**, 151 (1936): *X-Ray Measurements on Diflavylene, Rubrene, and Related Compounds*.
- [249] L. Huang, Q. Liao, Q. Shi, H. Fu, J. Mab, and J. Yao, *J. Mater. Chem.* **20**, 159 (2010): *Rubrene Micro-crystals from Solution Routes: Their Crystallography, Morphology and Optical Properties*.
- [250] M. D. Curtis, J. Cao, and J. W. Kampf, *J. Am. Chem. Soc.* **126**, 4318 (2004): *Solid-State Packing of Conjugated Oligomers: From π -Stacks to the Herringbone Structure*.
- [251] Y. Ishii, T. Shimada, N. Okazaki, and T. Hasegawa, *Langmuir* **23**, 6864 (2007): *Wetting-dewetting Oscillations of Liquid Films during Solution-mediated Vacuum Deposition of Rubrene*.
- [252] T. Shimada, Y. Ishii, K. Ueno, and T. Hasegawa, *J. Cryst. Growth* **311**, 163 (2008): *Nucleation on the Substrate Surfaces during Liquid Flux-mediated Vacuum Deposition of Rubrene*.
- [253] P. Zhang, X. Zeng, J. Deng, K. Huang, F. Bao, Y. Qiu, K. Xu, , and J. Zhang, *Jpn. J. Appl. Phys.* **49**, 095501 (2010): *Growth Mechanism of Large-Size Rubrene Single Crystals Grown by a Solution Technique*.
- [254] Y. Su, J. Liu, L. Zheng, Z. Ding, and Y. Han, *RSC Adv.* **2**, 5779 (2012): *Polymer Assisted Solution-processing of Rubrene Spherulites via Solvent Vapor Annealing*.
- [255] Y. Chen and I. Shih, *Appl. Phys. Lett.* **94**, 083304 (2009): *High Mobility Organic Thin Film Transistors Based on Monocrystalline Rubrene Films Grown by Low Pressure Hot Wall Deposition*.
- [256] M.-C. Blüm, E. Cavar, M. Pivetta, F. Patthey, and W.-D. Schneider, *Angew. Chem. Int. Ed.* **44**, 5334 (2005): *Conservation of Chirality in a Hierarchical Supramolecular Self-Assembled Structure with Pentagonal Symmetry*.
- [257] M. Pivetta, M.-C. Blüm, F. Patthey, and W.-D. Schneider, *Angew. Chem. Int. Ed.* **47**, 1076 (2008): *Two-Dimensional Tiling by Rubrene Molecules Self-Assembled in Supramolecular Pentagons, Hexagons, and Heptagons on a Au(111) Surface*.

BIBLIOGRAPHY

- [258] C. H. Hsu, J. Deng, C. R. Staddon, and P. H. Beton, *Appl. Phys. Lett.* **91**, 193505 (2007): *Growth Front Nucleation of Rubrene Thin Films for High Mobility Organic Transistors.*
- [259] C. Zhang, C. Du, H. Yan, S. Yuan, and L. Chi, *RSC Adv.* **3**, 15404 (2013): *Influence of Self-Assembled Monolayers on the Growth and Crystallization of Rubrene Films: A Molecular Dynamics Study.*
- [260] L. Raimondo, E. Fumagalli, M. Moret, M. Campione, A. Borghesi, and A. Sassella, *J. Phys. Chem. C* **117**, 13981 (2013): *Epitaxial Interfaces in Rubrene Thin Film Heterostructures.*
- [261] E. Fumagalli, M. Campione, L. Raimondo, A. Sassella, M. Moret, L. Barba, and G. Arrighetti, *J. Synchrotron Rad.* **19**, 682 (2012): *Grazing-incidence X-ray Diffraction Study of Rubrene Epitaxial Thin Films.*
- [262] T. Djuric, A. Thierry, W. Grogger, S. Abd Al-Baqi, H. Sitter, and R. Resel, *Physica E* **41**, 1718 (2009): *Morphology and Crystallographic Properties of Rubrene Thin Films Grown on Muscovite(001).*
- [263] S.-W. Park, S. H. Jeong, J.-M. Choi, J. M. Hwang, J. H. Kim, and S. Im, *Appl. Phys. Lett.* **91**, 033506 (2007): *Rubrene Polycrystalline Transistor Channel Achieved through in situ Vacuum Annealing.*
- [264] P. R. Ribič and G. Bratina, *Surf. Sci.* **602**, 1368 (2008): *Initial Stages of Growth of Organic Semiconductors on Vicinal (0001) Sapphire Surfaces.*
- [265] P. R. Ribič and G. Bratina, *J. Phys. Chem. C* **111**, 18558 (2007): *Ripening of Rubrene Islands.*
- [266] P. R. Ribič and G. Bratina, *J. Vac. Sci. Technol. B* **25**, 1152 (2007): *Influence of Substrate Morphology on Growth Mode of Thin Organic Films: An Atomic Force Microscopy Study.*
- [267] Y. Luo, M. Brun, P. Rannou, and B. Grevin, *phys. stat. sol. (a)* **204**, 1851 (2007): *Growth of Rubrene Thin Film, Spherulites and Nanowires on SiO₂.*
- [268] H. Zaglmayr, L. Sun, G. Weidlinger, S. A. Al-Baqi, H. Sitter, and P. Zeppenfeld, *Synth. Met.* **161**, 271 (2011): *Initial Stage of Crystalline Rubrene Thin Film Growth on Mica (001).*

- [269] P. Scherrer, Nachr. Ges. Wiss. Göttingen, Math-Phys Kl. **1918**, 98 (1918): *Bestimmung der Größe und der inneren Struktur von Kolloidteilchen mittels Röntgenstrahlen.*
- [270] C. Lorch, R. Banerjee, C. Frank, J. Dieterle, A. Hinderhofer, A. Gerlach, and F. Schreiber, J. Phys. Chem. C **119**, 819 (2015): *Growth of Competing Crystal Phases of α -sexithiophene Studied by Real-time X-ray Scattering.*
- [271] *The Molecule-Metal Interface*, edited by N. Koch, N. Ueno, and A. T. S. Wee (2013), Wiley VCH (Weinheim).
- [272] G. Heibel, S. Duhm, I. Salzmann, A. Gerlach, A. Strozecka, J. Niederhausen, C. Bürker, T. Hosokai, I. Fernandez-Torrente, G. Schulze, S. Winkler, A. Wilke, R. Schlesinger, J. Frisch, B. Bröker, A. Vollmer, B. Detlefs, J. Pflaum, S. Kera, K. J. Franke, N. Ueno, J. I. Pascual, F. Schreiber, and N. Koch, Nature Chem. **5**, 187 (2013): *Charged and Metallic Molecular Monolayers through Surface-Induced Aromatic Stabilization.*
- [273] G. Heibel, I. Salzmann, S. Duhm, and N. Koch, Chem. Mater. **23**, 359 (2011): *Design of Organic Semiconductors from Molecular Electrostatics.*
- [274] A. Gerlach, T. Hosokai, S. Duhm, S. Kera, O. T. Hofmann, E. Zojer, J. Zegenhagen, and F. Schreiber, Phys. Rev. Lett. **106**, 156102 (2011): *Orientational Ordering of Nonplanar Phthalocyanines on Cu(111): Strength and Orientation of the Electric Dipole Moment.*

BIBLIOGRAPHY

LIST OF OWN PUBLICATIONS

- **F. Anger**, T. Breuer, A. Ruff, M. Klues, A. Gerlach, R. Scholz, S. Ludwigs, G. Witte, F. Schreiber *J. Phys. Chem. C* *accepted*, “Enhanced Stability against Oxidation of Rubrene by Partial and complete Fluorination”
- **F. Anger**, R. Scholz, A. Gerlach, F. Schreiber *J. Chem. Phys.* **2015** 142, 224703, “Vibrational modes and changing molecular conformation of perfluororubrene in thin films and solution”
- **F. Anger**, H. Glowatzki, A. Franco Cañellas, C. Bürker, A. Gerlach, R. Scholz, Y. Sakamoto, T. Suzuki, N. Koch, F. Schreiber *J. Phys. Chem. C*, **2015**, 119, 6769, “Interface Dipole and Growth Mode of Partially and Fully Fluorinated Rubrene on Au(111) and Ag(111)”
- R. Banerjee, J. Novák, C. Frank, M. Girleanu, O. Ersen, M. Brinkmann, **F. Anger**, C. Lorch, J. Dieterle, A. Gerlach, J. Drnec, S. Yu, F. Schreiber *J. Phys. Chem. C*, **2015**, 119, 5225, “Structure and Morphology of Organic Semiconductor-Nanoparticle Hybrids Prepared by Soft Deposition”
- **F. Anger**, R. Scholz, E. Adamski, K. Broch, A. Gerlach, Y. Sakamoto, T. Suzuki, F. Schreiber *Appl. Phys. Lett.*, **2013**, 102, 013308, “Optical properties of fully and partially fluorinated rubrene in films and solution”
- **F. Anger**, J. O. Ossó, U. Heinemeyer, K. Broch, R. Scholz, A. Gerlach, F. Schreiber *J. Chem. Phys.*, **2012**, 136, 054701, “Photoluminescence spectroscopy of pure pentacene, perfluoropentacene, and mixed thin films”

LIST OF OWN PUBLICATIONS

- K. Broch, U. Heinemeyer, A. Hinderhofer, **F. Anger**, R. Scholz, A. Gerlach, F. Schreiber Phys. Rev. B, **2011**, 83, 245307, "Optical evidence for intermolecular coupling in mixed films of pentacene and perfluoropentacene"
- **F. Anger**, Diplomarbeit
"Photoluminescence and Raman spectroscopy of pentacene/perfluoropentacene mixed thin films"

DANKSAGUNG

Diese Doktorarbeit ist das Ergebnis langjähriger Forschung, die ohne das helfende Mitwirken und die Unterstützung vieler anderer nicht möglich gewesen wäre. Da man dem fertigen Text in der Regel nicht immer ansieht, wieviel (Vor)Arbeit, Diskussionen und Anregungen im kleineren und größeren Kreis darin wirklich enthalten sind, soll an dieser Stelle der Versuch unternommen werden, all jenen gerecht zu werden, die an anderer Stelle oft zu unrecht unerwähnt bleiben.

Bei Prof. Dr. Frank Schreiber möchte ich mich für das Ermöglichen dieser Arbeit und das in mich gesetzte Vertrauen bedanken. Es ist nicht alltäglich, ein Projekt übertragen zu bekommen, das die Erforschung komplett neuer Materialien zum Ziel hat, die noch dazu hochaktuelle Derivate eines der bekanntesten organischen Halbleiter sind, und mit deren stets knappen Vorräten verantwortungsvoll zu haushalten war.

In diesem Zusammenhang möchte mich auch bei Prof. Dr. Toshiyasu Suzuki and Prof. Dr. Yuichi Sakamoto für die Zurverfügungstellung der fluorierten Rubrenderivate bedanken, deren Synthese sicherlich nicht unkompliziert und ohne Risiko ist.

Besonderer Dank gebührt Dr. Alexander Gerlach, der mir in allen Teilen meiner Arbeit für Fragen und Diskussionen mit unwahrscheinlicher Geduld zugänglich war und dessen zumeist einfach praktikable Ideen meine Herangehensweise maßgeblich mitbestimmten.

Mein wichtigster externer Ansprechpartner außerhalb unserer Arbeitsgruppe war mit Sicherheit Dr. Reinhard Scholz, der mir in vielen insbesondere theoretischen Fragen mit vielen Anregungen zu Seite stand. Er hat ganz wesentlichen Anteil an der Menge und Qualität der quantenchemischen Rechnungen, die ich an den High Performance Computing Ressourcen an der Uni Tübingen durchgeführt habe, und mit ihm diskutieren konnte.

Danken will ich an dieser Stelle auch den Sekretärinnen unserer Arbeitsgruppe, Sabine Ehrlich, Hannah Maurer und Alexandra Rötschke, die alle für sich in ihrer stets warmherzigen Art für die Belange der Doktoranden und Diplomanden eingetreten sind und mir auf unkomplizierte Weise erlaubt haben, mich auf die wissenschaftliche Arbeit zu konzentrieren.

Für das Begutachten der Arbeit danke ich den Berichterstattem, darunter insbesondere Prof. Dr. Alfred Meixner für die Co-Betreuung der Doktorarbeit.

Ich könnte die Liste der Personen, denen gegenüber ich mich an dieser Stelle verbunden fühle, fast unendlich fortsetzen, sehe mich aber auch gleichzeitig gegenüber dem Leser verpflichtet, in meinen Ausführungen knapp zu bleiben, und so mögen mir es diejenigen nachsehen, die im Folgenden den Eindruck haben, zu kurz gekommen zu sein.

Bei allen weiteren Kollegen in unserer Arbeitsgruppe möchte ich mich für viele lehrreiche fachliche Diskussionen, aber auch für eine angenehme Arbeitsatmosphäre bedanken, deren Ursprung oft in vielen Gesprächen über fachliche Themen hinaus entstanden ist. Darunter, insbesondere an Dr. Alexander Hinderhofer, Antoni Franco Cañellas, Bernd Hofferberth, Berthold Reisz, Dr. Christoph Bürker, Christopher Lorch, Evelyn Adamski, Dr. Fajun Zhang, Dr. Felix Roosen-Runge, PD. Dr. Hajo Schöpe, Dr. Hossein Yamani, Dr. Jiří Novák, Johannes Dieterle, Klaus Hagdorn-Wittern, Prof. Dr. Martin Oettel, Miriam Klopotek, Mostafa Mortazavifar, Olga Matsarskaja, Dr. Rupa Banerjee und Simon Weimer.

Dank auch an viele Freunde für die gemeinsame Zeit, die mir durch Sport oder Spieleabende die Zeit verschönerten, Alena Fischer, Alexander Horst, Andreas Deuchert, Dr. Carla Cederbaum, Dr. Christian Stehle, Frieder Dechent, Dr. Gerhard Bräunlich, Ingo Czerwinski, Dr. Jan-Jonas Lampart, Dr. Johannes von Kehler, Manuel Förderer, Maximilian Geissler, und viele weitere.

Für die langjährige Unterstützung bedanke ich mich bei meinen Eltern und Geschwistern, sowie insbesondere bei meiner Freundin Sabine Eckert. Danke für die schöne gemeinsame Zeit.

CURRICULUM VITAE

FALK HERBERT ANGER, FREIBURG IM BREISGAU, GERMANY — 24 OCTOBRE 1982

Education

- | | |
|-----------|--|
| 10/2010 | Phd at the Institut für Angewandte Physik |
| -8/2015 | at the Eberhard Karls Universität Tübingen, Thesis supervisor: Prof. Frank Schreiber
Thesis title: "Electronic, Vibronic, and Structural Properties of Fluorinated Rubrene" |
| 8/2010 | Diplom (MSc level) in physics. Grade: Very good
Eberhard Karls Universität Tübingen, Thesis supervisor: Prof. Frank Schreiber
Thesis title: "Photoluminescence and Raman spectroscopy
of pentacene/perfluoropentacene mixed thin films" |
| 2005 | Prediploma in physics and prediploma in mathematics
Eberhard Karls Universität Tübingen |
| 2002-2003 | Civil service (at the University Clinics in Tübingen) |
| 1993-2002 | Eberhard-Ludwigs-Gymnasium in Stuttgart (high school) |

Work/study abroad

- | | |
|---------|--|
| 9/2009 | Internship at MATGAS, campus de la Universitat Autònoma in Barcelona (Spain) |
| -2/2010 | Photoluminescence and Raman spectroscopy studies for diploma thesis. |
| 12/2006 | Internship at the University hospital in Tromsø (Norway) |
| -3/2007 | Evaluation of radiation doses with thermoluminescence dosimeter. |